



**Six degree of freedom active vibration
isolation using quasi-zero stiffness
magnetic levitation**

Tao Zhu

**School of Mechanical Engineering
The University of Adelaide
South Australia 5005
Australia**

A thesis submitted in fulfillment of the requirements
for the degree of Doctor of Philosophy in Mechanical Engineering
on 23 September 2013. Qualified on 17 December 2013

Abstract

Vibration is recognised as one of the most significant disturbances to the operation of mechanical systems. Many traditional vibration isolator designs suffer from the trade-off between load capacity and isolation performance. Furthermore, in providing sufficient stiffness in the vertical direction to meet payload weight requirements, isolators are generally overly stiff in the remaining five degrees of freedom (DOF). In order to address the limitations of traditional isolator designs, this thesis details the development of a 6-DOF active vibration isolation approach. The proposed solution is based on a magnetic levitation system, which provides quasi-zero stiffness payload support in the vertical direction, and inherent zero stiffness in the other five DOFs. The introduced maglev isolator also allows the static force and moment inputs from the payload to be adaptive-passively balanced using permanent magnets.

In this thesis, the theoretical background of the proposed maglev vibration isolation method is presented, which demonstrates the ability of the maglev system to achieve the intended vertical payload support and stiffness in the six degrees of freedom. Numerical models for calculating the forces and torques in the proposed maglev system are derived, and the analysis of the cross-coupling effects between the orthogonal DOFs of the isolator is also presented based on the developed system models. A mechanism is introduced by which the cross-coupling effects can be exploited to achieve load balancing for static inputs using permanent magnet forces alone.

Following the development of the theoretical model, the mechanical design of the maglev isolator is presented. The designs of the various control systems that are necessary to enable the operation of the maglev isolator are explained. The presented control algorithms achieve three functions: stabilisation of the inherently unstable maglev system, adaptive-passive support of the payload using the cross-coupling effects introduced previously, and autonomous magnet position tuning for online system performance optimisation.

Abstract

Following the discussion of the controller design, a 6-DOF skyhook damping system is presented. The active damping system creates an artificial damping effect in the isolation system to reduce the vibration transmissibility around the resonance frequency of the system. The vibration transmissibilities of the developed maglev isolator were measured in 6-DOF, and results are presented for various combinations of controller settings and damping gains. Through comparisons between the measured performance of the physical system and the predicted performance from theory, the developed maglev vibration isolator demonstrated its practical ability to achieve high performance vibration isolation in six degrees of freedom.

Statement of Originality

This work contains no material which has been accepted for the award of any other degree or diploma in any university or other tertiary institution and, to the best of my knowledge and belief, contains no material previously published or written by another person, except where due reference has been made in the text.

I give consent to this copy of my thesis when deposited in the University Library, being made available for loan and photocopying, subject to the provisions of the Copyright Act 1968. I also give permission for the digital version of my thesis to be made available on the web, via the University's digital research repository, the Library catalogue, the Australasian Digital Theses Program (ADTP) and also through web search engines, unless permission has been granted by the University to restrict access for a period of time.

Tao Zhu

Acknowledgements

I would like to acknowledge all of the people who have contributed to this thesis or supported me during my time as a postgraduate student.

First and foremost I would like to thank my three supervisors Ben Cazzolato, Anthony Zander and Will Robertson. Without their continued guidance, encouragement and technical assistance I would not have finished this thesis. I could not have asked for three better supervisors.

I am thankful to all of the staff in the electronics and mechanical workshop for assisting me with my designs and experiments and repairing the equipment I have broken, as well as to Dr Andrew Fleming for his assistance on the design of a signal processing system used in this research.

I would like to thank all of my friends here at The University of Adelaide who made my postgraduate experience so enjoyable. In particular, I would like to thank Shi Zhao, Nikan Torghabeh, Christy Hassan, Tommie Liddy, Saleh Mahmoud and Erwin Hamminga, whom I have shared the office and insightful discussions with.

Finally, I wish to express my great appreciation to my partner Xue Jin for her endless encouragement and support and for her great tolerance of my unbearable temper during the stressful months of the thesis writing.

Contents

1	Introduction.....	1
1.1	Introduction and research significance.....	1
1.2	Research aims and achievements.....	4
1.3	Structure of the thesis.....	6
1.4	Publications arising from this thesis	9
2	Literature Review.....	11
2.1	Introduction	11
2.2	Passive vibration isolation.....	13
2.2.1	Common passive isolators	13
2.2.2	Vibration transmissibility and isolator resonance	14
2.2.3	Linear and nonlinear passive isolation.....	16
2.2.4	Quasi-zero stiffness vibration isolation.....	18
2.3	Active vibration control.....	21
2.3.1	Active vibration control system configurations.....	21
2.3.2	Tonal and broadband active vibration control	23
2.3.3	Relative and inertial space measurements.....	24
2.3.4	Displacement, velocity and acceleration feedback	25
2.4	Maglev for vibration isolation.....	27
2.4.1	Stability of magnetic levitation	27
2.4.2	Maglev isolators	30
2.5	Research gaps and significance.....	40

Contents

2.5.1	6-DOF ultra low stiffness payload support.....	41
2.5.2	Non-contact payload support.....	41
2.5.3	Inherent design trade-off between payload capacity and vibration attenuation.....	42
2.5.4	Autonomous maglev system tuning.....	42
2.5.5	6-DOF fully active skyhook damping.....	43
3	Background Theory and Methods.....	45
3.1	Introduction.....	45
3.2	Significance of stiffness and damping.....	46
3.2.1	Vibration transmissibility and isolator compliance.....	46
3.2.2	Relative damping and inertial space damping.....	49
3.3	Modelling the maglev system.....	54
3.3.1	Kinematic model of the maglev.....	54
3.3.2	Dynamic model of the maglev system.....	55
3.4	Calculation of magnetic forces and torques.....	58
3.4.1	3D to 1D calculation simplification.....	58
3.4.2	1-D calculation of forces between cylindrical magnets.....	61
3.4.3	Assumptions for calculating the magnetic forces and torques.....	63
3.5	6-DOF modelling of the floater forces and torques.....	67
3.5.1	Analytical model of the forces and torques.....	67
3.5.2	Numerical model of the forces and torques.....	71
3.6	6-DOF levitation stiffness.....	74
3.6.1	Quasi-zero stiffness in the vertical direction (Z).....	74

3.6.2	Zero stiffness in the horizontal directions (X and Y)	78
3.6.3	Zero stiffness in the rotational DOFs (α , β and γ).....	84
3.7	Adaptive-passive payload support.....	89
3.7.1	Supporting the payload weight.....	89
3.7.2	Adaptive-passive support for horizontal static loads	90
3.7.3	Adaptive-passive support static payload moments.....	92
3.8	Conclusion	93
4	Development of the Maglev Isolator	95
4.1	Introduction	95
4.2	Design of the 6-DOF maglev isolator	96
4.2.1	Floater Assembly.....	96
4.2.2	6D floater position monitoring	97
4.2.3	Frame assembly and actuators	99
4.2.4	Frame Magnet position control	101
4.2.5	Potential applications of the design	102
4.3	The manufactured vibration isolation system	103
4.4	Conclusion.....	105
5	Real-Time Control Systems.....	107
5.1	Introduction	107
5.2	Maglev stability control	109
5.2.1	Composition of the stability control system.....	109
5.2.2	Controller stiffness and maglev stability.....	112

Contents

5.2.3	Cross coupling of sensor measurements.....	114
5.2.4	Controller realisation and tuning	115
5.3	Adaptive-passive payload support	117
5.3.1	External disturbance monitoring.....	117
5.3.2	Supporting the payload weight	119
5.3.3	Supporting the horizontal forces and rotational torques	122
5.3.4	Comments on the interference and cross coupling of the adaptive-passive payload support	125
5.4	Autonomous maglev tuning	127
5.5	Conclusion and control system integration.....	129
6	System Performance.....	131
6.1	Introduction.....	131
6.2	Performance of the laser sensors.....	132
6.2.1	Sensor electric noise.....	132
6.2.2	Linearity of the laser sensor dynamic response	134
6.3	Performance of the actuation system.....	136
6.3.1	Determining the actuator sensitivity.....	136
6.3.2	Linearity of the actuation system.....	138
6.4	Floater structural vibration modes and resonance frequencies.....	141
6.5	Performance of the maglev stability control.....	147
6.5.1	Position command tracking (high controller gains)	147
6.5.2	Levitation induced vibration (low controller gains)	149
6.6	Performance of the adaptive-passive payload support.....	151

6.7	Performance of the maglev auto-tuning system	154
6.8	Conclusion	156
7	6-DOF Active Skyhook Damping	159
7.1	Introduction	159
7.2	Operating principles and system design	160
7.3	Inertial space velocity sensing	163
7.3.1	Multi-stage hybrid filtering for geophone signals	163
7.3.2	Geophone magnetic shielding	169
8	Experimental Measurements of Vibration Transmissibility	173
8.1	Introduction	173
8.2	6-DOF vibration excitation	174
8.3	6-DOF transmissibility of the isolator	177
8.4	6-DOF isolator cross coupling	183
8.5	Transmissibility with skyhook damping	186
9	Conclusions and Future Research	195
9.1	Summary of thesis.....	195
9.1.1	Theoretical background	196
9.1.2	Design of the mechanical and control systems	197
9.1.3	Performance of the maglev vibration isolator.....	198
9.2	Conclusion	200
9.3	Future research	202
9.3.1	Non-linear controller structure for maglev system stabilisation.....	202

Contents

9.3.2	Centralised control for multi-isolator applications	203
9.3.3	Passive maglev stabilisation	203
	Appendix A: Inherent instability of passive magnetic levitation	218
	Appendix B: Floor vibration in the research laboratory	219
	Appendix C: Coefficients of the polynomial fitting for maglev force and torque modelling.....	222
	Appendix D: System Component Specifications	224
D.1	Relevant specifications of the Acuity AR200-12 laser displacement sensor ..	224
D.2	Specifications of the magnets and solenoids.....	225
D.3	Relevant specifications of the dSPACE DS1103 real-time control system.....	226
D.4	Relevant specifications of the Maxon servo-amplifier	228
D.5	Relevant specifications of the B&K 4381 accelerometer.....	229
D.6	Relevant specifications of the SM-24 Geophone.....	230
D.7	Relevant specifications of the MB-Modal 110 shaker	231
	Appendix E: Geophone Analogue Filter Circuit.....	232
	Appendix F: Drawings of the Isolator Mechanical Design	235

List of Figures

Figure 2.1: Transmissibility of a linear mass-spring-damper system.....	15
Figure 2.2: Schematic representation of the simplest system which can exhibit quasi-zero stiffness. (Carrella, 2007)	19
Figure 2.3: Typical force-displacement characteristic of the isolator shown in Figure 2.2, (Carrella, 2007).....	19
Figure 2.4: Geometry of the proposed near-zero-spring-rate device (Krishna & Shrinivasa, 2009)	20
Figure 2.5: Schematic of the quasi-zero stiffness isolator with Euler buckled beams (Liu <i>et al.</i> , 2013).....	21
Figure 2.6: General configurations of active vibration control systems.....	22
Figure 2.7: Schematic of spin stabilised magnetic levitation (Simon <i>et al.</i> , 1997).	29
Figure 2.8: Schematic of servomechanism levitation stabilisation system.	30
Figure 2.9: Photograph of the single DOF quasi-zero stiffness vibration isolator (Robertson <i>et al.</i> , 2006).	31
Figure 2.10: Schematic of a maglev spring with quasi-zero stiffness at $h=0$ (Robertson <i>et al.</i> , 2009).	32
Figure 2.11: Theoretical transmissibilities of the maglev spring (Robertson <i>et al.</i> , 2009).	32
Figure 2.12: Schematic of the single DOF vibration isolation table (Mizuno <i>et al.</i> 2007).	33
Figure 2.13: Frequency response of the vibration isolation table to direct disturbance (Mizuno <i>et al.</i> 2007).	34
Figure 2.14: A photograph of the 3-DOF zero compliance vibration isolator (Hoque <i>et al.</i> , 2006).	35
Figure 2.15: Schematics of the 3-DOF zero compliance vibration isolator system components (Hoque <i>et al.</i> , 2006).	35
Figure 2.16: A photograph of the 6-DOF zero compliance vibration isolation table (Mizuno <i>et al.</i> , 2006).	36
Figure 2.17: Schematic of the 6-DOF zero compliance vibration isolation system components (Mizuno <i>et al.</i> , 2006).	36

List of Figures

Figure 2.18: Structure of the HSLDS isolator (Zhou & Liu, 2010).	38
Figure 2.19: Interacting forces between the mass and the EM for varying currents through the electromagnets (Zhou & Liu, 2010).....	38
Figure 2.20: Nonlinear vibration isolator with quasi-zero stiffness characteristic (Xu <i>et al.</i> , 2013).....	39
Figure 2.21: Stiffness of the system when $D < D_{qzs}$, $D = D_{qzs}$ and $D > D_{qzs}$ (Xu <i>et al.</i> , 2013).....	40
Figure 3.1: Schematic of a single-DOF linear spring-damper isolator subject to ground excitation.	47
Figure 3.2: Vibration transmissibility plot using Equation (2.1) with different supporting stiffness, $c = 1 \text{ N/ms}^{-2}$; $m = 1 \text{ kg}$	48
Figure 3.3: Comparison between relative damping and inertial space damping.	50
Figure 3.4: Displacement transmissibility of a linear vibration isolator with relative damping.	51
Figure 3.5: Displacement transmissibility of a linear vibration isolator with inertial space damping.....	52
Figure 3.6: Schematic of the magnetic levitation system	54
Figure 3.7: Block diagram of the floater dynamic model.....	57
Figure 3.8: forces resulting from horizontal displacement between two magnets....	59
Figure 3.9: Comparison between the 3D method and the 1D approximation for calculating F_Y	60
Figure 3.10: Schematic of two coaxial cylindrical magnets.....	62
Figure 3.11: Free body diagram of the floater under horizontal displacement.....	65
Figure 3.12: Total magnetic torque due to horizontal floater displacement ($H_{\text{cyl}} = 25.4 \text{ mm}$, $D_{\text{cyl}} = 50.8 \text{ mm}$, $p_{12} = p_{43} = 100 \text{ mm}$, magnetization = 1.48 Tesla , $l = 208 \text{ mm}$).	66
Figure 3.13: Free body diagram of the maglev system model.....	67
Figure 3.14: Force displacement behaviour of the maglev system in the vertical direction (Z). See Table 3.2 for details of parameters used to define the system.	75

Figure 3.15: Floater force-displacement behaviour of F_Z with cross-DOF displacements.	77
Figure 3.16: Free body diagram of the floater under horizontal displacement	79
Figure 3.17: Floater force-displacement behaviour of F_X with cross-DOF displacements.	82
Figure 3.18: Floater force-displacement behaviour of F_Y with cross-DOF displacements.	83
Figure 3.19: A schematic of the floater under rotational displacement	85
Figure 3.20: Floater force-displacement behaviour of T_α with cross-DOF displacements.	86
Figure 3.21: Floater force-displacement behaviour of T_β with cross-DOF displacements.	87
Figure 3.22: Vertical force-displacement relationships of the maglev isolator for various nominal magnet separations.....	89
Figure 3.23: Torque-displacement behaviour of the maglev system under horizontal displacements with various nominal magnet separations.	93
Figure 4.1: The Floater Assembly.....	97
Figure 4.2: The Floater Assembly with the Laser Sensor Array	99
Figure 4.3: Detailed CAD model of the frame assembly.....	100
Figure 4.4: CAD model of the frame magnet position control unit.....	102
Figure 4.5: 6-DOF vibration isolation table concept created using four of the proposed maglev vibration isolators.	103
Figure 4.6: The manufactured 6-DOF maglev vibration isolator.	104
Figure 4.7: Detailed view of the manufactured Magnet Position Control unit	104
Figure 5.1: Subsystems of the maglev stability control.	109
Figure 5.2: Vertical levitation stiffness with stabilisation controller ($p = 100\text{mm}$)..	113
Figure 5.3: Cross coupled laser sensor measurement error.....	115
Figure 5.4: Structure of the maglev stability controller.....	116
Figure 5.5: Controller structure of the adaptive-passive payload weight support ..	119

List of Figures

Figure 5.6: Command magnet travelling speed vs. DC control current.	120
Figure 5.7: Controller structure for adapting disturbance in the α direction.	123
Figure 5.8: Command floater travelling speed vs. DC control current.	123
Figure 5.9: Command floater angular speed vs. DC control current.	125
Figure 5.10: Auto-tuning process for minimising the levitation stiffness in the vertical direction.	128
Figure 5.11: Integration of the control systems.	130
Figure 6.1: Measurement of the noise spectrum of the Acuity AR-200-12 laser sensor.	133
Figure 6.2: Noise spectrum of the Acuity AR-200 laser sensor (FFT properties: DC coupled, 128 averages, 1600 lines, Hanning window, 24,000Hz sampling frequency).	133
Figure 6.3: Experimental layout of the linearity testing for the laser sensor.	134
Figure 6.4: Bode plot between the laser sensor and the B&K accelerometer, along with the coherence of the measurement (FFT properties: DC coupled, 128 averages, 1600 lines, Hanning window, 24,000Hz sampling frequency).	135
Figure 6.6: Actuation force vs. solenoid current.	137
Figure 6.5: Experimental arrangement of the actuator sensitivity test.	137
Figure 6.7: Experimental setup of the actuator linearity test.	138
Figure 6.8: Frequency response of the actuation system (FFT properties: DC coupled, 128 averages, 1600 lines, Hanning window, 24,000Hz sampling frequency). ...	140
Figure 6.9: Equipment arrangement of the laser vibrometer for structural mode identification.	142
Figure 6.10: Photograph of the actuation method for broadband floater excitation.	142
Figure 6.11: Directions of the laser vibrometer scans.	143
Figure 6.12: Laser vibrometer scan and structural modes in the XY plane (FFT properties: DC coupled, 128 averages, 1600 lines, Hanning window, 20,000Hz sampling frequency).	144

Figure 6.13: Laser vibrometer scan and structural modes in the XZ plane (FFT properties: DC coupled, 128 averages, 1600 lines, Hanning window, 20,000Hz sampling frequency).....	145
Figure 6.14: Laser vibrometer scan and structural modes in the YZ plane (FFT properties: DC coupled, 128 averages, 1600 lines, Hanning window, 20,000Hz sampling frequency).....	146
Figure 6.15: Maglev position command tracking in 6-DOF	148
Figure 6.16: Levitation induced vibration: (a) in the X, Y and Z directions; (b) in the α , β and γ directions (FFT properties: DC coupled, 128 averages, 1600 lines, Hanning window, 24,000Hz sampling frequency).	150
Figure 6.17: Payload inputs into a supporting structure.	151
Figure 6.18: Control current time history data in the adaptive-passive payload support test.....	153
Figure 6.19: Floater pose time history data in the adaptive-passive payload support test.	153
Figure 6.20: Magnet position history during the vertical stiffness minimisation performance test.	155
Figure 7.1: System layout of the 6-DOF skyhook damping system.	160
Figure 7.2: Anticipated frequency response of the geophone loop shaping filter... ..	164
Figure 7.3: Frequency response of the analogue geophone loop shaping filter (FFT properties: DC coupled, 128 averages, 1600 lines, Hanning window, 24,000Hz sampling frequency).....	167
Figure 7.4: Frequency response of the digital geophone loop shaping filter (FFT properties: DC coupled, 128 averages, 1600 lines, Hanning window, 24,000Hz sampling frequency).....	167
Figure 7.5: Layout of the linearity testing for the laser sensor.....	168
Figure 7.6: Frequency response of the hybrid filtered inertial velocity measurement system (FFT properties: DC coupled, 128 averages, 1600 lines, Hanning window, 24,000Hz sampling frequency).	169
Figure 7.7: Exploded CAD model of the shielding can and geophone.....	170
Figure 7.8: Frequency response between shielded and non-shielded geophones exposed to solenoid electromagnetic field excitation (FFT properties: DC coupled, 128 averages, 1600 lines, Hanning window, 24,000Hz sampling frequency).	171

List of Figures

Figure 7.9: Experimental arrangement of the geophone shielding can performance test.....	171
Figure 8.1: 6-DOF excitation platform (current view showing Y direction excitation).	174
Figure 8.2: CAD assemblies of the 6-DOF excitation platform.....	175
Figure 8.3: Vibration transmissibilities of the isolator in six DOFs. Red curve: measured isolator response; Blue curve: predicted isolator response with assumed zero stiffness (FFT properties: DC coupled, 128 averages, 1600 lines, Hanning window, 24,000Hz sampling frequency).....	178
Figure 8.4: Schematic of the individual PID stabilisation control loop.	179
Figure 8.5: Measurements of the cross coupling between DOFs. Horizontally across represents the input axis, vertically represents the response axis (FFT properties: DC coupled, 128 averages, 1600 lines, Hanning window, 24,000Hz sampling frequency).....	184
Figure 8.6: Comparison between the theoretical and experiment transmissibilities with various skyhook damping coefficients in the translational DOFs (FFT properties: DC coupled, 128 averages, 1600 lines, Hanning window, 24,000Hz sampling frequency).	188
Figure 8.7: Comparison between the theoretical and experiment transmissibilities with various skyhook damping coefficients in the rotational DOFs (FFT properties: DC coupled, 128 averages, 1600 lines, Hanning window, 24,000Hz sampling frequency).	189
Figure 8.8: 6-DOF isolator transmissibility with active skyhook damping (FFT properties: DC coupled, 128 averages, 1600 lines, Hanning window, 24,000Hz sampling frequency).	192
Figure B.1: Displacement of laborotary floor vibration in mm (FFT properties: DC coupled, 128 averages, 3200 lines, Hanning window, 24,000Hz sampling frequency).....	220
Figure B.2: Displacement of laborotary floor vibration in inch (FFT properties: DC coupled, 128 averages, 3200 lines, Hanning window, 24,000Hz sampling frequency).....	221
Figure D.1: SM-24 series geophone form SENSOR (SENSOR, 2013).	230
Figure E.1: Circuit diagram of the analogue geophone filter (outer layer).	233
Figure E.2: Circuit diagram of the analogue geophone filter (inner layer).	234

List of Tables

Table 3.1: Physical parameters used in the 3D and 1D force calculations.....	60
Table 3.2: Physical properties of the cylindrical magnets.	63
Table 3.3: Physical representations of the vectors in pose polynomial.	73
Table 4.1: Physical properties of the isolation system	105
Table 6.1: PID gains used in the levitation position command tracking test	148
Table 6.2: PID gains used in the normal operation condition	150
Table 6.3: Results of the tests of isolator system components and controllers.....	156
Table D.1: Specifications of the Acuity AR200-12 laser displacement sensor.....	224
Table D.2: Specifications of the primary levitation magnet.	225
Table D.3: Specifications of the secondary actuator magnet.	225
Table D.4: Specifications of the solenoid.....	225
Table D.5: Specifications of the dSPACE DS1103 real-time control system.	226
Table D.6: Specifications of the Maxon servo-amplifier.....	228
Table D.7: Specifications of the B&K 4381 accelerometer.	229
Table D.8: Specifications of the SM-24 Geophone.	230
Table D.9: Specifications of the MB-Modal 110 shaker.....	231

Chapter 1

Introduction

1.1 Introduction and research significance

Vibration is recognised as one of the most significant disturbances to the operation of mechanical systems. In the manufacturing and tooling industry, external vibration decreases the productivity and the end product quality. In automotive and aerospace environments, vibration can also influence the accuracy of measurement systems, and adversely affect experiments.

In laboratories and many high-tech manufacturing applications, passive isolation solutions are often applied to attenuate ground-borne vibrations due to the simplicity, low cost and robustness of the passive systems. For example, common solutions include installing rubber mounting pads between the machine and floor (Harris, 1996; Nakra, 1998), or adding passive spring/dampers to the mechanical structure (Soong and Dargush, 1997).

In most conventional passive isolator designs, where mechanical couplings with linear stiffness are used to support the payload weight, a trade-off is unavoidable when determining the required stiffness of the mechanical support. Load capacity and effective vibration isolation are the two most important aspects in the design of a vibration isolator. To support the payload, the isolator uses forces generated by

Chapter 1 Introduction

deflection in the resilient supporting structure. Therefore, large stiffness is required for supporting the payload weight to avoid excessive structural deflection. Conversely, to improve the vibration isolation performance, a low stiffness coupling is desirable in order to reduce the vibration transmissibility and resonance frequency of the isolation system (Neild and Wagg, 2010). Therefore, the contradiction in the design criteria is unavoidable.

Another problem in most of the conventional vibration isolator designs is that they do not perform equally well in all directions. These isolation systems are often only effective in a single degree of freedom (DOF), such as the spring-damper based designs, which can only attenuate vibrations in the direction along the spring and damper. However, the energy of structural vibrations is normally contained in more than one degree of freedom. In practice, it often spans the 6-DOF space. The cross coupling between each DOF significantly limits the performance of the single DOF designs since it allows the vibration energy to propagate into the primary isolation direction through structural coupling. For advanced applications, such as in semiconductor manufacturing and gravitational wave monitoring (LIGO Scientific Collaboration, 2012) where stringent multi-DOF vibration attenuation becomes necessary, the single DOF designs are not able to provide sufficient vibration isolation.

A common approach to enhance vibration isolation is through active vibration control techniques, which can substantially improve the isolation performance over what can be achieved by passive solutions, especially in the low frequency region. Active vibration control is most effective for vibrations characterised below 200Hz due to limitations posed by system hardware. For vibration isolation above 200Hz, the performance of passive systems is generally acceptable (Howard, 1999). Therefore, active vibration control techniques are generally combined with passive systems to create a hybrid isolation system achieving high performance, and delivering fail-safe vibration isolation.

Among the methods of active vibration control, magnetic levitation (maglev) has attracted significant research attention over the last decade as an approach to realise

1.1 Introduction and research significance

active vibration control. Electromagnets used in maglev systems are able to exert forces in a non-contact and controllable fashion. They often provide larger actuation bandwidth than mechanical actuators (such as hydraulic actuators) since no motion of mass objects is required for generating actuation forces. Therefore electromagnetic actuators are favourable in improving the performance of active vibration control systems. Permanent magnets are commonly seen in maglev systems as well. The nonlinear force-displacement relationship between magnets, although typically an undesirable characteristic, can be used to create supporting structures with desired nonlinear stiffness behaviour, and the stiffness non-linearity can be utilised to benefit vibration isolation applications. Several researchers have applied these inherent advantages of maglev to develop vibration isolation systems. A number of maglev based experimental isolators were built and tested in the last decade (Mizuno *et al.*, 2007; Carrella *et al.*, 2008; Robertson *et al.*, 2009; Frizenschaf *et al.*, 2011; Janssen *et al.*, 2013). However, only limited performance improvements were shown in multi-DOF vibration isolation.

Roberson *et al.* (2006) proposed a single DOF vibration isolator design using magnetic levitation, which provides the inspiration for the research in this thesis. The single DOF vibration isolation system is able to provide quasi-zero (near zero) levitation stiffness in the vertical direction while supporting the payload weight with static magnetic forces at the same time. The research presented in this thesis extends the previously proposed maglev design. Through uniquely developed mechanical and control algorithms, the maglev design has the potential to realise zero stiffness in all the other five DOF, which makes it a perfect candidate for developing a high performance multi-DOF vibration isolator.

This research is focused on how to develop a maglev based vibration isolation solution which effectively attenuates external vibration in all six DOFs. This thesis demonstrates the development of a unique maglev based vibration isolator, which realises quasi-zero/zero stiffness (quasi-zero stiffness in the vertical direction and zero stiffness in the remaining five directions) levitation in all the directions, and is able to support heavy payload with static magnetic forces. This feature enables the proposed

Chapter 1 Introduction

vibration isolation system to eliminate the design trade-off between payload support and vibration isolation, which is often unavoidable in the traditional isolator designs incorporating linear stiffness elements. The research presented in this thesis also investigates the method to apply active vibration control to the proposed maglev isolator. A 6-DOF skyhook damping system is developed to further improve the vibration isolation performance of the combined system. This unique maglev solution has been demonstrated to have the potential to outperform most of the conventional mechanical isolator designs.

1.2 Research aims and achievements

The aim of this research is to develop a maglev based vibration isolation system that attenuates external vibration in all six DOFs and is thus able to address the disadvantages identified in conventional isolator designs. To achieve this aim, the research can be divided into the following objectives.

- Identify the limitations of current vibration isolator designs.
- Investigate current techniques for improving vibration isolation performance in both active and passive vibration control areas.
- Develop new design concepts for realising maglev vibration isolation to address the identified problems that exist in the current isolator designs.
- Mathematically model the proposed designs to theoretically examine the feasibility and performance of the proposed maglev isolator.
- Develop a physical maglev vibration isolator based on the proposed design for experimental examination.
- Develop unique active control algorithms to enable system operation and optimise system performance.

1.2 Research aims and achievements

- Develop active vibration control approach for the proposed maglev isolation system to further improve the vibration isolation performance.
- Experimentally examine the performance of the proposed methods and designs and experimentally verify the advantages of the new maglev vibration isolator design.

In order to achieve these objectives, new work generated from this research are:

- Proposition of a novel maglev based vibration isolator design to realise 6-DOF vibration isolation.
- Theoretical demonstration of the ability of the design to create quasi-zero/zero stiffness levitation in all six DOFs.
- Development of a physical maglev vibration isolator for experimental validation of the proposed designs.
- Development and implementation of a low noise 6-DOF maglev stabilisation system to ensure the stability of the levitation.
- Development and implementation of novel control algorithms to realise adaptive-passive payload support and autonomous system tuning.
- Development and implementation of a 6-DOF skyhook damping system to apply active vibration control for further performance improvements in vibration isolation.
- Development of a 6-DOF vibration excitation platform for testing purposes to obtain vibration transmissibility measurements of the developed maglev vibration isolator.
- Experimental validation of the performance of the proposed 6-DOF maglev vibration isolation solution.

1.3 Structure of the thesis

This thesis begins by presenting a literature review of vibration isolation in Chapter 2. Common methods of passive vibration isolation are presented firstly, which include discussions on both linear and non-linear vibration isolation approaches. Quasi-zero stiffness concept is also introduced as an effective method to concurrently realise low stiffness vibration isolation and payload weight support. Following the discussions on passive vibration isolation, common methods of active vibration isolation are reviewed. Attenuation of tonal and broadband vibration is discussed, and advantages and disadvantages are summarised for active vibration isolation using displacement, velocity or acceleration feedback. In this chapter, magnetic levitation is introduced as a method to achieve vibration isolation. A number of examples are presented to demonstrate previous developments on maglev vibration isolation, which includes discussions on the quasi-zero stiffness maglev system proposed by Robertson *et al.* that forms the fundamentals of the research presented in this thesis. The identified research gaps and the significance of this research are concluded at the end of this chapter.

The theoretical background of this research is presented in Chapter 3. A kinematic model of the proposed maglev system is demonstrated, followed by the discussions on the calculation methods used to analytically determine the magnet forces and torques in the maglev system. A simplified method for calculating the magnetic forces and torques is proposed, which improves the calculation speed by allowing the estimation of the 3D forces and torques using a 1D approach. Polynomial regression is used next to obtain a numerical model of the proposed maglev system, which further reduces the calculation time by two orders of magnitude. Using the derived system models, levitation stiffness of the maglev system is calculated in all six DOFs. It is shown that the maglev system is able to provide quasi-zero stiffness levitation in the vertical direction while supporting the payload weight with a static magnetic force, and the levitation stiffness in the remaining five DOFs are zero. Cross-coupling effects between each pair of orthogonal DOFs are presented based on the system models

1.3 Structure of the Thesis

derived previously, and a method is proposed to utilise the identified cross-coupling effects to realise adaptive-passive payload support in multi-DOFs.

Chapter 4 presents a mechanical design to physically realise the proposed maglev vibration isolation method for experimental validation of the proposed theories. The design includes a 6-DOF levitation position sensing system, a 6-DOF solenoid actuation system, magnet position control units and the isolator frame structure for integrating all the sub-systems. Both CAD models of the design and photographs of the manufacture isolator are presented.

Chapter 5 demonstrates the control system designs proposed to enable the operation of the maglev isolator, as well as to realise all the intended functionalities discussed in Chapter 3. A maglev stability control system is presented firstly, which uses the 6-DOF position sensing and actuation systems to maintain a stable levitation position during the operation of the maglev isolator. Controller designs for realising adaptive-passive payload support in multi-DOFs are discussed next. The adaptive-passive payload support controllers enable the system to autonomously adjust the separations between the magnets and change the levitation position of the payload to actively balance the static force and torque inputs from the payload. An additional control system is also proposed at the end of the chapter, which automates the tuning process of the maglev system to maintain the quasi-zero stiffness characteristic in the vertical direction.

The performance of both the mechanical and control systems are assessed in Chapter 6 to identify the practical difficulties in realising the proposed maglev vibration isolation method. The characteristics of each system component are examined and discussed individually, and the experimental results are presented to demonstrate the effectiveness of the adaptive passive payload support and maglev auto-tuning systems. The results of 3D laser vibrometer scans are shown as well to identify the structural vibration modes of the proposed mechanical system of the isolator.

The design of a 6-DOF skyhook damping system is presented in Chapter 7. The skyhook damping system aims to attenuate vibration transmissibility of the maglev

Chapter 1 Introduction

isolator close to the system resonance frequencies in multiple DOFs. The design of a geophone array is presented, which monitors the inertial velocity of the levitated payload in 6-DOFs. A hybrid filtering method is proposed to extend the usable linear bandwidth of the geophones from 10Hz to 1Hz, so that the skyhook damping system can be more effective at low frequencies.

The vibration transmissibilities of the maglev system are presented in Chapter 8. This chapter starts by introducing the design of a 6-DOF vibration excitation platform, which is purposely built to excite the maglev isolator in 1-DOF at a time for all six DOFs. The measured vibration transmissibilities are presented next for various skyhook damping coefficients. These experimental results are compared with the theoretical transmissibilities derived by assuming zero inherent levitation stiffness in all six DOFs. By comparing the experimental and theoretical zero stiffness results, the isolator is proved to be able to realise quasi-zero/zero inherent levitation stiffness in all the six DOFs. It is also discussed that the overall system stiffness exhibited in the transmissibility measurements is mainly induced by the control system for maintaining the stability of the levitation. The experimental results for cross-coupled transmissibilities are shown at the end of this chapter, which validates the theoretical cross-coupling behaviours predicted in Chapter 3.

Finally, Chapter 9 provides a summary of this thesis, and concludes the results and findings of this research. Potential future works are also suggested as continuations of work presented in this thesis.

1.4 Publications arising from this thesis

The journal and conference publications arising from the research are as follows:

Journal publications

- Zhu, T., Cazzolato, B., Robertson, W., Zander, A., 2013. Vibration isolation using six degree-of-freedom quasi-zero stiffness magnetic levitation with adaptive-passive payload support and autonomous levitation optimisation. *Mechanical Systems and Signal Processing*, Manuscript under review.
- Zhu, T., Cazzolato, B., Robertson, W., Zander, A., 2013. Vibration isolation using six degree-of-freedom quasi-zero stiffness magnetic levitation. *Journal of Sound and Vibration*, Manuscript under review.

Conference publications

- Zhu, T., Cazzolato, B., Robertson, W., Zander, A., 2011. The development of a 6 degree of freedom quasi-zero stiffness Maglev vibration isolator with adaptive-passive load support. In: *Proceedings of the 15th International Conference on Mechatronics Technology*, Melbourne.

Chapter 2

Literature Review

2.1 Introduction

Vibration isolation has been an active research area for over a hundred years. A great number of designs and approaches have been proposed in this period, and the performance of vibration isolation systems have been dramatically improved over time. Prior to 1980, research in vibration isolation was mainly focused on passive approaches. With the developments made in computer sciences, digital control of mechanical systems was realised, which offers great flexibility in controller designs. As more complicated controller algorithms were able to be realised using digital control techniques, active vibration control became a very active research field since 1980.

In the past couple of decades, numerous studies and developments have been reported in the field of vibration isolation, which include both active and passive approaches based on linear or nonlinear systems. This literature review provides a brief summary of the recent advances made in vibration isolation, and identifies the current research gaps for further improving the performance of vibration isolation systems. The following topics have been identified in this literature review and form separate sections.

Chapter 2 Literature Review

Passive vibration isolation

This section reviews the developments made towards vibration isolation using passive means. Common methods for isolating both ground-borne vibration and onboard machine vibration are summarised. Comparisons between the linear and nonlinear solutions are also discussed.

Active vibration isolation

This section covers the common approaches to attenuate vibration using active control methods. The discussion contains two categories of active vibration isolation, control of tonal excitations and control of broadband excitations. Three general classes of mechanical design of the active control system are analysed, as well as a comparison between active vibration attenuation using displacement, velocity and acceleration feedback control.

Maglev for vibration isolation

In this section, magnetic levitation is introduced together with its applications and engineering designs. Stability problems of passive magnetic levitation are demonstrated, as well as methods commonly used for stabilising magnetic levitation systems. The potential of magnetic levitation in the field of vibration isolation is discussed, and several examples of previously developed maglev based vibration isolators are presented.

Research gaps and significance

The identified research gaps are presented in this section. The discussion includes descriptions of the potential improvements that can be made based on the current approaches, as well as methods proposed to address the identified problems in the research area.

2.2 Passive vibration isolation

Passive vibration isolation refers to vibration isolation using passive methods, such as installing rubber pads and mechanical springs between structure interfaces (Fahy and Walker, 1998). There are a great number of passive vibration isolators that are used extensively in engineering applications. The aspects common to these isolator designs are that they all employ a resilient structure to support the payload, and a damping component to absorb the residual vibration energy on the payload. The system characteristics of these passive designs are such that they are generally un-adjustable unless the system components are replaced.

2.2.1 Common passive isolators

The most commonly used structure among the passive isolator designs is the spring-damper assembly, which includes a mechanical spring to support and stabilise the payload, and a damping mechanism of some sort, either in the form of a dedicated element or inherent in the material itself, to absorb the vibration energy. This type of isolator design is widely used in industry since it has been thoroughly studied and system components are widely available at relatively low cost (Rivin, 2003). A common example of the spring-damper design is the suspension systems used in vehicles to isolate the vehicle from road roughness. They can also be found in some modern washing machines to isolate drum vibration during the spinning cycle.

Elastomeric pads can be used as isolators. Common resilient materials used in manufacturing of isolation pads are cork, felt, fibreglass, and metal mesh (Vér and Beranek, 2006). Such pads are normally very convenient and inexpensive as they can be easily cut into sizes required to fit various applications. The physical characteristics of the elastomeric pads can be controlled by selecting the pad dimensions. The area of the pad is chosen according to the weight of the load to be supported, and the thickness is chosen to provide the desired stiffness.

Another type of vibration isolation system that has found considerable use in vibration sensitive applications is the pneumatic isolator (or sometimes referred to as

Chapter 2 Literature Review

the air spring isolator). These isolators obtain their resilience from the pressure of compressed air in a confined volume. Air springs can be designed to have relatively small effective stiffness, while still being able to support a heavy payload. This enables air spring designs to deliver improved vibration isolation performance compared to mechanical spring systems since smaller isolator stiffness results in lower system natural frequency, and hence, lower vibration transmissibility. Practical air springs typically can provide fundamental resonance frequencies that may be as low as approximately 1 Hz (Vér and Beranek, 2006).

Pendulum vibration isolators are less commonly seen in traditional engineering applications. This type of isolator is primarily used in places where horizontal vibration isolation is more critical. The pendulum type isolators are normally able to provide ultra-low system natural frequency in the horizontal direction, and the system characteristics are controllable by designing the pendulum dimensions (Stephens *et al.*, 1990). Some of the designs also combine springs in the vertical direction to enable the isolator to attenuate vertical and horizontal vibrations simultaneously.

2.2.2 Vibration transmissibility and isolator resonance

The vibration isolation performance of an isolation system is often quantified by the vibration transmissibility of the isolator. It is the function characterising the transmissibility in the frequency domain, and is sometimes referred to as the isolator transfer function in some contexts. In general, vibration transmissibility is the ratio between the input and output of a vibration isolation system. It can be categorised into two types, force transmissibility and motion transmissibility. For example, in the case of an isolator for attenuating ground vibration, the force transmissibility is described as the fraction of the base excitation force transmitted to the payload, and the motion transmissibility is defined as the ratio between the motion intensity of the ground vibration and the payload vibration. Clarence (2005) has demonstrated that both the force and motion transmissibilities are equivalent due to the reciprocity characteristics in linear systems and it is sufficient to consider only one of them. In the research presented in this thesis, due to the relative simplicity of measuring payload motions,

2.2 Passive vibration isolation

the performance of the proposed maglev isolator was characterised using motion transmissibilities. The definition of motion intensity is normally in three forms: displacement, velocity and acceleration. Hence, motion vibration transmissibility can be sub-classified into these three forms. Since the three physical quantities are the different orders of the same system dynamics, the transmissibilities calculated for these three types of motion intensity have the same magnitude.

Figure 2.1(a) shows a typical single DOF linear mass-spring-damper system, and its transmissibility is shown in Figure 2.1(b), where $m=1\text{kg}$, $k=100\text{N/m}$ and $c=4\text{N}/(\text{ms}^{-1})$ are the payload mass, spring stiffness and the damping coefficient used to generate the transmissibility plot, respectively. In this scenario, the transmissibility (T) of the mass-spring-damper is defined as the ratio between the payload displacement, x , and the base displacement, y . It is calculated as (Harris, 1996):

$$T = \frac{x}{y} = \sqrt{\frac{1 + (2\zeta f/f_n)^2}{(1 - f^2/f_n^2)^2 + (2\zeta f/f_n)^2}}, \quad (2.1)$$

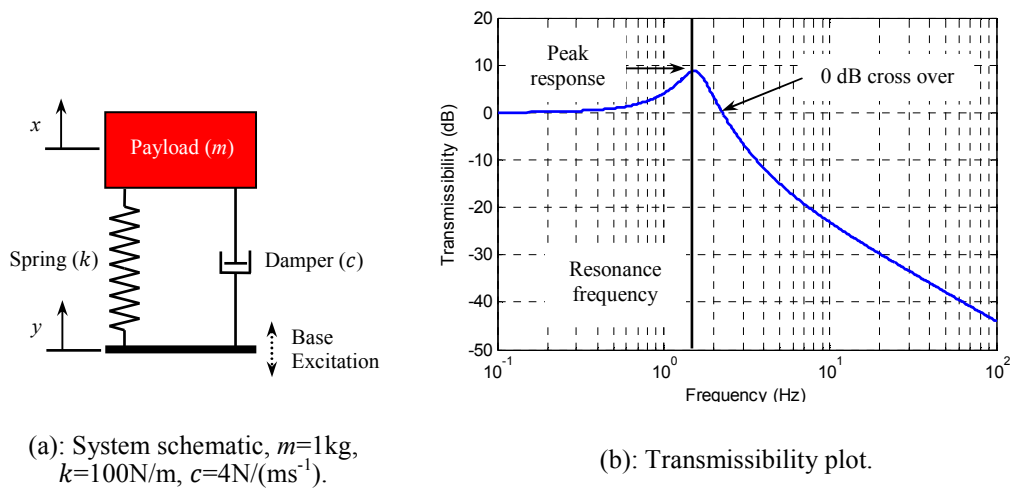


Figure 2.1: Transmissibility of a linear mass-spring-damper system.

Chapter 2 Literature Review

where f represents the base excitation frequency and $f_n = \frac{1}{2\pi} \sqrt{\frac{k}{m}}$ is the natural frequency of the isolation system. m , c and k are the payload mass (in kg), the damping coefficient (in N/ms^{-2}) and the spring stiffness (in N/m) respectively, and $\zeta = \frac{c}{2\sqrt{km}}$ represents the damping ratio of the isolator.

The evaluation of the vibration isolation performance normally includes (but is not limited to) assessing the three key aspects of the transmissibility curve, resonance frequency, 0 dB cross over and peak response. The resonance frequency represents the frequency at which the maximum displacement (the peak response) of the payload occurs. The peak response of the payload is generally larger than the base excitation amplitude of the system with only relative damping (demonstrated in Section 3.2.2), and is hence adverse the advise to isolating the external vibration. Therefore, in general, the design of the isolator should be made (normally by adding damping) such that the peak response of the isolator is acceptable for its target application. The 0dB cross over frequency, equals to $\sqrt{2}f_n$, is the marginal frequency where the payload and base have the same motion amplitudes. The isolation system starts to attenuate vibration beyond this frequency and the attenuation increases at certain rates depending on the characteristics of the isolator. The value of the 0 dB cross over frequency is directly related to the resonance frequency. An increase in the resonance frequency will result in an increase in the 0dB crossover frequency, and vice versa. Since vibration attenuation is only achieved beyond the 0 dB cross over frequency, it is generally desirable to have low isolator resonance frequency (and thus 0 dB cross over frequency) so that vibration attenuation is achieved from as low a frequency as possible. Section 3.2.2 will further discuss the practical method used in this research to achieve low system resonance frequency.

2.2.3 Linear and nonlinear passive isolation

Passive vibration isolators normally use a resilient structure to support the payload. According to the elastic behaviour of the supporting structure, passive vibration isolators can be categorised into linear and nonlinear types.

2.2.3.1 Linear vibration isolation

The structural stiffness of a linear vibration isolator remains constant regardless of either isolator static deflection (caused by the payload weight) or dynamic deflection (caused by the dynamic load exerted from external disturbances). A typical example is the coil spring isolator, where the spring force is a linear function of the spring deformation. In these isolators, the payload sensitivity to external disturbance is fixed, and is dependent on the stiffness of the supporting structure. A complete review of linear vibration isolation can be found in numerous undergraduate texts, for example, “Passive Vibration Isolation” (Rivin, 2003), which contains both theories and extensive examples of the applications of linear vibration isolators. Therefore, this content is not repeated here.

2.2.3.2 Nonlinear vibration isolation

Nonlinear vibration isolation theories have witnessed significant developments due to pressing demands for high performance vibration isolation. The stiffness and/or damping of the resilient structures used in these designs behave in a nonlinear fashion so that, by combining multiple non-linear supporting structures, the overall stiffness of the isolator can be more flexibly tuned to suit different applications (Ibrahim, 2008). Some common applications of nonlinear vibration isolators include: isolation of diesel engines in marine vessels; isolation of space craft; isolation of vehicle passengers from road disturbances; isolation of vibration generated by hand-held tools; and isolation of buildings, bridges, storage tanks and oil pipelines from destructive impacts from earthquakes.

In theory, nonlinear isolator designs are normally capable of achieving lower vibration transmissibility and resonance frequency than their linear counterparts. This is because in nonlinear designs a high stiffness supporting structure is not always necessary to support the payload weight. Many researchers have conducted studies to develop various isolator designs using nonlinear approaches (Ibrahim, 2008). Early theoretical work includes that presented by Den Hartog (1931), who developed an exact solution for analysing symmetric systems with both coulomb and viscous

Chapter 2 Literature Review

damping when subjected to a known harmonic forcing function. Dange and Gore (1978) investigated the magnitude of stiffness nonlinearity required in designing nonlinear vibration isolators with reference to the system resonance frequencies and vibration transmissibility, which were predicted under assistance of an analogue computer. With significantly improved computation power, Jiang *et al.* (2002) conducted a similar analysis using the finite element method.

Research was also conducted towards physical realisation of theoretical designs of nonlinear vibration isolation systems. A passive nonlinear mechanical isolator consisting of discrete mass, stiffness and damping elements was considered by Nayfeh *et al.* (1997) and Yu *et al.* (2006). Their method was able to greatly reduce the system resonance response and the level of transmitted vibration through the uniquely designed nonlinear stiffness behaviour. Winterflood *et al.* (2002) proposed a single DOF isolator which utilised the nonlinearity from Euler springs. In their design, the Euler spring buckling mode was used to construct a mechanical isolator that achieved a fundamental resonance frequency of less than 2 Hz. Azadi *et al.* (2011) also proposed and experimentally analysed the performance of a variable stiffness mount (VSM). In their design, the nonlinear resilient structure was constructed using a series of linear strings. The nonlinearity of the resultant system was controlled by prestressing the linear strings.

It is common to use mechanical linkages (such as coil springs and elastic strings) to create supporting structures with nonlinear stiffness. However, field forces (such as magnetic and gravitational forces) are becoming an increasingly popular method to introduce nonlinear system stiffness (Section 2.4).

2.2.4 Quasi-zero stiffness vibration isolation

As discussed previously, low payload supporting stiffness is favoured for vibration isolation purposes. Since the 1980s, the work in nonlinear vibration isolation has resulted in development of several designs that can achieve quasi-zero payload supporting stiffness (Alabuzhev *et al.*, 1989; Platus, 1991; Carrella *et al.*, 2008; Shaw, *et al.*, 2013; Yoshikazu *et al.*, 2013). Carrella *et al.* (2007) demonstrated and analysed

2.2 Passive vibration isolation

a very simple design for achieving quasi-zero stiffness using three linear springs, shown in Figure 2.2. By selecting the spring stiffness (k_o , k_v) and geometric parameters (L_o , h_o , a , θ_o), point P can have a vertical supporting force equal to f with zero vertical stiffness at that point. This can also be observed in the presented force-displacement characteristic plot, shown in Figure 2.3. At the equilibrium point (x_e), the vertical stiffness (slope of the curve) at point P is zero.

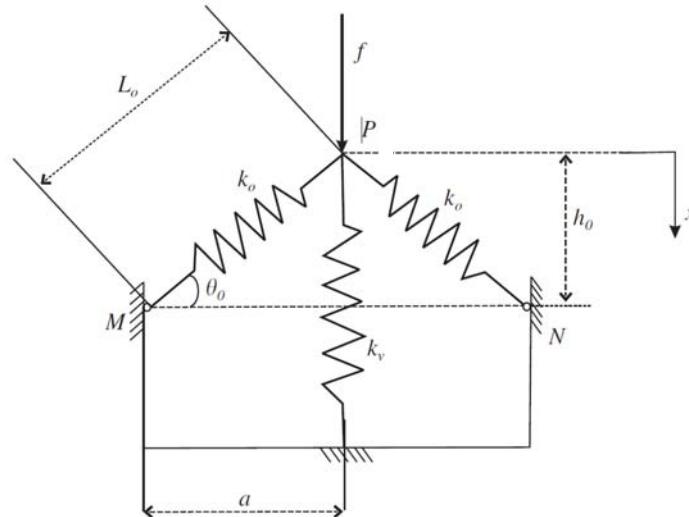


Figure 2.2: Schematic representation of the simplest system which can exhibit quasi-zero stiffness. (Carrella, 2007)

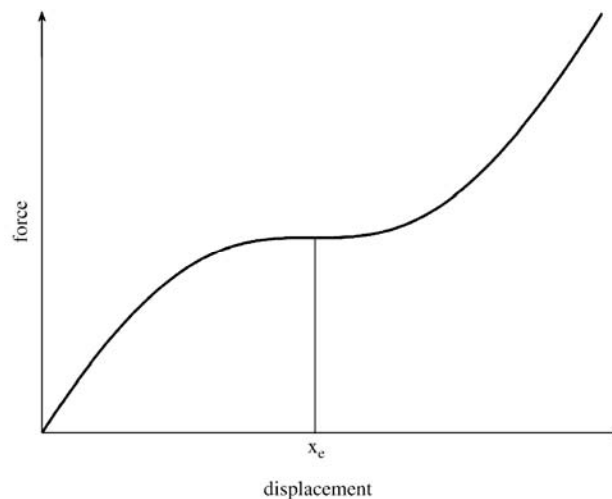


Figure 2.3: Typical force-displacement characteristic of the isolator shown in Figure 2.2, (Carrella, 2007).

A similar isolator design was presented by Krishna and Shrinivasa (2009), which has also achieved near zero spring rate also by combining three uniquely located linear

Chapter 2 Literature Review

coil springs. Figure 2.4 shows a schematic of their proposed design. In their system, the non-linear payload support structure is formed by two lateral springs and one vertical spring, having stiffness of k_s and k_c respectively. The vertical spring is used to support the static weight of the payload, and the orientation of the lateral springs are tuned together with the length of the vertical spring so that, at a specific point, the lateral spring stiffness cancels the stiffness of the vertical payload support spring. Therefore, this system is able to achieve quasi-zero vertical stiffness while supporting the payload with a static spring force.

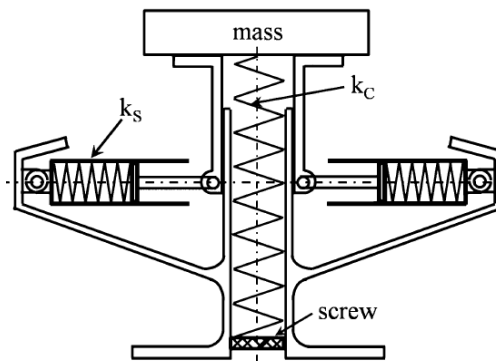


Figure 2.4: Geometry of the proposed near-zero-spring-rate device (Krishna & Shrinivasa, 2009)

Instead of creating quasi-zero stiffness using only linear stiffness elements, nonlinear structures, such as Euler buckled beams, may be applied to the design of quasi-zero stiffness isolators. Liu *et al.* (2013) proposed a quasi-zero stiffness isolator design (shown in Figure 2.5), which used Euler buckled beams to form the lateral supporting members with negative stiffness. By tuning the design parameters, the vertical support stiffness to the payload (m) is quasi-zero at the equilibrium point.

The research presented in this thesis uses a novel design of magnetic levitation system to realise quasi-zero stiffness payload support in the vertical direction. In addition, the 6-DOF maglev isolator design offers zero-stiffness payload support in all the other five DOFs. The maglev isolator employs active control systems to both stabilise the levitation as well as provide disturbance rejection. An overview of active control strategies relevant to vibration isolation are covered in Section 2.3. The previous work

2.3 Active vibration isolation

on magnetic levitation and its relevant applications in the vibration isolation field will be reviewed in Section 2.4.

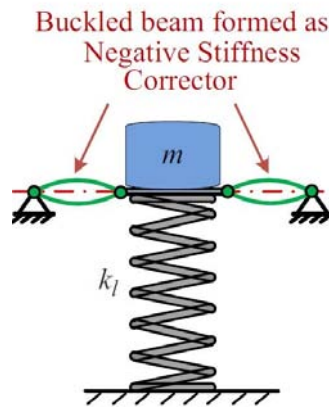


Figure 2.5: Schematic of the quasi-zero stiffness isolator with Euler buckled beams (Liu *et al.*, 2013)

2.3 Active vibration control

Active vibration control refers to methods of attenuating vibration using actuators to drive the system based on a control law and estimates or measurements of the inputs to the system and its response to these inputs. It is able to substantially improve the isolation performance over that achieved with passive systems. In general, an active vibration control system contains three subsystems in addition to a passive isolator, which are: a vibration monitoring component to measure the vibration condition in real-time, a control system to execute the algorithms for attenuating vibration, and an actuation system, commanded by the control system, to carry out the required physical actions. Depending on the mechanical layout, hardware performance and controller algorithms, active vibration control systems can be configured to treat different types of vibration.

2.3.1 Active vibration control system configurations

The common physical configuration of active vibration control systems may be categorised into three classes: the inertial type, the parallel type, and the series type (Howard, 1999), which are shown in Figure 2.6.

Chapter 2 Literature Review

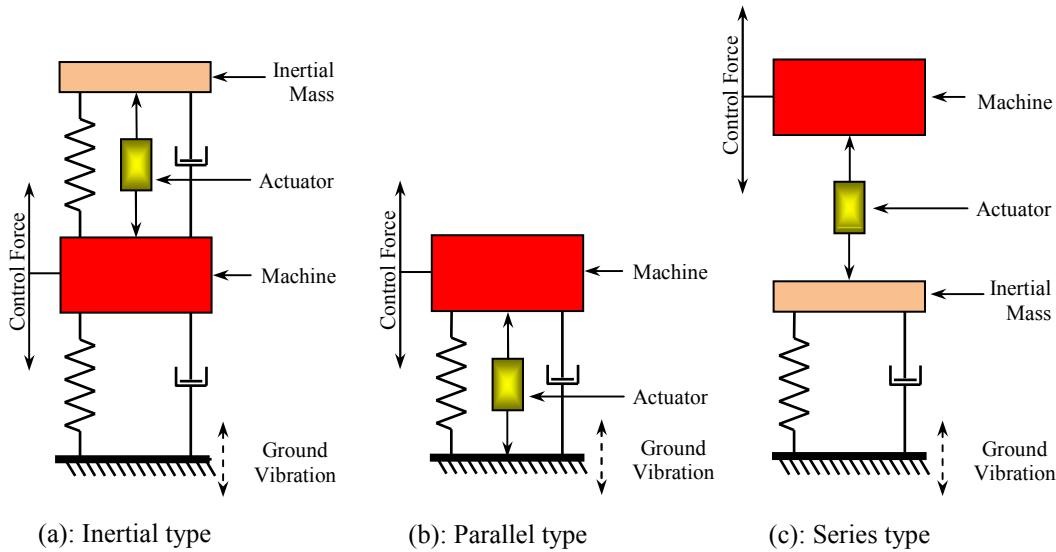


Figure 2.6: General configurations of active vibration control systems.

The inertial type (Tanaka & Kikushima, 1988; Zimmerman & Cudney, 1989; Benassi & Elliott, 2004) and the series type (Ross *et al.*, 1989; Sutcliffe *et al.*, 1989; Hoque *et al.*, 2006; Mizuno *et al.*, 2007) systems use an actuator and an inertial mass to generate a reaction force to counteract the vibration within the structure of the machine. These two types of systems generally have poor performance at low frequencies since the actuator is attached to the inertial mass, where large force at low frequencies will result in excessive inertial mass displacement. The inertial type systems support the weight of the inertial mass and machine with mechanical springs, while the series type requires the actuator system to carry the weight of the machine, which significantly increases the stress on the actuators. However, the series type active vibration control systems are two stage designs (mechanical passive stage and active control stage), which provides fail-safe protection should the active stage malfunction.

The parallel type design (Jenkins, 1989; Howard & Hansen, 1997; Preumont *et al.*, 2007) has the actuator connected in parallel to the mechanical supporting spring. This method is used in the research presented in this thesis to achieve active vibration control on the proposed maglev isolator. This is because the parallel configuration is capable of generating much larger control forces than the inertial and series type designs since the actuator is directly connected to a fixed structure. Hence, active

vibration control can be more effectively applied at low frequencies with this arrangement.

2.3.2 Tonal and broadband active vibration control

According to the frequency characteristic of the disturbance, vibration can be categorised into tonal or broadband excitations. Active vibration control for each of these two types of vibration generally takes different approaches.

2.3.2.1 Active control of tonal disturbance

Tonal disturbance refers to vibrations with a discrete power spectrum concentrated at one or more frequency points. These disturbances are often a result of cyclic inputs, which are commonly seen in rotating machines. The characteristic frequency of the disturbance is directly related to the operation speed of the rotating machines.

Early studies of active tonal vibration control were concentrated on using feedback control techniques (Olson, 1956; Conover, 1956; Balas & Canavin, 1977; Balas, 1978). These methods involve obtaining an error criterion from the measured vibration level, and using it to generate a proportional signal for controlling the actuators that counteract the primary vibration. By adjusting the amplitude and phase of this proportional control signal, the active vibration control system is able to minimise the residual vibration (Howard, 1999). However, in certain circumstances, such as with small error signals, the controller gain must be relatively large for the active vibration control to be effective. This may lead to instabilities in the control system due to dynamics of the controller hardware. For this reason, feed-forward systems are preferred for active tonal vibration control since the technique itself is inherently stable.

In the early 1990s, feed-forward techniques were effectively applied to actively attenuate harmonic disturbances (Jenkins *et al.*, 1990; Sommerfeldt & Tichy, 1990), such as vibrations resulting from unbalanced rotating machinery. This is mainly due to the ease of obtaining a reference signal for the feed-forward technique. For

Chapter 2 Literature Review

example, the characteristic frequency of the vibration caused by rotating machinery is related to the operating speed of the machine, and a reference signal can be obtained from a tachometer.

2.3.2.2 Active control of broadband disturbance

It is simpler to apply active vibration control to tonal disturbances than to broadband excitations. This is because the reference signal needed for tonal vibration control can normally be predicted from knowledge of the surrounding environment or the operation of the machine itself (Fuller *et al.*, 1996). However, the reference signal used in active control of broadband excitation cannot be predicted and has to be acquired in real-time using various sensors. The dynamics of the sensing and actuation systems can significantly limit the effectiveness of the active vibration control, which poses great challenges to the designs for attenuating broadband vibration.

Active control of broadband vibration is currently a very active research field. Feedback control (Benassi *et al.*, 2004; Preumont *et al.*, 2007; Ahmed Abu and Preumont, 2011) and feed-forward control (Yasuda *et al.*, 1996; Anderson & How, 1997; Jia *et al.*, 2010) have both been investigated for reducing the system vibration transmissibility in various applications. In the research presented in this thesis, one of the main aims is also to incorporate 6-DOF active vibration cancellation in the proposed maglev isolator.

2.3.3 Relative and inertial space measurements

It should also be noted that the choice of active vibration control approach and the performance of each method significantly depend on whether the feedback signal is measured in the relative frame or the inertial frame. The relative frame measurements often refer to measurements obtained by comparing the target states (acceleration, velocity or displacement) to that of a fixed point. For example, laser displacement sensors measure object distance by calculating the separation between the target and the sensor itself. The inertial frame measurements (also called absolute measurements)

2.3 Active vibration isolation

are obtained by quantifying target states in the inertial space, and are not the relative values to any known spatial point. For example, accelerometers and geophones measure the absolute acceleration and velocity of an object respectively. In general, active vibration control techniques effectively create a virtual linkage between the control target and the measurement frame of the feedback signal. Take Figure 2.6(b) as an example of an active vibration control system. In this case, if the machine states are measured relative to the ground, for ground vibration isolation, the active vibration control system will aim to weaken the connection between the machine and the ground so that the machine is less sensitive to ground motion. However, if the machine states are instead obtained in the inertial space, the active control system will need to strengthen the connection to the inertial frame since the inertial frame is considered to be absolutely stationary, and by firmly attaching the machine to the inertial frame, it is insensitive to ground motion.

2.3.4 Displacement, velocity and acceleration feedback

As mentioned previously, an active vibration control system uses actuators to counteract vibration according to the feedback vibration signal. The command signal to the actuation system is normally defined as the product (multiplication) of the vibration signal and the transfer function of the controller algorithm at each frequency. The vibration signal measured by the motion sensor can be the displacement, the acceleration or the velocity of the vibrating object. As a result, different control effort and controller algorithm designs are needed for each type of the feedback signal, and each method has distinct advantages and limitations.

Displacement feedback is considered to be a method of changing the static or dynamic stiffness of the system. In displacement feedback controllers, the actuation force often has a direct relationship to the displacement of the object. Hence, the control algorithms can be designed specifically to realise designed system stiffness behaviour so that the system frequency response is controllable (Hodges, 1989; Benassi & Elliott, 2004; Preumont, 2002). In the research presented in this thesis, one of the aims is to reduce the system natural frequency to the lowest possible value. In

Chapter 2 Literature Review

ordinary vibration isolation systems with finite stiffness, this is achievable by introducing an actively controlled structure that generates a negative stiffness to reduce the stiffness of the supporting structure. However, in the proposed maglev isolator design, the stiffness of the supporting structure is quasi-zero in all the DOFs (Section 3.6). Further reduction of stiffness will lead to negative overall stiffness, which causes system instability. Therefore, the displacement feedback method is not suitable for the proposed quasi-zero stiffness maglev isolator design.

Acceleration feedback control is another method of modifying the system frequency response. It alters the equivalent dynamic mass of the controlled object since the command actuation force is directly related to the magnitude of the acceleration of the object (Fuller & Elliott, 1996; Preumont *et al.*, 2001; Abu Hanieh & Preumont, 2010). In practice, there are often difficulties in realising direct acceleration feedback control due to controller stability problems. These are caused by signal phase distortions resulting from the high-pass and low-pass filters embedded in the system electronics, such as sensors, actuators and amplifiers (Brennan *et al.*, 2007). In the literature, some designs claimed to have used acceleration feedback (Futami *et al.*, 1983; Kwak *et al.*, 2002; Zhu *et al.*, 2005) for active vibration control. However, the dynamic order of the acceleration feedback was altered before feeding back to the control algorithms.

For a long period of time, velocity feedback control has been recognised as a simple and robust method for active vibration control (Dorf, 1967; Balas, 1979; Li & Goodall, 1999; Ahmadian *et al.*, 2004; Tao & Mak, 2006; Lang *et al.*, 2009). It has been successfully applied to achieve active vibration control for dedicated equipment (Serrand & Elliott, 2000; Elliott *et al.*, 2001; Kim *et al.*, 2001). The velocity feedback strategy is unconditionally stable when the sensors and actuators are collocated (Goh & Caughey, 1985), which allows larger control gains to be applied so that the peak vibration level (system response at resonance) can be substantially reduced. However, care should be taken when designing the controller so that the dynamics of the actuator and velocity transducer do not lead to system instabilities (Goh & Caughey, 1985). The research presented in this thesis applies velocity feedback control to achieve active vibration cancellation. A 6-DOF skyhook damping system is proposed

2.4 Maglev for vibration isolation

in Chapter 7 for reducing the peak response of the proposed maglev vibration isolator. Section 3.2.2 will introduce the fundamental theories of skyhook damping, as well as a performance comparison between relative damping and inertial damping (skyhook damping).

2.4 Maglev for vibration isolation

Magnetic levitation technologies are used in a broad range of applications. It is commonly known as the technology commonly associated with high speed transportation, for example, the maglev train, which employs magnetic levitation forces to replace the conventional supporting wheels as a method of reducing frictional drag (Wang *et al.*, 2005). In industry applications, magnetic levitation is often found in the form of maglev bearings used to reduce the rotational drag of machine shafts (Hirani & Samanta, 2007; Sun & Feng, 2011). Maglev systems in the aforementioned applications are designed to maintain a constant levitation gap (Hasirci *et al.*, 2011; Zhou *et al.*, 2011), which normally induces high levitation stiffness. It can also be used to create low stiffness couplings to serve vibration isolation applications since the nonlinear force-displacement relationship between magnets can often be used to design a magnetic payload support of favourable stiffness behaviour. This section reviews the areas related to applications of maglev in vibration isolation.

2.4.1 Stability of magnetic levitation

As a result of Earnshaw's theorem (Earnshaw, 1842), passive magnetic levitation using only passive static magnetic fields is inherently unstable. Therefore, a stabilisation method has to be used to enable the stable operation of a maglev system.

2.4.1.1 Earnshaw's theorem of instability

Earnshaw's theorem (Earnshaw, 1842) stated that it is not possible to maintain a stable stationary equilibrium configuration solely by static, macroscopic and paramagnetic fields since the forces acting on any paramagnetic object in any

Chapter 2 Literature Review

combination of gravitational, electrostatic and magneto-static fields will make the object's position unstable along at least one axis. This theory can be understood in a simpler way as: stable magnetic levitation is not achievable with only static magnetic fields and magnets with stationary dipole directions. A summary of the mathematical proof of Earnshaw's theorem is shown in Appendix A.1.

2.4.1.2 Passive maglev stabilisation

Earnshaw's theorem shows that the position of a stationary dipole in a static magnetic field is inherently unstable. However, the dipole can still be stabilised using a passive and alternating magnetic field. Spin stabilised magnetic levitation is a maglev system which is stabilised by a fast rotating magnetic field (Simon *et al.*, 1997). An example of a simple spin stabilised magnetic levitation system is shown in Figure 2.7. The magnetic top is levitated via a repulsive force from the ring-shaped permanent magnet underneath. The rotational instabilities are controlled by the gyroscope effect from spinning at a specific speed. Levitron has applied this levitation theory on developing a toy called: The amazing anti-gravity top (Levitron, 2012). No engineering applications of the spin stabilised maglev have been reported as yet. Due to the spinning motion required for stabilisation, this technique is not considered suitable for application in a maglev isolator.

Diamagnetic levitation is another form of passive magnetic levitation has another form as diamagnetic levitation. This type of maglev uses the repulsion of a diamagnetic material (materials with relative permeability less than one) to magnetic fields to achieve levitation. Previous work has demonstrated a number of examples of maglev using diamagnetism (Ikezoe *et al.*, 1998; Berry, 1997; Chetouani *et al.*, 2006) which includes the demonstration of a prototype maglev train built using super conductors. Simon and Geim (2000) demonstrated the theories behind diamagnetic levitation in "Diamagnetic levitation: Flying frogs and floating magnets". Due to the low payload capacity and stabilisation issues related to diamagnetic levitation, it is not considered suitable for application to this research.

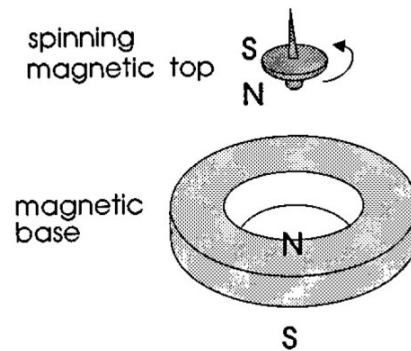


Figure 2.7: Schematic of spin stabilised magnetic levitation (Simon *et al.*, 1997).

2.4.1.3 Active maglev stabilisation

In modern maglev systems, almost all designs use a servomechanism type stabilisation system to maintain the position of the levitated object. In general, this technique uses sensors to monitor the position of the levitation, and uses actuators (commonly the electromagnetic type) to control the position of the levitated object to be at the desired point.

Figure 2.8 shows a schematic of the servomechanism type stabilisation system. In the control algorithm, the levitation position error is calculated between the sensor measured position and the command position. The error signal is then sent to a controller which commands the actuators to maintain the floating object at a desired location. In this research, a servomechanism system is used to stabilise the proposed quasi-zero stiffness maglev, with the aim of developing a suitable control algorithm to realise high performance 6-DOF levitation control for isolating vibrations.

Previous researchers have investigated a number of designs for stabilising maglev systems (Choi *et al.*, 2003; Gentili & Marconi, 2003; Wang *et al.*, 2005; Khamesee & Shameli, 2005; Verma *et al.*, 2005; Yang *et al.*, 2009; Zhang & Menq, 2007; Janssen *et al.*, 2012). System noise has also been addressed in some low noise control approaches for maglev based isolation systems. Some recent works includes a K-filter based design proposed by Yang *et al.* (2009), which aims to achieve accurate maglev

Chapter 2 Literature Review

positioning for applications where noisy position sensors are used. A back-stepping based controller design was reported by Wai and Lee (2008), who have investigated three types of back-stepping control approaches designed for maglev rail systems. A classic PID control approach was proposed by Su *et al.* (2004), in which the levitation stiffness and damping are directly controlled through the proportional and derivative gains of the PID controller. A tracking differentiator was also embedded in the differentiation loop to suppress noise. However, in order to realise accurate positioning, the designs discussed above all induced high levitation stiffness, which is counter to the criterion necessary for vibration isolation, and therefore, cannot be applied to the proposed maglev vibration isolator in this research.

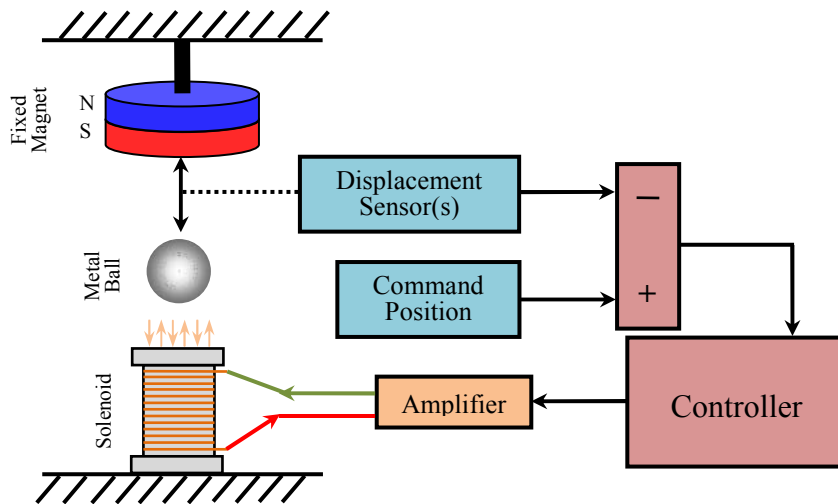


Figure 2.8: Schematic of servomechanism levitation stabilisation system.

2.4.2 Maglev isolators

Magnetic levitation has attracted a large amount of research attention for a substantial period of time. However, studies and developments related to maglev applied to vibration isolation have been mainly concentrated in the last decade. This is partially due to the recent improvements in the computational power and affordability of the controller hardware which enables flexible and high performance digital control to be applied to the maglev systems. This section reviews a few recent examples of developments in the maglev vibration isolation field. Other researchers have also made substantial contribution to the literature, including Nagaya and Ishikawa (1995), Choi *et al.* (2003), Ding, *et al.* (2010), Janssen *et al.* (2013).

2.4.2.1 Single DOF Quasi-zero stiffness vibration isolator

Robertson *et al.* (2006) developed a single-DOF quasi-zero stiffness active vibration isolator, a photograph of which is shown in Figure 2.9. Using four uniquely located permanent magnets, the design is able to create a levitation system whose stiffness approaches zero at the equilibrium point (where the gaps between the top and bottom pair of magnets are equal). The maglev system is passively stabilised through a mechanical coupling hinge in all the DOFs except the vertical direction. At the equilibrium position, the maglev is marginally stable vertically. Active stabilisation using back-stepping techniques was also applied to regulate the vertical position of the levitation.

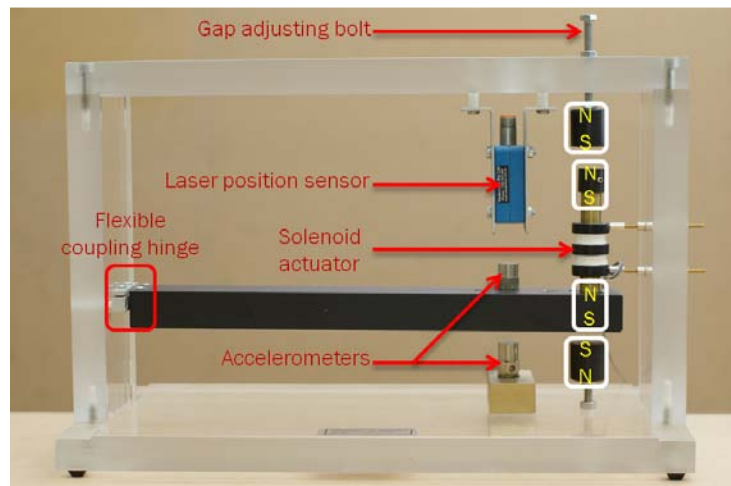


Figure 2.9: Photograph of the single DOF quasi-zero stiffness vibration isolator (Robertson *et al.*, 2006).

The design of the quasi-zero stiffness maglev concept was compared to a simple repelling maglev in terms of vibration transmissibility to demonstrate the advantages of the quasi-zero stiffness design. Robertson *et al.* (2009) further analysed the quasi-zero stiffness maglev design. Figure 2.10 is a schematic of the maglev spring with quasi-zero stiffness at $h=0$ to isolate displacement x from disturbance vibration y . In the figure, large arrows indicate the direction of polarisation of the magnets. Cubic magnets are used for the analysis with side length a , distance $2ad$ between the centres of the fixed magnets, and displacement of the floating magnet from the zero stiffness

Chapter 2 Literature Review

position of ah . The theoretical transmissibilities of the quasi-zero stiffness maglev spring design are shown in Figure 2.11, which shows the normalised force $f_z(d, h)$ vs. displacement h curves of the quasi-zero stiffness magnetic system for a range of normalised gap d . Single points correspond to the exact solution; solid lines correspond to the approximation given by Eq. (15) in the paper. The force vs. displacement curves clearly show that the system achieved localised zero stiffness at $h=0$, which is termed ‘quasi-zero stiffness’. It was shown in the research presented in this thesis that this unique quasi-zero stiffness maglev design has the potential to realise quasi-zero stiffness in all six DOFs, and forms the fundamental concept for this research project.

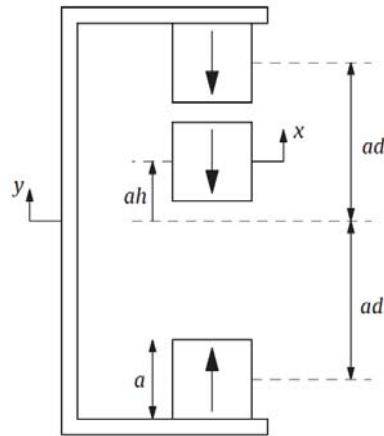


Figure 2.10: Schematic of a maglev spring with quasi-zero stiffness at $h=0$ (Robertson *et al.*, 2009).

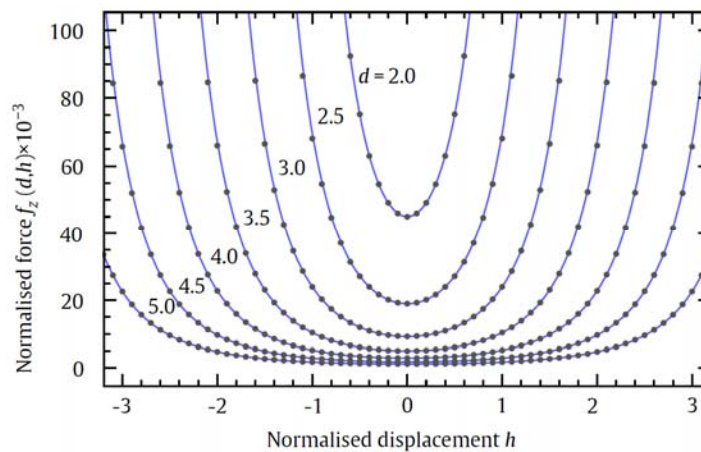


Figure 2.11: Theoretical transmissibilities of the maglev spring (Robertson *et al.*, 2009).

2.4.2.2 Maglev vibration isolator with infinite stiffness

A single DOF vibration isolation table was developed by Mizuno *et al.* (2007) using magnetic levitation for isolating onboard payload vibration. A schematic of the mechanical system and an outline of the maglev components are shown in Figure 2.12. In this design, the system aims to actively attenuate the onboard vibrations and reject step disturbances from payload changes. A so called zero compliance control algorithm was applied, using a PD controller, to create a negative stiffness component (Mizuno *et al.*, 2003) so that the overall system stiffness is infinitely large. This can be explained mathematically by the following. According to Figure 2.12(b), the overall system stiffness can be written as

$$k = \frac{k_1 k_2}{k_1 + k_2} + k_d \quad , \quad (2.2)$$

where k_1 is the spring stiffness supporting the maglev component, k_2 is the effective stiffness of the maglev component, and k_d is the spring stiffness supporting the table top (m_2). The controller in this system aims to realise a negative stiffness using the maglev component such that $k_2 = -k_1$. Therefore, the overall stiffness k approaches infinity.

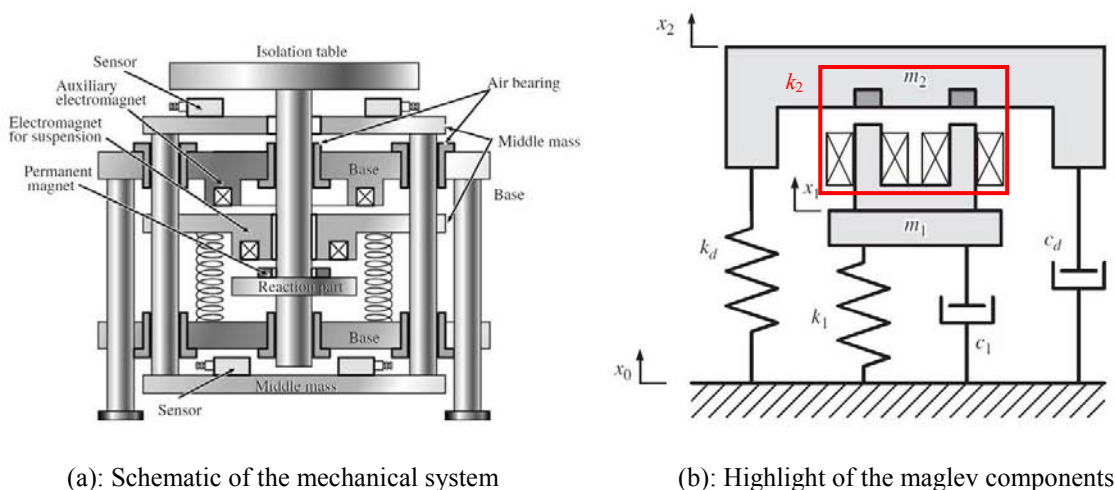


Figure 2.12: Schematic of the single DOF vibration isolation table (Mizuno *et al.* 2007).

Chapter 2 Literature Review

The zero compliance theory aims to create a linkage between the table top and the ground with infinite stiffness, so that the onboard disturbances will not result in table top displacement. Therefore, the structure has no compliance to external forces, and the position of the table top can be stabilised. Figure 2.13 shows the measured frequency response of the physical system. During the test, the table top was excited using an electromagnet with a harmonic force output. The frequency response was calculated using the force input as the input signal, and the table top/middle mass displacements as the output signal. From Figure 2.13, the isolation table demonstrated the ability to actively reduce the on board disturbances.

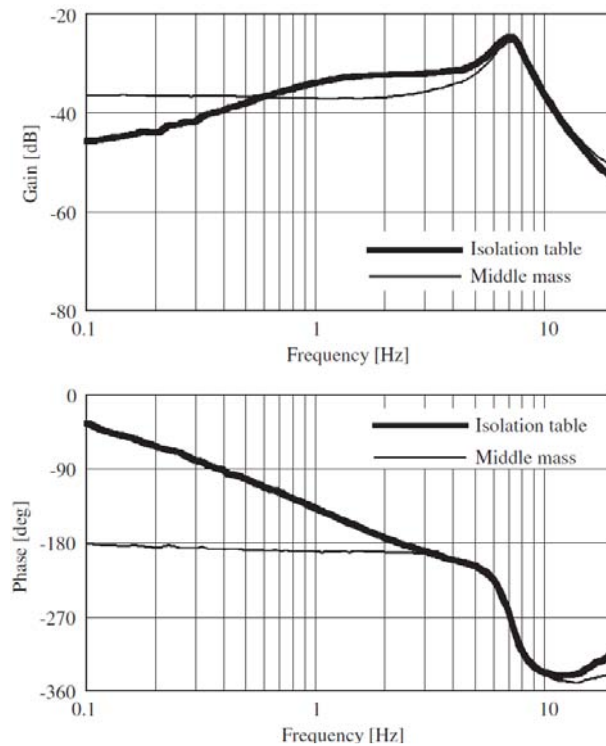


Figure 2.13: Frequency response of the vibration isolation table to direct disturbance (Mizuno *et al.* 2007).

The zero compliance design theory was not only used in single DOF systems, but was also applied to build a multi-DOF maglev isolator. A 3-DOF isolation table was designed and built by Hoque *et al.* (2006) based on the zero compliance theory. Figure 2.14 and Figure 2.15 shows a photograph and schematics of the developed system respectively. In this 3-DOF system, three of the zero-compliance magnetic

2.4 Maglev for vibration isolation

control units (Figure 2.15) were applied to realise active direct disturbance rejection in the vertical, pitch and roll directions.



Figure 2.14: A photograph of the 3-DOF zero compliance vibration isolator (Hoque *et al.*, 2006).

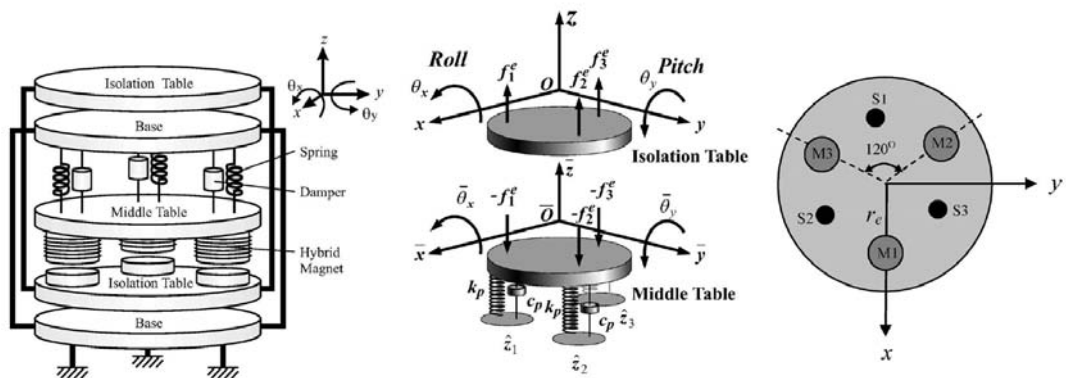


Figure 2.15: Schematics of the 3-DOF zero compliance vibration isolator system components (Hoque *et al.*, 2006).

In this multi-DOF system, the infinite stiffness control was carried out using both localised and centralised approaches. The localised method commands the three actuators individually through three SISO (Single Input Single Output) controllers, whereas the centralised control method (mode control) sends commands to all the actuators using a three channel MIMO (Multiple Input Multiple Output) controller. In both control modes, the isolation system showed the ability of attenuating onboard

Chapter 2 Literature Review

disturbances in the three DOFs. However, the results also indicated that no ground vibration isolation was achieved at low frequencies.

Based on the zero compliance design theory, Mizuno *et al.* (2006) also investigated a 6-DOF system built with six of the negative stiffness magnetic actuators. A photograph of the developed isolation table is shown in Figure 2.16. In the 6-DOF design, multiple actuators and zero-compliance maglev components (shown in Figure 2.17, subsystems 1 to 4 and actuators a to f) were used to realise the zero compliance control in all the six DOFs.

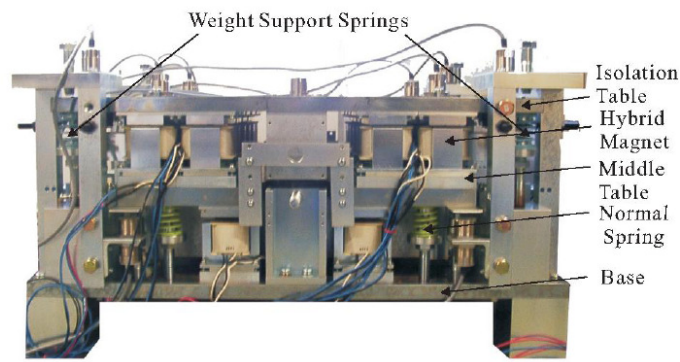


Figure 2.16: A photograph of the 6-DOF zero compliance vibration isolation table (Mizuno *et al.*, 2006).

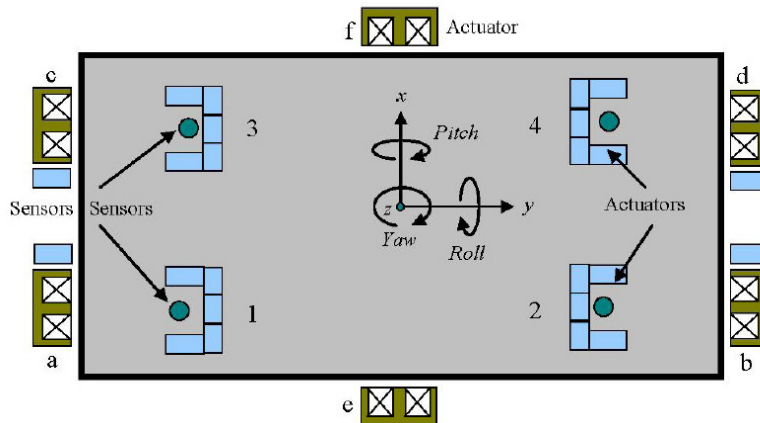


Figure 2.17: Schematic of the 6-DOF zero compliance vibration isolation system components (Mizuno *et al.*, 2006).

2.4 Maglev for vibration isolation

The zero compliance design theory aims to attenuate the onboard vibration generated by the payload by introducing an infinite stiffness ground coupling effect, which contradicts the interests of isolating the payload from ground-borne vibrations. The rigid linkage created by the negative stiffness control assists all ground vibration to propagate through to the payload without any attenuation, and even magnifies the vibration around resonance frequencies. Therefore, this method is not considered suitable for applications in this research.

2.4.2.3 HSLDS vibration isolator

The HSLDS (High Static Low Dynamic Stiffness) isolator design (Zhou & Liu, 2010) is a passive method that uses a static electromagnetic field to augment the magnetic field from permanent magnets. The resultant magnetic field is controlled by altering the characteristics of the electromagnetic field. Figure 2.18 shows the structure of the HSLDS isolator, and Figure 2.19 is the experimentally measured force-displacement relationship between the mass (permanent magnet) and the electromagnets.

From Figure 2.18, it can be seen that the flat beam used to support the permanent magnet has a higher stiffness in the vertical direction and a lower stiffness horizontally. Therefore, the device is able to support a heavy payload while isolating horizontal disturbances with a low stiffness. When electric current is supplied to the coils of the electromagnets, the resultant force-displacement relationship is changed accordingly. Figure 2.19 shows several curves corresponding to different values of current magnitudes. The slope of these force-displacement curves represents the stiffness of the magnetic coupling. It can be seen that with certain electric current, the stiffness is almost zero for a small range of displacement values (marked by the black dots on Figure 2.19), which indicate that this design is able to achieve a near-zero stiffness for isolating horizontal vibrations. One disadvantage of this design is that it has continuous power consumption in order to generate the static electromagnetic field. Furthermore, it only offers isolation in a single DOF.

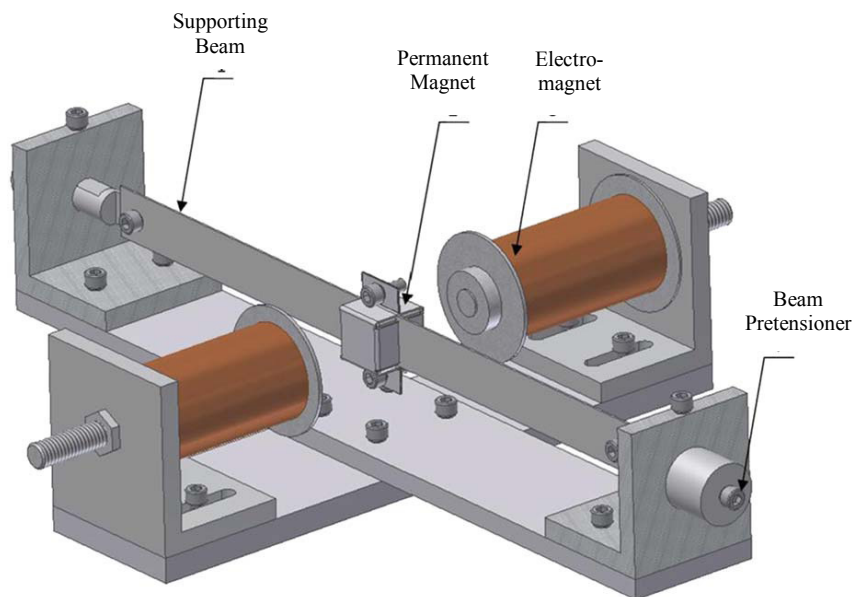


Figure 2.18: Structure of the HSLDS isolator (Zhou & Liu, 2010).

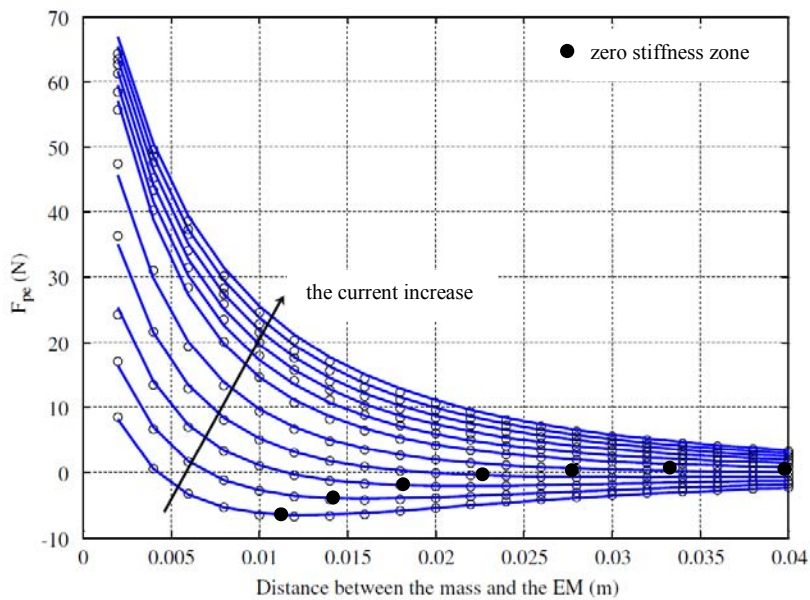
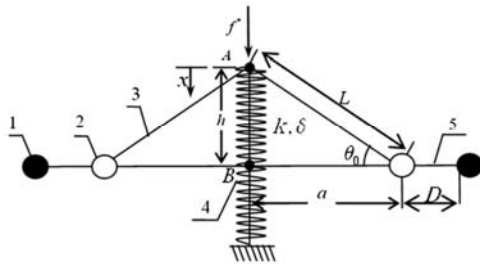


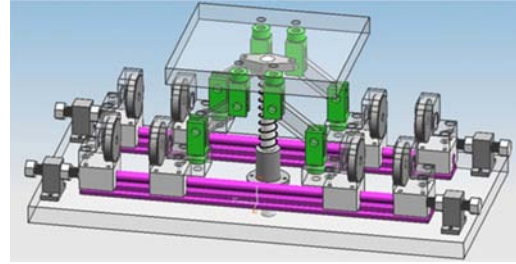
Figure 2.19: Interacting forces between the mass and the EM for varying currents through the electromagnets (Zhou & Liu, 2010).

2.4.2.4 Nonlinear vibration isolator with quasi-zero stiffness

As introduced in Section 2.2.4, multiple supporting elements can be combined to create structures with quasi-zero stiffness. Xu *et al.* (2013) proposed and analysed a nonlinear magnetic vibration isolator with quasi-zero stiffness characteristic. Figure 2.20 shows a system schematic and CAD model of their nonlinear magnetic vibration isolator.



(a) Schematic representation of the QZS system in the initial position before loading a mass. 1- Fixed magnet, 2-free sliding magnet, 3-connecting rod, 4-coil spring, and 5-linear guide.



(b): Prototype model of the proposed isolation system.

Figure 2.20: Nonlinear vibration isolator with quasi-zero stiffness characteristic (Xu *et al.*, 2013).

In Figure 2.20(a), L , h , a , θ_0 and D represent the geometric parameters of the system as labeled. k is the vertical spring stiffness, f^* is the spring compression force from the payload weight, and x is the vertical payload displacement from the equilibrium point (A) where the vertical spring force equals the payload weight. The system design uses a compressed (by δ) vertical coil spring to support the weight of the payload, and two sets of permanent magnet pairs on both sides of the spring to create negative stiffness. The negative stiffness created by the magnet pairs counteracts the positive stiffness of the vertical spring through the oblique connecting rod, and the whole system is tuned by adjusting the distance between the magnets (D) to realise quasi-zero stiffness. Figure 2.21 shows the theoretical vertical stiffness of the isolator for various magnet separations, where D and D_{qzs} are the magnetic separation and the separation required to realise quasi-zero vertical stiffness. The figure clearly shows that the stiffness of the isolator is zero in the vertical direction at $x = 0$ when $D = D_{qzs}$.

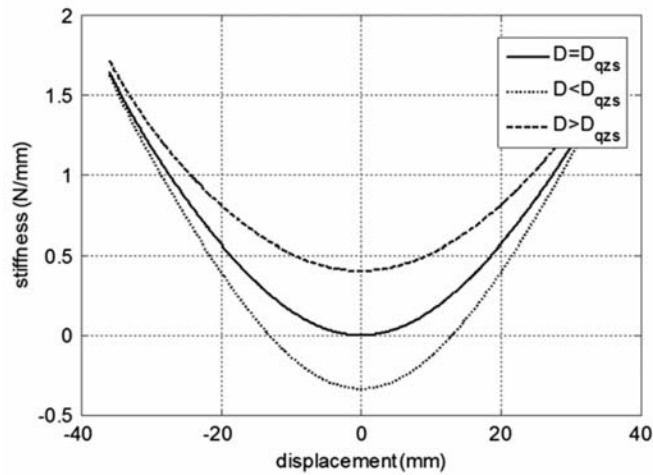


Figure 2.21: Stiffness of the system when $D < D_{qzs}$, $D = D_{qzs}$ and $D > D_{qzs}$ (Xu *et al.*, 2013).

Xu *et al.* (2013) successfully demonstrated the quasi-zero stiffness characteristic of the proposed isolator system in a single-DOF. However, this design used guide rails and linear bearings for mechanical constraint purposes. The stiction between moving components can significantly degrade the system performance with low acceleration excitations. In addition, the accurate tuning required to achieve the quasi-zero vertical stiffness may be difficult in practice since the isolator stiffness may not be easily observable.

2.5 Research gaps and significance

The aim of this research is to develop a novel approach for ground-borne vibration isolation, which has the potential to substantially improve the isolation performance over the previous passive and active isolator designs. To achieve this aim, firstly, the literature of vibration control was investigated to identify the factors that limit the performance of the previous isolator designs. Novel design concepts were then proposed to address the identified disadvantages. The following subsections summarise some of the main gaps associated with the existing vibration control techniques.

2.5.1 6-DOF ultra low stiffness payload support

A few methods have been reported to be able to achieve low stiffness payload support (Winterflood *et al.*, 2002; Zhou & Liu, 2010; Janssen *et al.*, 2013; Xu *et al.*, 2013). However, these methods are only capable of realising low stiffness support in one DOF, which limits the vibration isolation performance in practical applications since vibrations are normally contained in more than one direction.

Robertson *et al.* (2006 & 2009) proposed and analysed a maglev vibration isolator which uses a maglev system to create a vertical spring that has quasi-zero stiffness at the equilibrium point. In the research presented in this thesis, it was discovered that the quasi-zero stiffness maglev arrangement has the potential to provide quasi-zero/zero (quasi-zero stiffness in the vertical direction and zero stiffness in all the other directions) stiffness in all six DOFs (Section 3.6), and is thus investigated in this research as a method to achieve high performance vibration isolation.

2.5.2 Non-contact payload support

The maglev vibration isolation approach presented in this thesis utilises a non-contact payload supporting mechanism. It completely eliminates friction and cogging that are inevitable in conventional supporting components such as spring-dampers and linear guides. Furthermore, parasitic modes in the spring elements observed at higher frequencies are also avoided. Non-contact vibration isolation is particularly beneficial for high-precision measurements such as scanning tunnelling microscopy and atomic force microscopy where vibration level of less than $1gal$ ($0.01m/s^2$) is obstacle. G. Binnig, a Nobel laureate, was the first person who succeeded in visualising a shape an atom. After encountering a series of hardships for isolating ground vibration, his final success was at the feat of introducing a non-contact levitation exploiting superconductivity for isolating ground vibration.

2.5.3 Inherent design trade-off between payload capacity and vibration attenuation

As mentioned previously that an inherent trade-off exists in isolator designs where payload is supported using a resilient structure. The trade-off between payload support and vibration isolation significantly limits the performance of conventional designs since the mechanical support of the payload is often stiffened in order to carry the required payload weight with allowable isolator deflection.

In order to achieve improved vibration isolation performance over the conventional designs, in this research a novel 6-DOF nonlinear maglev system is proposed as a method of isolating ground-borne vibration. It enables quasi-zero stiffness payload support in all six DOFs while also providing a static levitation force to support the payload. The work of this project also includes the development of an adaptive-passive payload support system (Section 3.7), which monitors the payload inputs (weight and torques) in real-time and adapts to the payload changes by adjusting the mechanical layout of the isolation system. This unique control algorithm allows the isolation system to avoid the design trade-off between load capacity and isolation performance, through which, the system performance (both vibratory and electrical) can be improved substantially.

2.5.4 Autonomous maglev system tuning

There have been a great number of vibration isolator designs proposed for improving various aspects of system performance. In some designs (Yi & Song, 1999; Winterflood *et al.*, 2002; Zhou & Liu, 2010; Azadi *et al.*, 2011; Xu *et al.*, 2013), the mechanical structure needs to be modified to optimise the system performance when there is a change to the system physical parameters, such as changes in payload weight, or changes in disturbance frequency or amplitude. Previously, the required modifications could only be carried out by either replacing system components (for example, by replacing the mechanical spring to change the structural stiffness), or manually changing the system mechanical properties using preinstalled adjusting mechanisms (such as creating initial internal stress using a built-in pretensioner).

2.5 Research gaps and significance

These methods all result in operation down time and, sometimes, performance degradation due to inaccuracies inherent to the manual processes. To the author's best knowledge, no auto-tuning algorithms have been applied to any maglev vibration isolators to optimise the system performance.

To address this gap, part of the aim of this research is to develop an auto-tuning algorithm (Section 5.4) that monitors the system performance parameters in real-time, and adjusts the physical layout of the system autonomously to maintain the optimised performance.

2.5.5 6-DOF fully active skyhook damping

As mentioned in Section 2.3.4, velocity feedback approaches have been recognised as effective and robust methods for active vibration control. They have been previously studied for many applications (Alleyne, 1995; Yoshimura *et al.*, 1997; Li & Goodall, 1999; Liu *et al.*, 2005; Liu *et al.*, 2008) including active/semi-active suspensions and machine vibration isolation, where artificial damping forces were used to reduce the amplitude of the system peak response.

Magnetic levitation is a non-contact payload support method with very limited inherent damping. Therefore, to improve the performance of maglev systems as vibration isolation devices, artificial damping is often required to control the peak response of the maglev. Skyhook damping is a method to produce damping effect in the inertial space since the damping force is applied according to the motion of the object relative to the inertial frame. It offers several advantages over traditional active damping systems where the target motion is measured relative to a fixed object (demonstrated in Section 3.2.2). However, the literature contains limited studies on the application of skyhook damping in a multi-DOF maglev system. This research investigates the method to develop a 6-DOF skyhook damping system, which allows artificial damping forces to be applied in a 6-DOF inertial frame. The development of a 6-DOF skyhook damping system is expected to reduce the vibration transmissibility of the maglev isolator close to the system resonance frequencies.

Chapter 3

Background Theory and Methods

3.1 Introduction

In this research, a quasi-zero stiffness magnetic levitation system is proposed, which forms the fundamentals of a novel maglev vibration isolation system. It is not only able to provide quasi-zero/zero stiffness magnetic coupling in all six DOFs, but can also generate supporting forces/torques to passively balance the static disturbances in all six directions.

This chapter explains the theoretical background of the magnetic levitation system, as well as the methods used to realise the designs. It starts with modelling of the maglev, which includes a kinematic model to demonstrate the arrangement maglev, and a dynamic model to analyse the system response to external forces and torques. Following the system modelling, current methodologies on calculating multi-dimensional magnetic forces are reviewed in Section 3.4, which also includes an explanation of the 1D approximation method proposed in this research to model the 3D system and increase calculation speed for real-time control and simulation purposes. Section 3.5 introduces the polynomial regression method used to derive a

Chapter 3 Background Theory and Methods

numerical model for calculating the forces and torques, which further reduce the calculation time by one order of magnitude. After introducing the calculation method, Section 3.6 demonstrates how the quasi-zero stiffness levitation is established in the 6-DOF space. The cross coupling effects between the translational and rotational DOFs are explained as well. Examples of theoretical applications of the cross forces/torques for balancing the external disturbances adaptive-passively are also shown in Section 3.7.

3.2 Significance of stiffness and damping

The two most important system parameters of a vibration isolation system are the stiffness and the damping ratio of the supporting structure. The amplitudes of these two parameters predominately define the performance of the vibration isolation system. Therefore, discussions are presented in this section to demonstrate how the vibration isolation performance can be improved by the proposed quasi-zero/zero stiffness maglev isolator.

3.2.1 Vibration transmissibility and isolator compliance

It was demonstrated in Section 2.2.2 that vibration isolation systems are only effective to disturbances with frequencies above the 0dB crossover frequency. To optimise the performance of a vibration isolator, in terms of minimising its vibration transmissibility, the system natural frequency is normally preferred to be as low as possible without compromising the other performance criteria (such as the allowable isolator compliance). The precise analytical relationship between the isolator stiffness and natural frequency is dependent on the stiffness behaviour of the supporting structure. For single DOF systems with linear stiffness, the relationship is simply:

$$f_n = \frac{1}{2\pi} \sqrt{\frac{k}{m}},$$
 where f_n , k and m are the natural frequency, stiffness and payload mass

of the isolation system. However, for a non-linear vibration isolator, the relation between the system stiffness and natural frequency is determined by the unique nonlinearity of the individual system, as well as being related to the amplitude of the

3.2 Significance of stiffness and damping

disturbance. The behaviour of such nonlinear vibration isolators is typically analysed using specialised nonlinear analysis software. Therefore, for simplicity, linear examples are used here to demonstrate the significance of the isolator stiffness.

Figure 3.1 is a schematic of a single-DOF spring-damper vibration isolator subject to ground excitation. The dynamics of this single DOF isolator are described as

$$m\ddot{x} + c(\dot{x} - \dot{y}) + k(x - y) = 0 \quad , \quad (3.1)$$

where m , c and k are the payload mass (in kg), the damping coefficient (in N/ms^{-2}) and the spring stiffness (in N/m) respectively.

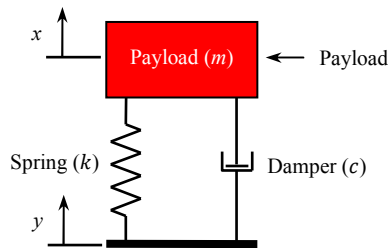


Figure 3.1: Schematic of a single-DOF linear spring-damper isolator subject to ground excitation.

Figure 3.2 is a plot generated using Equation (3.1) with various supporting stiffness. As discussed previously, vibration isolators are only effective for rejecting disturbances at frequencies above the 0dB crossover frequency. From Figure 3.2, for $f > f_n$, the vibration transmissibility at each individual frequency increases with the increasing system stiffness. The increase in system stiffness also causes an increase in the peak response of the isolator since the stiffness increase effectively reduces the system damping ratio. Therefore, to reduce the amount of vibration transmitted to the payload, the stiffness of the isolator is preferred to be as low as possible.

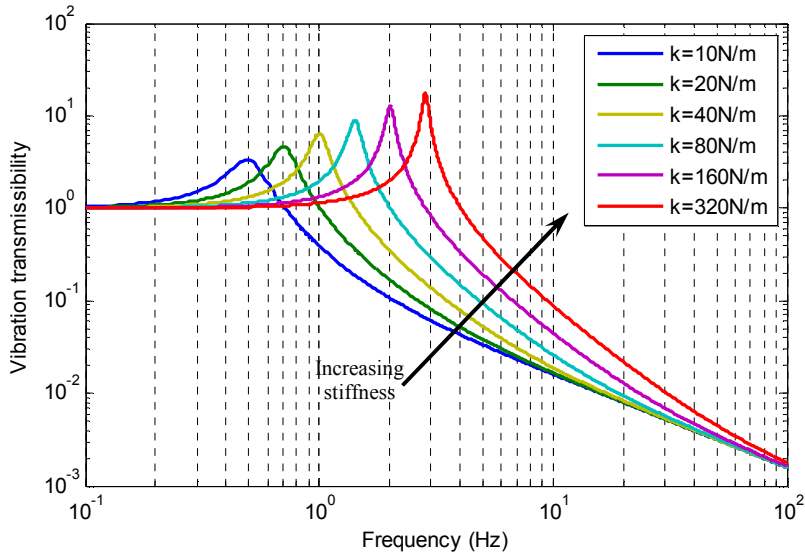


Figure 3.2: Vibration transmissibility plot using Equation (2.1) with different supporting stiffness, $c = 1 \text{ N/ms}^{-2}$; $m = 1 \text{ kg}$.

When the payload is supported by a resilient structure with linear stiffness, such as a mechanical spring with linear stiffness, k , the static deflection, d , resulting from the dead weight of the payload, w , is $d = w/k$. Therefore, in order to reduce the static deformation, which is often necessary due to operational requirements or spatial restrictions in the design, a larger stiffness is preferred. This is contrary to the requirements for reducing the vibration transmissibility. Therefore, the design of a traditional vibration isolator can only optimise one performance factor by sacrificing the performance of the other.

In the 6-DOF maglev vibration isolator design proposed in this thesis (Section 4.2), instead of generating the payload supporting force from the deformation of an elastic structure or mechanical springs, two pairs of rare earth magnets are used to provide the static supporting force. Through the proposed control systems (Section 5.3), the separating distances between the magnets are actively adjusted according to the real-time payload condition so that the static magnetic supporting forces balance the payload weight. Therefore, in the proposed 6-DOF maglev isolator design, it is not necessary to undesirably stiffen the supporting structure to avoid excessive static

3.2 Significance of stiffness and damping

deflection of the isolator. Section 3.6 will also demonstrate how the nonlinear magnetic forces are used to generate quasi-zero stiffness levitation in the vertical direction.

3.2.2 Relative damping and inertial space damping

Damping is an effective approach for dissipating vibration energy and reducing the amplitude of oscillations. It exists in almost all vibration isolation devices. Damping can be introduced by three ways: passive damping, such as through a mechanical dashpot; active damping, such as by a servo damper with speed sensor and force actuator; and semi-active damping, such as using a mechanical viscous damper with an actively controlled flow rate valve to adjust the magnitude of the damping force. In general, the purpose of these mechanisms is to exert a damping force (F_d) on the target object to oppose its motion. There are four common types of damping system models, which are Coulomb damping, viscous damping, aerodynamic damping and structural damping. The relationship between the damping force (F_d) and the motion of the object (x and \dot{x}) for these four types of damping models are

$$F_d = -\mu_k N \text{ (Coulomb damping)} \quad (3.2)$$

$$F_d = -c_v \dot{x} \text{ (Viscous damping)} \quad (3.3)$$

$$F_d = -c_a \dot{x}^2 \text{ (Aerodynamic damping)} \quad (3.4)$$

$$F_d = -hx \text{ (Structural damping)} \quad (3.5)$$

where x and \dot{x} are the displacement and velocity of the object; μ_k and N are the kinetic friction coefficient and normal contact force between the object surfaces respectively; and c_v , c_a and h represent the damping coefficient for the viscous damping, the aerodynamic damping and the structural damping, respectively. In engineering applications, especially for vibration attenuation purposes, viscous

Chapter 3 Background Theory and Methods

damping is the preferred damping model due to the linear relationship it has between the damping force and the velocity of the object. It is also the chosen damping model in this research for realising the 6-DOF skyhook damping, which will be described in Chapter 7.

It was briefly discussed in Section 2.3.3 that the motion of an object can be expressed in both relative and inertial space. In damping systems, the choice of reference space significantly affects the performance of the damping system, especially for disturbance frequencies above the 0dB crossover frequency. Figure 3.3 shows examples of both relative space damping and inertial space damping (also known as skyhook damping). In Figure 3.3(a), the damper is attached between the base and the payload. Therefore, the damping force on the payload is dependent on the relative velocity between the payload and the fixed base. However, in Figure 3.3(b), the damping effect exists between the fixed inertial frame and the payload, and the magnitude of the damping force is calculated based on the absolute velocity (the velocity relative to a fixed inertial space) of the payload.

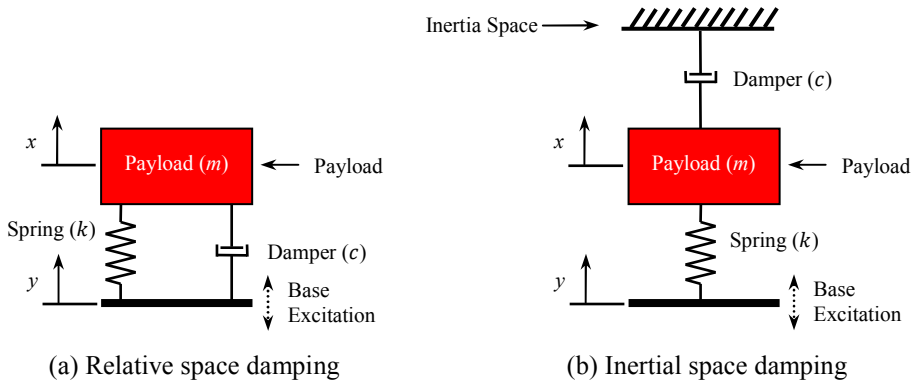


Figure 3.3: Comparison between relative damping and inertial space damping.

Under base excitation, the dynamics of the systems described by Figure 3.3(a) (relative damping) and Figure 3.3 (b) (inertial damping) can be written as

$$m\ddot{x} + (\dot{x} - \dot{y})c + (x - y)k = 0, \text{ and} \quad (3.6)$$

3.2 Significance of stiffness and damping

$$m\ddot{x} + \dot{x}c + (x - y)k = 0 \quad (3.7)$$

respectively. The displacement transmissibility of these systems under base excitation can be calculated by (Meirovitch, 1986)

$$T_r = \frac{x}{y} = \sqrt{\frac{1 + j2\zeta(f/f_n)}{1 - (f/f_n)^2 + j2\zeta(f/f_n)}} \quad (3.8)$$

$$T_i = \frac{x}{y} = \sqrt{\frac{1}{1 - (f/f_n)^2 + j2\zeta(f/f_n)}} \quad (3.9)$$

respectively, where k is the spring stiffness, m is the payload mass, ζ is the relative damping ratio defined as $\zeta = \frac{c}{2\sqrt{km}}$, and f and f_n are the disturbance frequency and system natural frequency respectively. The subscripts r and i represent relative damping and inertial damping, respectively.

Figure 3.4 and Figure 3.5 show the frequency response of the payload relative to a base excitation under relative damping and inertial space damping respectively. In terms of vibration transmissibility, the inertial space damping has clear advantages over the relative damping method.

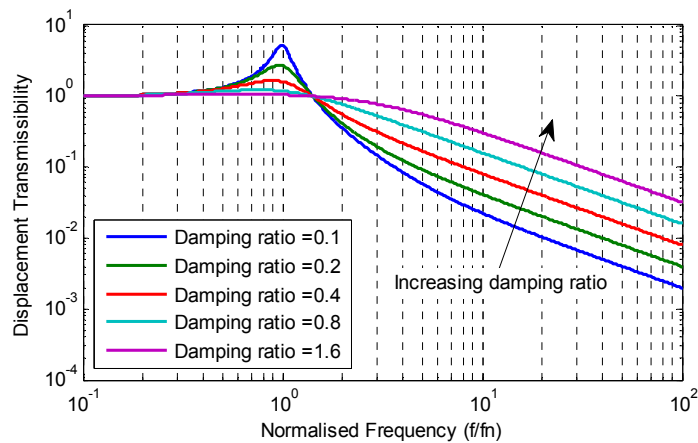


Figure 3.4: Displacement transmissibility of a linear vibration isolator with relative damping.

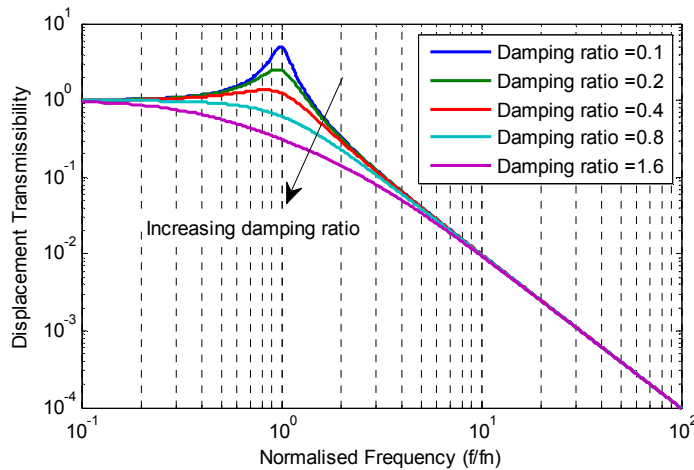


Figure 3.5: Displacement transmissibility of a linear vibration isolator with inertial space damping.

In Figure 3.4, the relative damping method has shown its effectiveness in attenuating the peak response when the system is driven at the natural frequency ($f/f_n = 1$). However, beyond the 0dB cross over frequency at $\sqrt{2}f_n$ (refer to Figure 2.1), the relative damping mechanism starts to adversely affect the isolation performance as shown in Figure 3.4, where the vibration transmissibility increases with increasing damping ratio. This can also be explained by considering the physical behaviour of the damper. In relative damping, the damping force is directly proportional to the relative speed of the payload to the base. Under base excitation, the damping effect resists the relative motion between the base and the payload. Therefore, relative damping attenuates the payload vibration when the transmissibility is greater than one, and increases the payload vibration when the transmissibility is smaller than one. The extreme scenario for relative damping is when $\zeta \rightarrow \infty$, which results in a rigid connection between the payload and the base, achieving no vibration isolation. This often results in a trade-off in designing the damping coefficient for a relatively damped system as higher amplitude attenuation at the system natural frequency ultimately leads to transmissibility increase at higher frequencies.

The trade-off in the selection of the damping ratio mentioned above does not exist for inertial space damping systems. Figure 3.5 shows that the inertial space damping has the ability to achieve significant reduction of the system peak response without

3.2 Significance of stiffness and damping

affecting the vibration isolation performance at higher frequencies. It is also demonstrated that the inertial space damping is able to attenuate the transmissibility to below 0 dB at frequencies lower than the system natural frequency. The effectiveness of the inertial space damping can be explained by taking the same extreme scenario where $\zeta \rightarrow \infty$. In this case, there exists a rigid connection between the payload and the fixed inertial space. Therefore, the payload remains stationary constantly, thus achieving full vibration isolation, i.e., the vibration transmissibility equals zero. However, practically constraints often restrict the maximum damping effect achievable from an inertial space damping system. The operation of inertial space damping relies on the accurate measurement of the absolute payload velocity in the inertial space. Fundamentals of physics suggest that it is impossible to practically measure the vibration velocity of the payload in the inertial space. Current methods of estimating the inertial space velocity often have poor performance at low frequencies due to the inherent dynamics of the measuring equipment. In addition, generation of damping forces in proportion to the payload absolute velocity often requires active feedback control systems. The phase shifts typically inherent to low frequency velocity measurements can destabilise the controller when the artificial damping coefficient is high. Therefore, the practical performance of inertial space damping is significantly limited by the performance of the velocity measuring sensors.

In this research, a 6-DOF inertial space damping system (referred to as skyhook damping) is proposed to actively attenuate the vibration of the floater assembly. Chapter 7 will demonstrate the underlying theory and the designs of the 6-DOF skyhook damping system, as well as a method developed to improve the low frequency performance of the geophones that are used as the absolute payload velocity sensors.

3.3 Modelling the maglev system

In order to analyse and demonstrate the proposed magnetic levitation concept, both kinematic and dynamic models of the maglev isolation system are presented in this section. The kinematic model explains the physical formation of the maglev, and the dynamic model describes the maglev response to external forces.

3.3.1 Kinematic model of the maglev

The structure of the proposed 6-DOF quasi-zero stiffness maglev is shown in Figure 3.6. It contains four rare earth magnets, two fixed (Magnets 1 and 4), and two floating (Magnets 2 and 3). The floating magnets are held together with a linkage bar to form a rigid assembly, which is named the “Floater”. The floater assembly is coupled with the fixed magnets by magnetic forces only. It is able to move freely in all six DOFs. Therefore, when connected to the payload, the floater carries the payload and also acts as a vibration isolator.

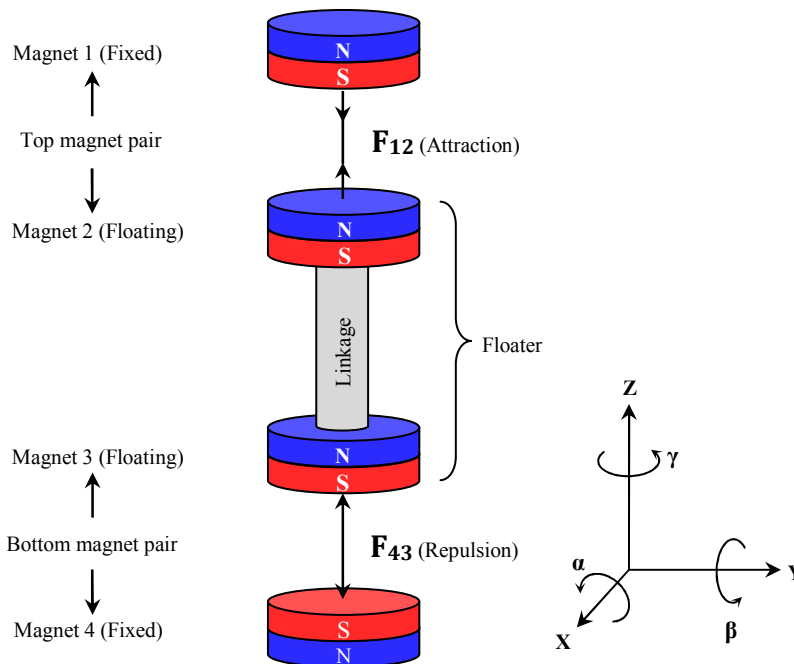


Figure 3.6: Schematic of the magnetic levitation system

In Figure 3.6, the directions of the magnetisation are indicated using both letters and colours, with N (blue) and S (red) representing the north and south poles of the

3.3 Modeling the maglev system

magnets respectively. The magnets are located such that the top pair (Magnet 1 and 2) has an attractive force between each other, and the bottom pair (Magnet 3 and 4) has a repulsive force. The benefits of this maglev arrangement will be demonstrated in the subsequent sections in this chapter.

The forces between the top and bottom pairs of magnets are indicated as \mathbf{F}_{12} and \mathbf{F}_{34} respectively, which are the vector representations of the forces in the translational directions, written as $\mathbf{F}_{12} = [F_{12X}, F_{12Y}, F_{12Z}]^T$ and $\mathbf{F}_{34} = [F_{34X}, F_{34Y}, F_{34Z}]^T$. The method used for calculating these forces is introduced in Section 3.4.

In this thesis, the 6-DOF geometric space used to define the dimensions and the physical parameters is a Cartesian coordinate system as shown in Figure 3.6. The individual directions in the space are named according to the Right Hand Rule, with the translational directions denoted as X, Y and Z, and the rotational DOFs as α , β and γ . The rotational directions may also be referred to as the pitch, roll and yaw directions respectively in some parts of the thesis.

3.3.2 Dynamic model of the maglev system

In order to mathematically simulate the performance of the maglev isolation system, a dynamic model of the maglev was built using state space modelling. The differential equations governing the motion of the floater in the six DOFs are

$$\left. \begin{aligned} m\ddot{x} &= F_X + f_X = 0 \\ m\ddot{y} &= F_Y + f_Y = 0 \\ m\ddot{z} &= F_Z + f_Z = 0 \\ J_{XX}\ddot{\alpha} &= T_X + \tau_X = 0 \\ J_{YY}\ddot{\beta} &= T_Y + \tau_Y = 0 \\ J_{ZZ}\ddot{\gamma} &= T_Z + \tau_Z = 0 \end{aligned} \right\} \quad (3.10)$$

where m is the floater mass, $x, y, z, \alpha, \beta, \gamma$ are the floater displacements within each DOF, and J_{ii} is the floater moment of inertia around the i^{th} axis. F_i and T_i represent the magnetic forces and torques generated between the permanent magnets. In the maglev design shown in Figure 3.6, the fixed magnets are attached to the ground and support the floater assembly. Hence, under ground excitation, the disturbances to the maglev

Chapter 3 Background Theory and Methods

system are considered to result in relative displacements between the fixed magnets and the floating magnets, which subsequently cause force variations between the magnets. Therefore, the ground disturbances to the maglev system are included in the F_i and T_i terms. Section 3.4 will demonstrate the calculation methods used to determine the magnetic forces and torques generated between the magnets. In Equation (3.10), f_i and τ_i are the external forces and torques generated by the active control systems, which are used for maglev stabilisation and active vibration attenuation purposes. Chapter 5 will demonstrate the detailed controller designs.

In a state space dynamic model, a stiffness term is generally included to describe the dynamic forces contributed by the system stiffness. In the 6-DOF maglev isolator model, the stiffness of the maglev system is nonlinear and quasi-zero around the nominal operating point in the vertical direction (when the centre of the floater is at the midpoint between the two fixed magnets, also explained in Section 3.6). Therefore, in the dynamic model of the 6-DOF maglev system, it is convenient to consider the floater to be a floating mass under no external constraint, and then treat the magnetic forces and torques (F_i and T_i) as the external force inputs to the floater so that the non-linear force-displacement relationship of the maglev system is handled by an additional non-linear model outside the linear state-space model of the floater, which is explained in Section 3.4. The block diagram shown in Figure 3.7 illustrates the integration of the non-linear force calculation and the linear state-space model of the floater. The mathematical expressions are shown in Equations (3.11) and Equation (3.12). The proposed 6-DOF maglev vibration isolator design allows the floater to be levitated without any physical contact to the supporting structure. Therefore, the passive damping forces on the floater can only arise from two possible sources, the air resistance due to the relative motion between the floater and the surrounding air, and eddy current drag due to the relative motion between the magnets and the adjacent metallic supporting structure. The design of the maglev vibration isolator (demonstrated in Section 4.2) was made with considerations for minimising the eddy current drag (by keeping sufficient separations between the magnets and the metallic components), and the aerodynamic drag on the floater is expected to be extremely

3.3 Modeling the maglev system

small due to the low motion speed of the floater. Therefore, the total passive damping force on the floater is considered to be negligible, and the associated damping terms in the system dynamic model were ignored.

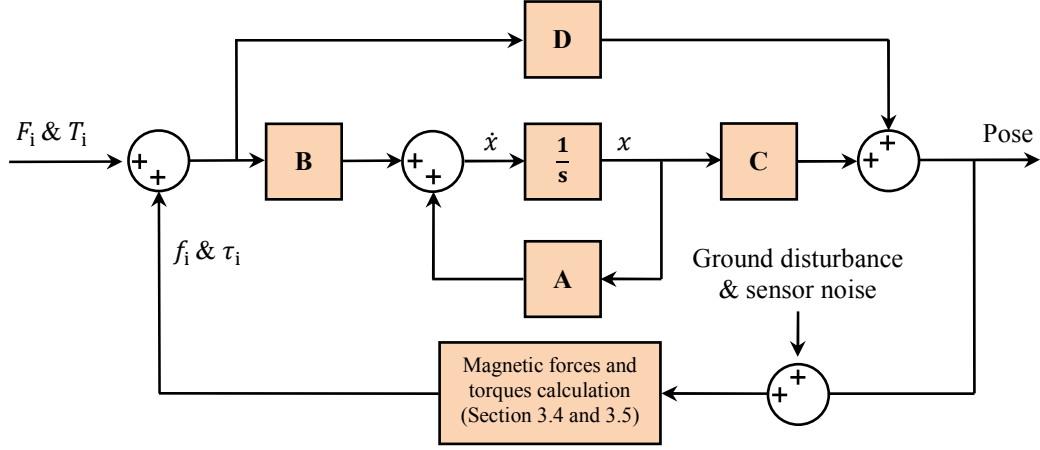


Figure 3.7: Block diagram of the floater dynamic model

$$\begin{aligned}
 \begin{bmatrix} \ddot{x} \\ \ddot{y} \\ \ddot{z} \\ \ddot{\alpha} \\ \ddot{\beta} \\ \ddot{\gamma} \end{bmatrix} &= \begin{bmatrix} 0 & 0 & 0 & 0 & 0 & 0 & 0 & 0 & 0 & 0 & 0 & 0 \\ 1 & 0 & 0 & 0 & 0 & 0 & 0 & 0 & 0 & 0 & 0 & 0 \\ 0 & 0 & 0 & 0 & 0 & 0 & 0 & 0 & 0 & 0 & 0 & 0 \\ 0 & 0 & 1 & 0 & 0 & 0 & 0 & 0 & 0 & 0 & 0 & 0 \\ 0 & 0 & 0 & 0 & 0 & 0 & 0 & 0 & 0 & 0 & 0 & 0 \\ 0 & 0 & 0 & 0 & 1 & 0 & 0 & 0 & 0 & 0 & 0 & 0 \\ 0 & 0 & 0 & 0 & 0 & 0 & 0 & 1 & 0 & 0 & 0 & 0 \\ 0 & 0 & 0 & 0 & 0 & 0 & 0 & 0 & 0 & 1 & 0 & 0 \\ 0 & 0 & 0 & 0 & 0 & 0 & 0 & 0 & 0 & 0 & 0 & 1 \\ 0 & 0 & 0 & 0 & 0 & 0 & 0 & 0 & 0 & 0 & 0 & 0 \end{bmatrix} \times \begin{bmatrix} \dot{x} \\ \dot{y} \\ \dot{z} \\ \dot{\alpha} \\ \dot{\beta} \\ \dot{\gamma} \end{bmatrix} + \begin{bmatrix} \frac{1}{m} & 0 & 0 & 0 & 0 & 0 \\ 0 & \frac{1}{m} & 0 & 0 & 0 & 0 \\ 0 & 0 & \frac{1}{m} & 0 & 0 & 0 \\ 0 & 0 & 0 & \frac{1}{J_{xx}} & 0 & 0 \\ 0 & 0 & 0 & 0 & \frac{1}{J_{yy}} & 0 \\ 0 & 0 & 0 & 0 & 0 & \frac{1}{J_{zz}} \\ 0 & 0 & 0 & 0 & 0 & 0 \end{bmatrix} \times \begin{bmatrix} F_x + f_x \\ F_y + f_y \\ F_z + f_z \\ T_x + \tau_x \\ T_y + \tau_y \\ T_z + \tau_z \end{bmatrix} \\
 \dot{x} \quad \underbrace{\hspace{10em}}_{\mathbf{A}} \quad x \quad \underbrace{\hspace{10em}}_{\mathbf{B}} \quad F_i \& T_i \tag{3.11}
 \end{aligned}$$

$$\begin{aligned}
 \begin{bmatrix} x \\ y \\ z \\ \alpha \\ \beta \\ \gamma \end{bmatrix} &= \begin{bmatrix} 0 & 1 & 0 & 0 & 0 & 0 & 0 & 0 & 0 & 0 & 0 \\ 0 & 0 & 0 & 1 & 0 & 0 & 0 & 0 & 0 & 0 & 0 \\ 0 & 0 & 0 & 0 & 1 & 0 & 0 & 0 & 0 & 0 & 0 \\ 0 & 0 & 0 & 0 & 0 & 1 & 0 & 0 & 0 & 0 & 0 \\ 0 & 0 & 0 & 0 & 0 & 0 & 1 & 0 & 0 & 0 & 0 \\ 0 & 0 & 0 & 0 & 0 & 0 & 0 & 1 & 0 & 0 & 0 \\ 0 & 0 & 0 & 0 & 0 & 0 & 0 & 0 & 1 & 0 & 0 \\ 0 & 0 & 0 & 0 & 0 & 0 & 0 & 0 & 0 & 1 & 0 \end{bmatrix} \times \begin{bmatrix} \dot{x} \\ \dot{y} \\ \dot{z} \\ \dot{\alpha} \\ \dot{\beta} \\ \dot{\gamma} \end{bmatrix} + \begin{bmatrix} 0 & 0 & 0 & 0 & 0 & 0 \\ 0 & 0 & 0 & 0 & 0 & 0 \\ 0 & 0 & 0 & 0 & 0 & 0 \\ 0 & 0 & 0 & 0 & 0 & 0 \\ 0 & 0 & 0 & 0 & 0 & 0 \\ 0 & 0 & 0 & 0 & 0 & 0 \end{bmatrix} \times \begin{bmatrix} F_x + f_x \\ F_y + f_y \\ F_z + f_z \\ T_x + \tau_x \\ T_y + \tau_y \\ T_z + \tau_z \end{bmatrix} \\
 \text{Pose} \quad \underbrace{\hspace{10em}}_{\mathbf{C}} \quad x \quad \underbrace{\hspace{10em}}_{\mathbf{D}} \quad F_i \& T_i \tag{3.12}
 \end{aligned}$$

3.4 Calculation of magnetic forces and torques

Analytical methods for calculating magnetic forces and torques have been previously investigated by a number of researchers (Akoun & Yonnet, 1984; Nagaraj, 1988; Furlani, 1993; Trimboli *et al.*, 1994; Carrella *et al.*, 2008; Ravaut *et al.*, 2009; Ravaut *et al.*, 2010; Janssen *et al.*, 2010; Robertson *et al.*, 2010). The proposed methods provide analytical solutions to calculate forces between both electric and permanent magnets of many shapes. This section describes the method used in this research for modelling the forces between magnets, as well as the modifications used to apply existing techniques to the system under consideration in this project.

3.4.1 3D to 1D calculation simplification

A key component of this research is the use of numerical simulations to model the dynamics of the proposed design. The feedback and feed-forward controls (Chapter 5) used to achieve stabilisation and disturbance rejection are necessary parts of the simulation. The desired analysis range for the transmissibility is 0-50Hz. To successfully model the controllers, an order of magnitude higher bandwidth is required in the simulation, i.e., 0-500Hz. Therefore, to avoid aliasing and stability issues in the continuous to discrete transformations necessary for simulation of the digital control, a sample rate of 1kHz is required. Calculation of the magnetic forces in the 3D space is generally very complicated. For the simulation undertaken here, two seconds of Matlab run time is typically required to obtain an estimation of the magnetic forces for one set of pose coordinates. This means that the 1kHz sampling rate used in the simulation will lead to approximately 2000 seconds of computer run time to obtain a 1 second record of simulated data, which is time consuming and impractical for research purposes. Therefore, to reduce the calculation time, in this research the 3D forces are approximated using a simplified single DOF method.

In the 3D calculations, all the forces in the X, Y and Z directions have to be modelled and calculated individually. However, with 1D approximations, the necessary modelling is reduced to only the coaxial force between the two magnets. Forces in

3.4 Calculation of magnetic forces and torques

each DOF can then be obtained simply through the geometric relationships between the three directions. Figure 3.8 shows a schematic of this approximation in the YZ plane, where d_Y and d_Z are the magnet separations in the Y and Z direction respectively. Two cases with equivalent relative positions of the magnet centres are shown to demonstrate the differences between the 3D and 1D calculation. In Figure 3.8(a), all the forces $\mathbf{F} = [F_X, F_Y, F_Z]$ are calculated explicitly using the method described by Akoun and Yonnet (1984). This method was programmed in Matlab by Robertson (2010) to perform the calculation. This method is relatively computationally expensive, and the calculation of forces is needed in all three directions. In contrast, the simplified 1D case (Figure 3.8(b)) only requires the coaxial (where the centre lines of the magnets are aligned) force (F_a) to be calculated using a considerably more simplified method proposed by Robertson (2009). In order to obtain forces in the three directions (X, Y, Z), the coaxial force is then projected onto the three axes of the coordinate system using the geometric transformation described in Equation (3.13). The combination of the coaxial force calculation and the geometric transformation is a significantly simpler method compared to the full 3D force calculation.

$$\begin{aligned}
 F_X &= \frac{F_a d_X}{\sqrt{d_X^2 + d_Y^2 + d_Z^2}} \\
 F_Y &= \frac{F_a d_Y}{\sqrt{d_X^2 + d_Y^2 + d_Z^2}} \\
 F_Z &= \frac{F_a d_Z}{\sqrt{d_X^2 + d_Y^2 + d_Z^2}}
 \end{aligned} \tag{3.13}$$

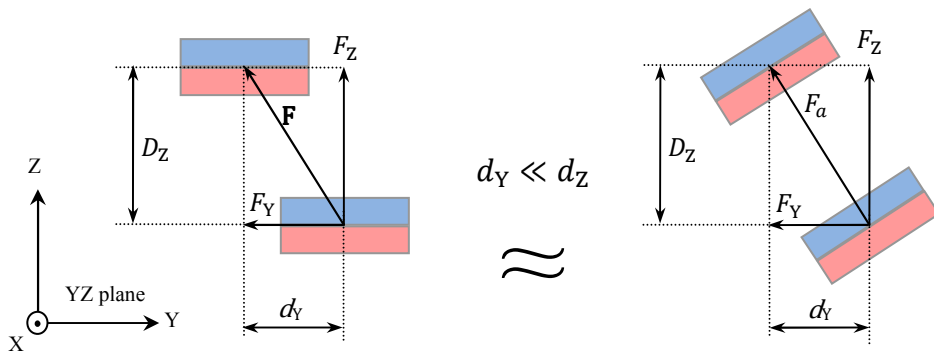


Figure 3.8: forces resulting from horizontal displacement between two magnets.

Chapter 3 Background Theory and Methods

A comparison between the force calculations using both the 3D and the 1D methods is shown in Figure 3.9 for the example case shown in Figure 3.8. Table 3.1 shows the geometric and magnetic parameters used in the force calculation.

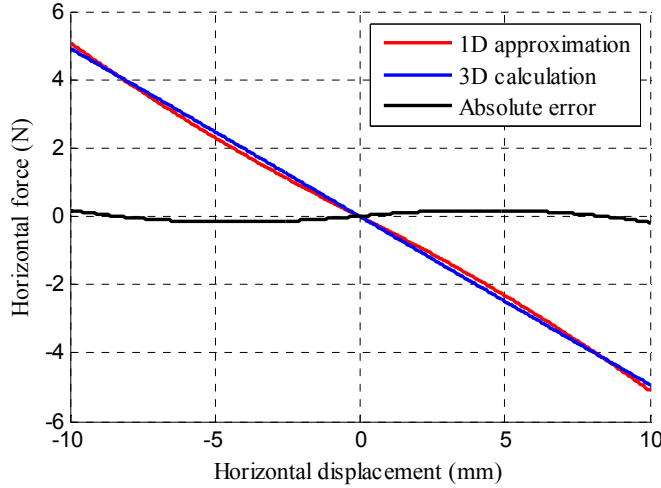


Figure 3.9: Comparison between the 3D method and the 1D approximation for calculating F_Y .

Table 3.1: Physical parameters used in the 3D and 1D force calculations

Parameter	Value
Magnet length	40mm
Magnet width	40mm
Magnet height	20mm
Magnetisation	1.48T
Vertical distance between magnet centres (d_Z)	100mm
Horizontal distance between magnet centres (d_Y)	-10mm to 10mm

The 1D approximation to the 3D forces was found to be reasonably accurate with small non-coaxial displacements (within about 10% of the coaxial displacement). For example, as shown in Figure 3.9, the 1D approximation is reasonably accurate when $|d_Y| \leq 0.1d_Z$. For the 100mm magnet vertical separation, the horizontal

3.4 Calculation of magnetic forces and torques

displacement range shown in the figure is $-100\text{mm} \leq d_y \leq 100\text{mm}$. The error (difference between the 1D and the 3D method) between the 1D and 3D methods remains within 0.17N throughout the -10mm to 10mm displacement range. Despite the small errors in the 1D approximation method, the magnetic force displacement relationship predicted by the 1D method fits the 3D results relatively well. It is not a primary focus in this research to accurately model the magnetic forces, and the 1D approximation provides a significant calculation time reduction. Therefore, the small calculation error introduced by the 1D approximation method is considered to be an acceptable compromise with computational speed in this research for investigating the stiffness behaviour of the proposed maglev system (shown in Section 3.6).

The above calculations and comparisons were based on cubic shaped magnets rather than cylindrical magnets used in the system model (Figure 3.6). This is due to the fact that, to the author's best knowledge, there was no practical approach available for calculating the 3D forces between cylindrical magnets when this analysis was carried out. A method of force calculation between cylindrical magnets was only available for estimating the coaxial forces, which is another reason why the 3D to 1D transformation is necessary for the modelling and simulation components of this research. It is considered reasonable to assume that both cubic and cylindrical magnets have similar force-displacement behaviours in the scenarios analysed here. Therefore, the 1D approximation method is also considered suitable for cylindrical magnets.

3.4.2 1-D calculation of forces between cylindrical magnets

The design of the proposed maglev vibration isolator (Section 4.2) uses cylindrical magnets to achieve the levitation. Therefore, the modelling and simulation of the proposed maglev vibration isolator was based on cylindrical magnets. Ravaud *et al.* (2010) proposed a method for estimating forces between coaxial cylindrical magnets. The method was simplified by Robertson *et al.* (2011) to improve its usability. The simplified equation for calculating the coaxial force between two cylindrical magnets is (Robertson *et al.*, 2011)

Chapter 3 Background Theory and Methods

$$F_Z = \frac{J_1 J_2}{2\mu_0} \sum_{i=1}^2 \sum_{j=3}^4 a_1 a_2 a_3 f'_Z [-1]^{i+j} , \quad (3.14)$$

where the intermediate expression is

$$f'_Z = K(a_4) - \frac{1}{a_2} E(a_4) + \left[\frac{a_1^2}{a_3^2} - 1 \right] \Pi \left(\frac{a_4}{1 - a_2} \mid a_4 \right) , \quad (3.15)$$

in which the new parameters are

$$\begin{aligned} a_1 &= z_i - z_j \\ a_2 &= \frac{[r_1 - r_2]}{a_1^2} + 1 \\ a_3^2 &= [r_1 + r_2]^2 + a_1^2 \\ a_4 &= \frac{4r_1 r_2}{a_3^2}, \quad 0 < a_4 \leq 1 . \end{aligned} \quad (3.16)$$

In Equations (3.14), (3.15) and (3.16), J_1 and J_2 are the magnetisations of the magnets in Tesla, $\mu_0 = 4\pi \times 10^{-7} \text{NA}^{-2}$ is the magnetic constant, $K(m)$, $E(m)$ and $\Pi(n|m)$ are the complete elliptic integrals of the first, second, and third kind respectively (more details on the elliptic integrals can be found in Robertson *et al.*, 2011), and r_1 and r_2 are the radii of the two cylindrical magnets having the axial positions of their faces at z_1, z_2, z_3 and z_4 shown in Figure 3.10.

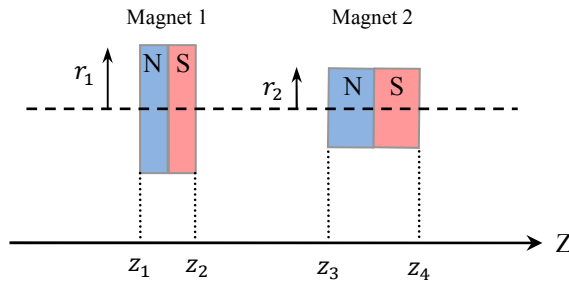


Figure 3.10: Schematic of two coaxial cylindrical magnets.

3.4 Calculation of magnetic forces and torques

Robertson *et al.* (2011) have also provided a Matlab script that can be used to conveniently perform the calculations for the forces between cylindrical magnets. The Matlab script was used together with the 1D approximation introduced previously to calculate the magnetic forces between the cylindrical magnets in the 3D space. The calculation results presented from Section 3.5 onwards are all based on cylindrical magnets. Table 3.2 lists the physical properties of the cylindrical magnets used, which correspond to the magnets selected for the mechanical design of the maglev vibration isolation system detailed later in this thesis.

Table 3.2: Physical properties of the cylindrical magnets.

Parameter	Value
Magnet diameter	50.8mm
Magnet thickness	25.4mm
Magnetisation	1.48T
Magnet type	Nickel plated rare earth magnet

3.4.3 Assumptions for calculating the magnetic forces and torques

In this thesis, the calculations of magnet forces are based on the following assumptions:

Assumption 1: The magnetisation is uniform across the volume of all magnets.

This assumption ensures that the effective centre of magnetisation is at the geometric centre of the magnets. Hence, the magnetic forces are also originated from the geometric centre of the magnets. In the subsequent sections, the determination of the nominal operation point of the floater (the midpoint between two fixed magnets, refer to Figure 3.11) will be directly related to the location of the centre of magnetisation.

Chapter 3 Background Theory and Methods

Assumption 2: All mechanical components have relative magnetic permeability equal to unity.

The analysis in the subsequent sections will show the stiffness behaviour of the proposed maglev vibration isolator in multiple DOFs. In order to realise the favourable force-displacement relationship of the maglev, it is essential that the floater has no external interference from the supporting isolator frame, and the flux of the magnetic field is not distorted. The material selection in the design of the physical isolation system (Chapter 4) has ensured, where possible, that all components in the maglev isolator behave as vacuum magnetically as if they were in a vacuum.

Assumption 3: Interaction forces between Magnet 1 and 3 and Magnet 2 and 4 (refer to Figure 3.6) are sufficiently small to be neglected.

For simplicity of the analysis, the force-displacement behaviour between the floater and the fixed magnets is assumed to be a result of the two magnet pairs (Magnet 1 and 2, and Magnet 3 and 4). Forces between Magnet 1 and 3 and Magnet 2 and 4 were calculated (using the method in Robertson *et al.*, 2011) to be 0.0312N with 100mm separation between the top and bottom magnet pairs. At this separation the total force between the top and bottom magnet pairs is 39.13N. Therefore, forces between Magnet 1 and 3 and Magnet 2 and 4 are assumed to have negligible influence on the floater force-displacement behaviour.

Assumption 4: Under small non-coaxial displacements (comparable to the magnitude of laboratory floor vibration presented in Appendix B), magnetic torques between the permanent magnet pairs (between Magnets 1 and 2, and between Magnets 3 and 4 in Figure 3.8(a)) are sufficiently small to be neglected.

Figure 3.11 is a free body diagram of the maglev system under horizontal displacement (non-coaxial displacement), where p_{12} and p_{43} are the nominal vertical separations between Magnet 1 and 2 and Magnet 3 and 4 respectively (when the floater has no angular displacement and the floater centre of gravity (COG) is at the mid-point between the two fixed magnets), $2l$ is the length of the floater between the

3.4 Calculation of magnetic forces and torques

two floater magnet centres, and y is the horizontal displacement in the Y direction. Under such displacement the torque around the floater COG (T_α) can arise from two sources: the magnetic torques between the two magnet pairs (T_{12} and T_{43}), and the mechanical torques created by forces F_{12Y} and F_{43Y} .

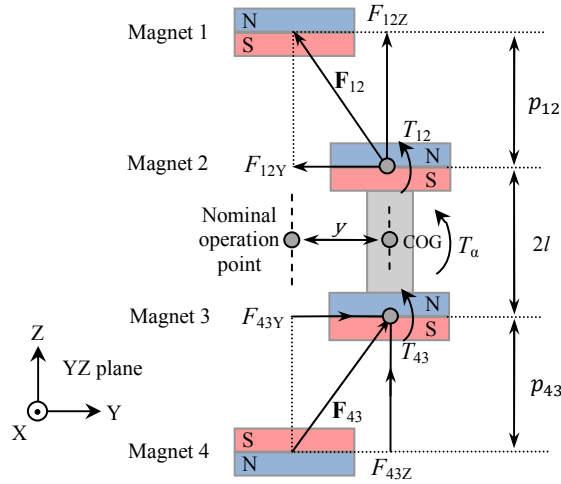


Figure 3.11: Free body diagram of the floater under horizontal displacement

The magnitude of the total magnetic torques ($T_{12} + T_{43}$) is calculated using the method proposed by Allag and Yonnet (2009). However, their original method was formulated to calculate magnetic torques between cubic magnets. To approximate the magnetic torque between the cylindrical magnets used in the maglev isolator design, the dimension of the cylindrical magnets were converted into an equivalent cubic magnet with the same cross-sectional area, thickness, and hence volume using

$$\begin{cases} H_{\text{cub}} = H_{\text{cyl}} \\ L_{\text{cub}} = \sqrt{\frac{\pi D_{\text{cyl}}^2}{4}} \\ W_{\text{cub}} = L_{\text{cub}} \end{cases}, \quad (3.17)$$

Chapter 3 Background Theory and Methods

where H_{cub} , L_{cub} and W_{cub} are the height, length and width of the cuboidal magnet respectively, and H_{cyl} and D_{cyl} are the height and diameter of the cylindrical magnet respectively.

Due to the constraints from the mechanical system design (Chapter 4), the maximum allowable floater horizontal displacement is bounded to be within $\pm 3\text{mm}$ from the nominal operation point, i.e., $-3\text{mm} \leq y \leq 3\text{mm}$. Figure 3.12 shows the calculated relationship between the total magnetic torque ($T_{12} + T_{43}$) and the floater horizontal displacement for $-3\text{mm} \leq y \leq 3\text{mm}$. It can be seen from Figure 3.12 that the total magnetic torque increases monotonically with an increase in the horizontal floater displacement. Hence, the largest possible total magnetic torque occurs at $y = 3\text{mm}$, and is 0.007038 Nm .

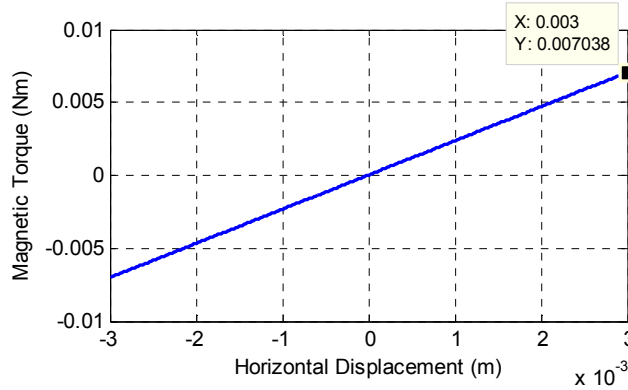


Figure 3.12: Total magnetic torque due to horizontal floater displacement ($H_{\text{cyl}} = 25.4\text{ mm}$, $D_{\text{cyl}} = 50.8\text{ mm}$, $p_{12} = p_{43} = 100\text{ mm}$, magnetization = 1.48 Tesla , $l = 208\text{ mm}$).

The mechanical torque resulting from the horizontal forces (F_{12Y} and F_{43Y}) is calculated using Equation (3.33). The magnitude of the mechanical torque at $y = 3\text{mm}$ is 0.2431 Nm (will also be shown in Figure 3.23(b)). It shows that the total magnetic torque ($T_{12} + T_{43}$) generated by the magnet pairs is only about 2.89% of the magnitude of the mechanical torque created by the horizontal forces (F_{12} and F_{43}). Therefore, for the sake of computational simplicity and simulation speed, the magnetic torques are neglected due to the complexity of modelling magnetic torques.

3.5 6-DOF modelling of the floater forces and torques

The proposed quasi-zero stiffness maglev system model was presented in Section 3.3.1. In the design, the floater assembly consists of two magnets that are rigidly connected via a mechanical linkage, and vibration isolation is achieved by attaching the payload to the floater assembly. Therefore, the forces and torques experienced by the floater as a rigid body is of primary interest, as it governs the vibration isolation performance of the maglev system. The previous sections have discussed the calculation of the magnetic forces between a pair of magnets. This section will explain the modelling method used to calculate the forces and torques experienced by the floater assembly as a rigid body.

3.5.1 Analytical model of the forces and torques

A free body diagram of the proposed quasi-zero stiffness maglev system is shown in Figure 3.13, where p_{12} and p_{43} are the nominal vertical separations between the top and bottom magnet pairs (when the floater has no angular displacement and the floater COG is at the nominal operation point), and $2l$ is the length of the floater

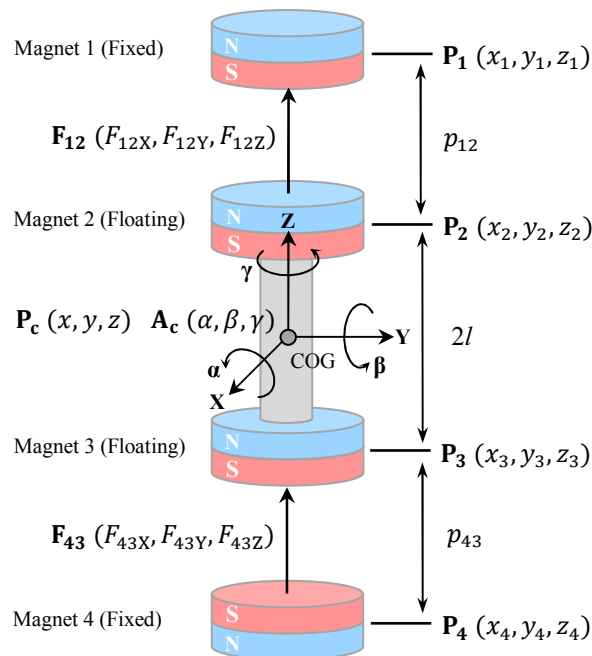


Figure 3.13: Free body diagram of the maglev system model.

Chapter 3 Background Theory and Methods

assembly between the two magnet centres. In Figure 3.13, a Cartesian coordinate system, with its origin at the midpoint between the two fixed magnets (the nominal operation point), is used to describe the positions of the magnet centres and the poses of the floater assembly. \mathbf{P}_1 , \mathbf{P}_2 , \mathbf{P}_3 , \mathbf{P}_4 and \mathbf{P}_c are the positions of the centres of Magnet 1, Magnet 2, Magnet 3, Magnet 4, and the floater respectively. \mathbf{A}_c is the angular displacement of the floater in the rotational DOFs (also refer to Equation (3.32)) defined as

$$\begin{aligned}\alpha &= \tan^{-1} \left(\frac{y - y_2}{z_2 - z} \right) \\ \beta &= \tan^{-1} \left(\frac{x_2 - x}{z_2 - z} \right) \\ \gamma &= \tan^{-1} \left(\frac{x_2 - x}{y_2 - y} \right)\end{aligned}\quad (3.18)$$

From the expressions presented previously on the 3D to 1D calculation simplification, it can be proven that \mathbf{F}_{12} has the same direction as the vector connecting the centres of Magnets 1 and 2 ($\mathbf{P}_1 - \mathbf{P}_2$), and similarly for \mathbf{F}_{43} . From Equation (3.13), it can be shown that the components of the forces acting between magnet pairs is given by

$$\left. \begin{aligned}F_{12X} &= \frac{|\mathbf{F}_{12}| \cdot (x_1 - x_2)}{|\mathbf{P}_1 - \mathbf{P}_2|} \\ F_{12Y} &= \frac{|\mathbf{F}_{12}| \cdot (y_1 - y_2)}{|\mathbf{P}_1 - \mathbf{P}_2|} \\ F_{12Z} &= \frac{|\mathbf{F}_{12}| \cdot (z_1 - z_2)}{|\mathbf{P}_1 - \mathbf{P}_2|} \\ F_{43X} &= \frac{|\mathbf{F}_{43}| \cdot (x_3 - x_4)}{|\mathbf{P}_3 - \mathbf{P}_4|} \\ F_{43Y} &= \frac{|\mathbf{F}_{43}| \cdot (y_3 - y_4)}{|\mathbf{P}_3 - \mathbf{P}_4|} \\ F_{43Z} &= \frac{|\mathbf{F}_{43}| \cdot (z_3 - z_4)}{|\mathbf{P}_3 - \mathbf{P}_4|}\end{aligned}\right\} \cdot \quad (3.19)$$

To calculate the magnetic forces along the X, Y and Z directions, the coordinates of the four magnets are required.

3.5 6-DOF modeling of the floater forces and torques

Magnets 1 and 4 are two fixed magnets. According to the geometric design of the maglev system (Appendix F), with 100mm nominal magnet separation ($p = p_{12} = p_{43} = 100\text{mm}$), the distance between the centres of the fixed magnets is 0.716m. This gives

$$\mathbf{P}_1 = [0 \quad 0 \quad p + l], \quad \mathbf{P}_4 = [0 \quad 0 \quad -p - l]. \quad (3.20)$$

The coordinates of the floating magnets change with the pose of the floater (\mathbf{P}_c and \mathbf{A}_c). However, the coordinates always satisfy the following geometric constraints:

$$\begin{aligned} x_2 - x &= -(x_3 - x) \\ y_2 - y &= -(y_3 - y) \\ z_2 - z &= -(z_3 - z) \\ (x_2 - x)^2 + (y_2 - y)^2 + (z_2 - z)^2 &= l^2. \end{aligned} \quad (3.21)$$

Solving Equations (3.18) and (3.21) for x_2, y_2, z_2, x_3, y_3 and z_3 yields

$$\begin{aligned} x_2 &= l \cdot \tan(\beta) \cdot \sqrt{\frac{1}{\tan^2(-\alpha) + \tan^2(\beta) + 1}} + x \\ y_2 &= l \cdot \tan(-\alpha) \cdot \sqrt{\frac{1}{1 + \tan^2(-\alpha) + \tan^2(-\alpha)\tan^2(\beta)}} \\ &\quad + y \\ z_2 &= l \cdot \sqrt{\frac{1}{1 + \tan^2(-\alpha) + \tan^2(\beta)}} + z \\ x_3 &= -l \cdot \tan(\beta) \cdot \sqrt{\frac{1}{\tan^2(-\alpha) + \tan^2(\beta) + 1}} + x \\ y_3 &= -l \cdot \tan(-\alpha) \cdot \sqrt{\frac{1}{1 + \tan^2(-\alpha) + \tan^2(-\alpha)\tan^2(\beta)}} \\ &\quad + y \end{aligned} \quad (3.22)$$

Chapter 3 Background Theory and Methods

$$z_3 = -l \cdot \sqrt{\frac{1}{1 + \tan^2(-\alpha) + \tan^2(\beta)}} + z$$

Hence, for any arbitrary floater pose $(x, y, z, \alpha, \beta, \gamma)$, the coordinates of the floater magnet centres can be calculated using Equation (3.22). Substituting Equations (3.20) and (3.22) in to Equation (3.19) gives

$$\begin{aligned} F_{12X} &= \frac{-|\mathbf{F}_{12}|(x + l \cdot \tan(\beta) \cdot H)}{\sqrt{(l + p - z - l \cdot H)^2 + (y - l \cdot \tan(\alpha) \cdot H)^2 + (x + l \cdot \tan(\beta) \cdot H)^2}} \\ F_{12Y} &= \frac{-|\mathbf{F}_{12}|(y - l \cdot \tan(\alpha) \cdot H)}{\sqrt{(l + p - z - l \cdot H)^2 + (y - l \cdot \tan(\alpha) \cdot H)^2 + (x + l \cdot \tan(\beta) \cdot H)^2}} \\ F_{12Z} &= \frac{|\mathbf{F}_{12}|(l + p - z - l \cdot H)}{\sqrt{(l + p - z - l \cdot H)^2 + (y - l \cdot \tan(\alpha) \cdot H)^2 + (x + l \cdot \tan(\beta) \cdot H)^2}} \\ F_{43X} &= \frac{|\mathbf{F}_{43}|(x - l \cdot \tan(\beta) \cdot H)}{\sqrt{(x - l \cdot \tan(\beta) \cdot H)^2 + (l + p + z - l \cdot H)^2 + (y + l \cdot \tan(\alpha) \cdot H)^2}} \\ F_{43Y} &= \frac{|\mathbf{F}_{43}|(y + l \cdot \tan(\alpha) \cdot H)}{\sqrt{(x - l \cdot \tan(\beta) \cdot H)^2 + (l + p + z - l \cdot H)^2 + (y + l \cdot \tan(\alpha) \cdot H)^2}} \\ F_{43Z} &= \frac{|\mathbf{F}_{43}|(l + p + z - l \cdot H)}{\sqrt{(x - l \cdot \tan(\beta) \cdot H)^2 + (l + p + z - l \cdot H)^2 + (y + l \cdot \tan(\alpha) \cdot H)^2}} \end{aligned} \quad (3.23)$$

where

$$H = \sqrt{\frac{1}{\tan(\alpha)^2 + \tan(\beta)^2 + 1}} \quad , \quad (3.24)$$

and the magnitudes of \mathbf{F}_{12} and \mathbf{F}_{43} can be determined using the method described in Section 3.4.2. Therefore, the 3D magnetic forces between the two pairs of magnets can now be calculated for any given floater pose. Thus, the resultant forces and torques $(F_X, F_Y, F_Z, T_\alpha, T_\beta, T_\gamma)$ experienced by the COG of the floater may be calculated as

3.5 6-DOF modeling of the floater forces and torques

$$\begin{aligned}
 F_X &= F_{12X} + F_{43X} \\
 F_Y &= F_{12Y} + F_{43Y} \\
 F_Z &= F_{12Z} + F_{43Z} \\
 T_\alpha &= F_{12Y} \cdot (z - z_2) + F_{43Y} \cdot (z - z_3) \\
 T_\beta &= F_{12X} \cdot (z_2 - z) + F_{43X} \cdot (z_3 - z) \\
 T_\gamma &= 0 \quad .
 \end{aligned} \tag{3.25}$$

In Equation (3.25), the torque around the floater COG in the γ direction is zero. This is due to the fact that the resultant force vectors between top and bottom magnet pairs always intersect the Z axis of the coordinate system shown in Figure 3.14.

3.5.2 Numerical model of the forces and torques

In the previous section, an analytical method for calculating the resultant forces and torques experienced by the COG of the floater was derived. However, even with the 3D to 1D simplification techniques (Section 3.4.1), calculating the forces and torques using the derived analytical model is still a complicated and time consuming process, especially when a large number of data points are needed for the analysis. To further simplify the calculation of the floater forces and torques, polynomial regression techniques were used to establish a numerical model of the floater forces and torques.

The polynomial model of the floater describes the relationship between the floater pose and the forces and torques experienced by the floater COG. The model has form

$$\mathbf{F} = \mathbf{K} \cdot \mathbf{X} , \tag{3.26}$$

where $\mathbf{F} = [F_X \ F_Y \ F_Z \ T_\alpha \ T_\beta \ T_\gamma]^T$ is the vector of floater forces and torques in 6-DOF, and \mathbf{K} is the coefficient matrix for the floater pose polynomial \mathbf{X} . The floater pose polynomial is a column vector derived from the translational (x, y, z) and the rotational (α, β, γ) displacements, and has the form

Chapter 3 Background Theory and Methods

$$\mathbf{X} = [\mathbf{X}_1 \mathbf{X}_2 \mathbf{X}_3 \mathbf{X}_4 \dots \mathbf{X}_{17} \mathbf{X}_{18} \mathbf{X}_{19}]^T, \quad (3.27)$$

where

$$\begin{aligned} \mathbf{X}_1 &= [1] \\ \mathbf{X}_2 &= [x \quad y \quad z \quad \alpha \quad \beta \quad \gamma] \\ \mathbf{X}_3 &= [x^2 \quad y^2 \quad z^2 \quad \alpha^2 \quad \beta^2 \quad \gamma^2] \\ \mathbf{X}_4 &= [x^3 \quad y^3 \quad z^3 \quad \alpha^3 \quad \beta^3 \quad \gamma^3] \\ \mathbf{X}_5 &= [xy \quad xz \quad x\alpha \quad x\beta \quad x\gamma] \\ \mathbf{X}_6 &= [x^2y \quad x^2z \quad x^2\alpha \quad x^2\beta \quad x^2\gamma] \\ \mathbf{X}_7 &= [xy^2 \quad xz^2 \quad x\alpha^2 \quad x\beta^2 \quad x\gamma^2] \\ \mathbf{X}_8 &= [yz \quad y\alpha \quad y\beta \quad y\gamma] \\ \mathbf{X}_9 &= [y^2z \quad y^2\alpha \quad y^2\beta \quad y^2\gamma] \\ \mathbf{X}_{10} &= [yz^2 \quad y\alpha^2 \quad y\beta^2 \quad y\gamma^2] \\ \mathbf{X}_{11} &= [z\alpha \quad z\beta \quad z\gamma] \\ \mathbf{X}_{12} &= [z^2\alpha \quad z^2\beta \quad z^2\gamma] \\ \mathbf{X}_{13} &= [z\alpha^2 \quad z\beta^2 \quad z\gamma^2] \\ \mathbf{X}_{14} &= [\alpha\beta \quad \alpha\gamma] \\ \mathbf{X}_{15} &= [\alpha^2\beta \quad \alpha^2\gamma] \\ \mathbf{X}_{16} &= [\alpha\beta^2 \quad \alpha\gamma^2] \\ \mathbf{X}_{17} &= [\beta\gamma] \\ \mathbf{X}_{18} &= [\beta^2\gamma] \\ \mathbf{X}_{19} &= [\beta\gamma^2] \end{aligned} \quad (3.28)$$

The physical representations of the vectors in Equation (3.28) are

3.5 6-DOF modeling of the floater forces and torques

Table 3.3: Physical representations of the vectors in pose polynomial.

Pose vector	Modelled relationship between force/torque and floater pose
\mathbf{X}_1	Constant force/torque term
\mathbf{X}_2	Linear dependence terms
\mathbf{X}_3	Quadratic dependence terms
\mathbf{X}_4	Cubic dependence terms
$\mathbf{X}_5, \mathbf{X}_6, \mathbf{X}_7$	Cross coupled dependence with x
$\mathbf{X}_8, \mathbf{X}_9, \mathbf{X}_{10}$	Cross coupled dependence with y
$\mathbf{X}_{11}, \mathbf{X}_{12}, \mathbf{X}_{13}$	Cross coupled dependence with z
$\mathbf{X}_{14}, \mathbf{X}_{15}, \mathbf{X}_{16}$	Cross coupled dependence with α
$\mathbf{X}_{17}, \mathbf{X}_{18}, \mathbf{X}_{19}$	Cross coupled dependence with β

Therefore, the floater force and torque model can be written as:

$$\begin{bmatrix} F_X \\ F_Y \\ F_Z \\ T_\alpha \\ T_\beta \\ T_\gamma \end{bmatrix} = \begin{bmatrix} k_{x1} & k_{x2} & \cdots & k_{x64} \\ k_{y1} & k_{y2} & \cdots & k_{y64} \\ k_{z1} & k_{z2} & \cdots & k_{z64} \\ k_{\alpha1} & k_{\alpha2} & \cdots & k_{\alpha64} \\ k_{\beta1} & k_{\beta2} & \cdots & k_{\beta64} \\ k_{\gamma1} & k_{\gamma2} & \cdots & k_{\gamma64} \end{bmatrix} \times [\mathbf{X}_1 \mathbf{X}_2 \mathbf{X}_3 \mathbf{X}_4 \cdots \mathbf{X}_{17} \mathbf{X}_{18} \mathbf{X}_{19}]^T . \quad (3.29)$$

In order to evaluate the coefficient matrix, \mathbf{K} , magnetic forces and torques were calculated for 15625 floater poses ($15625=5^6$, based on five linearly spaced data point in each direction, for six DOFs in total) using the analytical model described in Section 3.5.1. The range of the floater poses covers -3mm to 3mm in the translational directions, and -1.08 to 1.08 degree in the rotational directions (these correspond to the ranges of floater motion constrained by the mechanical design shown in Chapter 4). The least squares fitting method using a pseudo-inverse was then applied to calculate the coefficients for the floater pose matrix based on the generated force and torque data. The results of the fitted coefficients for the \mathbf{K} matrix are shown in Appendix C. The R squared coefficient of the fitting process is 1 for calculations in

Chapter 3 Background Theory and Methods

all of the six directions (the six rows in the \mathbf{K} matrix), which indicates the orders of the terms used in the pose polynomial are adequate, and the coefficients calculated accurately describe the force/torque behaviour of the maglev system. Determination of the \mathbf{K} matrix allows calculation of magnetic forces and torques through Equation (3.29). The numerical model based calculation reduced the computational time by two orders of magnitudes compared to calculations using the analytical model shown in Section 3.5.1.

For the sake of simplicity, the force and torque data used for the fitting were generated with a constant nominal separation of $p = 100\text{mm}$. The fitted model is only a representation of the maglev force-displacement for $p = 100\text{mm}$. However, the force-displacement behaviour of the maglev has the same characteristics for other separations.

3.6 6-DOF levitation stiffness

It was mentioned in the previous chapters that the proposed maglev isolator can realise quasi-zero stiffness levitation in the vertical direction, and zero stiffness in the remaining five DOFs. This section demonstrates the theoretical realisation of the quasi-zero/zero levitation stiffness.

3.6.1 Quasi-zero stiffness in the vertical direction (Z)

A major advantage of the proposed maglev isolator over traditional isolator designs is the ability of the maglev system to realise quasi-zero payload support stiffness in the vertical (Z) direction, while still providing a static payload supporting force. Figure 3.14 shows a case where the floater moves in the vertical direction. Using the calculation method outlined in Section 3.4, the relationship between the vertical displacement (z) and the total vertical magnetic force F_z is shown in Figure 3.14(b), where $p = 100\text{mm}$ is chosen to be the nominal separation between the magnets in this case. Table 3.2 lists the parameters of the magnets used to obtain the plot data.

3.6 6-DOF levitation stiffness

In Figure 3.14 (b), the slope of the tangent line to the force-displacement curve is the stiffness of the levitation in the vertical direction. It can be seen that at the nominal operating position, where the COG of the floater is at the midpoint between the two fixed magnets, the stiffness of the levitation is zero. For a displacement (comparable to the displacement of the laboratory floor vibration, Appendix B) within a small region around the nominal operating position, the levitation stiffness remains close to zero. Therefore, in the vertical direction, the magnetic levitation has quasi-zero stiffness around the nominal operating point.

In Figure 3.14(b), the vertical magnetic force (F_Z , approximately 39N in this case) at the nominal operating position is the load capacity of the isolator with a magnet separation of $p = 100\text{mm}$. This vertical force is designed to be used to balance the weight of the payload and is not the result of elastic deformation of the supporting structure. Therefore, the maglev system is able to provide quasi-zero levitation stiffness while still generating a passive magnetic force to support the static weight of the payload. This feature allows the 6-DOF maglev isolator design to avoid the usual compromise made between load capacity and isolation performance, which normally exists in linear vibration isolation systems.

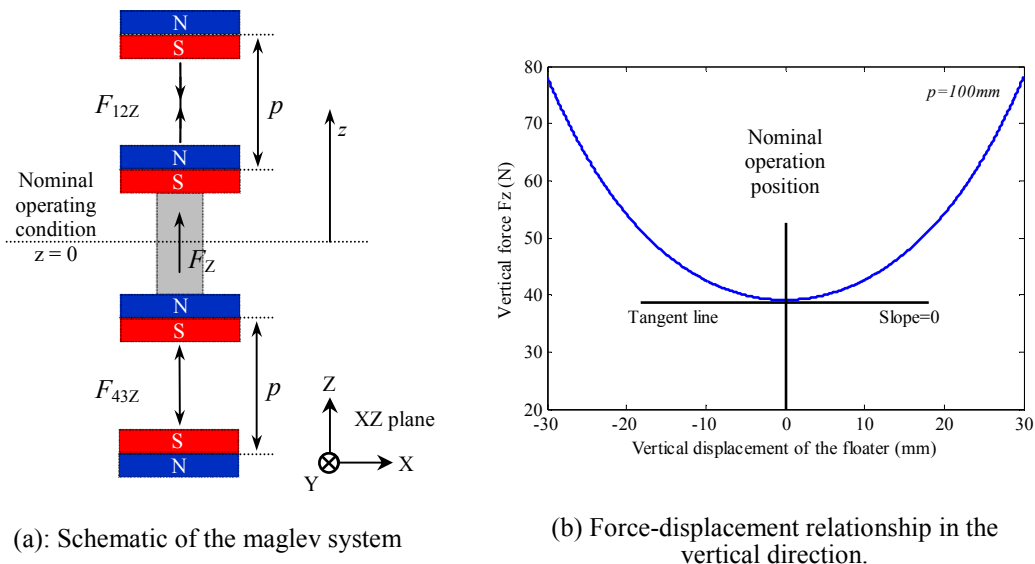


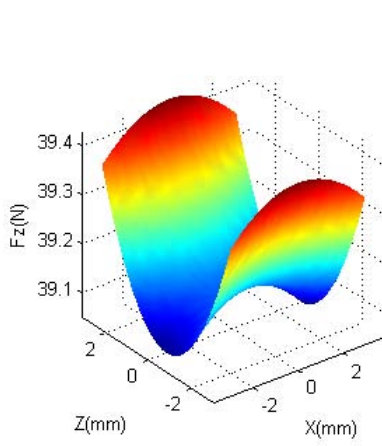
Figure 3.14: Force displacement behaviour of the maglev system in the vertical direction (Z). See Table 3.2 for details of parameters used to define the system.

Chapter 3 Background Theory and Methods

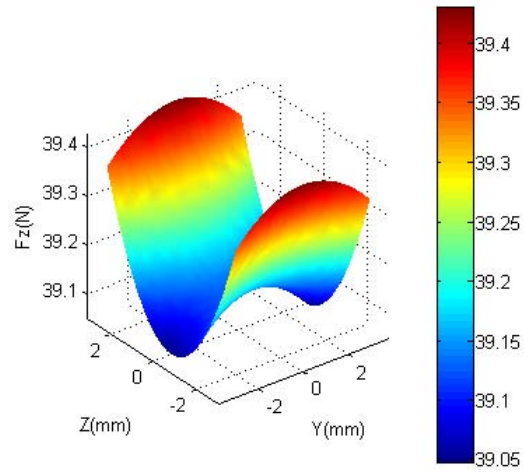
In the analysis of the above example, the floater motion was constrained by the motion of the floater in the vertical direction. However, it is also important to investigate the sensitivity of the vertical magnetic force to the displacements in the remaining five DOFs since external vibrations propagate in multiple directions. Using the numerical model of the maglev derived in Section 3.5.2, the vertical magnetic force, F_z , was calculated with combined floater displacements from two orthogonal DOFs. Figure 3.15 shows force-displacement relationships when the vertical displacement is combined with floater motions in the remaining five DOFs.

The five subplots of Figure 3.15 show the magnitudes of the vertical force when the Z (vertical) displacements is combined with the X, Y, α and β displacement respectively. From Figure 3.15(a) to Figure 3.15(d), it can be seen that the vertical magnetic forces are dependent on the magnitudes of both displacements, and with any given vertical displacement (z), the vertical force has the maximum value when the displacement in the other direction is zero. The cross-coupling from the X, Y, α and β directions to the Z direction result from the magnet coaxial misalignments introduced by the corresponding displacements. Motions in these four DOFs effectively increase the distances between both the top and bottom magnet pairs, thus reducing the forces generated between the magnets. In addition, the coaxial misalignment between the floater magnets and the fixed magnets means that only a portion of the total magnetic force is in the vertical direction, which also explains why the vertical magnetic forces is a maximum at zero displacements at any fixed vertical displacement (z). The cross-coupling effect is undesirable in this instance where the maglev system is used as a vibration isolation device. The disturbance to the vertical direction may be introduced from other DOFs through the cross-coupling effects. However, it can be observed from Figure 3.15 that, at the nominal operation point (displacements in all DOFs equal zero), the cross-coupling stiffness is quasi-zero between Z and the four DOFs X, Y, α and β . Therefore, during operation of the maglev isolator, the floater should be levitated at the nominal operation point to optimise the vibration isolation performance in multiple DOFs.

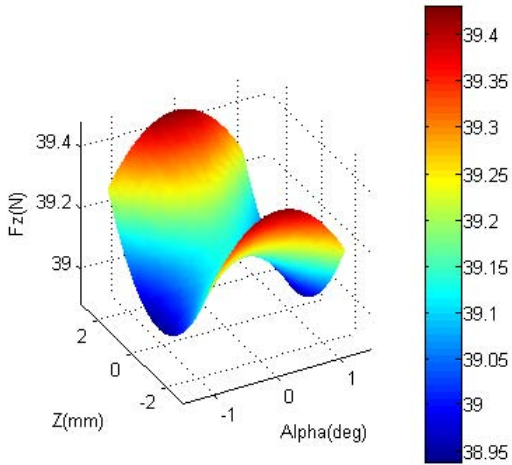
3.6 6-DOF levitation stiffness



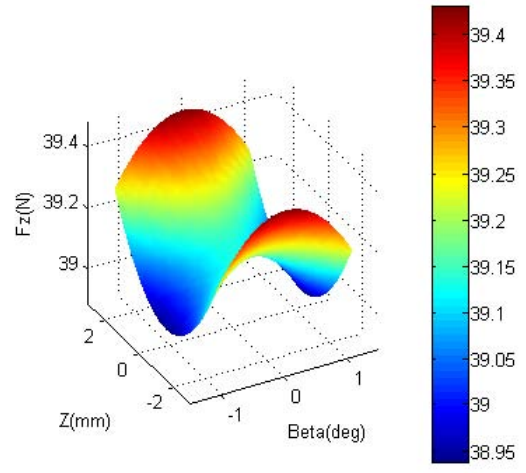
(a): F_z in the ZX plane.



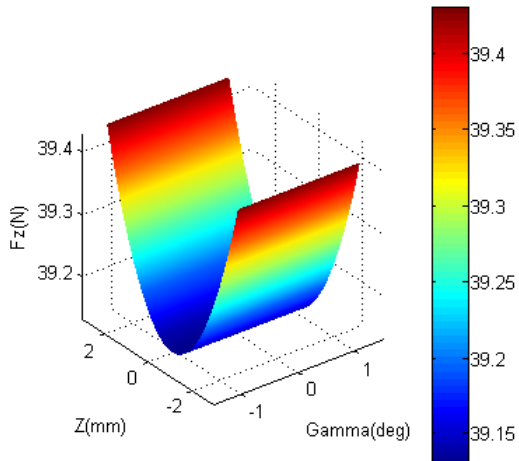
(b): F_z in the ZY plane.



(c): F_z in the Z α plane.



(d): F_z in the Z β plane.



(e): F_z in the Z γ plane.

Figure 3.15: Floater force-displacement behaviour of F_z with cross-DOF displacements.

Chapter 3 Background Theory and Methods

Figure 3.15(e) shows that the vertical force generated by the maglev system is not related to the displacement in the γ direction. This can also be observed from the system models that the γ displacement has no influence on the forces and torques in the other directions.

3.6.2 Zero stiffness in the horizontal directions (X and Y)

As mentioned previously, the proposed maglev system is able to achieve zero levitation stiffness in the horizontal directions (X and Y). Figure 3.16 shows a free body diagram of the floater in the YZ plane with a displacement in the Y direction. The forces experienced by the floater from both pairs of fixed magnets are resolved as shown in the figure. With floater displacement only in the Y direction, Equation (3.22) may be simplified to

$$\left\{ \begin{array}{l} F_{12Y} = |F_{12}| \cdot \frac{-y}{\sqrt{y^2 + p_{12}^2}} \\ F_{12Z} = |F_{12}| \cdot \frac{p}{\sqrt{y^2 + p_{12}^2}} \\ F_{43Y} = |F_{43}| \cdot \frac{y}{\sqrt{y^2 + p_{43}^2}} \\ F_{43Z} = |F_{43}| \cdot \frac{p}{\sqrt{y^2 + p_{43}^2}} \end{array} \right. \quad (3.30)$$

for calculating the forces and torques shown in Figure 3.16.

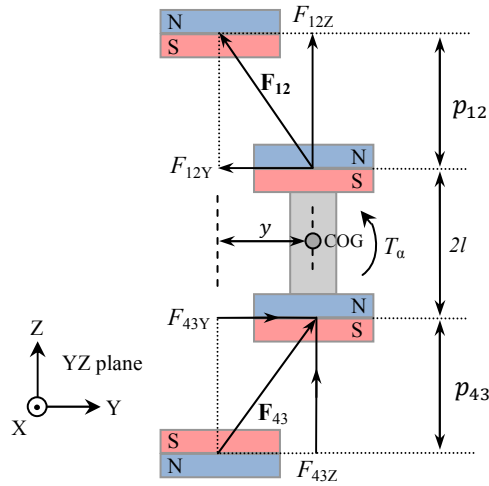


Figure 3.16: Free body diagram of the floater under horizontal displacement

Under the nominal operating condition, where $p_{12} = p_{43}$, it can be observed that the vector forces between the two pairs of magnets have the same magnitudes, i.e. $|\mathbf{F}_{12}| = |\mathbf{F}_{43}|$. Hence, from Equation (3.30), it can be shown that

$$F_Y = F_{12Y} + F_{43Y} = 0 \quad (3.31)$$

for all values of y . Therefore, the total force experienced by the floater in the Y direction is zero regardless of the displacement, which leads to the conclusion that the stiffness in the Y direction remains zero under the nominal operating condition. The derivations for demonstrating the zero levitation stiffness in the X direction are identical to the preceding discussion. For a displacement in the X direction, the equations for calculating the relevant forces in the XZ plane become

$$\begin{cases} F_{12X} = |\mathbf{F}_{12}| \cdot \frac{-x}{\sqrt{x^2 + p_{12}^2}} \\ F_{12Z} = |\mathbf{F}_{12}| \cdot \frac{p}{\sqrt{x^2 + p_{12}^2}} \\ F_{43X} = |\mathbf{F}_{43}| \cdot \frac{x}{\sqrt{x^2 + p_{43}^2}} \\ F_{43Z} = |\mathbf{F}_{43}| \cdot \frac{p}{\sqrt{y^2 + p_{43}^2}} \end{cases} \quad (3.32)$$

Chapter 3 Background Theory and Methods

Hence, under the nominal operation condition, where $|\mathbf{F}_{12}| = |\mathbf{F}_{43}|$, the total magnetic force in the X direction can be shown to be equal to zero using the same principles. With evidence of zero stiffness levitation in both the X and Y directions, it is reasonable to conclude that the levitation stiffness equals zero in any arbitrarily direction within the XY plane.

The realisation of zero levitation stiffness in the horizontal plane (XY plane) requires equal distances between the two magnet pairs. However, this does not always hold during operation of the isolator due to the multi-DOF nature of the external vibration. Hence, the force displacement behaviour of the horizontal floater forces was examined under combined displacements. Figure 3.17 and Figure 3.18 show the cross-DOF sensitivity of the horizontal forces in the X and Y directions respectively.

It can be seen from Figure 3.17(a) and Figure 3.18(a) that the horizontal force in either the X or Y direction remains zero for any displacement in the XY plane (the colour gradient on the flat plane is caused by the force calculation uncertainties, which are on the order of 10^{-14} N). This agrees with the expression for the zero horizontal stiffness derived previously. Figure 3.17(b) and Figure 3.18(b) show that the displacement in the vertical direction changes the zero stiffness property of the maglev in both the X and Y directions. This is because the vertical displacement interrupts the condition $|\mathbf{F}_{12}| = |\mathbf{F}_{43}|$, needed for achieving the zero horizontal stiffness. As shown by Figure 3.17(b), the vertical displacement changes the horizontal stiffness linearly from $\frac{dF_x}{dx} = 0\text{N/m}$ at $z = 0\text{mm}$ to a maximum of $\frac{dF_x}{dx} = 55.033\text{N/m}$ at $z = 3\text{mm}$ (displacement constraint from the mechanical isolator design shown in Chapter 4). At the current magnet nominal separation ($p = 100\text{mm}$) for this analysis, the vertical payload supporting force is 39.13N (Figure 3.22). This corresponds to a payload of approximately 4kg. Hence, with this combination of payload mass and system stiffness, the natural frequency of the system in the horizontal direction is $f_{n_x} = \frac{1}{2\pi} \sqrt{\frac{k}{m}} = 0.5903\text{Hz}$. This indicates that, even with the highest possible stiffness, the system is still expected to provide excellent vibration isolation in the X direction. Therefore, with small vertical excitations (comparable to

3.6 6-DOF levitation stiffness

the magnitude of the displacement of the laboratory floor vibration, Appendix B), the stiffness induced in the horizontal directions has no significant impact on the vibration isolation performance. The same conclusion can be made from Figure 3.18(b) for the Y direction.

Figure 3.17(d) and Figure 3.18(c) show the cross coupling effects of β to X coupling and α to Y coupling respectively. The figures show that a given angular displacement in the β direction will create a constant force in the X direction for all x (displacement in the X direction). Similarly, a given α displacement will have the same effect in the Y direction. These cross-coupling effects can also be analytically observed from Figure 3.19. In the figure, it was shown that a rotation in the α direction creates a horizontal force in the Y direction, and is calculated as

$$F_Y = F_{12Y} + F_{43Y} \quad (3.33)$$

for the cross-coupled force in the Y direction, and

$$F_X = F_{12X} + F_{43X} \quad (3.34)$$

for the cross-coupled force in the X direction. These cross coupling effects are undesirable in terms of vibration isolation since they introduce disturbances into the horizontal direction from the rotational excitations. However, with a static and controlled (using a maglev position controller discussed in Section 5.2) floater rotation, this side cross coupling effect can be utilised to balance the horizontal force input from the external payload. In Section 3.7.2, explanation will be given on how the cross coupling force is used to balance the payload horizontal force input.

Chapter 3 Background Theory and Methods

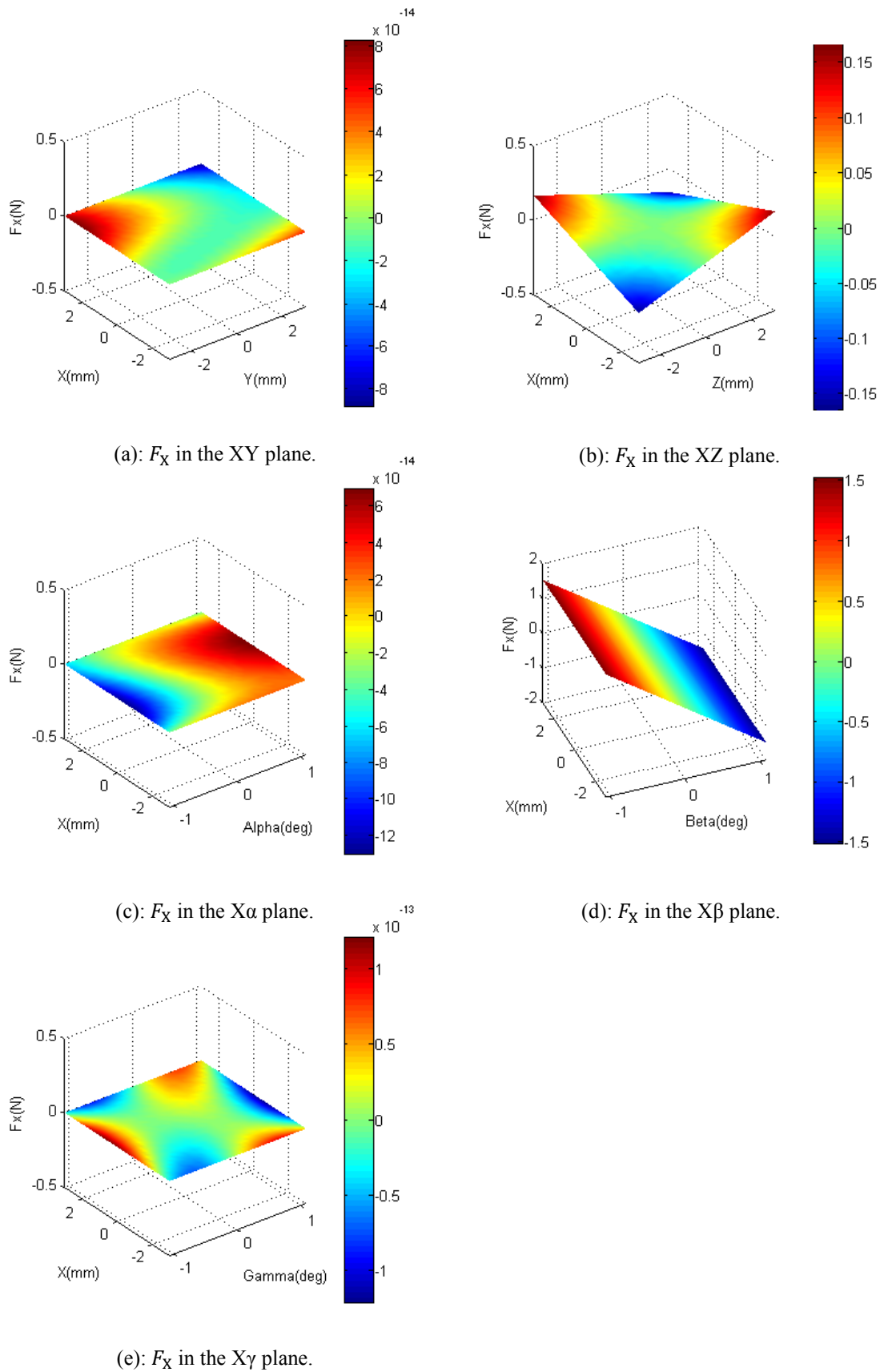
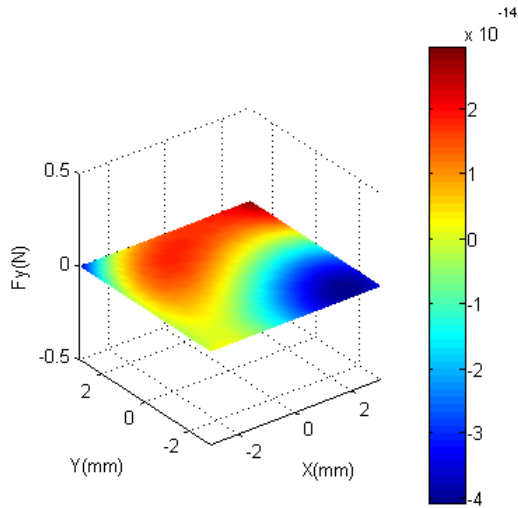
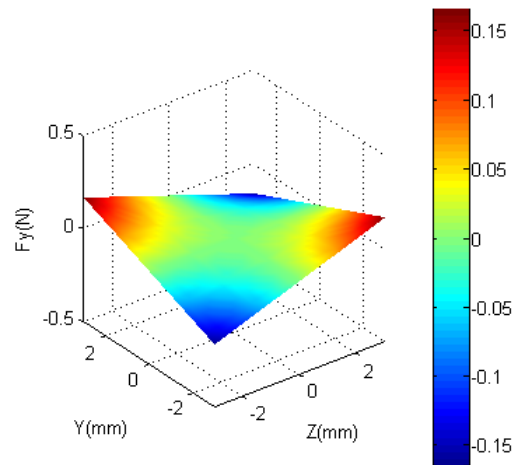


Figure 3.17: Floater force-displacement behaviour of F_X with cross-DOF displacements.

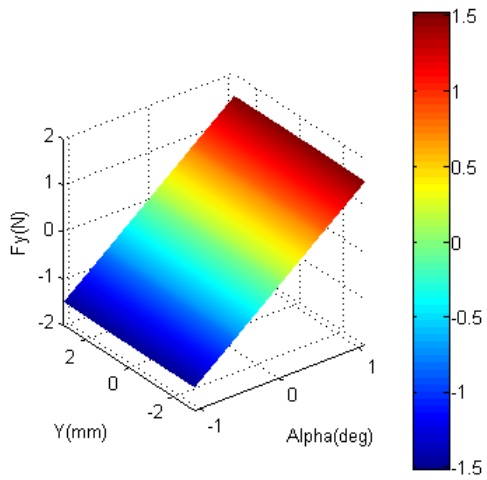
3.6 6-DOF levitation stiffness



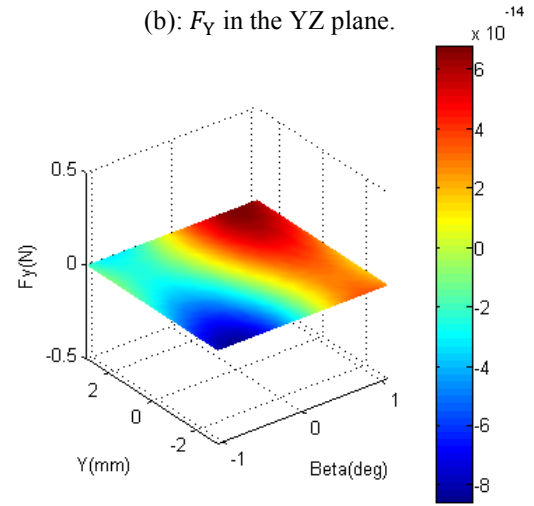
(a): F_Y in the YX plane.



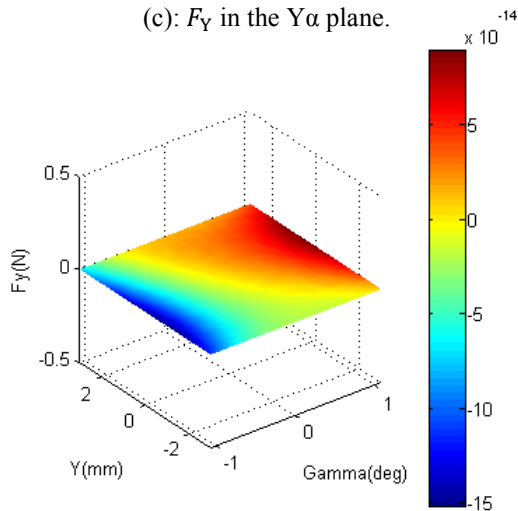
(b): F_Y in the YZ plane.



(c): F_Y in the $Y\alpha$ plane.



(d): F_Y in the $Y\beta$ plane.



(e): F_Y in the $Y\gamma$ plane.

Figure 3.18: Floater force-displacement behaviour of F_Y with cross-DOF displacements.

3.6.3 Zero stiffness in the rotational DOFs (α , β and γ)

The levitation stiffness of the proposed maglev system is also zero in the three rotational DOFs. An example is shown in Figure 3.19 where the floater is rotated in the YZ plane (in the α direction). Under such a rotational displacement ($-\alpha$), neglecting the magnetic torques between the two pairs of magnets (Section 3.4.3), the mechanical torque generated by the magnetic forces around the centre of the floater can be calculated as

$$T_{\alpha} = F_{12Y} \cdot l' - F_{43Y} \cdot l' , \quad (3.35)$$

where l' is the vertical distance (the lever arm for the torque) between the centre of the floater and the floater magnet. It is evident from Figure 3.19 that when the floater is at the nominal operating condition (equal nominal separation between the magnet pairs), the horizontal forces, F_{12Y} and F_{43Y} , have the same magnitude. Therefore,

$$T_{\alpha} = F_{12Y} \cdot l' - F_{43Y} \cdot l' = 0 . \quad (3.36)$$

This shows that for any rotational displacement in the α direction, $T_{\alpha} = 0$. Therefore, the floater has zero levitation stiffness in the α direction. Due to symmetry, the same principles can be applied to demonstrate the zero stiffness property of the maglev in the β direction.

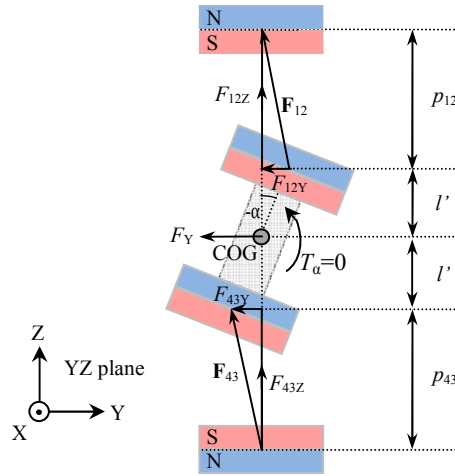


Figure 3.19: A schematic of the floater under rotational displacement

The preceding analysis assumed zero floater displacement in the remaining DOFs. To investigate the torque displacement behaviour in the 6-DOF space, the mechanical torque on the floater was examined for cases with combined displacements. Figure 3.20 and Figure 3.21 show the torque displacement behaviour of the floater for various displacement combinations. In Figure 3.20(b) and Figure 3.21(a), cross-coupling was shown between Y and α directions and X and β directions respectively. For a given horizontal displacement in the Y direction, a constant torque is generated for all α (angular displacement in the α direction), and with a fixed displacement in X, a constant torque is created in the β direction for all β . Again, this cross coupling effect was also shown analytically in Figure 3.16 for a horizontal displacement, y . The mechanical torque created is

$$T_{\alpha} = F_{12Y} \cdot l - F_{43Y} \cdot l. \quad (3.37)$$

Similarly, with an x displacement, the torque in β direction is

$$T_{\beta} = -F_{12X} \cdot l + F_{43X} \cdot l. \quad (3.38)$$

Chapter 3 Background Theory and Methods

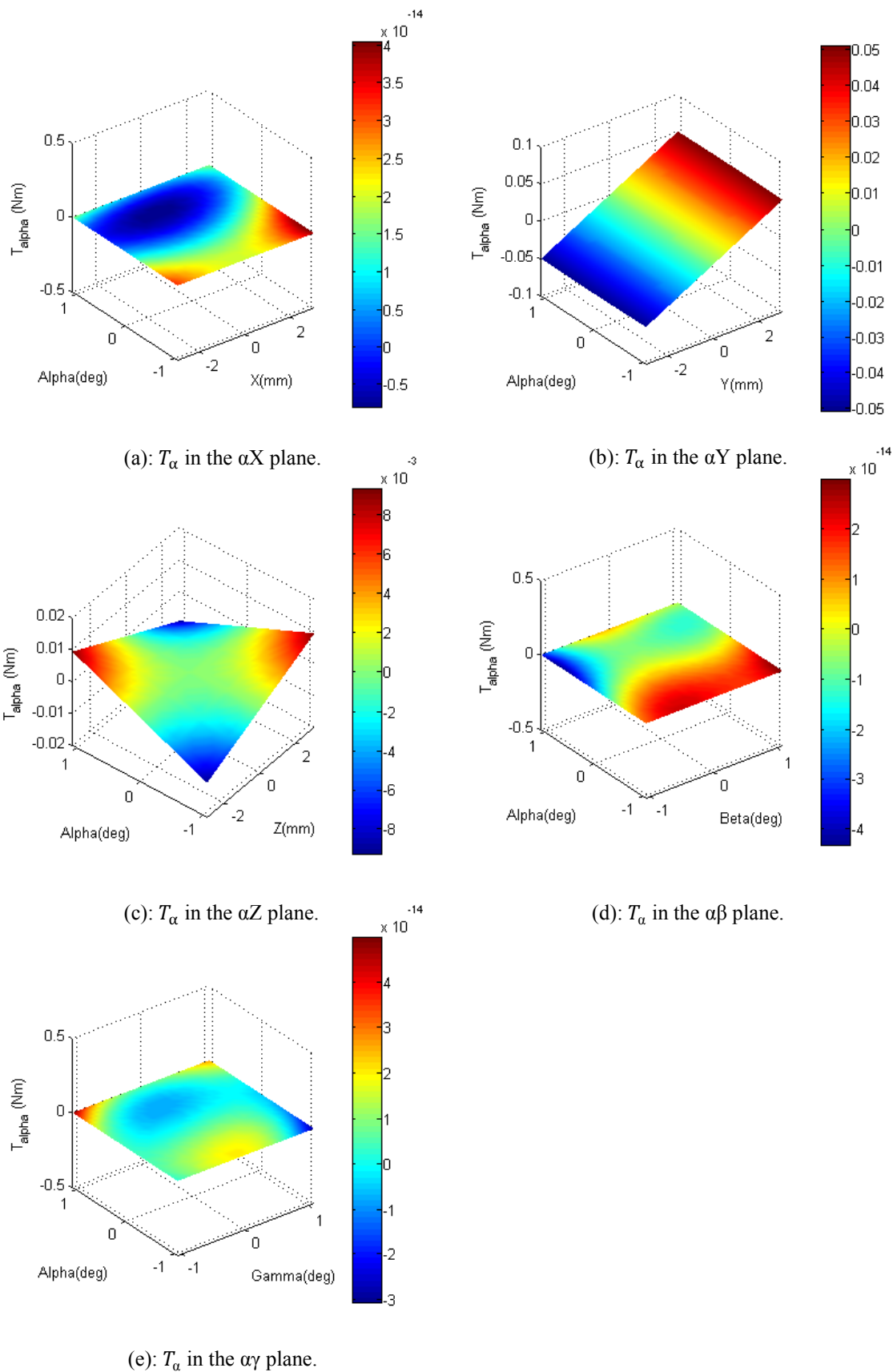


Figure 3.20: Floater force-displacement behaviour of T_α with cross-DOF displacements.

3.6 6-DOF levitation stiffness

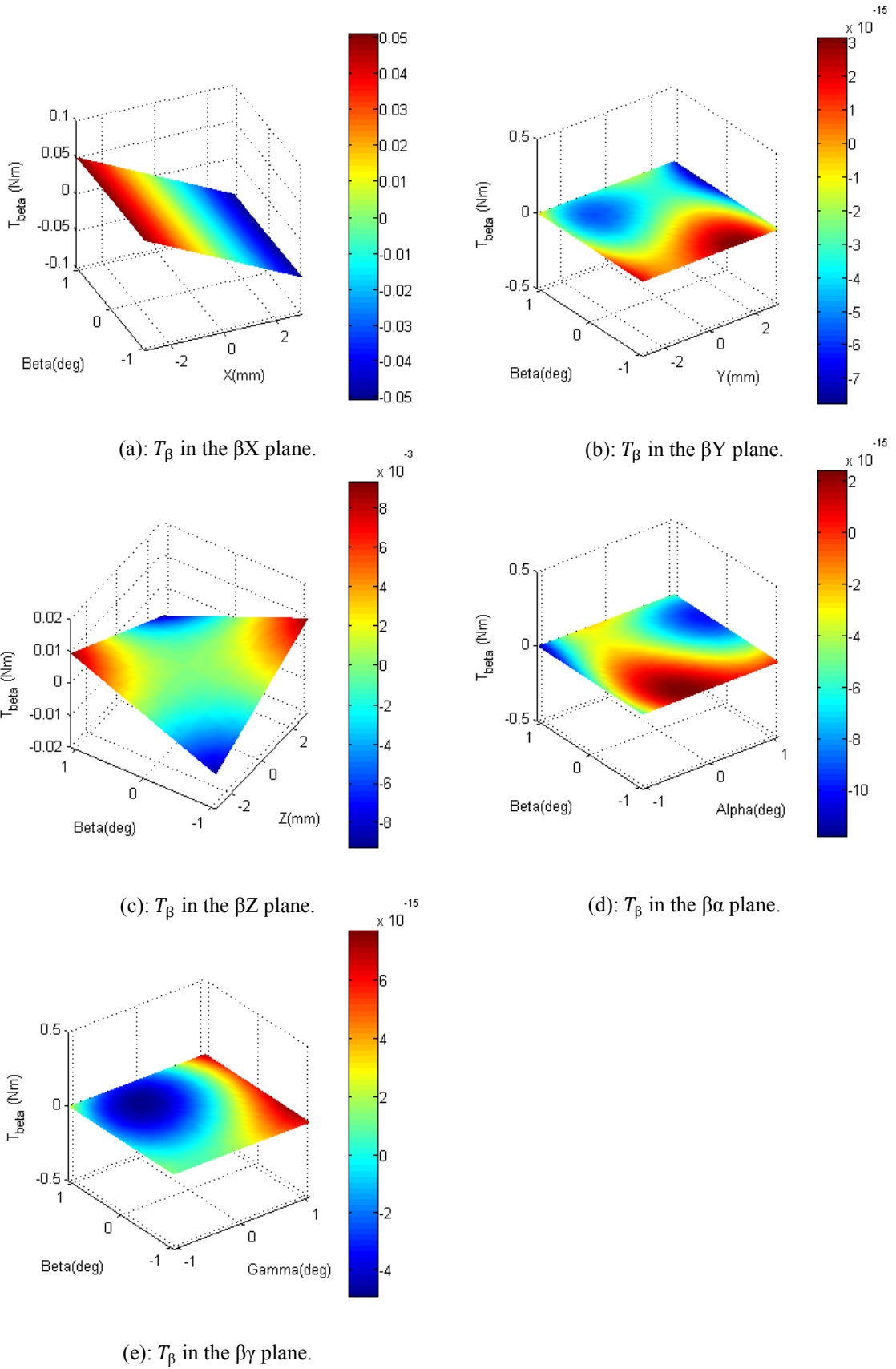


Figure 3.21: Floater force-displacement behaviour of T_β with cross-DOF displacements.

Chapter 3 Background Theory and Methods

The cross coupling effects shown are also undesirable in terms of isolating external vibrations. However, with a static and controlled floater horizontal motion, the torques created by the cross coupling effect may be used to balance the static moments input from the payload (shown in Section 3.7.3 and 5.3.3).

In Figure 3.20(c) and Figure 3.21(c), a similar cross coupling effect is shown between the vertical (Z) and the rotational (α and β) directions. The displacement in the Z direction increases the rotational stiffness of the maglev linearly from 0Nm/rad to a maximum of $\frac{dT_\alpha}{d\alpha} = 0.4952\text{Nm/rad}$ at $z = 3\text{mm}$. According to the mechanical design of the isolator, the floater moment of inertia is $J_{XX} = 0.0853\text{kgm}^2$ (Table 4.1). Therefore, in the α direction, the maximum natural frequency is $f_{n_\alpha} = \frac{1}{2\pi} \sqrt{\frac{k}{J_{XX}}} = 0.3835\text{Hz}$, which is an indication of the excellent rotational vibration isolation that is achievable by the system even at the largest rotational stiffness induced by cross coupling. Therefore, with the small rotational excitation that the isolator would experience during normal operation, the introduced rotational stiffness is not expected to influence the vibration isolation performance of the maglev isolator in the rotational DOFs.

In the proposed maglev vibration isolation system, the levitation stiffness is zero in the γ direction. This is due to the fact that the system is axisymmetric and as such there are neither mechanical constraints nor magnetic force constraints on the floater. The floater is able to move freely without any interference, and the γ direction is only actively stabilised using the maglev positioning control (discussed in Section 5.2). Therefore, theoretically, the maglev system itself has inherent zero stiffness in the γ direction.

3.7 Adaptive-passive payload support

The adaptive-passive payload support is an active control mechanism which adjusts the physical arrangement of the maglev system with the objective that the payload is only supported using the forces and torques generated by the permanent magnets. The following sections introduce the theoretical realisation of the proposed multi-DOF adaptive-passive payload support.

3.7.1 Supporting the payload weight

In Section 3.6.1, it was shown that the proposed maglev system has the ability to support the payload weight with a static magnetic force while providing a quasi-zero stiffness support in the vertical direction. This section explains how the magnitudes of the static supporting force can be adjusted to match the supporting force to the weight of the payload.

Considering the vertical displacement example shown in Figure 3.22(a), the force-displacement relationship of the floater is now plotted for several nominal magnet separations (p), as shown in Figure 3.22(b). At the nominal operating position, the vertical force values represent the static supporting forces that the maglev generates,

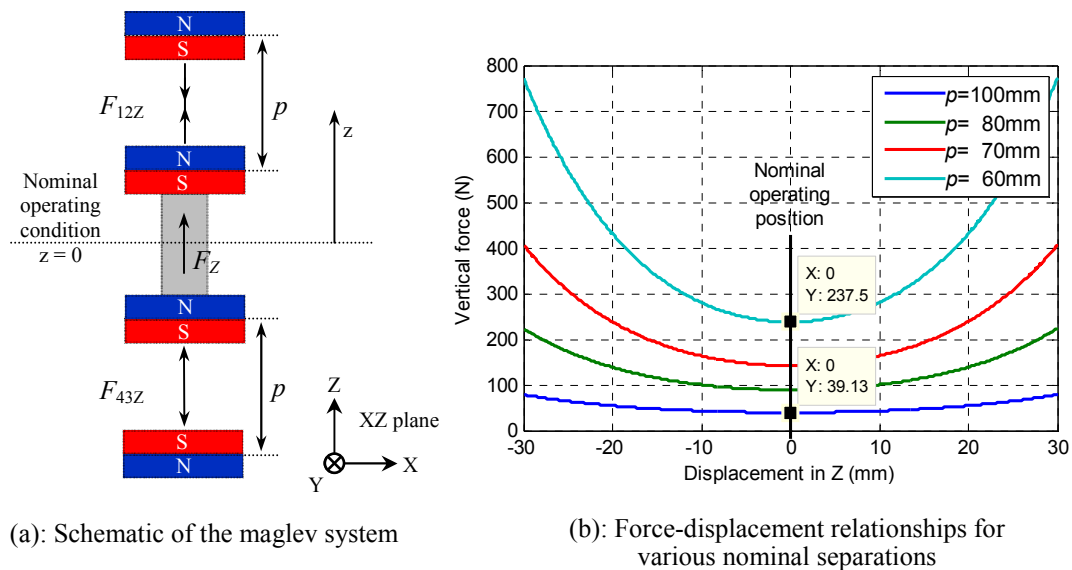


Figure 3.22: Vertical force-displacement relationships of the maglev isolator for various nominal magnet separations.

Chapter 3 Background Theory and Methods

which vary with magnet separation distance. For example, supporting forces of 237.5N and 39.13N are generated at 60mm and 100mm nominal separations respectively. It is evident that the static magnet supporting force is a continuous function ($F_z = f(p)$) and monotonically increases with a decrease in the magnet gaps. Hence, for a given payload weight, within the maximum supporting capacity of the magnets (when $p = 2 \times 0.5h$, where h is the magnet thickness), there is always a separation distance p where $f(p)$ equals the weight of the payload.

In this research, a novel control algorithm was proposed to achieve adaptive-passive payload support. This controller actively monitors the payload condition in real time, and adjusts the magnet separations to autonomously match the magnetic support force to the payload weight. The adaptive-passive payload weight support control algorithm will be discussed in Section 5.3.2

The adaptive-passive payload support allows the maglev to increase payload capacity by reducing the nominal separation between magnets. However, it should also be noticed from Figure 3.22(b) that reducing the nominal separation between the magnet pairs causes a reduction in the effective displacement range where quasi-zero levitation stiffness is achieved. Therefore, when designing an isolator based on the proposed quasi-zero stiffness levitation system, the floater weight should be kept at a minimum to allow use of larger nominal magnet separation for a certain payload. This is because the static supporting force generated by the maglev system needs to carry the combined weight of the floater and the payload (the payload is connected and carried by the floater to achieve vibration isolation).

3.7.2 Adaptive-passive support for horizontal static loads

Horizontal static loads refer to the static (DC coupled) disturbances on the floater that may occur in the X and Y directions. These loads may be introduced by an unbalanced payload or misalignments in the mechanical systems, and are able to be adaptive-passively balanced using the forces generated by the permanent magnets. Figure 3.18(c) demonstrates the cross coupling effect between the translational and rotational DOFs. A magnetic force F_Y is generated as a result of a rotational

3.7 Adaptive-passive payload support

displacement in the α direction, which is the same cross coupling effect shown in Figure 3.17(d) between X and β directions. Figure 3.23(b) shows the relationship between the horizontal force and the angular displacement for several magnet separations. Please note that Figure 3.23 (b) was obtained using the analytical model of the maglev system given by Equation (3.25) since the numerical model was only established for $p = 100\text{mm}$.

From Figure 3.23(b), it can be seen that the horizontal force F_Y increases monotonically with the increase in the rotational angle for small angles (in this case, angle α is considered small if $l \cdot \sin(\alpha) \leq 0.1p$). Therefore, with controlled floater rotation in the α direction, the magnitude of the horizontal magnetic force can be adjusted to match the external static disturbance in the Y direction, and likewise, the disturbance in the X direction can be balanced by rotating the floater in the β direction. The proposed control algorithm and its realisation to achieve autonomous adaptive-passive lateral force support are discussed in Section 5.3.3.

As discussed previously, the rotations in the α and β directions will not influence the zero stiffness characteristics of the horizontal levitation. It was shown in Figure 3.17(d) and Figure 3.18(c) that fixed angular displacements in the α and β directions will create only constant forces in the Y and X direction respectively. Therefore, the stiffness of the levitation in the X and Y directions remain zero. The cross coupling between the vertical and rotational directions (shown in Figure 3.15(c) and Figure 3.15(d)) also suggests that rotations in the α and β direction reduce the vertical payload supporting force. However, the design of the adaptive-passive payload support system enables simultaneous adaption in multiple DOFs. Hence, once the balance between the payload weight and the vertical supporting force is interrupted, the active control system (discussed in Section 5.3) will immediately adjust the nominal separations between the magnet pairs to re-establish the appropriate passive support conditions for the payload weight.

3.7.3 Adaptive-passive support static payload moments

In the rotational DOFs, static disturbances may exist in the form of moments around the centre of the floater. This may be caused by an asymmetrical floater mass distribution, or torques exerted by the payload connected to the floater. In Section 3.6.3, it was shown that a mechanical torque can be generated by the magnet forces when the floater is horizontally displaced. This section explains how this magnetic torque may be used to adaptive-passively balance the static moment inputs from the payload.

Figure 3.23(a) shows a schematic where a torque T_α is generated with a horizontal floater displacement y . This cross coupling effect can also be observed from Figure 3.20(b) and Figure 3.21(a). The torque in the α direction, as demonstrated in Figure 3.23(b), increases monotonically with an increase in y (for $y \leq 0.1p$). Therefore, in the α direction, for a given moment input within the capacity of the maglev, it is always possible to obtain a magnetic torque to counter balance the static moment disturbance by shifting the floater levitation position in the Y direction. Due to symmetry, the same supporting torque can be generated in the β direction by displacing the floater along the X axis. Section 5.3.3 details the control approach proposed to realise autonomous adaptive-passive support for balancing the static torque disturbances. Similarly, horizontal floater displacements for generating balancing torques will not affect the zero stiffness property of the maglev in the rotational directions since the cross coupled torques have constant magnitudes. The reduction in the vertical payload supporting force due to the horizontal displacements will also be actively accommodated by the simultaneous adaption process in multiple DOFs.

The third rotational DOF is the γ direction. Under normal operation of the maglev isolator, there is unlikely to be a static disturbance within this DOF, neither from the payload nor within the mechanical structure of the isolator. Hence, adaptive-passive support of moments within this DOF is unnecessary. It is also not possible to realise adaptive-passive payload support in the γ direction with the current design of the

maglev system since the magnet arrangement is incapable of generating passive torques in the γ direction.

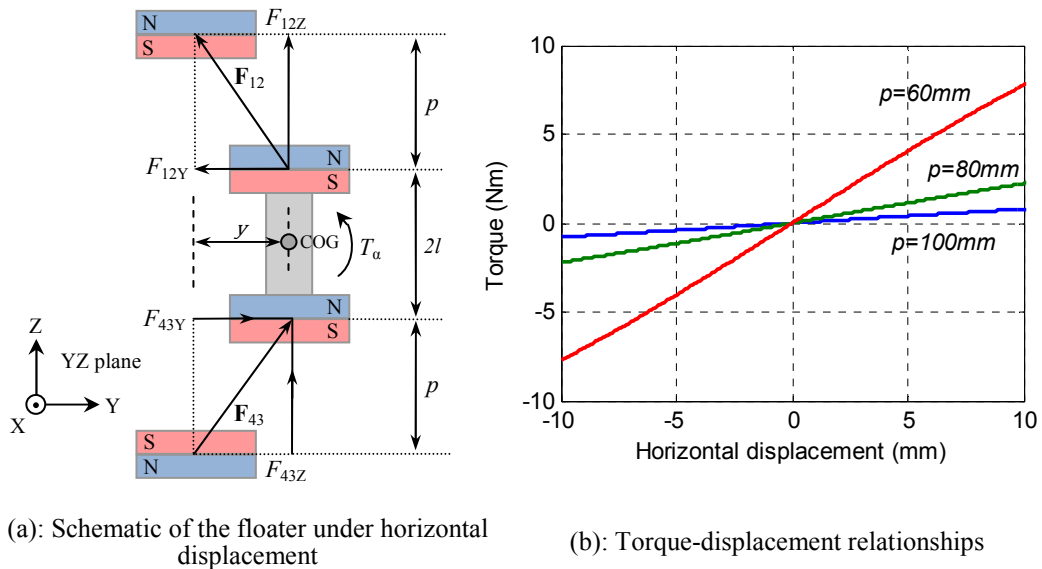


Figure 3.23: Torque-displacement behaviour of the maglev system under horizontal displacements with various nominal magnet separations.

3.8 Conclusion

In this chapter, the significance of the isolator stiffness and damping coefficient are demonstrated in terms of their effects on vibration isolation performance. A structural model of the proposed maglev system was presented to provide an outline of the quasi-zero stiffness maglev concept. Following the structural model, a 6-DOF dynamic model of the floater assembly was also derived to describe the floater dynamic response to external force and torque inputs, which will be used in later chapter when deriving the theoretical system performance. Calculation methods and assumptions for the magnetic forces and torques are discussed, as well as the approaches used in this research to simplify the calculations in order to improve the calculation execution speed and allow effective demonstration of the key points of the design concepts.

It was demonstrated the proposed maglev system is able to provide quasi-zero stiffness levitation in the Z direction, and zero stiffness in the remaining 5 DOFs.

Chapter 3 Background Theory and Methods

Cross-coupled stiffness of the maglev system were investigated and between each pair of orthogonal DOFs. The cross coupling effects were identified to exist between the rotational and translational DOFs (excluding the γ direction). It was discussed that these cross coupling effects are unlikely to have significant impact on the performance of maglev system as a vibration isolator. Following the discussion of the cross coupling effects, the operating principles of the proposed adaptive-passive payload support were presented, which uses the cross coupling effects to passively support the payload. It was shown that, in the vertical direction, the maglev load capacity is able to be adjusted by altering the separations between the two pairs of magnets, and the payload horizontal forces and rotational moments can be adaptive-passively supported by changing the floater pose.

Chapter 4

Development of the Maglev Isolator

4.1 Introduction

In this research, a maglev based 6-DOF vibration isolation approach is proposed, as well as a number of concepts that allow this novel vibration isolator to both provide quasi-zero/zero stiffness levitation in all six directions and support the payload forces and moments adaptive-passively. In order to validate the previously derived expressions through experiments, and to assess the difficulties in practical realisation of the theories, a physical 6-DOF maglev vibration isolator was designed and constructed. The mechanical system of the vibration isolator is an exact physical realisation of the maglev system described in Chapter 3, therefore, all the proposed methodologies and expected isolation performance improvements are able to be validated using the established mechanical system.

The design of the 6-DOF maglev vibration isolator was completed using CAD (Computer Aided Design) packages. In this chapter, the design of the floater assembly, the frame assembly, the magnet position control, as well as the 6-DOF floater position sensing and actuation systems are outlined individually, together with explanations of

Chapter 4 Development of the Maglev Isolator

the functionality of each subsystem. CAD models of the isolator design are presented, and an example showing the potential applications of the isolator design is also presented. Photographs of the manufactured mechanical system are shown at the end of this chapter.

4.2 Design of the 6-DOF maglev isolator

The 6-DOF quasi-zero stiffness vibration isolator was created based on the proposed maglev concepts discussed in Section 3.3. Several subsystems were also designed to realise the unique concepts explained in Chapter 3. This section demonstrates the detailed designs of the 6-DOF maglev isolator, as well as the working principles and integration of the subsystems.

4.2.1 Floater Assembly

The Floater Assembly is the core component of the maglev system. It is magnetically levitated during operation and therefore isolates the connected payload from external vibrations. Figure 4.1 shows a CAD model of the floater assembly. The floater assembly is held together using a six legged floater centre frame, which is linked to the payload through the payload connection beam. The two permanent magnets located at the top and bottom of the floater are the floater magnets, which are paired with the frame magnets (Figure 4.4) to create the quasi-zero stiffness maglev system. The floater centre frame also holds another six smaller actuator magnets. Solenoids are used together with these actuator magnets to form the 6-DOF active actuation system, which is explained in Section 4.2.3.

4.2 Design of the 6-DOF maglev isolator

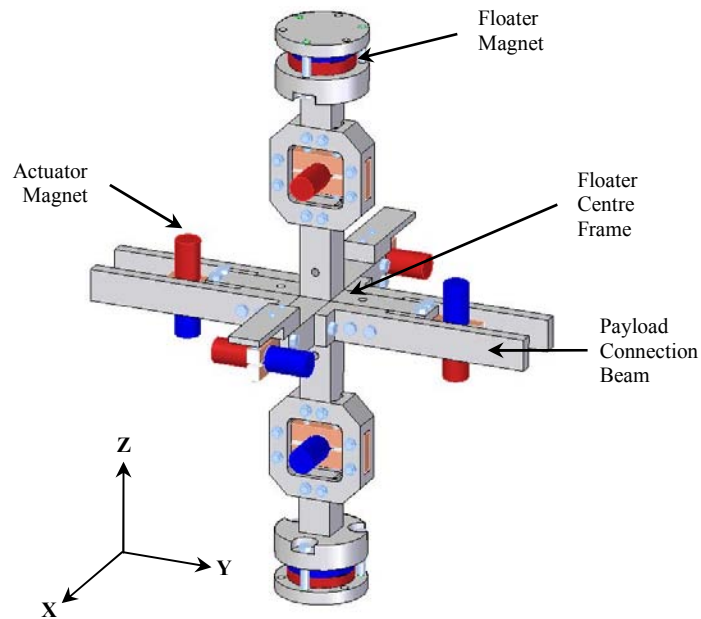


Figure 4.1: The Floater Assembly

4.2.2 6D floater position monitoring

As mentioned in Section 2.4.1, an active maglev stabilisation system is necessary to enable the operation of the magnetic levitation. This requires a sensing system that is able to determine, in real time, the position of the floater in the 6-DOF space. A noncontact position sensor is preferred since mechanical couplings form paths for external vibration to be transmitted. There are four main types of non-contact displacement sensors on the market that are commonly used for active control purposes, and these are discussed as follows

Inductive sensor

An inductive displacement sensor generates an alternating magnetic field which induces eddy currents in nearby metallic objects. The induced eddy current in the measuring target changes the resultant impedance of the coil inside the sensor. The sensor then determines the separation between itself and the object according to the

Chapter 4 Development of the Maglev Isolator

associated change in the coil impedance. In maglev systems, electromagnets and permanent magnets are often present, which can cause dramatic changes to the surrounding magnetic fields, and therefore, potentially disrupt displacement measurements using inductive sensors. Therefore inductive sensors are not suitable for the maglev isolation system.

Ultrasonic sensor

This type of sensor sends an ultrasonic wave towards the measuring target and calculates the distance by examining the time differences between the incident and the reflected ultrasonic wave. Ultrasonic sensors normally have relatively long response times and poor accuracy when compared to other types of displacement sensors. The poor measurement quality of ultrasonic sensors will result in noise in the maglev stability control system, which will be amplified by the position control actuators to introduce undesired vibration. Therefore ultrasonic sensors are not preferred in this design.

Capacitive sensor

A capacitive sensor measures the capacitance between two conductive objects to calculate the relative distance. This type of sensor can provide great accuracy and fast response. However, for measuring large distances, a large capacitive head is required (approximately 1cm diameter for every 1mm of measuring range (Boehm, 1993)). The capacitive type sensors also require small air gaps between the sensor and the measuring target. Therefore, capacitive sensors are not suitable for application in this research.

Laser displacement sensor

The most common type of laser position sensor uses a coherent light source which is directed towards the measuring object and measures the angle between the incident and the reflected beam to calculate the object distance relative to the sensor head. One important feature of such laser sensors is that they are immune to magnetic field fluctuations, which ensures undisturbed measurements in maglev systems. In this

4.2 Design of the 6-DOF maglev isolator

design, laser sensors were chosen to be the displacement sensors for their magnetic immunity, relatively large measurement range, high bandwidth and good accuracy.

The six-dimensional position of the floater is monitored using a purpose built Laser Sensor Array (Figure 4.2), which is used to estimate the 6-DOF floater coordinates for the levitation position controller at a frequency of 1250Hz. In Figure 4.2, which shows the floater assembly and the laser sensor array, the red coloured arrows indicate the laser beams and the associated measuring point. Section 5.2 will discuss the maglev stability control system, which uses this Laser Sensor Array to generate the floater position feedback signal. Specifications of the laser sensors selected for the physical system are detailed in Appendix D.1.

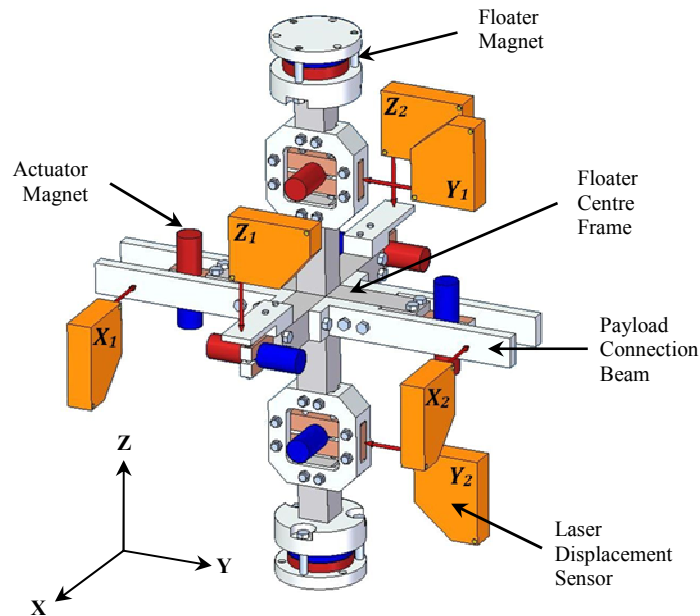


Figure 4.2: The Floater Assembly with the Laser Sensor Array

4.2.3 Frame assembly and actuators

The Frame Assembly is a cubic bar frame that surrounds the Floater Assembly, as shown in Figure 4.3. The Frame Assembly provides attaching points for the solenoid actuators, the laser sensors and the fixed magnets (Frame Magnets). It is also connected to four supporting legs which allow the whole system to stand on the ground, as shown in Figure 4.4. Figure 4.3(a) shows a rendered 3D CAD model of the

Chapter 4 Development of the Maglev Isolator

floaters and frame assembly with four of the solenoid actuators. There are two solenoids fitted on each side of the cubic frame assembly with one actuator magnet. By using two solenoids, this design doubles the actuation capacity compared to using a single solenoid, and also makes the forces symmetric on both sides of the actuator magnet. Each pair of solenoids located on the same face of the cubic frame assembly is operated in series, and forms one actuation unit with doubled force capacity. With the forces generated by the four solenoid actuators shown in Figure 4.3(a), noncontact actuation is achieved within the XZ plane, i.e. in the Z and β directions, as indicated by the arrows. The vertical actuation force (F_Z) is generated by collectively driving the actuators in the same direction, while the torque in the β direction (T_β) is created using force differential between the two pairs of actuators. Therefore, if the remaining eight actuators are inserted in the other two planes (XY plane and YZ plane), as shown in Figure 4.3(b), the floater is able to be controlled in the full 6-DOF space.

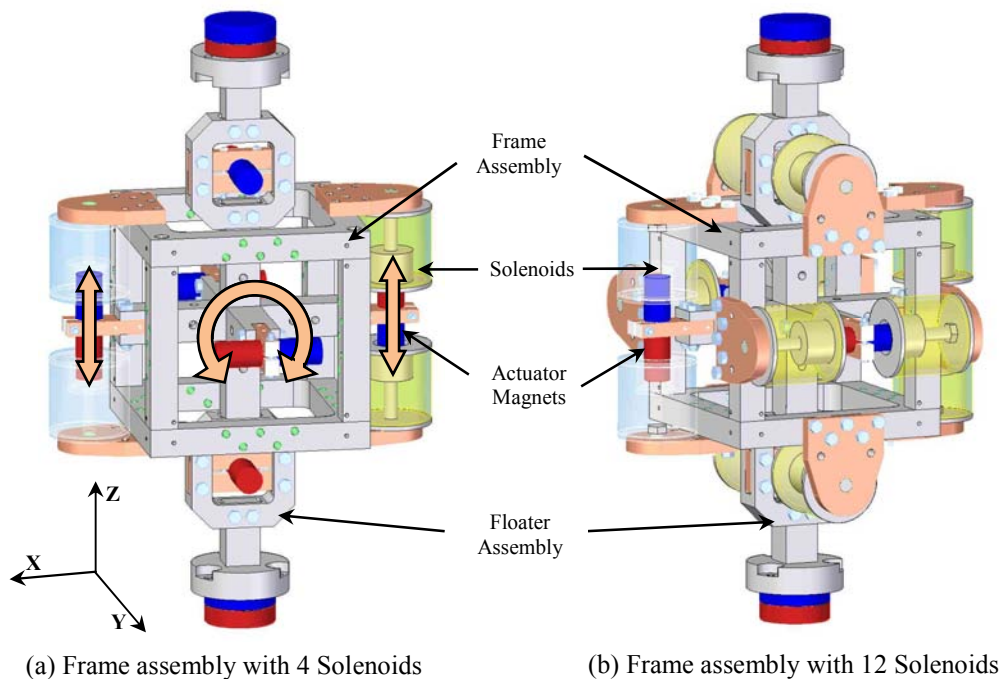


Figure 4.3: Detailed CAD model of the frame assembly.

In the design, the inner walls of the solenoid cavity are set to have a 3mm clearance to the surfaces of the actuator magnets. Therefore, the floater is able to travel up to $\pm 3\text{mm}$ in the three translational directions. The mechanical constraints in both the actuation system design and the frame assembly design also allow a ± 1.1 degrees

4.2 Design of the 6-DOF maglev isolator

angular displacement in each of the rotational DOFs. The solenoid design is explained in detail in Section 6.3.

4.2.4 Frame Magnet position control

In the maglev isolator design, there are two frame magnets located on the top and bottom side of the frame assembly, as shown in Figure 4.4(a). The frame magnets are paired with the floater magnets such that the top pair of magnets generates an attractive force and the bottom pair generates a repulsive force, so that the resultant levitation stiffness is quasi-zero in the vertical direction (discussed in Section 3.6), and zero in all five other DOFs (discussed in Section 3.6.2 and Section 3.6.3).

As demonstrated in Section 3.7, the load capacity of the maglev is adjustable by controlling the separations between the frame and floater magnets. Therefore, a magnet positioning mechanism was designed to adaptively change the vertical location of the frame magnets. Two of the proposed frame magnet control units are fitted to the top and bottom of the frame assembly in order to support the fixed magnets.

Each frame magnet position controller consists of four linear drives, which are synchronised through a timing belt pulley system driven by a drive motor. Through the linear drives, the rotational motion of the electric motor is converted to translational motion of the frame magnet so that the separation between the magnets can be automatically controlled.

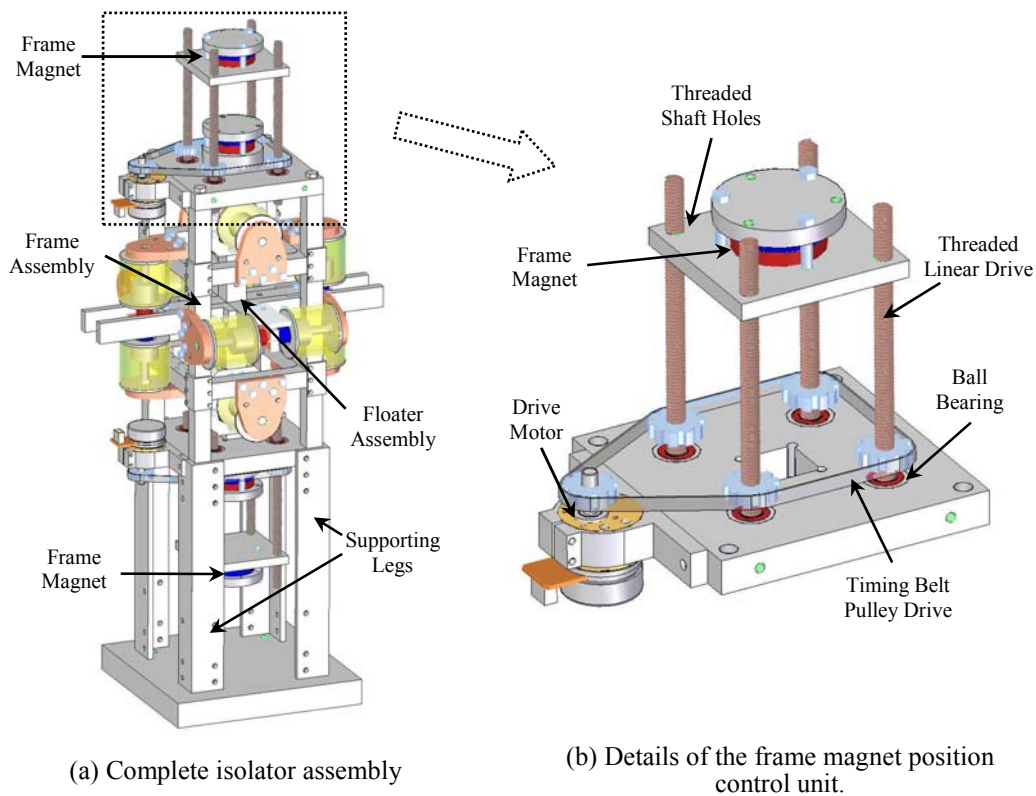


Figure 4.4: CAD model of the frame magnet position control unit.

4.2.5 Potential applications of the design

The 6-DOF maglev isolator is designed to provide 6-DOF vibration isolation to any structure attached to the floater. The payload connection beam is able to be connected to any existing mechanical system so that the target system is isolated from ground-borne vibration at the supporting point. In practice, likely that several of the proposed isolators would be required to support the target system. An example is shown in Figure 4.5, where four of the maglev isolators are used to create a 6-DOF vibration isolation table.

4.3 The manufactured vibration isolation system

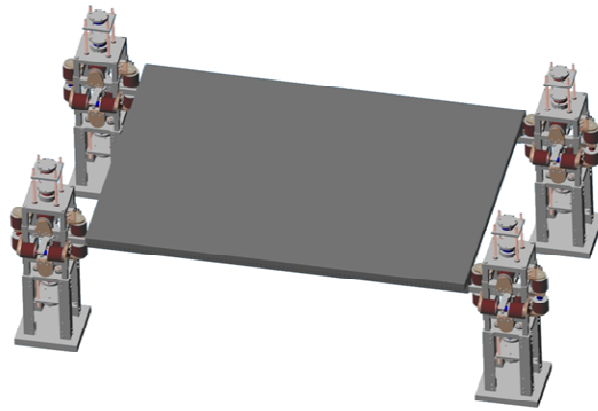


Figure 4.5: 6-DOF vibration isolation table concept created using four of the proposed maglev vibration isolators.

4.3 The manufactured vibration isolation system

The design of the 6-DOF maglev vibration isolator was manufactured in order to test the mechanism in practice. Figure 4.6 shows a photograph of the fully assembled mechanical system, and Figure 4.7 is a detailed view of the Magnet Position Control unit designed to adjust the separations between the magnets.

The floater frame and body frame of the isolator are manufactured from Grade 6061 Aluminium alloy, and the fasteners used to assemble the isolator are mainly made of austenitic stainless steel or copper. These materials have a relative magnetic permeability very close to unity, which means that they have negligible influence on an applied magnetic field, and therefore, do not interfere with either the permanent magnets or the solenoid actuators. Table 4.1 lists the important physical properties of the mechanical system.

Chapter 4 Development of the Maglev Isolator

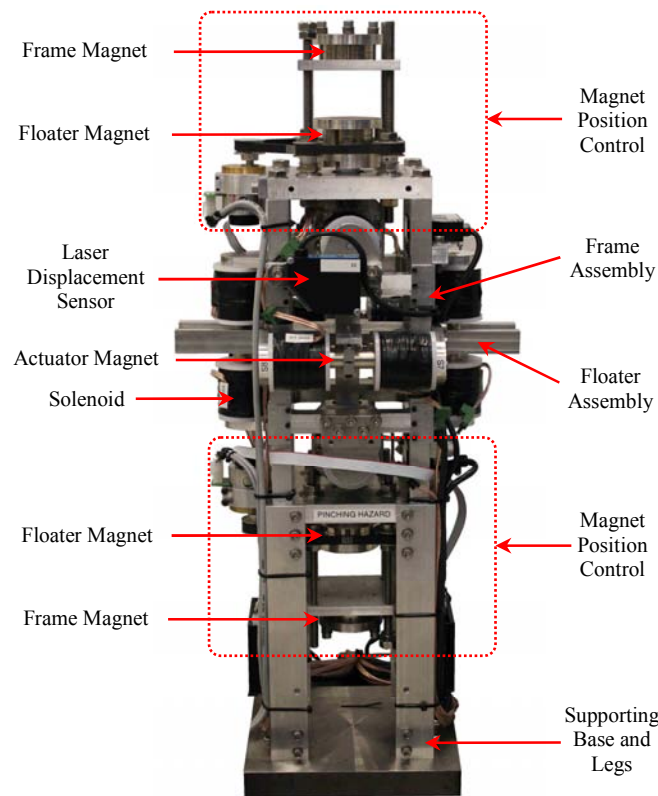


Figure 4.6: The manufactured 6-DOF maglev vibration isolator.

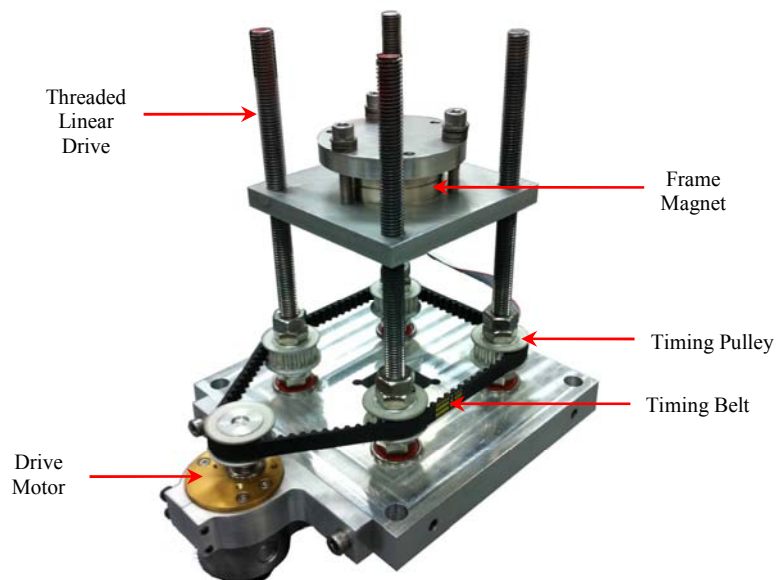


Figure 4.7: Detailed view of the manufactured Magnet Position Control unit

Table 4.1: Physical properties of the isolation system

Item	Description
Frame material	Aluminium 6061-T6
Mass	Frame: 19.6kg Floater: 6.408kg
Floater moments of inertia	$J_{XX}=0.0853\text{kgm}^2$ $J_{YY}=0.0851\text{kgm}^2$ $J_{ZZ}=0.0186\text{kgm}^2$
Dimensions of full isolator	Length: 230mm Width: 230mm Height: 1020mm
Primary magnets (Magnet 1, 2, 3 and 4 in Figure 3.6)	Ø50.8mm × 25.4mm; Grade: N52; Magnetization: 1.48T, refer to Appendix D.2 for more details
Secondary magnet (Actuator magnet)	Ø19.05mm × 76.2mm; Grade: N52; Magnetization: 1.48T refer to Appendix D.2 for more details
Allowable floater motion	Translational: $\pm 3\text{mm}$; Rotational: $\pm 1.1\text{deg}$

The majority of the structural components of the isolator were CNC machined. General tolerance, ISO 2768-fine, were used during manufacturing. Although all parts manufactured were of high finish quality, mechanical misalignments could still be observed due to the complexity of the isolator structural. These misalignments potentially influence the performance of control systems, as well as the vibration isolation performance of the overall system. The performance degradation due to mechanical misalignments will be discussed in future chapters together with the affected sub-systems.

4.4 Conclusion

In this chapter, a mechanical design of the maglev isolator was demonstrated, which is a physical realisation of the proposed concept of maglev vibration. The intended functionality of each subsystem was discussed based the CAD models of the design, and photographs of the isolator were also presented to demonstrate the integration between various sub-systems.

The mechanical design firstly provided a method to monitor the 6-D pose of the floater in real-time, followed by the discussion of the actuation system designed to

Chapter 4 Development of the Maglev Isolator

exert magnetic forces and torques to the floater in 6-DOF. A frame magnet position control unit was also proposed as a mechanism to relocate the frame magnets in the vertical direction. Hence the separations between the magnet pairs may be actively controlled.

Chapter 5

Real-Time Control Systems

5.1 Introduction

This research aims to develop a novel maglev based vibration isolation solution that is able to improve the isolation performance over conventional designs. Chapter 4 has presented the detailed mechanical design proposed to realise the 6-DOF quasi-zero/zero stiffness magnetic levitation. Another significant part of this research is the development of the active control systems to enable the operation of the 6-DOF maglev vibration isolator and to achieve the anticipated system performance. This chapter will discuss three unique control algorithms that were designed for the maglev isolator, namely, maglev stability control, adaptive-passive payload support and autonomous maglev tuning.

Maglev stability control

The maglev stability control is a feedback control system designed to stabilise the levitation position of the floater in all six DOFs. It includes a 6-DOF laser sensing system to monitor the location of the floater relative to the frame in real time, and a 6-DOF solenoid actuation system to place the floater at the desired levitation position.

Chapter 5 Real-Time Control Systems

Adaptive-passive payload support

The adaptive-passive payload support is a control algorithm that actively modifies the mechanical arrangement of the maglev system to support the static payload inputs using the forces generated by the permanent magnets. In this chapter a unique method is proposed to estimate the magnitude of the input forces and torques, and is followed by the control algorithm designs that use these force and torque estimates as feedbacks to adaptive-passively support the payload in all six DOFs. System integration of the adapting controllers is demonstrated at the end of this section.

Autonomous maglev tuning

In order to achieve quasi-zero stiffness levitation, it is necessary to levitate the floater at the nominal operation position, which is defined to be the condition when the centre of the floater is at the midpoint between the centres of the fixed magnets. However, the presence of mechanical misalignments makes it extremely difficult in practice to open-loop estimate the location of the nominal operation position. Therefore, a maglev auto-tuning algorithm is proposed, which actively monitors the levitation stiffness and power consumption and minimises these factors to optimally locate the nominal operation position. This system also minimises unnecessary levitation power consumption caused by misalignments in the mechanical and sensing systems.

5.2 Maglev stability control

As introduced in Section 2.4.1, stable magnetic levitation cannot be achieved using only static passive magnetic fields. This implies that magnetic levitation itself is inherently unstable, and therefore, an active stabilisation system must be designed for the maglev system to enable its stable operation as an isolator.

5.2.1 Composition of the stability control system

Stability of the maglev can be considered as the ability of the system to maintain a stable levitation position. The stability control system designed for the proposed maglev isolator is an active feedback control system which maintains the floater at a desired levitation position. It consists of two components; a 6-DOF floater position sensing system and a 6-DOF actuation system. The schematics of the subsystems are shown in Figure 5.1.

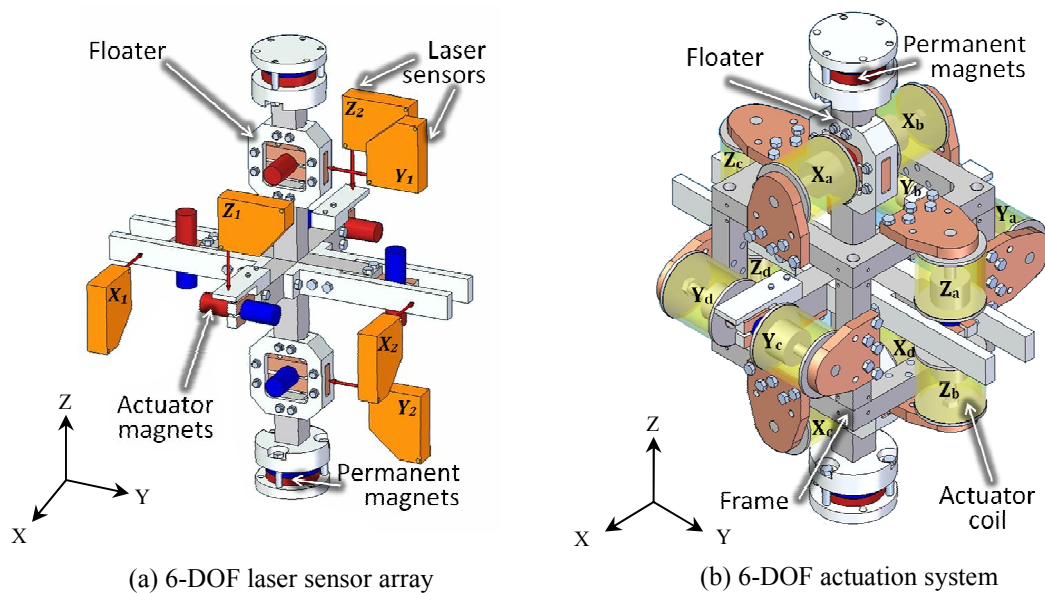


Figure 5.1: Subsystems of the maglev stability control.

Chapter 5 Real-Time Control Systems

The floater position sensing system shown in Figure 5.1(a) uses six laser sensors to measure the displacement of the floater at each monitoring point. The floater linear (x, y, z) and angular (α, β, γ) positions are then derived from the laser sensor feedback according to

$$\left\{ \begin{array}{l} x = \frac{x_1 + x_2}{2} \\ y = \frac{y_1 + y_2}{2} \\ z = \frac{z_1 + z_2}{2} \\ \alpha = \arctan \frac{y_2 - y_1}{L_y} \\ \beta = \arctan \frac{z_2 - z_1}{L_z} \\ \gamma = \arctan \frac{x_2 - x_1}{L_x} \end{array} \right. , \quad (5.1)$$

where x_i, y_i and z_i are the measured displacements from the corresponding laser sensors, and $L_X = L_Y = L_Z = 270\text{mm}$ are the distances between each pair of coaxial sensor monitoring points.

The floater actuation system, shown in Figure 5.1(b), is designed to apply forces and torques to the floater in order to relocate the floater to the desired levitation position. It contains six pairs of solenoids and six actuator magnets to enable actuation in all six DOFs (as discussed in Section 4.2.3). The combined actuation force and torque are calculated as

$$\left\{ \begin{array}{l} f_X = f_{X_a} + f_{X_b} + f_{X_c} + f_{X_d} \\ f_Y = f_{Y_a} + f_{Y_b} + f_{Y_c} + f_{Y_d} \\ f_Z = f_{Z_a} + f_{Z_b} + f_{Z_c} + f_{Z_d} \\ t_\alpha = \frac{1}{2} L'_X \left((f_{Z_a} + f_{Z_b}) - (f_{Z_c} + f_{Z_d}) \right) \\ t_\beta = \frac{1}{2} L'_Y \left((f_{X_a} + f_{X_b}) - (f_{X_c} + f_{X_d}) \right) \\ t_\gamma = \frac{1}{2} L'_Z \left((f_{Y_a} + f_{Y_b}) - (f_{Y_c} + f_{Y_d}) \right) \end{array} \right. , \quad (5.2)$$

where f_{kl} ($k \in (X, Y, Z), l \in (a, b, c, d)$) represent the actuation forces generated by the associated solenoids, and $L'_X = L'_Y = L'_Z = 220\text{mm}$ are the distances between

5.2 Maglev stability control

the actuation points and the centre of the floater (equivalent to the centre of gravity due to the symmetrical design of the floater).

In Section 2.4.1, a variety of controller structures used to stabilise magnetic levitations were discussed. Hence, the maglev stabilisation control is designed based on linear PID controllers with transfer function

$$C_i = P_i + \frac{I_i}{s} + D_i s \quad . \quad (5.3)$$

where P_i , I_i and D_i ($k \in (X, Y, Z, \alpha, \beta, \gamma)$) are the proportional, integrative and derivative gain of the controller respectively. Six decentralised SISO (single input single output) loops, each containing a PID controller, were used to stabilise the levitation in six DOFs. A linear controller structure was used since the nonlinear levitation stiffness contributed by the maglev was shown to be limited and can thus be neglected (This is experimentally demonstrated in Chapter 8). The PID type controller is chosen for its ability to directly control the levitation stiffness and damping. By using six SISO loops, the isolator performance is able to be configured individually in each direction.

The decoupled solenoid actuation system also justifies the selection of the SISO controller structure. Due to the fact that every pair of solenoids are driven in series to generate the same actuation force, Equation (5.2) can be simplified to

$$\left\{ \begin{array}{l} f_X = 2f_{X_a} + 2f_{X_c} \\ f_Y = 2f_{Y_a} + 2f_{Y_c} \\ f_Z = 2f_{Z_a} + 2f_{Z_c} \\ t_\alpha = \frac{1}{2} L'_X \left((2f_{Z_a}) - (2f_{Z_c}) \right) \\ t_\beta = \frac{1}{2} L'_Y \left((2f_{X_a}) - (2f_{X_c}) \right) \\ t_\gamma = \frac{1}{2} L'_Z \left((2f_{Y_a}) - (2f_{Y_c}) \right) \end{array} \right. \quad . \quad (5.4)$$

From the mechanical design of the actuation system, it can be seen that, when the floater is at the nominal operation position, the actuation forces/torques in each DOF are orthogonal to all the other DOFs, which shows that the actuation system is

Chapter 5 Real-Time Control Systems

decoupled in the 6-DOF space under nominal operation of the isolator. This can also be seen from Equation (5.4) since there always exists a set of unique solutions to the solenoid forces ($f_{Xa}, f_{Xc}, f_{Ya}, f_{Yc}, f_{Za}, f_{Zc}$) for an arbitrary given set of required actuation forces/torques ($F_X, F_Y, F_Z, T_\alpha, T_\beta, T_\gamma$). Therefore, the actuation system is decoupled in the 6-DOF space under nominal operation condition, and SISO (single input single output) control loops may be used to allow decoupled performance control in stabilising the maglev in each DOF. Section 6.5.1 will experimentally demonstrate that the actuation system is decoupled between the six DOFs during nominal operation.

The complete decoupling of the actuation system only exists when the floater is levitated at the nominal operation position. However, cross coupling will occur when the levitation position is not at the nominal point, such as when the adaptive passive payload support system changes the levitation position to balance the static external loads (Section 3.7). In practice, cross coupling effects may also be introduced by imperfections in the mechanical hardware, such as mechanical misalignments, and inconsistencies between the dynamics of the twelve solenoids. These cross coupling effects will result in undesirable cross-DOF actuations. However, direct elimination of the causes of the cross coupling effects is very difficult. In the design of the 6-DOF maglev isolator presented here, the undesirable floater motion caused by the cross coupling effects is actively compensated for by the maglev stability control system, which, in real-time, monitors the floater motion and maintains the command levitation pose.

5.2.2 Controller stiffness and maglev stability

The inherent stiffness of the maglev is quasi-zero in the vertical direction. However, a stability controller is necessary to enable the stable operation of the maglev system, which introduces additional stiffness to the maglev system. Figure 5.2(b) compares the vertical levitation stiffness between the maglev system alone and the system with the stability controller. In Figure 5.2(b), the blue curve represents the vertical stiffness of the maglev system derived by differentiating the vertical force (F_{12Z}) with respect to the floater vertical displacement. At the nominal operation point, the system stiffness equals zero. In general the maglev system is only stable when the overall

5.2 Maglev stability control

vertical levitation stiffness is positive. Therefore, with the maglev system alone, stable levitation in the vertical direction is only achieved with negative floater displacement, and at the nominal operating point ($z = 0$) the maglev system is marginally stable. By using a linear PID controller to stabilise the maglev isolator, a constant stiffness, determined by the magnitude of the controller proportional gain, is added to the maglev system. The green curve in Figure 5.2(b) describes the vertical levitation stiffness with an additional 100N/m stiffness induced by the stability controller. With the introduced stability controller, the system remains stable for displacements below 1.49mm. Hence, stable levitation is achievable in a wider displacement range compared to the maglev system with no controller. By increasing the stiffness of the stability controller, stable levitation can be achieved with larger floater displacement. However, as discussed before, an increase in system stiffness degrades the vibration isolation performance. Therefore, in theory, the controller stiffness should be tuned to the minimum magnitude required

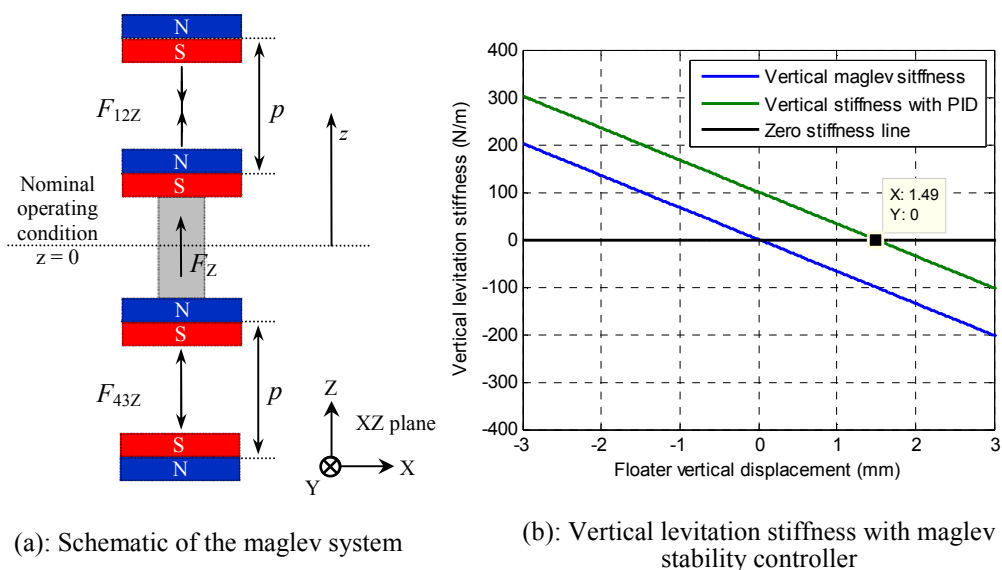


Figure 5.2: Vertical levitation stiffness with stabilisation controller ($p = 100\text{mm}$).

Chapter 5 Real-Time Control Systems

for maintaining levitation stability according to the displacement requirement of the application. For example, in the case shown in Figure 5.2(b), 100N/m is required if the stability needs to be maintained up to 1.49mm of floater vertical displacement. However, in practical situations, the controller stiffness necessary for maintaining levitation stability is often significantly larger than the theoretical magnitude. This can be caused by electronic hardware noise, sensor and actuator dynamics and cross-coupling effects. In practice, tuning of controller stiffness should be carried out based on the response of the physical maglev system.

It is also noteworthy that the controller induced stiffness only exists in the bandwidth of the active control system. The control system has been designed with the low-pass filters (Equation (5.5)), which attenuate the actuator control signals beyond 200Hz. For disturbance frequencies above 200Hz, the maglev vibration isolator essentially exhibits the quasi-zero stiffness characteristic in the vertical direction.

5.2.3 Cross coupling of sensor measurements

It should be noted that Equation (5.1) provides only an approximation of the location of the floater COG in 6-DOF space. With floater motions in multiple DOFs, geometric factors of the floater may couple into the laser measurements since the displacement sensors are not directly pointed at the COG of the floater. An example is shown in Figure 5.3(a), which shows a condition where the laser sensor acquires the correct floater position in the Y direction. When the floater is displaced in both the Z and the α directions, as shown in Figure 5.3(b), an error (Δy) is introduced in the Y displacement measurement due to the angular displacement (α) around the X axis. The mechanical constraint of the current design allows a maximum of 1.1degrees of floater rotation in the α direction. This is also the angle at which Δy reaches maximum, and calculated as $\Delta y = z \cdot \tan(\alpha)$. With the largest possible floater displacement of 3mm in the Z direction (constrained by the mechanical design), the maximum value of Δy is 0.0576mm, which is 0.96% of the 6mm span of the allowable floater displacement in the Y direction. Therefore, for simplicity of the controller design, the cross coupling effect in the laser sensor measurements was neglected.

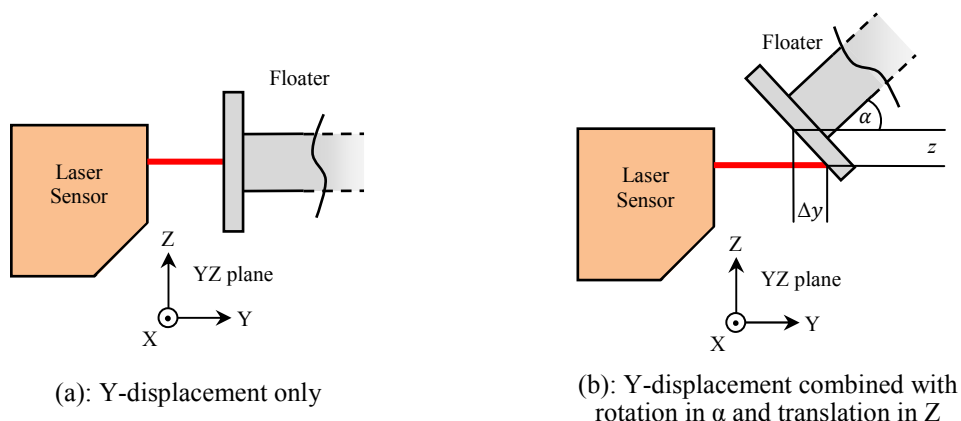


Figure 5.3: Cross coupled laser sensor measurement error.

5.2.4 Controller realisation and tuning

The structure of the maglev stability controller is shown in Figure 5.4. Six SISO PID controllers are used in parallel for floater position regulation in the six DOFs. Each PID controller is paired with a power amplifier that is operated in the current control mode (in this mode, the internal current control loop of the amplifier ensures the amplifier output current is directly proportional to its input command signal) to directly control the actuation force generated by each solenoid. The feedback signals to the PID controllers are the positions of the floater relative to the isolator frame, as measured by the laser sensors. Therefore, the proportional gain of the PID controller directly controls the stiffness of the levitation, the derivative gain controls the relative levitation damping, and the integral control loop eliminates levitation position offset. To avoid exciting high frequency structural modes of the floater and amplifying electronic noise, each PID controller output is passed through a second order low-pass filter ($LP(s)$) with 200Hz cut-off frequency, written as

$$LP(s) = \frac{\omega_{LP}^2}{(s + \omega_{LP})^2}, \omega_{LP} = 200 \text{ Hz} \approx 1257 \frac{\text{rad}}{\text{s}}, \quad (5.5)$$

where ω_{LP} is the cut-off frequency of the low-pass filter, and s is the complex frequency variable of the Laplace Transform.

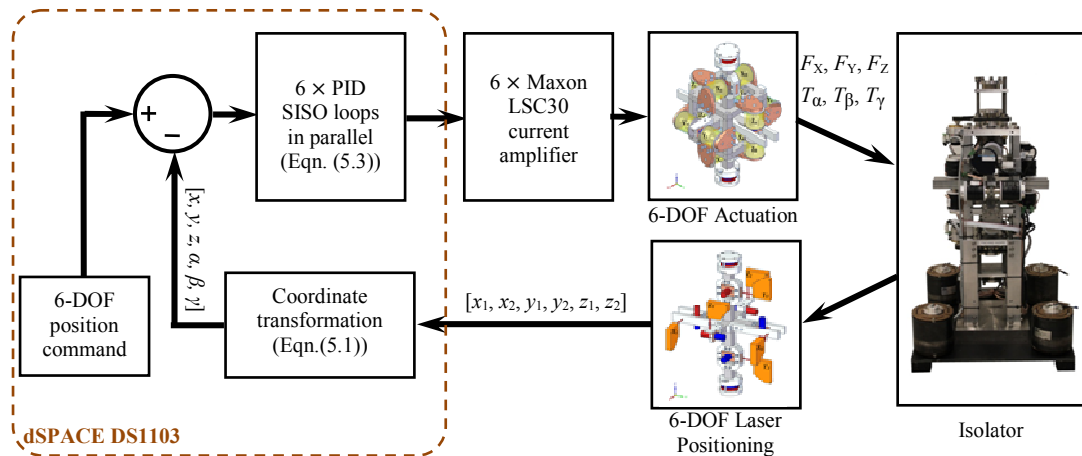


Figure 5.4: Structure of the maglev stability controller.

To isolate ground-borne vibration, low levitation stiffness is desirable since it reduces the vibration transmissibility and the system natural frequency. The proportional gain of the PID controller is thus tuned to the minimal value necessary for stabilising the levitation. Relative damping between the floater and the frame reduces vibration amplification at system resonances. However, as shown in Section 3.2.2, it also adversely affects the vibration isolation performance beyond the natural frequency of the system. Therefore, the derivative gain should be kept at the minimal value required to maintain adequate attenuation to the isolator peak response and to maintain the stability of the loop. The role of the integral loop in the PID controller is to generate static forces/torques needed for positioning the floater. However, with the assistance from the adaptive-passive payload support, the output from the integral loops should be quasi-zero since the static disturbance from the payload is adaptively balanced using the permanent magnets (discussed in Section 5.3).

In the physical system, a dSPACE DS1103 platform was used to execute the controller designs. The digital controller was run at 10000Hz, which was the maximum frequency achievable in practice for the designed control systems. Using the maximum sampling speed ensures the minimum time delay due to digital sampling, and hence, results in minimum phase distortion to the signals within the control system. Matlab Simulink and dSPACE Control Desk were used to program

and configure the controller algorithms. The specifications of the dSPACE DS1103 can be found in Appendix D.3, and the specifications of the Maxon motor controller are listed in Appendix D.4.

5.3 Adaptive-passive payload support

In Chapter 3, it was shown that the maglev system is able to generate a static levitation force to support the payload weight, and the cross coupling forces and torques may also be used to balance static disturbances in other DOFs. With appropriate control system designs, the passive supporting forces and torques generated by the permanent magnets are able to be controlled to precisely match the magnitude of the external loads. Therefore, the static loads are balanced using the permanent magnets only, which negates the need for an electro-magnetic actuation system to generate supporting forces which is typically power intensive. This section will discuss the proposed control algorithms to realise the adaptive-passive payload support in the physical system.

5.3.1 External disturbance monitoring

Adaptive-passive payload support is a process of matching the generated static supporting force/torque to the magnitude of the static disturbance force/torque experienced by the floater. This requires the determination of the external forces and torques so that the corresponding control effort can be applied to realise the adaptive-passive payload support. Conventional approaches for acquiring the magnitudes of the forces and torques commonly involve the use of load cells, which measure the relative forces and torques between the two objects firmly connected to the load cell. However, the maglev system is a non contact supporting mechanism. Measuring the forces and torques experienced by the floater using load cells requires the floater to be firmly connected to a fixed external structure, which forfeits the ability of the system to isolate vibrations. An alternative approach is mounting the entire isolator on a 6-DOF load cell, which does not require a solid connection between the floater and the isolator frame. The external static disturbances can then be estimated by deriving

Chapter 5 Real-Time Control Systems

system kinematics and force balances. However, the estimates obtained using this method can be inaccurate depending on the system design. The extremely complex structural design and system dynamics of the 6-DOF maglev isolator make this method unsuitable for achieving accurate adaptive-passive payload support in multiple DOFs. Therefore, the conventional method of measuring forces and torques using load cells is not applicable in this design, and an alternative method was developed for estimating the forces and torques during normal system operation.

The proposed method to estimate the external forces and torques is through monitoring the electric current drawn by the actuation system when maintaining a steady levitation. In order to maintain a desired floater position during levitation, the actuation system must provide supplementary forces and torques to balance the external loads on the floater. At steady state, the actuation forces and torques are directly proportional to the current drawn by the corresponding solenoids. When all the external loads are supported using permanent magnets, which is the aim of the adaptive-passive payload support system, the mean current drawn by the actuation system should be close to zero. Therefore, since the actuator amplifier is operated in the current control mode, the adaption process of the adaptive-passive payload support is equivalent to the process of minimising the DC (low frequency) component of the amplifier command signals. In the design, the DC components of the amplifier command signals in all six DOFs are extracted using six identical second order low-pass filters with 0.5Hz cut-off frequency. Details of the DC component extraction are explained in the following sections together with controller designs for achieving the adaptive-passive payload support.

During the DC component signal acquisition, it is important that the position of the floater (relative to the laser sensors) is stable so that the DC components of the command signals accurately reflect the difference in the magnitudes between the static payload inputs and the static forces and torques generated by the permanent magnets. The controllers presented in Sections 5.3 and 5.4 also require these forces and torques to be measured continuously while the floater levitation position is commanded to change along a special path. Hence, during the system operational

modes when the DC component signal is needed, it is essential that the maglev stability controller has excellent position command tracking ability. Therefore, the maglev stability controller is set to a mode with much higher stiffness and damping during the operation periods when DC component signal acquisition is necessary. More details of this secondary stability controller are discussed in Section 6.5.1.

5.3.2 Supporting the payload weight

The magnitude of vertical payload supporting force generated by the permanent magnets of the maglev can be changed by altering the separations between the top and bottom magnet pairs (refer to Section 3.6). Figure 5.5 shows the controller structure designed to automate the process of matching the maglev supporting force to the payload weight.

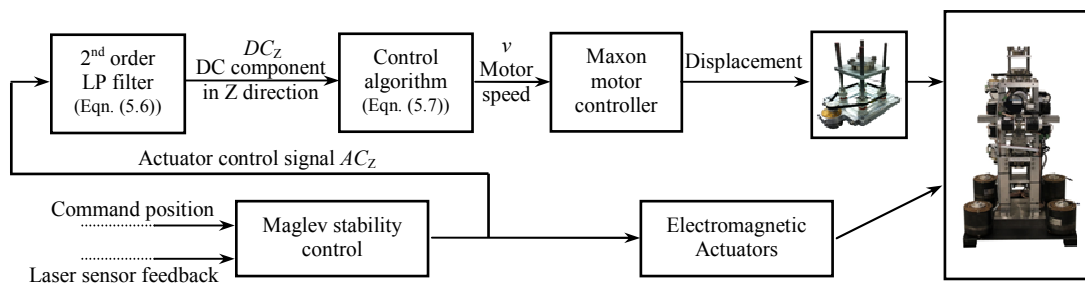


Figure 5.5: Controller structure of the adaptive-passive payload weight support

During system operation, it is desired that the floater levitation is constantly maintained to be at the nominal operation position. Ideally, with optimum system tuning, the separations between the magnets should be set to result in a vertical levitation force equalling the weight of the payload. Therefore, under the nominal operation condition with optimum system tuning, the electromagnetic actuation system (detailed in Section 4.2.3) does not need to generate any static supporting forces. In order to automate this system tuning process, the proposed adaptive-passive support controller uses the magnet position control units (Section 4.2.4) to adjust the separations between the magnet pairs according to the real-time DC components of the actuation currents. When the electromagnetic actuators are required to generate a static upward force for the payload levitation, the adaptive-passive support controller will command the magnet position control to reduce the separations between the

Chapter 5 Real-Time Control Systems

magnet pairs until the vertical levitation force from the permanent magnets is increased to the magnitude of the payload weight (the DC component of the actuator command signal becomes zero). Similarly, when the actuation system is generating a static downward force, the magnet separations are increased to reduce the excessive vertical levitation force.

In Figure 5.5, DC_i ($i \in (X, Y, Z, \alpha, \beta, \gamma)$) represents the DC component of the actuator control signal (AC_i) in each of the six DOFs, which is estimated using the second order low-pass filters written as

$$\frac{DC_i}{AC_i} = \frac{\omega_{LP}^2}{(s + \omega_{LP})^2}, \omega_{LP} = 0.5 \text{ Hz} \approx 1.57 \text{ rad/s} . \quad (5.6)$$

where ω_{LP} is the cut-off frequency of the low-pass filter, and v represents the permanent magnet travelling speed (positive v increases magnet separation). The control algorithm used is a two-state fuzzy logic controller described by

$$v = \begin{cases} -v_H \cdot \text{sign}(DC_Z), & |DC_Z| \geq a \\ -v_L \cdot DC_Z, & |DC_Z| < a \end{cases} , \quad (5.7)$$

where $v_H = 0.5 \text{ mm/s}$ and $v_L = 2 \text{ mm/(sA)}$ are the high and low magnet travelling speed gains, and $a = 0.05 \text{ A}$ is the actuator current threshold for switching the controller state. A plot of magnet travelling speed (v) versus DC control current (DC_Z) is shown Figure 5.10.

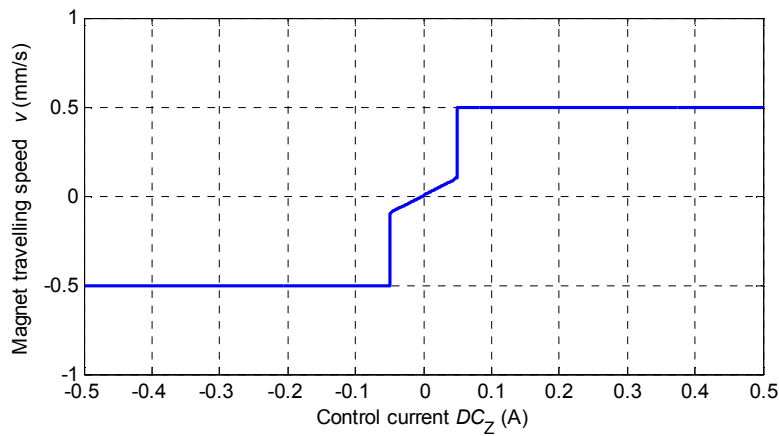


Figure 5.6: Command magnet travelling speed vs. DC control current.

5.3 Adaptive-passive payload support

The magnet travelling speed is controlled by two Maxon motor controllers (one for the top magnet position control unit, and one for the bottom unit). Through the internal control loops, the motor controllers operate the drive motors (shown Figure 4.4) at the command speed.

As discussed in Section 5.3.1, the DC component of the actuator control current is obtained using a low-pass filter with cut-off frequency at 0.5Hz. The dynamics of the low-pass filter means the sensing system has a “slow” response to changes in the monitored forces and torques experienced by the floater. When the adaptive-passive payload support controller is activated, it adjusts the separations between the magnets to change the vertical magnetic forces generated by the permanent magnets. If the magnet separation is changed at excessive rates, the slow response of the sensing system may result in instability of the adaption controller. The maximum magnet travelling speed has to be limited for the sake of controller stability. The first state of the fuzzy logic controller described by Equation (5.7) assigns a constant travelling speed to the frame magnets. The magnitude of this constant travelling speed is the maximum value allowed, determined through experimental trails, without compromising the stability of the adaption controller. When the magnitude of the required actuator control current (DC_z) is higher than a , the motor controllers operate the system at the maximum allowable speed (v_H) for fast adaption.

The second state of the adaption controller uses proportional control logic, which reduces the magnet travelling speed when the magnitude of the vertical force generated by the permanent magnets approaches the weight of the payload. Hence, the proportional controller can increase the accuracy of the adaption process, and prevent oscillatory behaviour at the equilibrium point, which would occur if constant magnet travelling speed were used during the entire adaption process. The appropriate gain of the proportional control (v_L) and the switching current threshold (a) were determined through experimental trails.

The operation of the adaptive-passive payload support disturbs the stability of the floater levitation position. Therefore, a sub-control logic was used to deactivate the

adaption controller when the adaption process is completed. If $|DC_Z| \leq 0.01A$ is true for 10 seconds, it marks the completion of the adaption process and the adaption controllers are deactivated. If $|DC_Z| \geq 0.01A$ is true for over 10 seconds, the adaption process is reactivated again to eliminate the static power consumption. The experimental system performance of the adaptive-passive payload support is reported in Section 6.6.

5.3.3 Supporting the horizontal forces and rotational torques

The control algorithm for adaptive-passively supporting four other DOFs, Y, Z, α and β , (as discussed in Section 3.7.3, passive floater support in the γ direction is not necessary) is similar to the weight adaption controller discussed in the previous section. However, instead of commanding the magnet position control units to adjust the separations between the permanent magnets, the adaption controller here commands the maglev stability controller to relocate the floater position to generate supporting forces and torques.

The controller structure shown in Figure 5.7 is an example of the adaption process for supporting the payload in the α direction. Let t represent the time, and C_Y represent the position command in the Y direction given by the adaption controller (relocating the floater in the Y direction generates torque in the α direction). The controller algorithm can be written as

$$C_Y = \begin{cases} \int P_H \times \text{sign}(DC_\alpha) dt, & \text{when } |DC_\alpha| \geq b \\ \int P_L \times DC_\alpha dt, & \text{when } |DC_\alpha| < b \end{cases}, \quad (5.8)$$

where $P_H = 0.1\text{mm/s}$ and $P_L = 2\text{mm/(sA)}$ are the high and low floater relocation speeds respectively; $b = 0.05A$ is the threshold for applying the different relocation speeds. Figure 5.8 shows the controller logic described by Equation (5.8). The magnitudes of the controller parameters were determined through experimental trails. Again, this controller structure allows fast adaption when actuator power consumption

5.3 Adaptive-passive payload support

is high, and trims the floater position slowly with greater accuracy when the control current drops below the low level threshold.

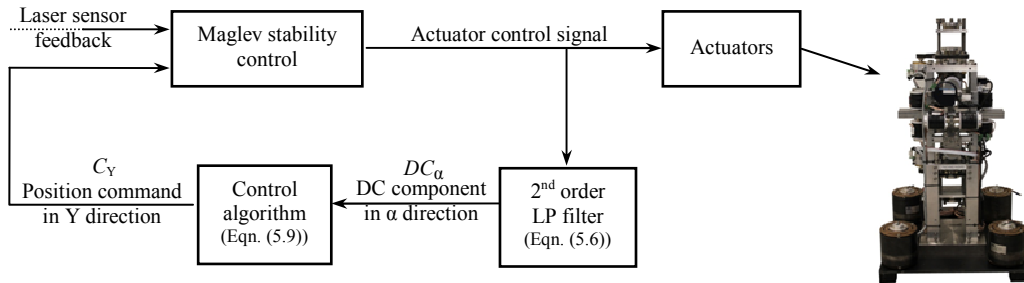


Figure 5.7: Controller structure for adapting disturbance in the α direction.

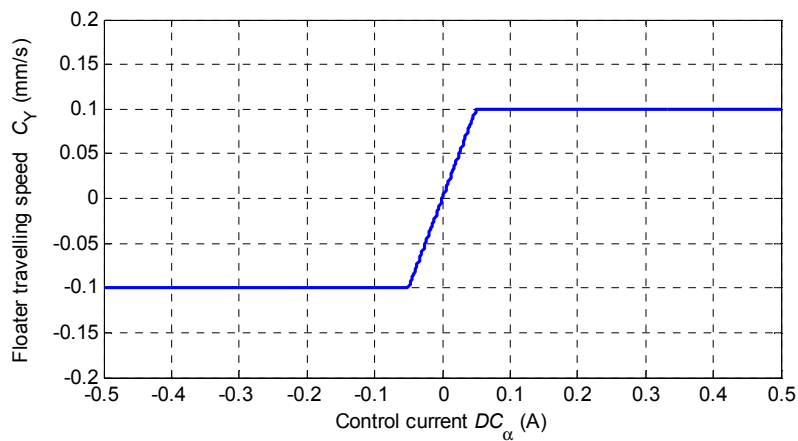


Figure 5.8: Command floater travelling speed vs. DC control current.

The DC control current (used as the controller feedback signal) is obtained by the external disturbance monitoring method discussed in Section 5.3.1. For the monitoring algorithm to accurately estimate the forces and torques experienced by the floater, the floater needs to have zero acceleration in all six DOFs. Therefore, in the adaption controller design, large floater acceleration should be avoided. This constraint applies to the adaption processes where the floater levitation position has to be adjusted to generate balancing forces and torques. Hence, as shown in Figure 5.8, the floater travelling speed is continuous between the two controller states as opposed to the discontinuity of the magnet travelling speed shown in Figure 5.6.

Chapter 5 Real-Time Control Systems

Similarly, the adaption processes for balancing the torques and horizontal forces introduce disturbances to the floater levitation. Therefore, the adaptive-passive payload support controller is disabled when DC_α is below 0.01A for more than 10 seconds, and is reactivated if DC_α is over 0.01A for more than 10 seconds. The adaptive-passive payload support can be realised using the same method in the β direction with the control logic

$$C_X = \begin{cases} \int P_H \times \text{sign}(DC_\beta) dt, & \text{when } |DC_\beta| \geq b \\ \int P_L \times DC_\beta dt, & \text{when } |DC_\beta| < b \end{cases} \quad (5.9)$$

The preceding control strategies is for adapting the moment disturbance in the rotational directions by displacing the floater in the translational directions. The same control logic is also suitable for adaptive-passively supporting the payload forces in the translational DOFs (X and Y). When adapting the horizontal payload force inputs, the maglev stability control is commanded to rotate the floater so that translational forces are generated to balance the static external forces (Section 3.7.2). The adaption controllers for the X and Y directions respectively are,

$$C_\alpha = \begin{cases} \int A_H \times \text{sign}(DC_Y) dt, & \text{when } |DC_Y| \geq b \\ \int A_L \times DC_Y dt, & \text{when } |DC_Y| < b \end{cases} \quad (5.10)$$

$$C_\beta = \begin{cases} \int A_H \times \text{sign}(DC_X) dt, & \text{when } |DC_X| \geq b \\ \int A_L \times DC_X dt, & \text{when } |DC_X| < b \end{cases} \quad (5.11)$$

where $A_H = 0.1\text{deg/s}$ and $A_L = 2\text{deg/(sA)}$ are the high and low floater rotation rates, which were determined using experimental trails. Figure 5.9 shows a plot of the command floater angular speed versus the DC control current in the Y direction.

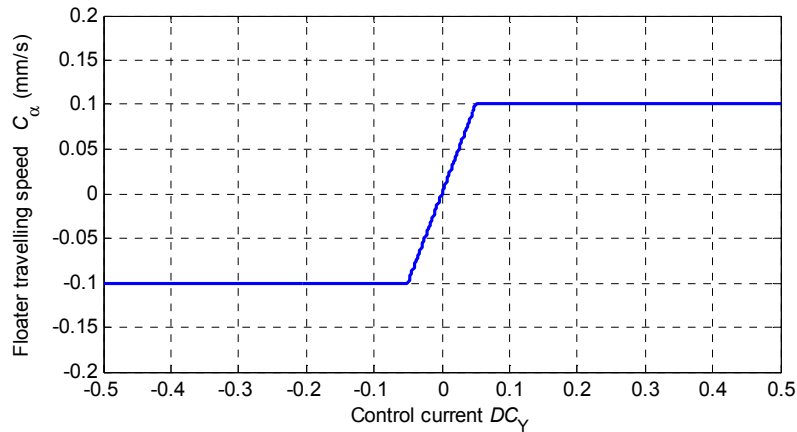


Figure 5.9: Command floater angular speed vs. DC control current.

5.3.4 Comments on the interference and cross coupling of the adaptive-passive payload support

The adaptive-passive payload support mechanism changes the positions of the permanent magnets and the floater levitation position to generate forces and torques for balancing the external inputs. It may appear that the levitation position offset introduced by the adaptive-passive payload support disturbs the quasi-zero/zero stiffness behaviour of the levitation. However, the stiffness of maglev system remains the same under static pose offsets introduced by the adaptive-passive payload support.

In the vertical direction, the adaptive-passive payload support system adjusts the positions of the frame magnets to change the supporting forces for the payload weight. Therefore, the levitation position of the floater COG is maintained at the vertical midpoint of the two frame magnets. Hence, the vertical separations between the two magnet pairs are equal, and the adaptive-passive payload support system has no impact on the stiffness characteristics of the maglev in the vertical direction.

The external static loads in the X and Y directions are balanced adaptive-passively by rotating the floater along the β and α directions respectively. As shown in Figure 3.17(d) and Figure 3.18(c), constant angular displacements in the β and α directions only result in static forces in the X and Y directions respectively. This effectively changes Equation (3.31) to

$$F_Y = F_{12Y} + F_{43Y} = f_Y \quad , \quad (5.12)$$

where f_Y is the constant cross coupling force resulting from the α rotation. Differentiating Equation (5.12) with respect to the Y displacement of the floater gives $\frac{dF_Y}{dy} = f'_Y = 0$. Hence, the zero horizontal levitation stiffness is maintained in the Y direction, and also in the X direction for the same reason. Similarly, Figure 3.20(b) and Figure 3.21(a) show that, with constant floater translations in the X and Y directions, only static torques are generated in the α and β directions respectively, which changes Equation (3.36) to

$$T_\alpha = F_{12Y} \cdot l' - F_{43Y} \cdot l' = t_\alpha \quad . \quad (5.13)$$

This also demonstrates that the zero stiffness property of the maglev is maintained in the α and β directions. Therefore, it can be concluded that the adaptive-passive payload support system does not influence the stiffness of the maglev system in any of the six DOFs.

In Section 3.6, cross coupling effects on the forces and torques were demonstrated between each pair of DOFs. The same cross coupling behaviour exist in the adaptive-passive payload support, which implies that the adaption process in one DOF may disturb the force/torque balance in the other DOFs. The design of the adaptive-passive payload support controller allows it to monitor and adapt static payload inputs simultaneously in multiple DOFs. Cross coupled disturbances are compensated in real-time by the controller within each DOF. Hence, at the completion of the adaption process, the force and torque balances are achieved simultaneously in all the DOFs. Section 6.6 will demonstrate a practical example of a successful multi-DOF adaption achieved by the proposed adaptive-passive payload support controller.

5.4 Autonomous maglev tuning

The proposed maglev vibration isolator is able to provide quasi-zero vertical levitation stiffness under nominal operation condition. Theoretically, the nominal operation condition is established when the COG of the floater is at the vertical midpoint of the two centres of the fixed magnets. However, in practice, it is difficult to accurately determine this midpoint position in space. In the physical isolator system, the position of the floater is determined using six laser sensors (discussed in Section 5.2) installed on the frame assembly, which measure the relative displacements between the sensor heads and the floater. Therefore, if the sensor heads are not positioned ideally, which is certainly the case in the practical situation, the sensor reported nominal operation position will not be the precise location for minimum vertical levitation stiffness. Additionally, the mechanical misalignments within the frame assembly will also affect the alignment of the fixed magnets, which further contributes to the difficulties in locating the vertical nominal operating position. To optimise the performance of the vibration isolation system, an auto-tuning system is proposed to autonomously minimise the vertical levitation stiffness according to the system states in real-time. This section will discuss the principles and designs of the auto-tuning system.

The auto-tuning system for minimising the vertical levitation stiffness firstly requires the real-time estimation of the levitation stiffness. In the system developed here, the levitation stiffness is derived from differentiating the vertical magnetic force (estimated using the DC acquisition method described in Section 5.3.1) with respect to the position of the floater COG relative to the frame magnets. Therefore, to be able to measure the vertical levitation stiffness, the relative motion between the frame magnets and the floater must be non-zero. In order to introduce relative motion between the floater and the frame magnets, the auto-tuning system was designed to use the magnet position control units to change the locations of the frame magnets while maintaining a stable floater levitation position (relative to the frame) using the maglev stability control. The frame magnets are driven collectively in the same direction with the identical speed. Hence, no relative motions exist between the two

Chapter 5 Real-Time Control Systems

frame magnets and the floater position changes relative to both of the fix magnets collectively.

Figure 5.10(a) shows a schematic of the auto-tuning process for minimising the vertical levitation stiffness. The floater levitation position is maintained at a fixed point by the maglev stability controller. The frame magnet offset (Δd) is controlled by the magnet positioning units. Figure 5.10(b) shows the theoretical levitation stiffness derived by differentiating the force-displacement relationships in Figure 3.22(b), plotted for multiple separations (p) between the magnet pairs.

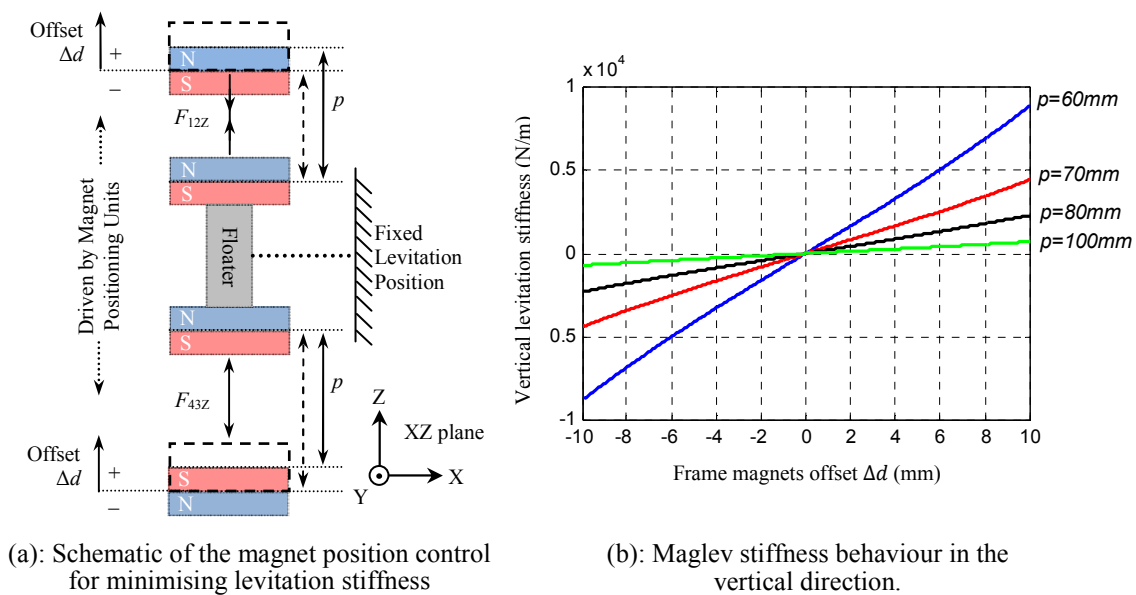


Figure 5.10: Auto-tuning process for minimising the levitation stiffness in the vertical direction.

Figure 5.10(b) shows that the stiffness of the levitation in the vertical direction increases monotonically with an increase in the magnet offset, and the stiffness is equal to zero at the point $\Delta d = 0$. Therefore the auto-tuning controller was designed to increase the magnet offset when the levitation stiffness is negative, and decrease the offset when positive stiffness is detected. This bang-bang control action will drive the frame magnet position to converge to the point where the levitation stiffness is equal to zero. When the levitation stiffness is reduced to below $e = 100\text{N/m}$, the system recognises this event as the completion of the auto-tuning process and

5.5 Conclusion and control system integration

deactivates the magnet positioning unit to prevent disturbances to the operation of the maglev. The controller algorithm is expressed as

$$\begin{cases} \Delta \dot{d} = -v_m \times \text{sign}\left(\frac{dDC_z}{d\Delta d}\right), & \left|\frac{dDC_z}{d\Delta d}\right| \geq e \\ \Delta \dot{d} = 0, & \left|\frac{dDC_z}{d\Delta d}\right| < e \end{cases}, \quad (5.14)$$

where $v_m = 0.1\text{mm/s}$ is the magnet relocation speed. The bang-bang controller structure was selected since it maintains a constant magnet travel speed (which introduces less disturbance to the estimation of the levitation stiffness than other controller algorithms) and is less sensitive to noise in the stiffness measurement. The chosen magnitudes of v_m and e were found to be a good combination to achieve fast and accurate maglev tuning resulting in an auto-tuning process that completes in 63s with less than 0.1mm tuning error. The practical performance of the auto-tuning system will be presented in Section 6.7.

5.5 Conclusion and control system integration

In this chapter, a number of active control systems were discussed, including the operation principles, sub-system structures and their physical realisation in the mechanical isolator system. The proposed control systems, together with the isolator mechanical design shown in Chapter 4, allow all the intended isolator functions to be realised on the developed physical isolator, and successfully demonstrates the possibility of developing a vibration isolation system based on the proposed maglev system. Figure 5.11 shows the integration of all the sub-control systems, as well as signal routing between the sub-controllers.

Chapter 5 Real-Time Control Systems

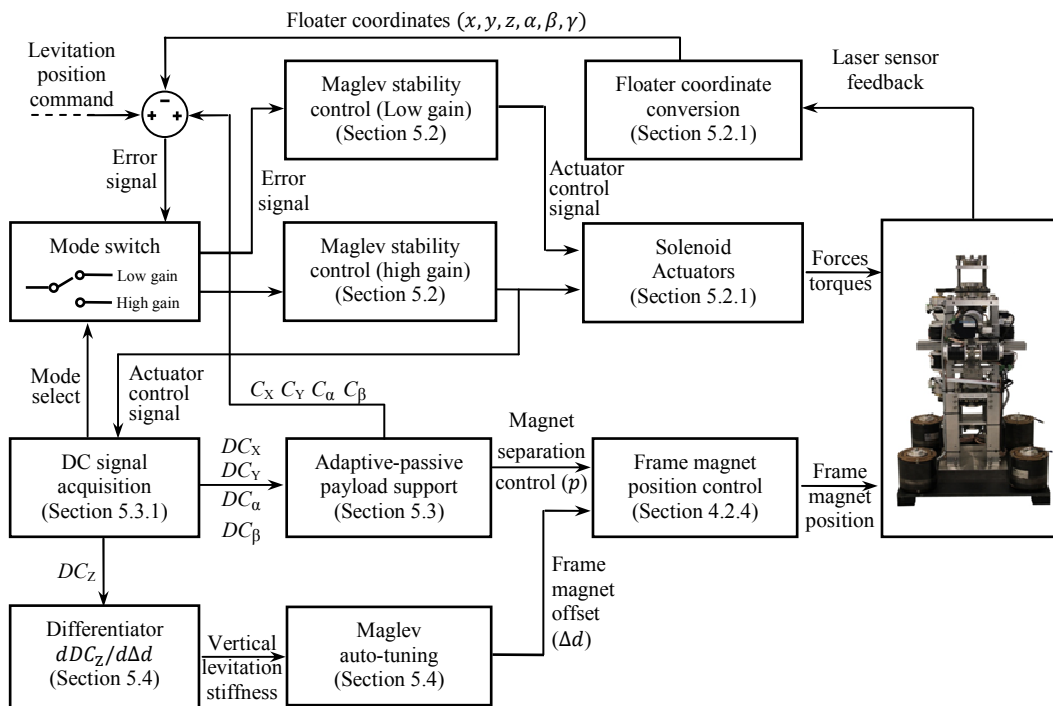


Figure 5.11: Integration of the control systems

The controller logics of the sub-control systems shown in Figure 5.11 are realised using the dSPACE DS1103 platform. The details of each controller design were discussed in the corresponding sections as labelled. Chapter 6 will individually demonstrate the experimental performance of each proposed sub-control system.

Chapter 6

System Performance

6.1 Introduction

This chapter quantifies the experimental performance of the developed 6-DOF quasi-zero stiffness maglev isolator. It includes results and discussions on the performance of the system electronics, the mechanical structure and various control systems. The measured vibration transmissibilities of the isolator in all six directions will be presented in Chapter 8.

This chapter is arranged as follows. It starts with discussions of the sensing and actuation systems. The laser sensors are examined in terms of the electric noise and the linearity of the dynamic response, and the performance of the actuation system is presented in terms of the force sensitivity and the linearity of the actuator dynamics in the frequency domain. This is followed by 3D measurements of the high frequency floater structural dynamics. The performance of the levitation stability control, the adaptive-passive payload support and the autonomous maglev tuning are presented in Sections 6.5, 6.6 and 6.7 respectively.

6.2 Performance of the laser sensors

In the developed maglev vibration isolator, the laser sensors monitor the position of the floater in real-time. The stability of the levitation is directly related to the quality of the sensor feedback signal. In order to identify the internal dynamics of the laser sensors, experiments were carried out to test both the electric noise and linearity of the sensors in the frequency domain.

6.2.1 Sensor electric noise

The effect of sensor noise is potentially significant in the maglev vibration isolator. The sensor signal is directly fed into the controller, and then into the amplifier (refer to the maglev stability controller structure in Section 5.2) which drives the solenoids. Electric noise produced by the laser sensor is amplified, which introduces motion disturbance to the floater. Therefore, it is important to study the noise spectrum of the selected laser sensors.

The laser sensors used in the design of the maglev isolator are the Acuity AR200-12 displacement sensors, which have a resolution of $3.8\mu\text{m}$ and a maximum sampling rate of 1250 samples per second. The detailed specifications of the sensors are tabulated in Appendix D.1. The noise spectrum was obtained from an FFT of the laser sensor output while measuring the distance between itself and a stationary white flat surface. During the measurement, the laser sensor and the target object were mounted on a stiff stand (which ensures that no relative motion exists between the sensor and the target within 0-500Hz) and 21mm apart (stand-off to middle of span distance). Figure 6.1(a) shows a picture of the Acuity laser sensor, and Figure 6.1(b) shows the experimental arrangement used to measure the noise spectrum of the laser sensor.

6.2 Performance of the laser sensors

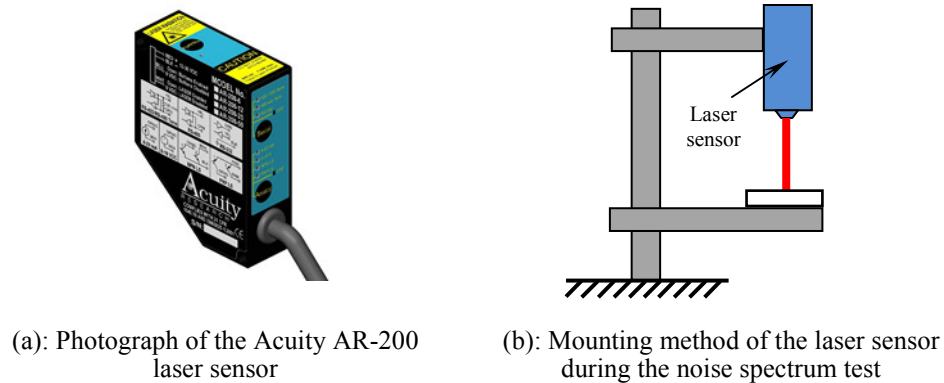


Figure 6.1: Measurement of the noise spectrum of the Acuity AR-200-12 laser sensor.

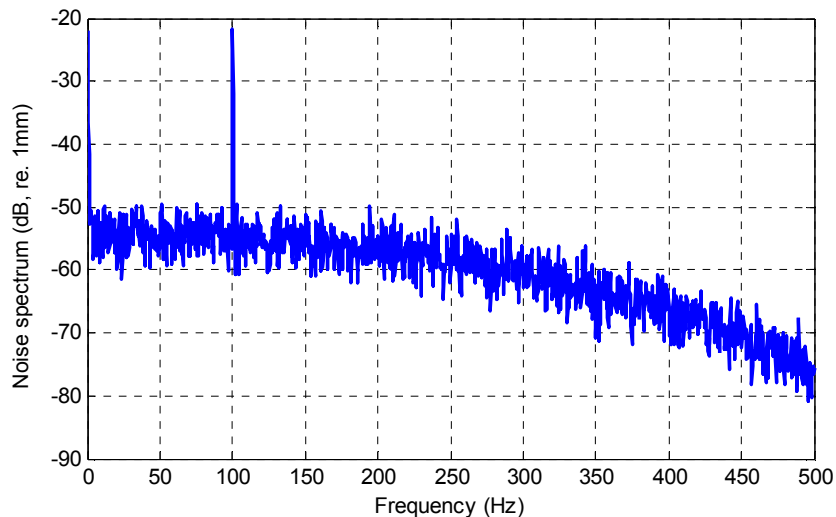


Figure 6.2: Noise spectrum of the Acuity AR-200 laser sensor (FFT properties: DC coupled, 128 averages, 1600 lines, Hanning window, 24,000Hz sampling frequency).

The noise spectrum was measured from 0Hz to 500Hz, which is sufficient to cover the 0Hz to 200Hz frequency range (Section 5.2.4) of the active control systems. The noise spectrum of the laser sensor is plotted in Figure 6.2. It can be seen from the noise spectrum that the electric noise generated by the laser sensor is of approximately the same order of magnitude as the sensor resolution ($3.8\mu\text{m}$). The spike in the spectrum around 100 Hz is likely to be a rectification of the 50Hz AC frequency in the DC power supply of the system. The noise generated by the laser sensor can be magnified by the maglev stability controller, and may induce vibrations

to the floater during levitation. The magnitude of the levitation induced vibration is quantified and discussed in Section 6.5.2.

6.2.2 Linearity of the laser sensor dynamic response

The dynamic response of the laser sensor is another factor that could impact the frequency response of the maglev stability control system. Therefore, the linearity of the laser sensor was also examined in the frequency domain. A linearity test was conducted in the 0-200Hz frequency range with the aim to identify, in the frequency range of the active control, the dynamic effects of the internal signal conditioning components of the laser sensor. The arrangement used for the linearity test is shown in Figure 6.3.

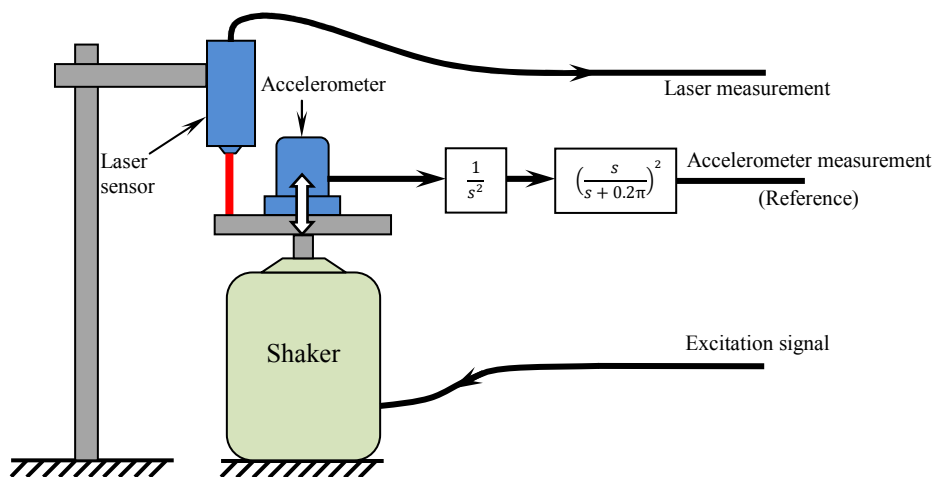


Figure 6.3: Experimental layout of the linearity testing for the laser sensor

The linearity of the laser sensor was assessed by comparing the laser sensor measurements to that of a calibrated B&K 4381 accelerometer (refer to Appendix D.5 for specifications), which is assumed to be linear from 0.1Hz to 4800Hz. In the test, the accelerometer was stud mounted to a shaker platform (excited with a swept sine signal, using a sweep rate of 1octave/min). The acceleration signal was double integrated in the charge amplifier (B&K 2635 with an internal second order high-pass filter at 0.1Hz) to obtain displacement measurements. Vibration of the shaker was also monitored by the laser sensor simultaneously. The linearity of the laser sensor is

6.2 Performance of the laser sensors

obtained by comparing the transfer function between the two measurements. The result is shown in Figure 6.4. It can be seen that the laser sensor has almost the same linear response as the accelerometer prior to 60Hz. From 60Hz onwards, the sensor response starts to roll-off at a very low rate. This is likely due to the low-pass filter in the laser sensor which has a 625Hz cut-off frequency for anti-aliasing purposes. At 200Hz, the maximum attenuation and phase distortion are approximately -0.9dB and 2.5degrees. Therefore, the laser sensor dynamics are not expected to have a significant influence on the performance of the levitation stability control system.

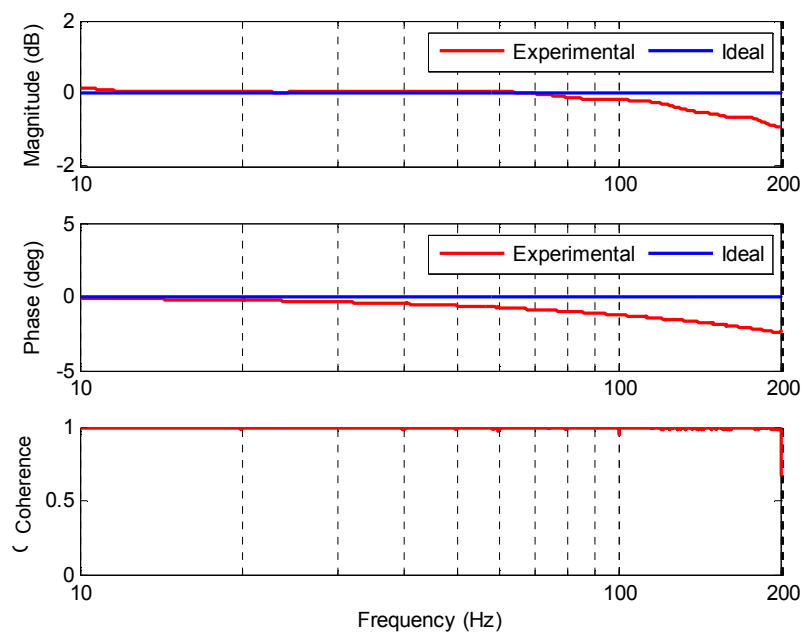


Figure 6.4: Bode plot between the laser sensor and the B&K accelerometer, along with the coherence of the measurement (FFT properties: DC coupled, 128 averages, 1600 lines, Hanning window, 24,000Hz sampling frequency).

6.3 Performance of the actuation system

In the maglev stability control, the actuators also play a very important role as they are the physical components that execute the control commands. It is necessary to assess the performance of the actuators in order to identify the potential performance degradations resulting from the actuator dynamics. This section presents the examinations of the actuation system and interpretations of the results.

6.3.1 Determining the actuator sensitivity

The solenoid actuators used in the maglev isolator have a special profile, which is uniquely designed to improve their actuation capacity. The most simple and accurate method to determine the solenoid sensitivity is through experimental means. The sensitivity of the solenoid actuator refers to the amount of magnetic force produced per ampere of electric current, i.e., $S=F/I$, where S , F and I represent the sensitivity factor, the magnetic force and the solenoid current respectively. When the maglev isolator is in normal operation, the only sources of relative motion between the solenoid and the actuator magnet are the ground disturbances (laboratory floor vibration, Appendix B) and vibrations induced by the levitation stability controller (Section 6.5.2). These relative motions have small magnitudes compared to the separation between the solenoid and actuator magnet (3mm). Therefore, the solenoid and actuator magnet can be assumed to be stationary relative to each other during the operation of the isolator, and the sensitivity factor of the solenoid is expected to be constant.

Figure 6.5 shows the experimental arrangement for the actuator sensitivity test. During the test, the actuator magnet was held stationary with a 3mm clearance to the inner wall of the solenoid cavity to simulate the geometric layout of the actuation system under nominal operation condition. Specifications of the actuator magnet and the solenoid can be found in Appendix D.2.

6.3 Performance of the actuation system

During the actuator sensitivity test, varying magnitudes of current were applied to the solenoid, and the actuation forces were measured using a force transducer. Figure 6.6 is a plot of the actuation force with respect to the supplied current. A linear fit to the data set verified the linear relationship between the actuation force and the solenoid current. The fitting function shows that the sensitivity factor of the actuators is 3.82N/A.

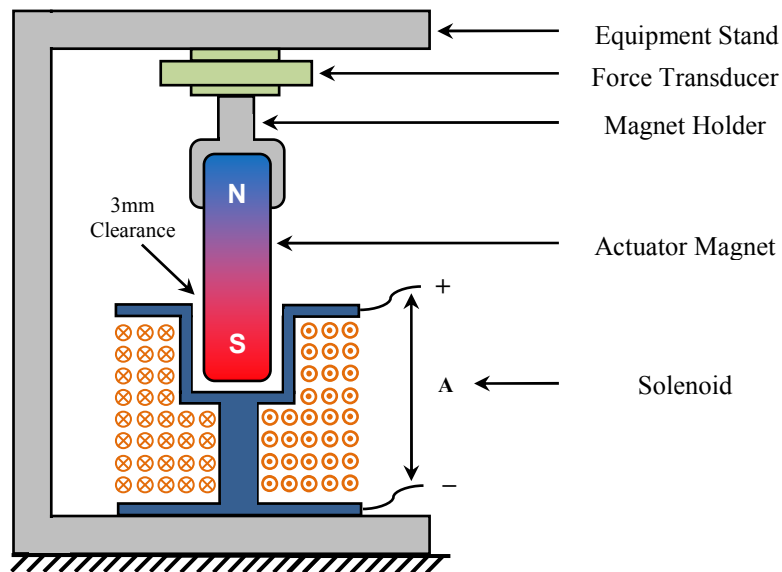


Figure 6.5: Experimental arrangement of the actuator sensitivity test.

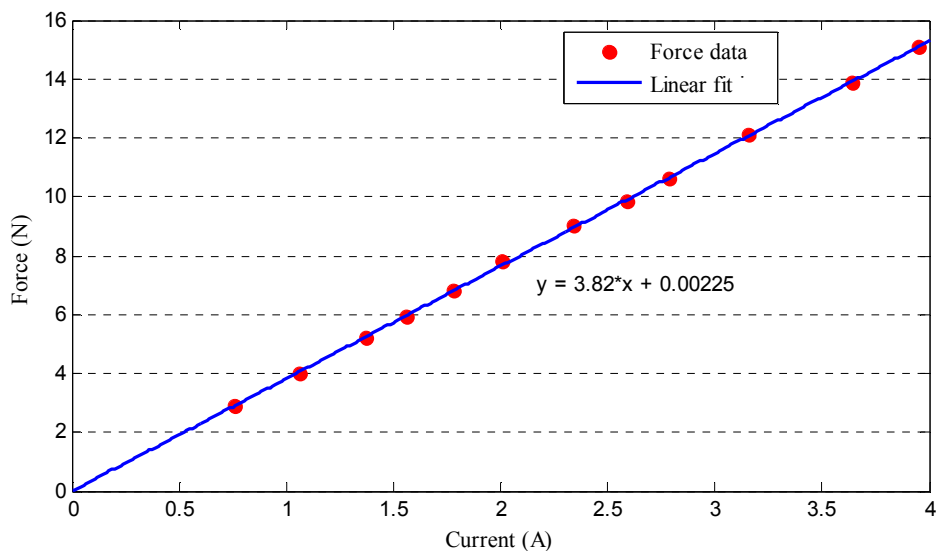


Figure 6.6: Actuation force vs. solenoid current

6.3.2 Linearity of the actuation system

Similar to that of the laser sensing system, the linearity of the actuation system in the frequency domain also significantly affects the dynamic response of the magnetic levitation. The dynamics of the actuation system consists of two parts in series; the dynamics of the solenoid and the dynamics of the amplifier. The frequency response of the actuation system (Solenoid + Amplifier) was obtained using the experiment illustrated in Figure 6.7.

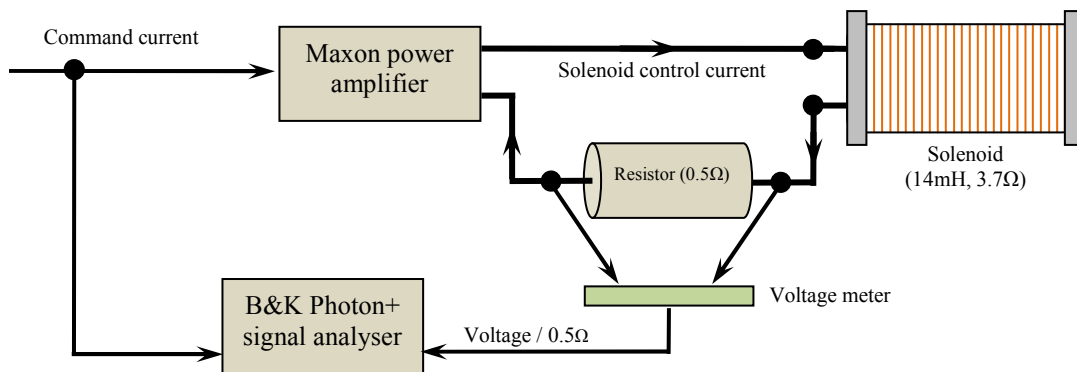


Figure 6.7: Experimental setup of the actuator linearity test

The transfer function of the solenoid may be derived from

$$V = iR + \frac{di}{dt}L \quad , \quad (6.1)$$

where V , R , L and i represent the voltage, resistance, inductance and current through the solenoid respectively. Taking the Laplace transformation of Equation (6.1) yields

$$\frac{V(s)}{i(s)} = \frac{1}{Ls + R} \quad . \quad (6.2)$$

The resistance and inductance of the solenoids were measured to be 3.7Ω and 0.014H respectively. Equation (6.2) indicates that the solenoid dynamics have the form of a gain and a low-pass filter having a cut off frequency at $\frac{R}{L} = \frac{3.7\Omega}{0.014\text{H}} \frac{\text{rad}}{\text{s}} = 42.06 \text{ Hz}$. This is not a desirable bandwidth for the active control systems of the maglev isolator.

6.3 Performance of the actuation system

The phase distortion induced by the actuator dynamics will reduce the gain margin and control system stability. In Chapter 7, a 6-DOF skyhook damping system will be proposed, which uses the same actuation system to realise active vibration control. The slow actuator dynamics will degrade the performance of the skyhook damping system. In order to improve the performance of the solenoid, the driving amplifier is set to the current regulation mode, in which an internal feedback controller in the amplifier is activated to regulate the output current according to the input command.

In the actuator linearity test, a resistor was connected in series with the solenoid in order to obtain the magnitude of the solenoid current using Ohm's Law ($I=V/R$). The value of the resistance was chosen to be 0.5Ω , which is the practical minimum resistance that minimises disruption to the actuator dynamics, as well as allowing reasonably large voltage drop across the resistor (maximum of 1V) for ease of measurement. During the experiment, the amplifier was commanded with a swept sine signal (2 Octave/min) from 1 Hz to 1000 Hz, and the transfer function between the command current and the solenoid current (estimated using the voltage drop across the sensing resistor and Ohm's Law) was recorded using a B&K Photon+ signal analyser.

Figure 6.8 shows the measured frequency response of the actuation system. The black curve describes the expected response of the solenoid; the blue curve describes the measured response of the actuation system when the amplifier was set to the voltage mode (the amplifier voltage output is directly proportional to the input command signal), and the red curve shows the improved system response obtained through the current regulation provided by the amplifier, and the dashed green curve is a second order fitted model ($H = \frac{132s+18497}{s^2+172s+18633}$) to the actuation system response with the amplifier in the current mode. The current control mode has shifted the usable actuation bandwidth ($\pm 3\text{dB}$) from 50 Hz to approximately 200 Hz, which will be shown in the subsequent sections to be sufficient for the active control purposes in this research. The poles of the actuation system are potentially able to be further placed at higher frequencies using loop shaping techniques. However, since the

Chapter 6 System Performance

performance of the actuation system in current control mode is sufficient for this research, the loop shaping method was not attempted.

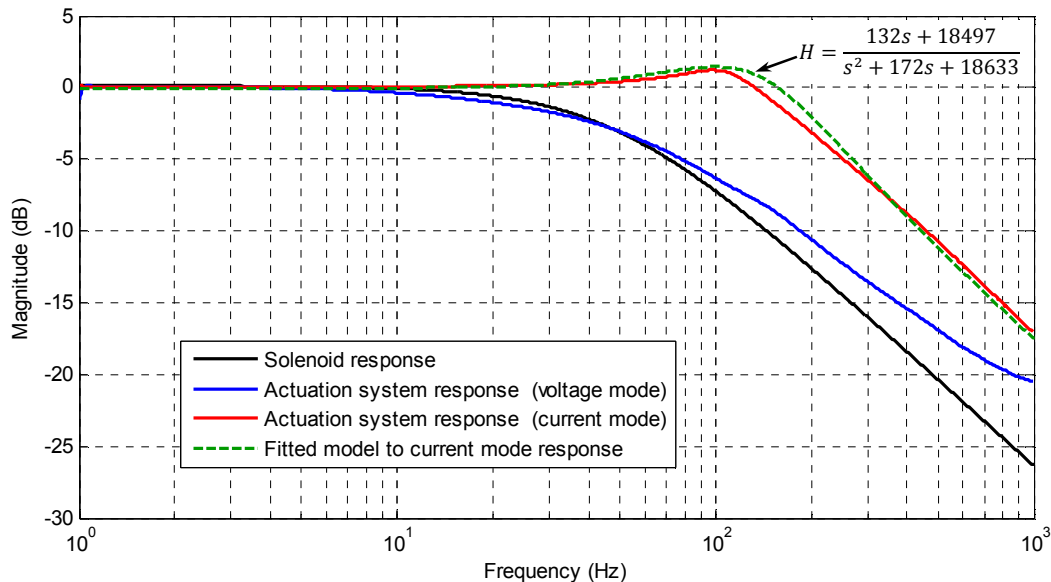


Figure 6.8: Frequency response of the actuation system (FFT properties: DC coupled, 128 averages, 1600 lines, Hanning window, 24,000Hz sampling frequency).

6.4 Floater structural vibration modes and resonance frequencies

In the 6-DOF maglev vibration isolator, the levitation is constantly stabilised through a feedback control system. The noise from the sensors and actuator amplifiers is likely to excite the floater structure in the frequency range of active control (0-200Hz). Disturbances and noise may be amplified significantly at frequencies of the floater structural resonances, and will transmit into the payload directly attached to the floater assembly. It is also important to identify the un-modelled system dynamics in the frequency band of active control to ensure that controller stability is not compromised by the non-rigid body modes of the floater assembly. Therefore, it is important to study the structural modes of the floater, and avoid excitations at its resonance frequencies.

To examine the structural resonances of the floater assembly, a Polytec PSV-400 3D laser vibrometer was used to obtain its resonance frequencies and the corresponding mode shapes. Three scans were completed to obtain the floater structural modes in three planes (XY, YZ and XZ plane). Figure 6.9 shows the experimental arrangement used for the laser vibrometer scans, and Figure 6.10 shows the actuator and magnet used to achieve non-contact broadband excitation. During the scans, the actuator was driven using white noise with 0-1000Hz bandwidth so that the structural resonances could be excited and observed using the laser vibrometer. The camera angles (scan angles) of the three scans are shown in Figure 6.11.

Figure 6.12, Figure 6.13 and Figure 6.14 show the laser vibrometer scanning grid and results for the XY, XZ and YZ planes respectively. In these figures, the first sub-plot shows the positions of the points (green) on the structure which were scanned, and the last sub-plot shows the spectrum of the average acceleration of the scanning points for each plane, which is a measure of the overall vibration intensity spectrum of the structure. The operating deflection shapes of the structural modes are also shown in the remaining sub plots.

Chapter 6 System Performance

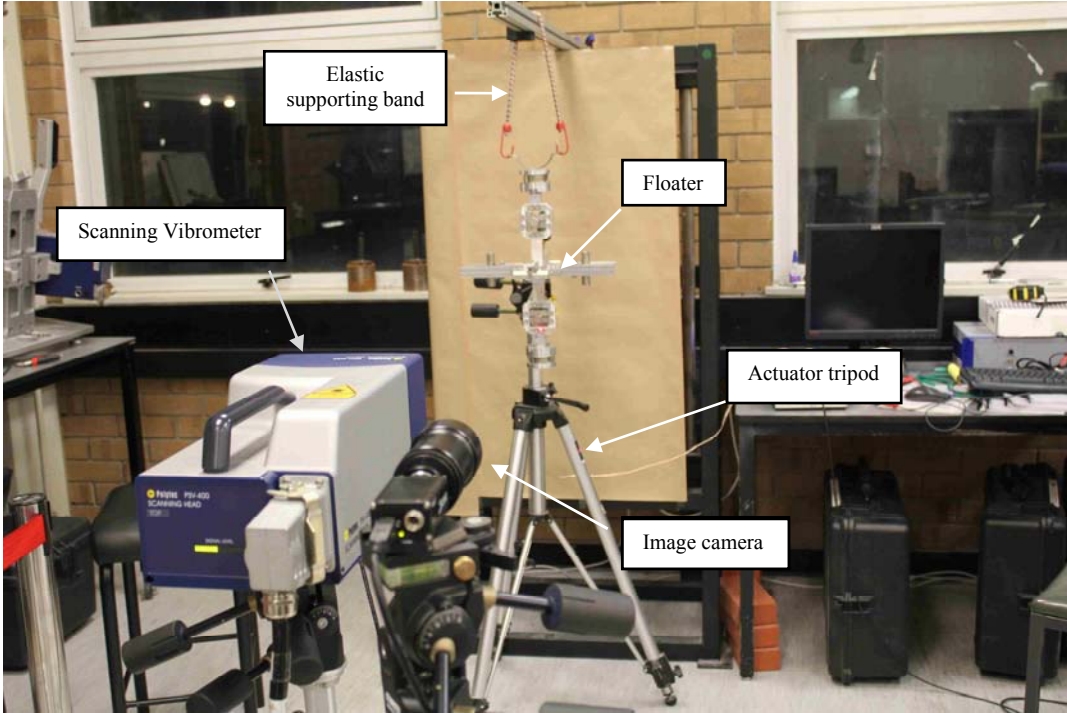


Figure 6.9: Equipment arrangement of the laser vibrometer for structural mode identification.

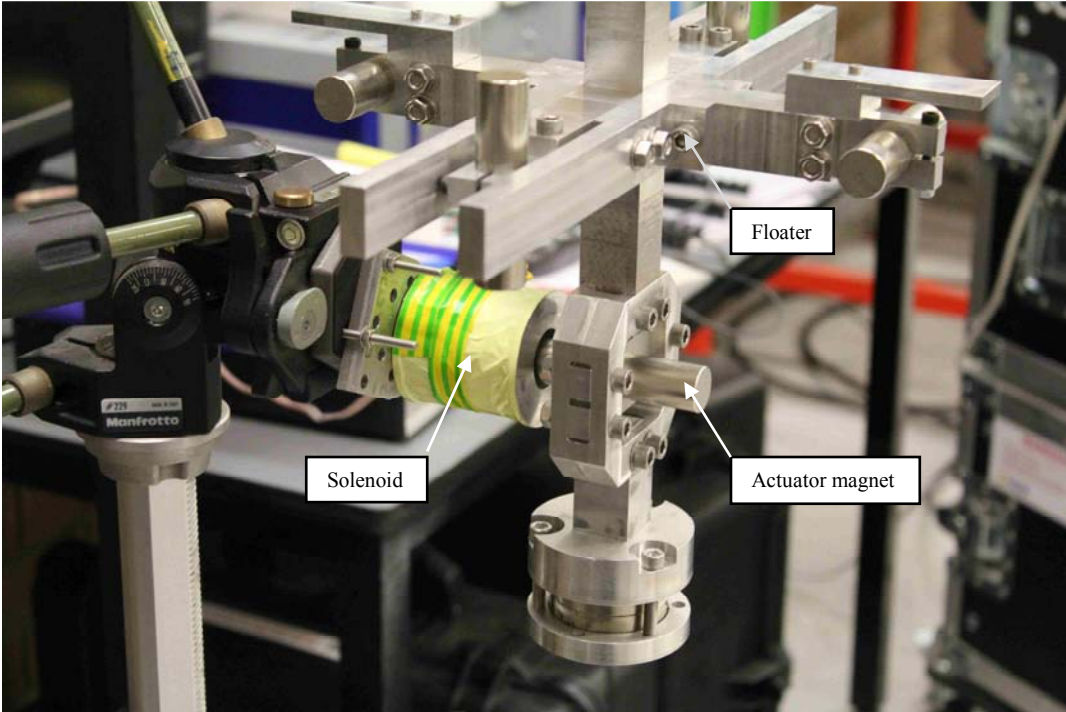


Figure 6.10: Photograph of the actuation method for broadband floater excitation.

6.4 Floater structural vibration modes and resonance frequencies

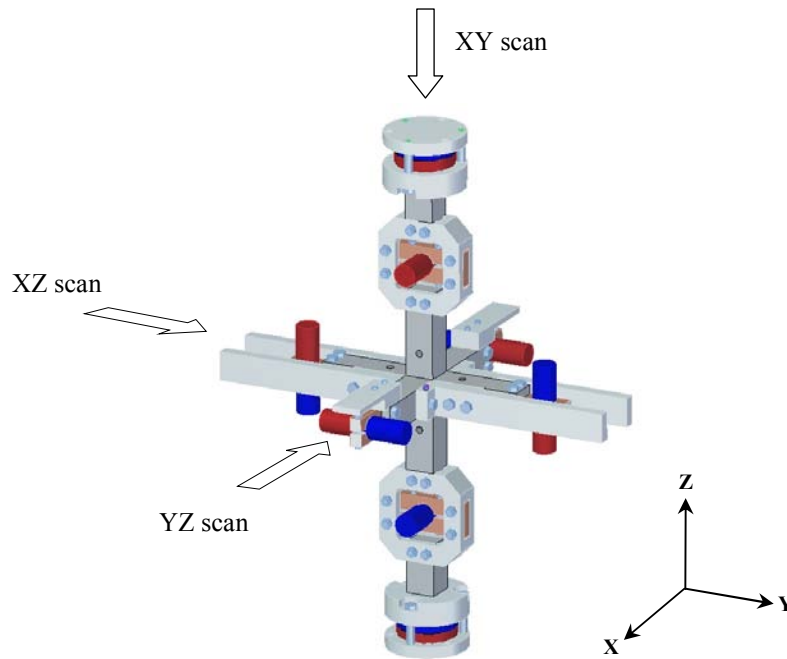
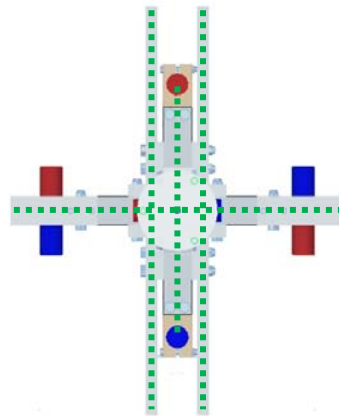


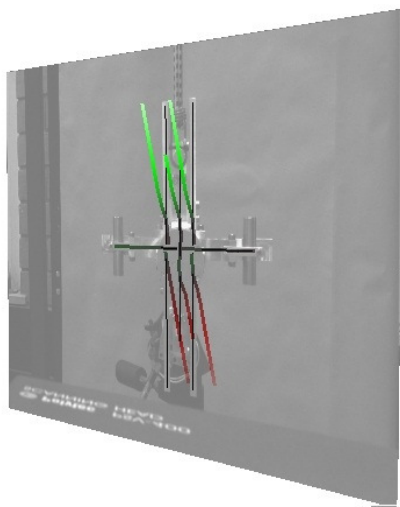
Figure 6.11: Directions of the laser vibrometer scans.

Through the three scans made using the laser vibrometer, the structural resonances were identified to be at 363Hz and 724Hz in the XY plane, 199Hz in the XZ plane, and 164Hz, 549Hz and 899Hz in the YZ plane. Ideally, it is desired to have no structural resonances within the frequency range of interest for active control (0Hz to 200Hz in this application) so that excitation of floater structural modes can be avoided. However, the design of the floater assembly exhibited two resonance modes below 200Hz, which are undesirable since these modes may be excited by the noise of the active control system used in the maglev isolator design. One potential solution to avoid the excitations of these resonant modes is to stiffen the floater structure to ensure that no resonances exist in the frequency range of active control. The problem of having resonances within the active control frequency range can also be solved by inserting notch filters in the controller to attenuate actuator energy output at floater resonance frequencies. However, neither of these methods was attempted in this research as the aim of the project is to improve the performance of the vibration isolation to seismic level disturbances (below 10 Hz), and the structural resonances within the nominal frequency range of interest did not significantly impact the system performance at these low frequencies.

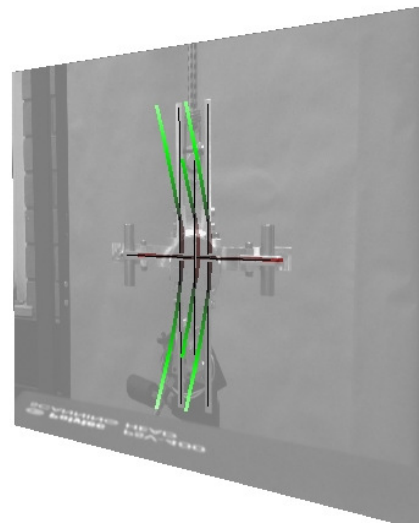
Chapter 6 System Performance



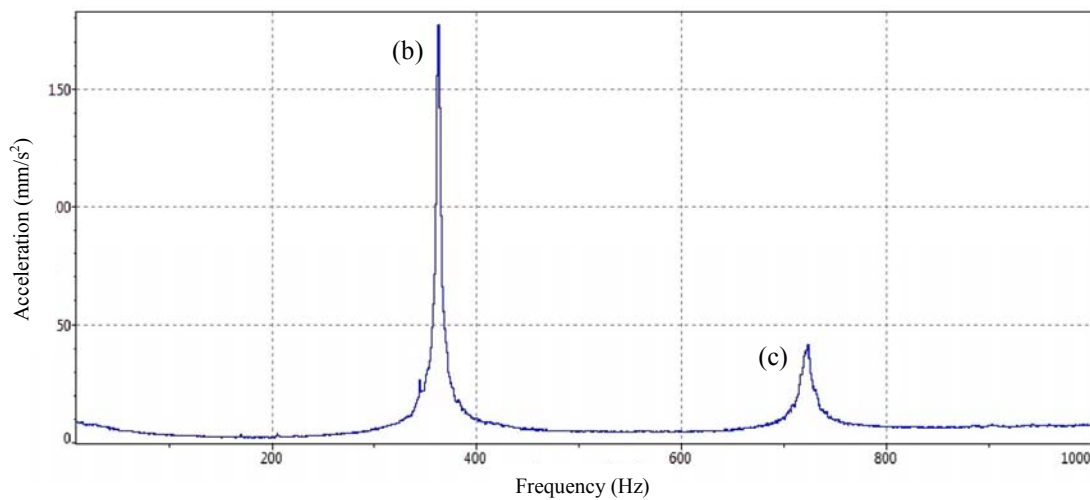
(a): Scanning grid of XY plane



(b): Ansymmetrical resonance mode at 363 Hz



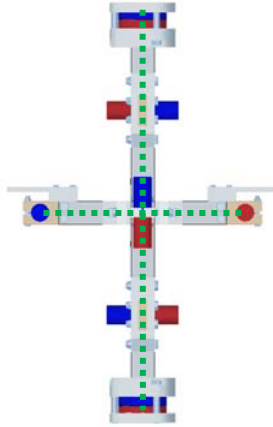
(c): Symmetrical resonance mode at 724Hz



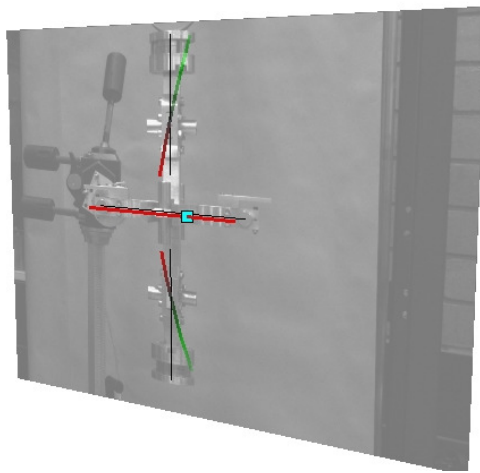
(d): Spectrum of the average acceleration of the scanning points in the XY plane.

Figure 6.12: Laser vibrometer scan and structural modes in the XY plane (FFT properties: DC coupled, 128 averages, 1600 lines, Hanning window, 20,000Hz sampling frequency).

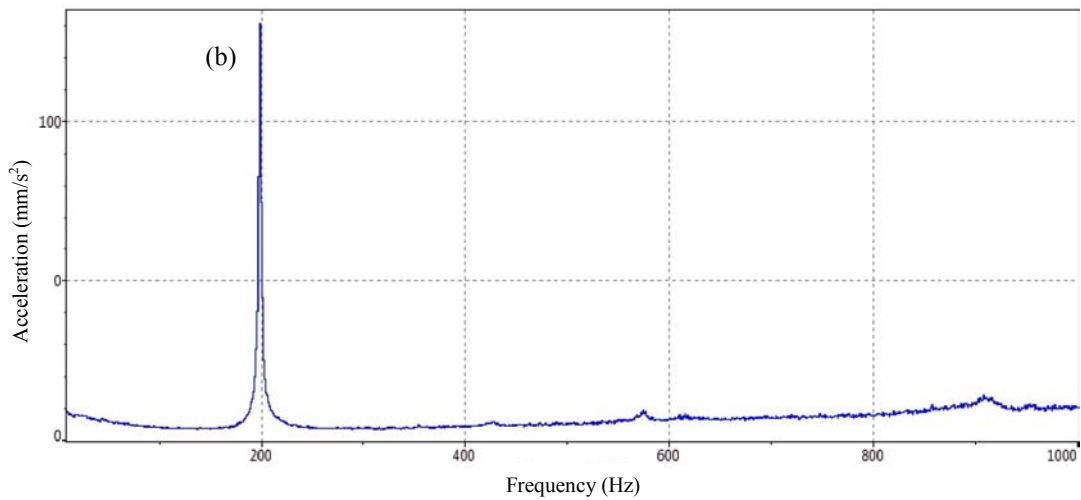
6.4 Floater structural vibration modes and resonance frequencies



(a): Scanning grid of XZ plane



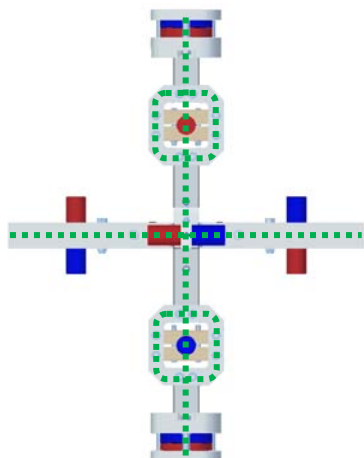
(b): Symmetrical resonance mode at 199 Hz



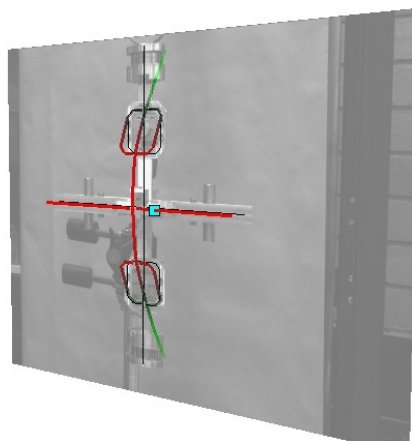
(c): Spectrum of the average acceleration of the scanning points in the XZ plane

Figure 6.13: Laser vibrometer scan and structural modes in the XZ plane (FFT properties: DC coupled, 128 averages, 1600 lines, Hanning window, 20,000Hz sampling frequency).

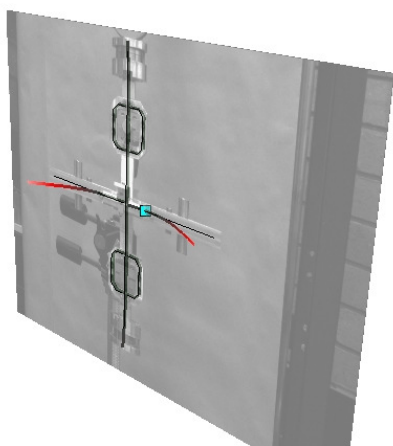
Chapter 6 System Performance



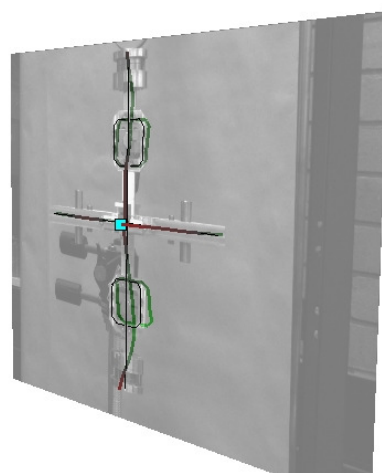
(a): Scanning grid of YZ plane



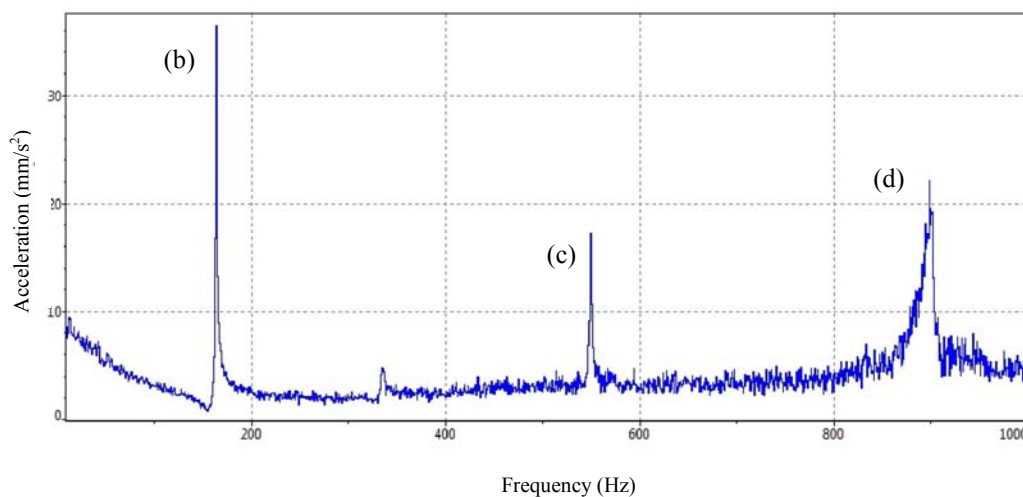
(b): Symmetrical resonance mode at 164 Hz



(c): Symmetrical resonance mode at 549 Hz



(d): Symmetrical resonance mode at 899 Hz



(e): Spectrum of the average acceleration of the scanning points in the YZ plane

Figure 6.14: Laser vibrometer scan and structural modes in the YZ plane (FFT properties: DC coupled, 128 averages, 1600 lines, Hanning window, 20,000Hz sampling frequency).

6.5 Performance of the maglev stability control

During nominal operation of the maglev isolator, the maglev stability control is responsible for creating a stable and low stiffness connection between the supporting structure and the floater so that the payload is isolated from external vibrations. The performance of the maglev stability control is vital to the overall vibration isolation performance. The maglev stability controller is designed to operate in two modes: normal operation mode and auto-tuning mode. The normal operation mode uses relatively low gains for the PID controllers to realise low stiffness levitation, and the auto tuning mode increases the PID gains to ten times the normal operation mode magnitudes so that accurate command tracking can be achieved (introduced in Section 5.3.1). The performance of the maglev stability control was assessed in two aspects: the command tracking ability for the high gain mode (auto-tuning mode), and the magnitude of the self-induced vibration for the low gain mode (normal operation mode).

6.5.1 Position command tracking (high controller gains)

The command tracking performance of the controller was examined by assessing its ability to track a changing command signal. During the test, the position command for each DOF was changed in a stepwise manner at 20-second intervals. Each step signal was maintained for three seconds before returning to the previous position command. Figure 6.15 shows the measured floater response to the changing command signal. The step sizes are 0.3mm and 0.1deg for the translational and rotational DOFs respectively. From Figure 6.15, it can be seen that the maglev stability control achieved accurate command tracking (± 0.01 mm error in translational DOFs, ± 0.005 degree error in rotational DOFs) with minimal settling time (approximately 0.1s) in all the DOFs. This demonstrates the command tracking ability of the maglev stability control, and hence ensures the accuracy of the external load monitoring algorithm used to estimate the force and torque inputs from the payload (Section 5.3.1). Table 6.1 lists the PID gains used during the controller command tracking test, which account for the gains across the system electronics. It should be noted that the

Chapter 6 System Performance

PID gains used during the position tracking test were set to allow accurate command tracking for the benefit of the external load monitoring system. This set of high gains is not used for normal operation to isolate ground vibrations.

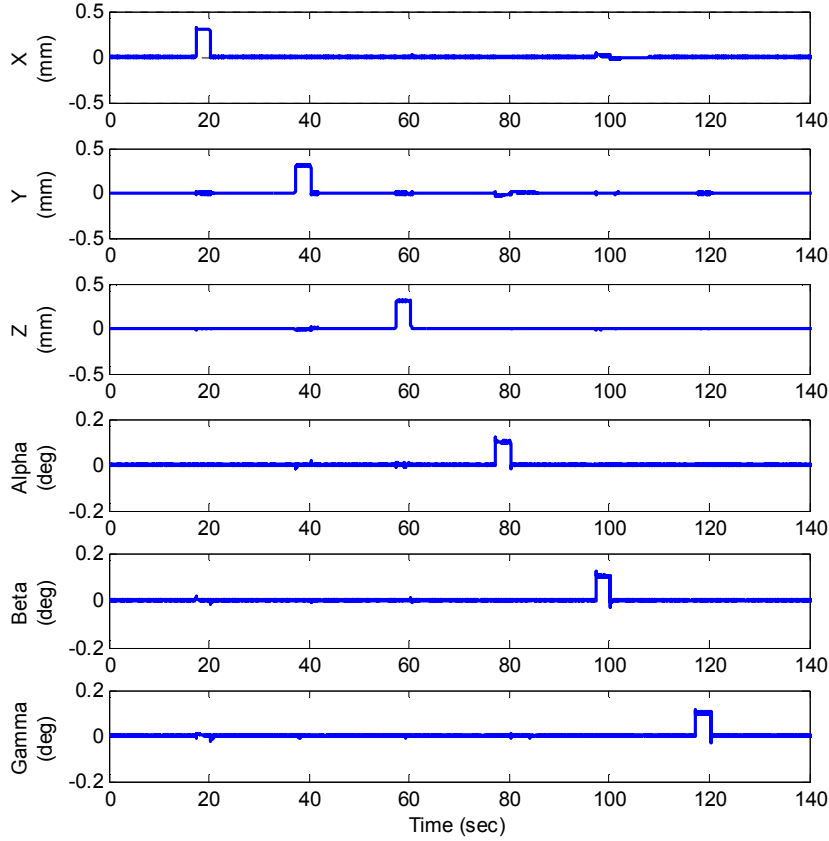


Figure 6.15: Maglev position command tracking in 6-DOF

Table 6.1: PID gains used in the levitation position command tracking test

Item	Value	Item	Value
P_X	22500 N/m	P_α	3200 Nm/deg
I_X	1125 N/m•s	I_α	2400 Nm/deg•s
D_X	263 N•s/m	D_α	34 Nm•s/deg
P_Y	22500 N/m	P_β	3200 Nm/deg
I_Y	1125 N/m•s	I_β	2400 Nm/deg•s
D_Y	263 N•s/m	D_β	34 Nm•s/deg
P_Z	6750 N/m	P_γ	640 Nm/deg
I_Z	675 N/m•s	I_γ	240 Nm/deg•s
D_Z	60 N•s/m	D_γ	12 Nm•s/deg

6.5 Performance of the maglev stability control

Figure 6.15 also shows that the actuation system is sufficiently well decoupled between the six DOFs. The actuation in each DOF only caused very limited disturbances to the other DOFs. These disturbances were mainly as a result of the slight uneven mass distribution of the floater. With high floater acceleration during the command tracking test, the uneven mass distribution could create cross-coupling forces and torques. However, the actuation system itself is well decoupled between the six actuation DOFs.

6.5.2 Levitation induced vibration (low controller gains)

The maglev stability controller operates in a low gain mode during normal operation to isolate ground vibration. Since the stability control system is a feedback controller that involves a number of sensors and electronics, a small amount of vibration may be induced by the feedback control mechanism due to noise from the system equipment. Since the levitation stabilisation system is used for vibration isolation, any vibration induced by the levitation controller is extremely undesirable. Therefore, it is important to quantify the amount of induced vibration and to maintain its magnitude to be below an acceptable threshold.

Table 6.2 is a list of the PID gains used in the normal operation mode. These gains were found experimentally to be a suitable combination that achieves the lowest levitation stiffness without compromising the stability of the maglev. Theoretically, since the maglev system has quasi-zero/zero stiffness in all the six DOFs, the required PID gains required to maintain a stable levitation for the proposed maglev isolator at the nominal operation point should be very small. However, due to the mechanical misalignments within the system and the noise from the system electronics, the PID gains tabulated in Table 6.2 are required for the current system hardware configuration.

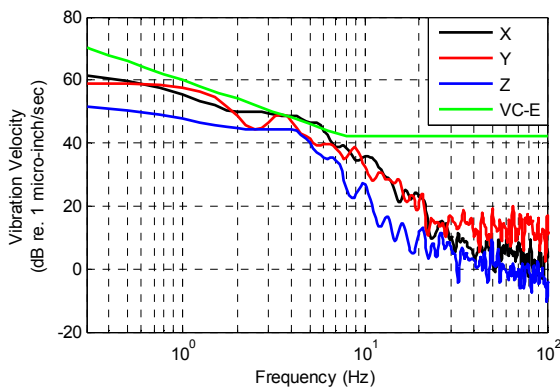
The levitation induced vibration was measured in the X, Y and Z directions using six filtered geophones (refer to Section 7.3.1 for details on geophone filtering) installed on the floater assembly (Figure 7.1 shows the geometric locations of the geophones). The measured vibration levels on the floater during normal operation of the isolator

Chapter 6 System Performance

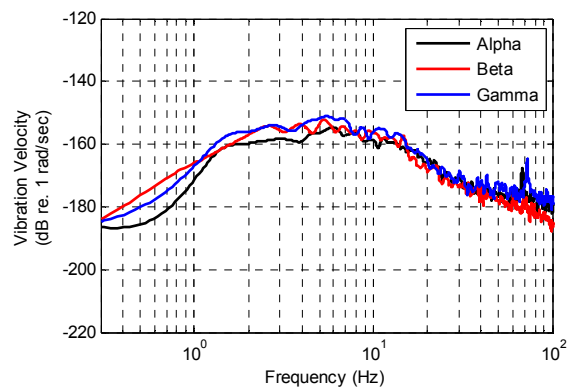
are presented in Figure 6.16. Figure 6.16(a) shows the residual translational floater vibrations in the X, Y and Z directions as measured in the research laboratory (Appendix B shows the laboratory floor vibration levels). The translational vibrations are compared with the VC-E vibration criterion (Miller, 1995), which is the most demanding criterion specified for the operation of extremely vibration-sensitive equipment. The results show that, in the translational directions, the magnitude of the residual vibration on the floater is below the VC-E threshold, which is an indication of the satisfactory performance achieved by the maglev stabilisation system. The self-induced vibrations in the rotational DOFs are shown in Figure 6.16(b). Unfortunately, no relevant standard has been found to assess the performance of the levitation system in the rotational DOFs.

Table 6.2: PID gains used in the normal operation condition

Item	Value	Item	Value
P_X	2250 N/m	P_α	320 Nm/rad
I_X	112.5 N/m•s	I_α	240 Nm/rad•s
D_X	26.3 N•s/m	D_α	3.4 Nm•s/rad
P_Y	2250 N/m	P_β	320 Nm/rad
I_Y	112.5 N/m•s	I_β	240 Nm/rad•s
D_Y	26.3 N•s/m	D_β	3.4 Nm•s/rad
P_Z	675 N/m	P_γ	64 Nm/rad
I_Z	67.5 N/m•s	I_γ	24 Nm/rad•s
D_Z	6 N•s/m	D_γ	1.2 Nm•s/rad



(a): Vibration in the X, Y and Z directions



(b): Vibration in the α , β and γ directions

Figure 6.16: Levitation induced vibration: (a) in the X, Y and Z directions; (b) in the α , β and γ directions (FFT properties: DC coupled, 128 averages, 1600 lines, Hanning window, 24,000Hz sampling frequency).

6.6 Performance of the adaptive-passive payload support

The function of the adaptive-passive payload support is to support the payload solely by using permanent magnet forces. As discussed in Section 5.3.1, the payload weight and moment changes (external loads) are detected by monitoring the DC components of the actuator control signals generated by the maglev stability controller. The aim of the adaptive-passive payload support is to eliminate the need for the solenoids to support the payload with electromagnetic forces. Therefore, the performance of the adaptive-passive payload support can be examined by observing the reduction in the actuator control current achieved during the adaptation process.

The performance of the adaptive-passive payload support was tested by placing an object on the floater (to simulate a static external disturbance) at an off-centred position. The additional payload has three inputs to the floater of the maglev isolator. Figure 6.17(a) shows an equivalent table supporting system to illustrate how static disturbances are introduced by adding an off-centred payload. Under this condition, the payload has introduced inputs through three axes into the supporting structure, which are

- Payload weight (caused by gravity)
- Pitching moment (caused by the payload offset in the X direction, shown in Figure 6.17(b))
- Rolling moment (caused by payload offset in the Y direction, shown in Figure 6.17(c)).

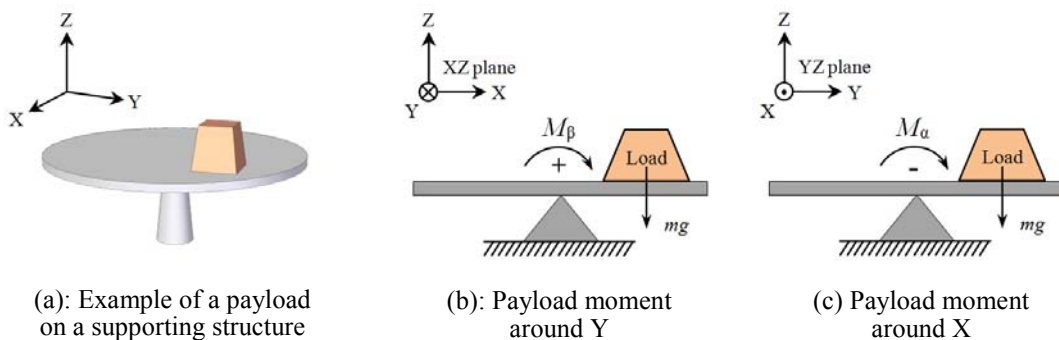


Figure 6.17: Payload inputs into a supporting structure.

Chapter 6 System Performance

The DC component of the actuation forces and torques were recorded in each DOF during the test, and are shown in Figure 6.18. The time history data for the first 50 seconds was taken with the adaptive-passive payload support deactivated. During the first 18 seconds, the floater was kept at steady state without additional payload. The floater levitation pose, presented in Figure 6.19, shows a stationary levitation with zero displacements in all six DOFs. After the first 18 seconds, an unbalanced payload was added to the floater, which introduced a downward force, a pitching moment and a rolling moment. The payload was added to the floater manually during the 18 to 25 second period, consequently, disturbances to the actuation forces and torques and levitation pose were observed in all six DOFs. During 20 to 50 seconds, the maglev stability controller adapted to the new payload condition through forces generated by the solenoid actuators, and the levitation pose returned to zero. As expected, increases in the actuation forces and torques were observed in the Z , α and β directions, which provided forces and torques for supporting the added payload.

After the payload addition, the adaptive-passive payload support was activated at the 50th second to start adapting the payload inputs using forces from the permanent magnets. It can be seen from Figure 6.18 and Figure 6.19 that the adaptive-passive payload support algorithm shifted the levitation position of the floater in the X and Y directions to balance the additional moments in the β and α directions respectively (theories in Section 5.3.3). The added payload weight was also accommodated by reducing the separations (not shown) between the magnet pairs (see Section 5.3.2), which caused some disturbance to the levitation position in the Z direction. During the adaptation process, small floater rotations in the α and β directions were also commanded by the adaptive-passive payload support controller, which was not expected since no horizontal force inputs were introduced by the payload addition. However, the horizontal forces on the floater that caused the commanded floater rotation were likely to be existing prior to the activation of the adaptive-passive payload support. These forces may be a result of slight floater imbalance and system mechanical misalignments. After the adaptation process, these undesirable horizontal forces were also adaptive-passively balanced, which is evidenced by the fact that almost no current was required in any of the six DOFs (Figure 6.18).

6.6 Performance of the adaptive-passive payload support

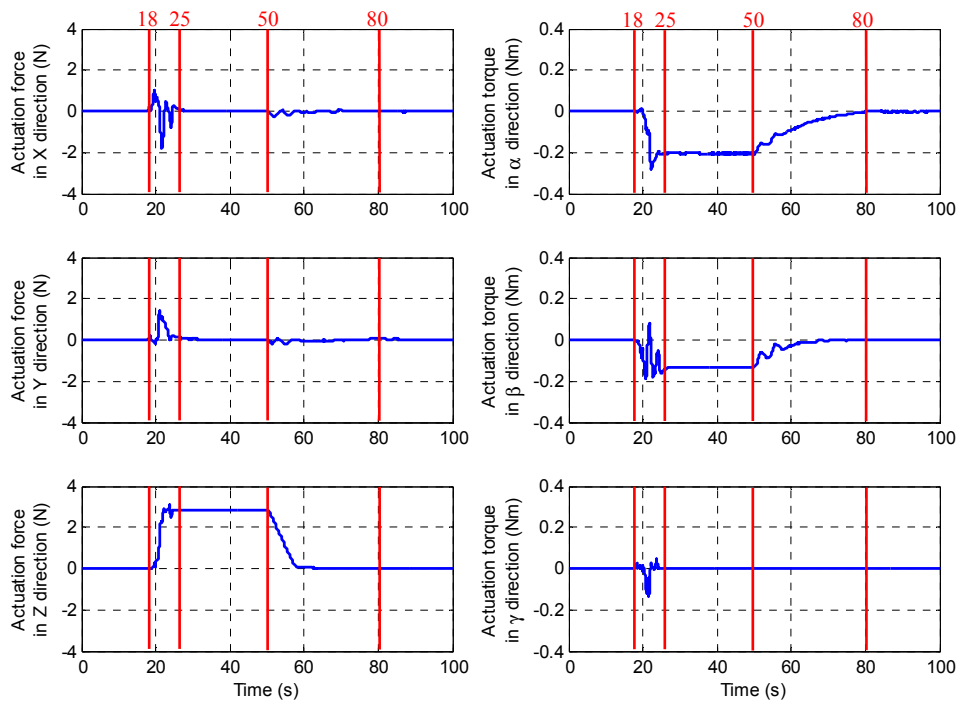


Figure 6.18: Control current time history data in the adaptive-passive payload support test.

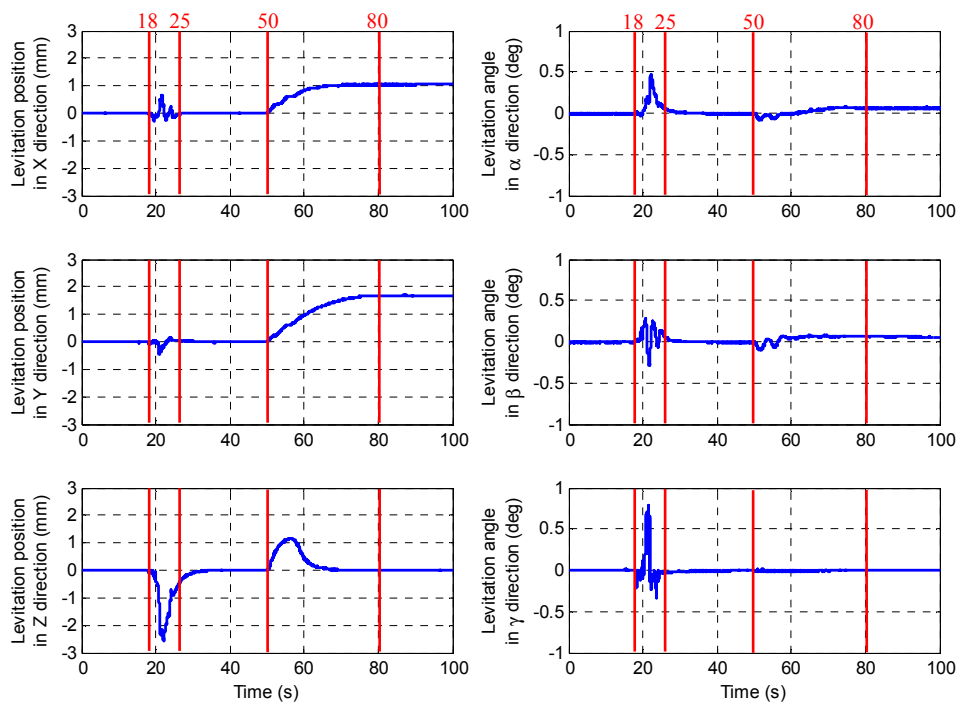


Figure 6.19: Floater pose time history data in the adaptive-passive payload support test.

Chapter 6 System Performance

In general, the actuation forces and torques generated by the solenoids are reduced following the activation of the adaptive-passive payload support controller at the 50th second. At the end of the adaptation process (80s), the static actuation forces and torques were reduced to nearly zero in all six DOFs. The support of the additional static payload weight and moments was fully transferred from the solenoid actuators to the permanent magnets by both relocating the floater horizontally and adjusting the separations between the magnet pairs. Using a power monitor connected to the power supply of the solenoid amplifiers, the measurements showed that the power consumption was reduced from 45W to less than 1W for levitating a mass of 6.693kg (0.285kg from the unbalanced payload + 6.408kg floater weight). Therefore, a minimum power reduction of 97.8% was achieved. The residual power consumption was mainly due to parasitic losses in the amplifiers and the solenoids, and only a very small fraction of this energy was transferred into kinetic energy to stabilise the floater. The effectiveness of the adaptive-passive payload support was experimentally validated.

6.7 Performance of the maglev auto-tuning system

The maglev auto-tuning is a sub-control system that automatically adjusts the positions of the permanent magnets to ensure the quasi-zero stiffness characteristic of the maglev in the vertical direction. The theory of the auto-tuning algorithm was introduced in Section 5.4, which explains how the magnet position control units are used to adjust the frame magnets collectively so that the COG of the floater can be located at the nominal operation point. It is noteworthy that this tuning process may also be carried out manually by locating the floater COG at the mid-point of the two frame magnets. However, manually tuning is only able to correct for geometric misalignments. Other factors, such as non-uniformity of the magnet magnetisation, cannot be accounted for in the manual tuning process. In addition, manual tuning is time consuming and inaccurate, which also reveals the value of the auto-tuning design.

A test was conducted to examine the performance of the auto-tuning system. Figure 6.20 shows the position offset history of the frame magnets (refer to Figure 5.10)

6.7 Performance of the maglev auto-tuning system

during the testing period. Prior to the test, the maglev system was manually tuned to the approximate (manual tuning has limited accuracy) nominal operation condition such that the vertical levitation stiffness is approximately quasi-zero. Hence, at the beginning of the test (0 sec point), the 0 offset position shows the approximate quasi-zero stiffness levitation position. During the first 66 seconds, the magnet positioning units were manually commanded to offset both of the frame magnets by about 4.8mm from the approximate quasi-zero stiffness position. This offset was deliberate, and the purpose was to assess the ability of the auto-tuning system to re-establish the quasi-zero stiffness levitation from the disturbed condition. At 61s, the auto-tuning algorithm was activated, and from 66s to 129s the auto-tuning system adjusted the position of the frame magnets according to the levitation stiffness monitored in real-time (refer to Section 5.4 for relevant theories and methods). It can be seen that the algorithm successfully positioned the frame magnets back to the quasi-zero stiffness position with a difference of less than 0.1mm from the manually tuned position. However, this difference could also be interpreted as the manual tuning being inaccurate by 0.1 mm. In general, the auto-tuning system has demonstrated its ability to establish the quasi-zero vertical levitation stiffness.

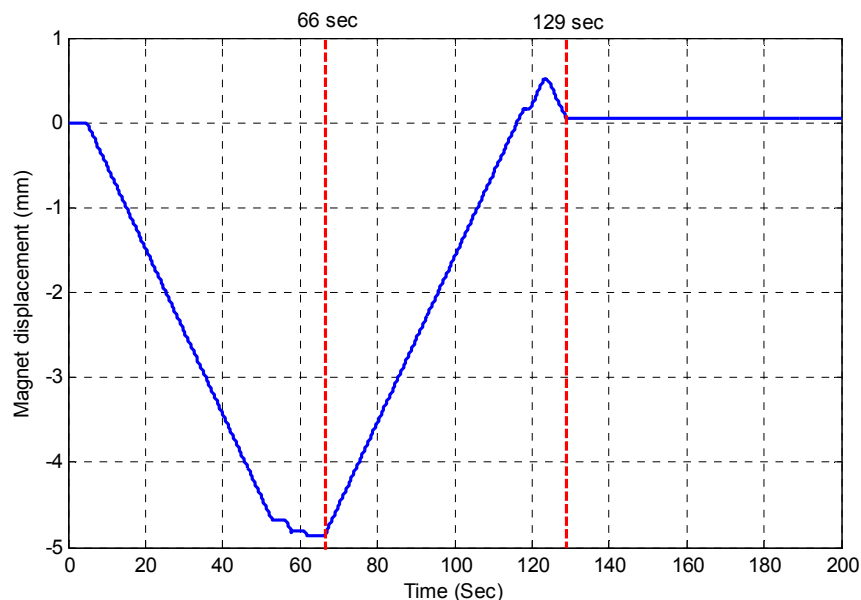


Figure 6.20: Magnet position history during the vertical stiffness minimisation performance test.

6.8 Conclusion

This chapter presented the experimental performance of both the mechanical and control systems. Table 6.3 summarises the results and findings.

Table 6.3: Results of the tests of isolator system components and controllers.

Item	Type of experiment	Results and comments
Laser sensors	<ul style="list-style-type: none"> • Electric noise test • Linearity of sensor dynamic response 	<ul style="list-style-type: none"> • Electric noise from the laser sensors is unlikely to have significant impact on the performance of the maglev stability control system. • The dynamic response of the laser sensor output was shown to be linear by comparing its response with a B&K accelerometer.
Actuators	<ul style="list-style-type: none"> • Force sensitivity factor • Linearity of actuator dynamic response 	<ul style="list-style-type: none"> • The force sensitivity of the solenoid actuator is approximately 3.82 N/A. • The linearity of the actuation system is acceptable up to about 200Hz with driving amplifiers in current regulation mode, which is sufficient for the active control purposes of this research.
Floater structural resonances	<ul style="list-style-type: none"> • Identification of resonance modes in 3D 	<ul style="list-style-type: none"> • The floater structural modes were identified within the 0 to 1000Hz region. The structural modes are at 363Hz and 724Hz in the XY plane, 199Hz in the XZ plane, and 164Hz, 549Hz and 899Hz in the YZ plane. Floater structural modes below 200Hz may amplify vibration on the floater. However, this can be solved by stiffening the structure or applying notch filters in the controller (not attempted in this research).
Levitation stability control	<ul style="list-style-type: none"> • Ability to maintain desired levitation position • Levitation induced vibration 	<ul style="list-style-type: none"> • The levitation stability control has been demonstrated to provide fast (0.1s settling time) and accurate position command tracking (± 0.01 mm error in translational DOFs, ± 0.005 degree error in rotational DOFs). • The levitation induced vibration level is below the most stringent vibration criterion (V-CE).
Adaptive-passive payload support	<ul style="list-style-type: none"> • Ability to adapt to the payload 	<ul style="list-style-type: none"> • The adaptive-passive payload support successfully adapted, using only forces from the permanent magnets, to the static payload inputs caused by the addition of an unbalanced payload. The actuation forces and torques were reduced to quasi-zero levels after the adaptation, achieving

6.8 Conclusion

		reduction in levitation power consumption of 97.8%.
Autonomous maglev tuning	<ul style="list-style-type: none">● Reduce the vertical levitation stiffness to quasi-zero level	<ul style="list-style-type: none">● The controller successfully established the quasi-zero vertical levitation stiffness from a manually disturbed levitation condition. The auto-tuned quasi-zero stiffness position differed by 0.1mm from the approximate quasi-zero stiffness position obtained through manual tuning.

Chapter 7

6-DOF Active Skyhook Damping

7.1 Introduction

In vibration isolation systems, damping mechanisms are commonly employed to reduce the vibration energy of the payload. The majority of the existing vibration isolation systems use viscous damping elements connected between the payload and isolator frame, hence, the damping force is created between the payload and the frame. This type of damping is commonly referred to as relative damping. Section 3.2.2 has demonstrated that although the relative damping method effectively attenuates vibration at the isolator resonance, it unavoidably increases the vibration transmissibility of the isolator at frequencies above resonance. Another damping method introduced in Section 3.2.2 is inertial space damping (also referred to as skyhook damping). This method was discussed in comparison with relative damping, and was shown to outperform the relative method in terms of reducing the overall vibration transmissibility of the isolator. The operation of the skyhook damping system presented in this Chapter is based on the absolute floater velocity feedback. Therefore, direct disturbances from on board sources can also be actively attenuated.

Chapter 7 6-DOF Active Skyhook Damping

Applications of inertial space damping in passive vibration isolators often require sophisticated system modifications and significantly increase the system cost. These factors affect the applicability of inertial space damping in vibration isolation systems. However, the proposed maglev vibration isolator is fully actuated in six DOFs, which allows seamless integration of the inertial space damping into the existing mechanical and control systems. This chapter explains the principles and designs of the skyhook damping system for the proposed 6-DOF maglev vibration isolator. It contains explanations on the system design to realise skyhook damping in all six DOFs, as well as the velocity sensor modifications employed to extend the linear frequency region of the velocity measurements. The effectiveness of the proposed 6-DOF skyhook damping system is demonstrated experimentally in Chapter 8.

7.2 Operating principles and system design

The aim of the skyhook damping system is to exert damping forces with magnitudes proportional to the vibration velocities of the floater of the 6-DOF maglev isolator. In order to realise skyhook damping in the proposed maglev isolator, a feedback control

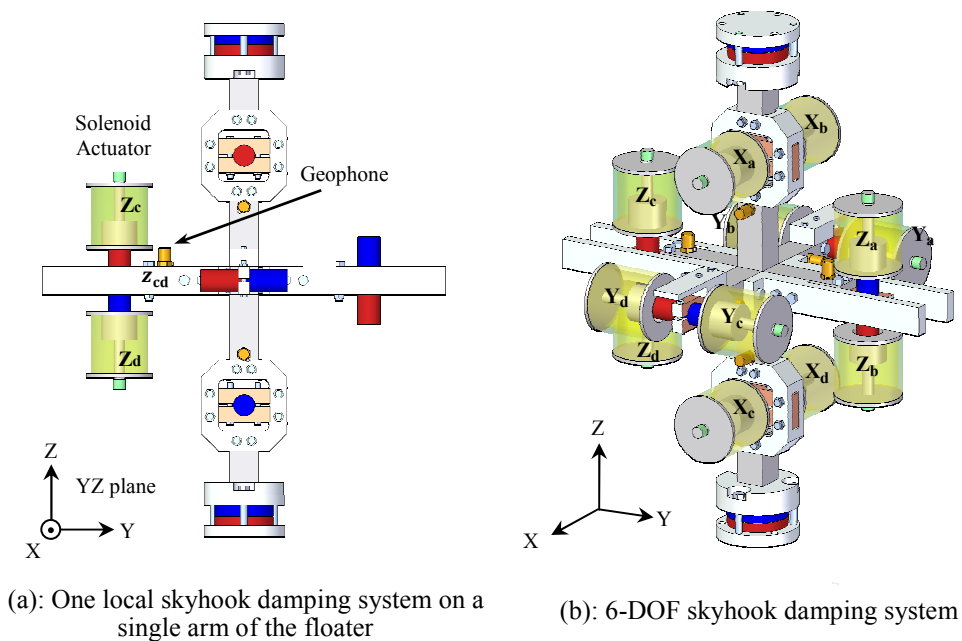


Figure 7.1: System layout of the 6-DOF skyhook damping system.

7.2 Operating principles and system design

system is needed to adjust the generated damping forces according to the magnitude of the floater velocities. Figure 7.1 shows the mechanical integration of the skyhook damping system with the floater.

Figure 7.1(a) illustrates a local skyhook damping system. It is comprised of a vibration velocity sensor (geophone) and a pair of solenoid actuators operated in series. The geophone measures the velocity of its position on the floater, and the controller then uses the solenoid actuator pair to generate a damping force with magnitude proportional to the measured velocity (refer to Equation (3.3)). This single skyhook damping system provides damping forces to one arm of the floater, of which there are six in total. With two sets of coplanar local damping systems, skyhook damping may be realised in two DOFs. For example, if there are two of the local damping systems, one on each side of the floater within the YZ plane (Figure 7.1(a)), skyhook damping will exist in both the Z and the α direction. Figure 7.1(b) shows a rendered image of the floater with six sets (one set per arm of the floater) of the local skyhook damping system. Therefore, with six of the local damping systems, inertial space damping is applied to the floater in all six DOFs. Equation (7.1) describes the control logic of the six local skyhook damping systems which are configured in parallel,

$$\begin{cases} DF_{X_{ab}} = sh_{X_{ab}} \cdot v_{X_{ab}} \\ DF_{X_{cd}} = sh_{X_{cd}} \cdot v_{X_{cd}} \\ DF_{Y_{ab}} = sh_{Y_{ab}} \cdot v_{Y_{ab}} \\ DF_{Y_{cd}} = sh_{Y_{cd}} \cdot v_{Y_{cd}} \\ DF_{Z_{ab}} = sh_{Z_{ab}} \cdot v_{Z_{ab}} \\ DF_{Z_{cd}} = sh_{Z_{cd}} \cdot v_{Z_{cd}} \end{cases}, \quad (7.1)$$

where DF_i and sh_i (N/(ms)) are the skyhook damping force and coefficient respectively for each arm of the floater, and v_i represents the inertial velocity measured by the i^{th} geophone. Please refer to Section 5.2.1 and Figure 7.1(a) for more details of the variables in Equation (7.1).

The velocity of the floater in the inertial frame may also be measured using accelerometers by integrating the acceleration signal. However, to achieve

Chapter 7 6-DOF Active Skyhook Damping

performance to that similar offered by the geophones for inertial velocity measurements (shown in Section 7.3.1), the system cost increases significantly. Therefore, geophones were chosen as a cost effective option for inertial velocity acquisition.

The geophones installed on the floater can also be used to monitor the floater vibration levels in all six DOFs. Chapter 8 will present the vibration transmissibility measurements obtained using the geophones installed on the floater. Equation (7.2) describes the derivation of the floater motion velocity in six DOFs, where d_x , d_y and d_z are the distances between each pair of geophones along the X, Y and Z axes of the floater respectively.

$$\begin{cases} \dot{x} = (v_{X_{ab}} + v_{X_{cd}})/2 \\ \dot{y} = (v_{Y_{ab}} + v_{Y_{cd}})/2 \\ \dot{z} = (v_{Z_{ab}} + v_{Z_{cd}})/2 \\ \dot{\alpha} = (v_{Z_{ab}} - v_{Z_{cd}})/d_y \\ \dot{\beta} = (v_{X_{ab}} - v_{X_{cd}})/d_z \\ \dot{\gamma} = (v_{Y_{ab}} - v_{Y_{cd}})/d_x \end{cases} \quad (7.2)$$

7.3 Inertial space velocity sensing

Accurate measurement of low frequency vibration velocity in the inertial frame is difficult due to the difficulties in obtaining a reference point in this frame. Current sensor technologies only allow the inertial space velocity to be approximated down to a certain low frequency where the sensor dynamics start to interfere. For the proposed 6-DOF skyhook damping system, it is essential to obtain the inertial space velocity of the floater down to low frequencies, and the quality of the velocity measurements dictates the final performance of the damping system. This section explains the velocity acquisition techniques used in this research to realise the proposed 6-DOF skyhook damping system.

7.3.1 Multi-stage hybrid filtering for geophone signals

In this research, six geophones are used to obtain the inertial velocity measurements of the floater. The SENSOR SM-24 model (specifications are listed in Appendix D.6) was found to be able to provide sufficient performance within the allocated budget. The selected sensor maintains a flat response to inertial space velocity down to 10Hz (Figure D.1 in Appendix D.6). The geophone sensitivity starts to roll off at 40dB/decade below the 10Hz resonance frequency. This is highly undesirable since the primary aim of the skyhook damping system is to attenuate vibration at isolator resonances, which are below 10 Hz (as will be shown in Chapter 8) for the proposed 6-DOF maglev isolator. Therefore, a dual-stage hybrid filtering method incorporating an analogue filter stage and a digital filter stage was used to relocate the measuring system poles to a lower frequency so that the flat response bandwidth of the geophones is extended to a lower limit. This filtering method was kindly suggested by Dr Andrew Fleming from the University of Newcastle.

The dynamics of the geophone can be expressed as

$$\frac{U(s)}{v(s)} = K \frac{s^2}{s^2 + 2\zeta_g \omega_g s + \omega_g^2} , \quad (7.3)$$

Chapter 7 6-DOF Active Skyhook Damping

where K is the post-resonance sensitivity of the geophone, and $U(s)$ and $v(s)$ are the voltage output and the inertial velocity of the geophone respectively. ζ_g is the damping ratio of the geophone and was chosen to be equal to 0.6 (refer to Appendix D.6). ω_g is the geophone natural frequency and is 10Hz. It was decided to relocate the resonance frequency of the velocity measuring system to a target value of 1Hz. Any further reduction in resonance frequency would have resulted in an extensive filter settling time. Therefore, the desired transfer function of the sensing system after the pole placement is

$$H_f(s) = \frac{U_f(s)}{v(s)} = K \frac{s^2}{(s + \omega_d)^2} , \quad (7.4)$$

where $\omega_d = 1\text{Hz}$ is the desired system resonance frequency, and $U_f(s)$ is the voltage output of the geophone with the pole placement filter. To achieve this pole placement design, the filter with a transfer function of

$$\frac{U_f(s)}{U(s)} = \frac{s^2 + 2\zeta\omega_g s + \omega_g^2}{(s + \omega_d)^2} \quad (7.5)$$

was used so that Equation (7.5) multiplies Equation (7.3) to give desired sensing system response shown in Equation (7.4). Figure 7.2 shows a frequency domain plot of the filter transfer function described in Equation (7.5).

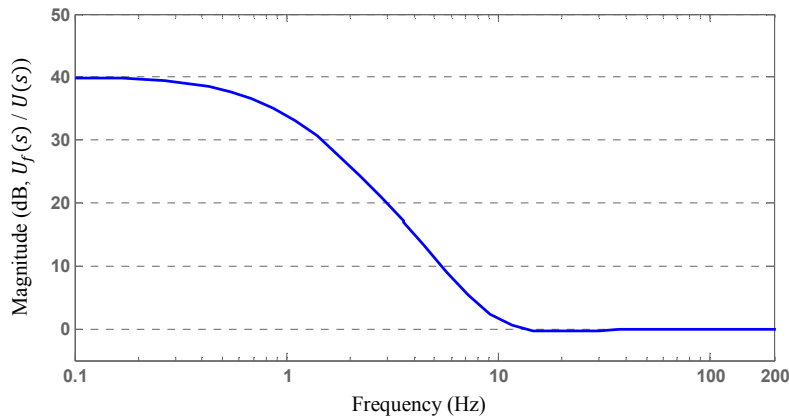


Figure 7.2: Anticipated frequency response of the geophone loop shaping filter.

7.3 Inertial space velocity sensing

This filter transfer function may be realised using digital filtering techniques. However, from Figure 7.2, it can be seen that a gain of 100 (40dB) at 0.1Hz is required for shaping the geophone dynamics. If the entire filter dynamics is achieved through purely digital means, quantisation error of the controller interface caused by the finite resolution of the analogue to digital converters is also amplified by 100 times. For the dSPACE DS1103 (specifications in Appendix D.3) platform used in this project to implement the digital controls, the analogue to digital converters (ADC) have -10V to 10V dynamic range with 16bit resolution. The quantisation error of the ADC is calculated as (National Instruments, 2006)

$$\frac{\text{Dynamic range}}{2^{\text{No.of bits of ADC}}} = \frac{20}{2^{16}} = 0.305 \text{ mV} . \quad (7.6)$$

The geophone has a sensitivity of 28.8V/ms^{-1} . Hence, if the quantisation error is magnified by 40dB to 30.5mV, the corresponding error velocity is calculated as $0.0305/28.8 = 1.06\text{mm/s}$. This error is relatively large compared to the magnitude of the floater velocity during normal operation, and hence is unacceptable in this application. Therefore, a hybrid method was designed to achieve the required filter transfer function.

The hybrid filtering method is a two stage filter design combining an analogue and a digital filter. The first analogue filtering stage is designed for amplifying the geophone signal in the pre-resonance frequency zone (1 to 10Hz), which avoids the undesired amplification of digital quantisation errors. The second stage contains a digital filter to further flatten the system response around the resonance frequency of the geophone. The use of this digital filter can avoid the complicated circuit designs of an equivalent analogue filter. The aim of the dual-stage hybrid filtering is to achieve a combined system transfer function described by Equation (7.5).

The transfer function (H_a) of the analogue filter for signal amplification is designed to be

$$H_a(s) = \left(\frac{s + \omega_g}{s + \omega_d} \right)^2 . \quad (7.7)$$

The circuit diagrams for achieving this transfer function are attached in Appendix E. The transfer function (H_d) for the digital stage of the filtering process realised using the dSPACE platform is

$$H_d(s) = \frac{s^2 + 2\zeta\omega_g s + \omega_g^2}{(s + \omega_g)^2} \quad (7.8)$$

The two stages of the filter are operated in series. The total system transfer function of the combined filter is the product of Equations (7.7) and (7.8), which is equal to Equation (7.5) as desired. The dynamic responses of both the analogue and digital filters were assessed experimentally using a Brüel & Kjær Photon+ signal analyser. The theoretical and experimental responses of the filters are plotted in Figure 7.3 and Figure 7.4 respectively. The two figures clearly show that both the analogue and digital filters have accurately achieved their anticipated transfer functions. The slight phase difference between the experimental and theoretical results for the digital filter is likely to be a result of the sampling delay caused by the digital controller operating at 10kHz, which theoretically introduces a phase shift of 7.2degrees at 200Hz.

7.3 Inertial space velocity sensing

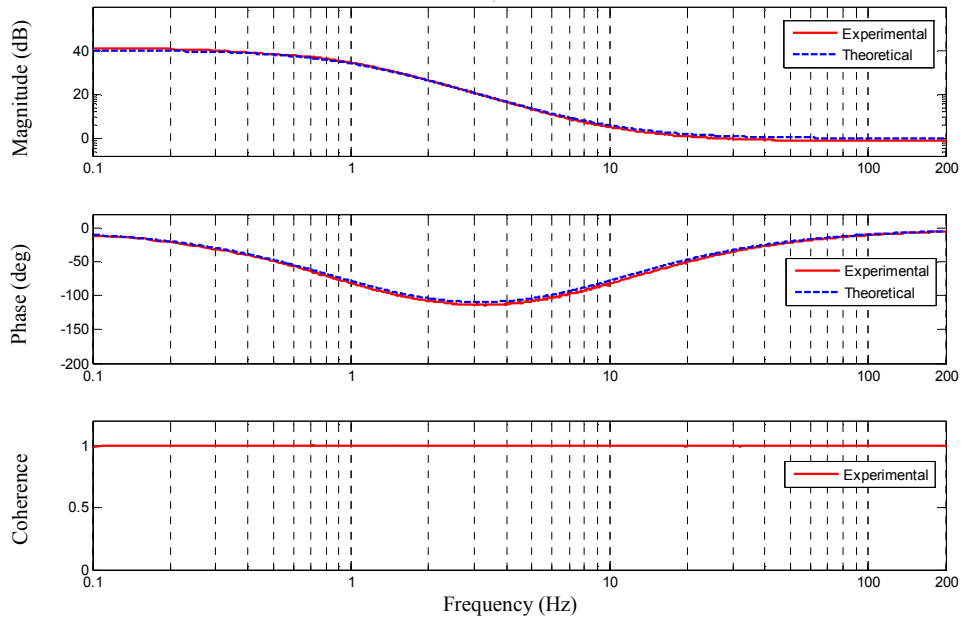


Figure 7.3: Frequency response of the analogue geophone loop shaping filter (FFT properties: DC coupled, 128 averages, 1600 lines, Hanning window, 24,000Hz sampling frequency).

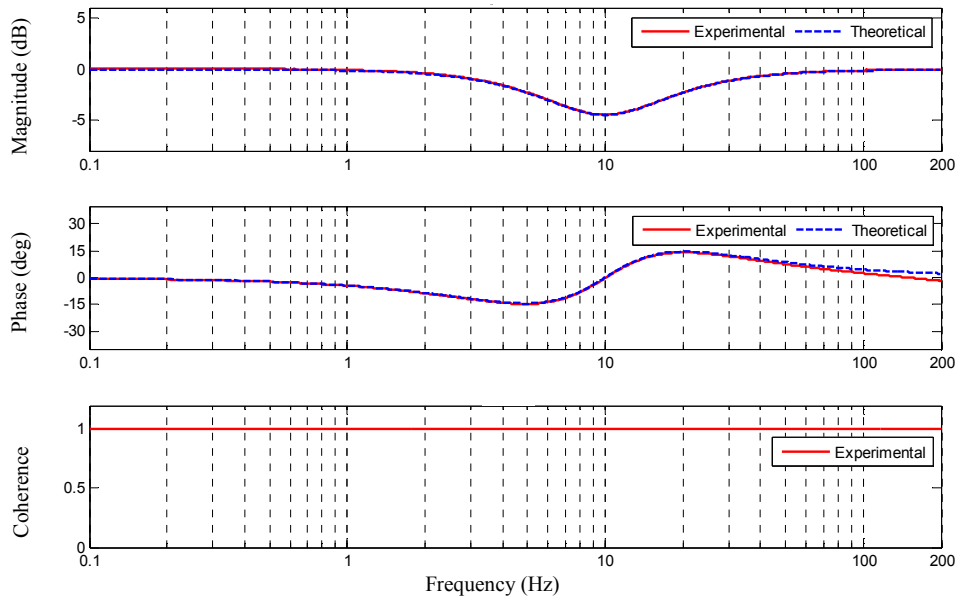


Figure 7.4: Frequency response of the digital geophone loop shaping filter (FFT properties: DC coupled, 128 averages, 1600 lines, Hanning window, 24,000Hz sampling frequency).

Chapter 7 6-DOF Active Skyhook Damping

After investigating the performance of the two filters, the dynamic response of the velocity measurement system was assessed by comparing the measurement results between the geophone and laser sensor which was shown in Section 6.2.2 to have a reasonably flat response in the 0 to 200Hz range. Figure 7.5 shows a schematic of the experimental arrangement for assessing the linearity of the velocity measurement system. The geophone was mounted on a steel platform driven by an electrodynamic shaker (LDS Test & Measurement, V201/3). The displacement of the vibrating platform was measured by both the laser sensor and the geophone. Integration of the geophone output generates displacement measurements, and a first order high-pass filter was used to eliminate the DC offset. The transfer function between the two measurements is plotted in Figure 7.6.

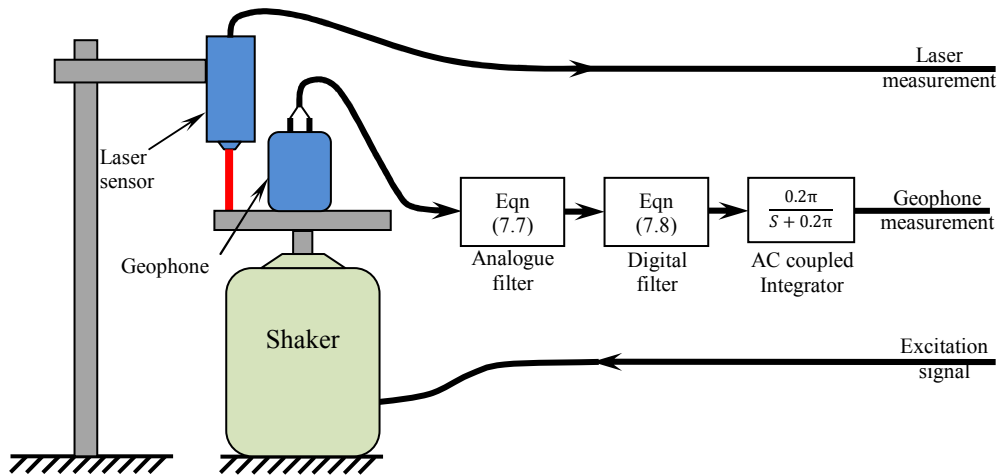


Figure 7.5: Layout of the linearity testing for the laser sensor

Figure 7.6 clearly shows that the experimental frequency response of the velocity measurement system closely fits the predicted response. The poles of the measuring system were successfully lowered in frequency by approximately one order of magnitude compared to the original geophone response without filtering (shown in Appendix D.6). The usable linear bandwidth of the geophone measurement system was extended down to approximately 1Hz.

7.3 Inertial space velocity sensing

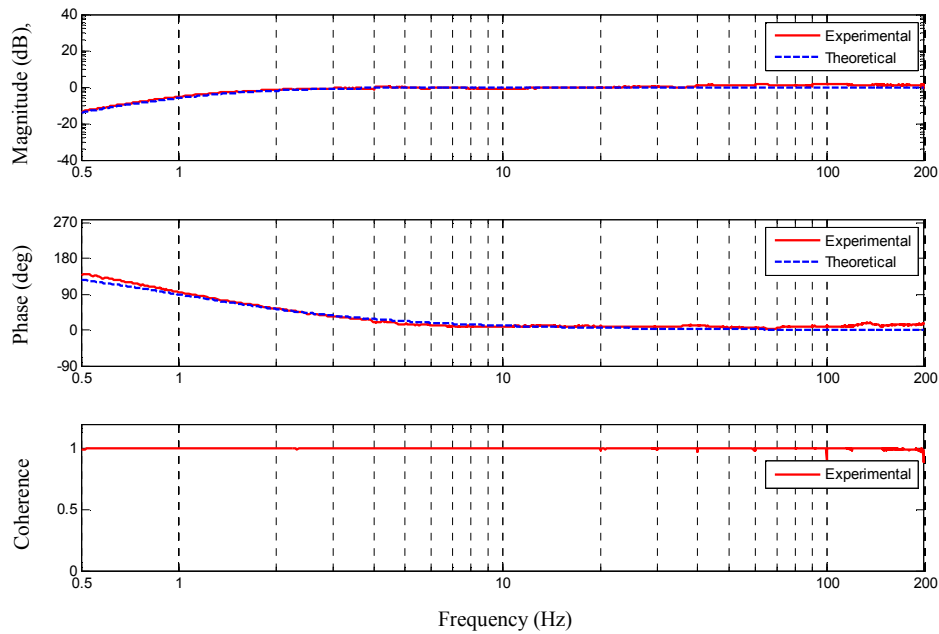


Figure 7.6: Frequency response of the hybrid filtered inertial velocity measurement system (FFT properties: DC coupled, 128 averages, 1600 lines, Hanning window, 24,000Hz sampling frequency).

7.3.2 Geophone magnetic shielding

The geophones are mounted on the six arms of the floater to monitor the vibration velocity. The locations of the geophones (shown in Figure 7.1(b)) are in close proximity of the solenoid actuators which are actively driven to stabilise the levitation. The operation of the solenoid actuators generates intense varying magnetic fields, which can be transmitted to the coils inside the geophone (refer to Figure D.1(a) in Appendix D.6) causing significant disturbance to the velocity measurements. Therefore, isolating the geophones from the generated electromagnetic field generated is essential for the operation of the skyhook damping system.

The magnetic shielding principle used in this design is to enclose the geophones in containers with high magnetic permeability. This approach is effectively to “short-circuit” the magnetic field around the geophone so that the magnetic flux around the geophone coil is significantly reduced. To obtain the optimum magnetic shielding, the shielding container was designed to be the maximum size for the available space between the floater and the frame. The material used for the shielding can is Electrical

Chapter 7 6-DOF Active Skyhook Damping

Steel due to its relative low cost, high machinability, and most importantly, high magnetic permeability (relative permeability is around 5000). The average wall thickness of the shielding can is 9mm. Figure 7.7 shows a CAD model of the shielding can design.

The shielding can performance was examined by determining the magnetic field reduction achieved by the shielding can compared to a non-shielded geophone. Figure 7.9 shows a schematic of the experimental arrangement. During the test, the solenoid was excited with white noise. Two geophones, one with shielding and one non-shielded, were placed on opposite sides of the solenoid at identical distances to the centre of the solenoid. The outputs from both geophones were recorded to provide the corresponding amount of electromagnetic interference received by the geophones.

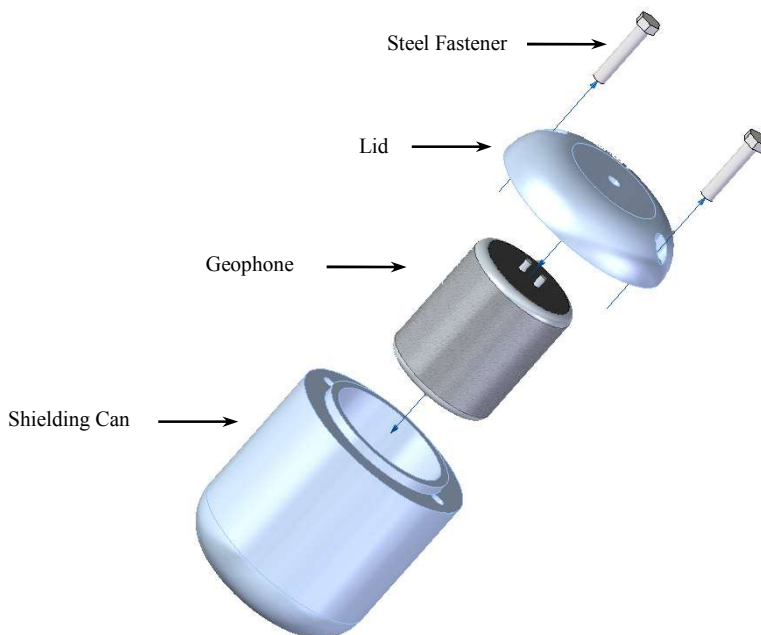


Figure 7.7: Exploded CAD model of the shielding can and geophone.

Figure 7.8 shows the transfer function between the two measured geophone outputs. The plot demonstrates that the shielding achieved a 30dB reduction in the low frequency interference. The shielding performance improves with an increase of the field frequency due to the electromagnetic properties of the shielding can design. This

7.3 Inertial space velocity sensing

design was found to provide sufficient sensor shielding for successful realisation of the skyhook damping system. The experimental results of the final skyhook damping system will be demonstrated in Chapter 8.

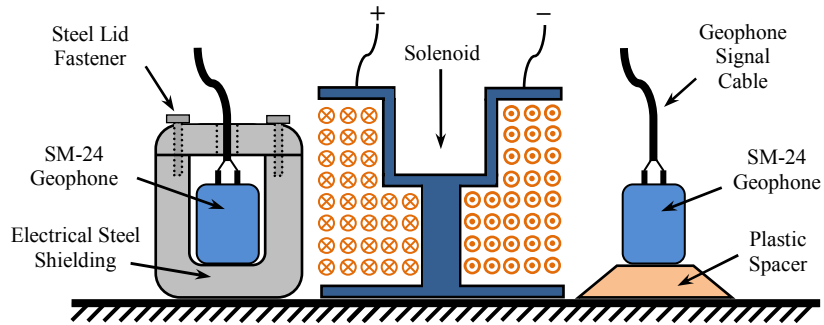


Figure 7.9: Experimental arrangement of the geophone shielding can performance test.

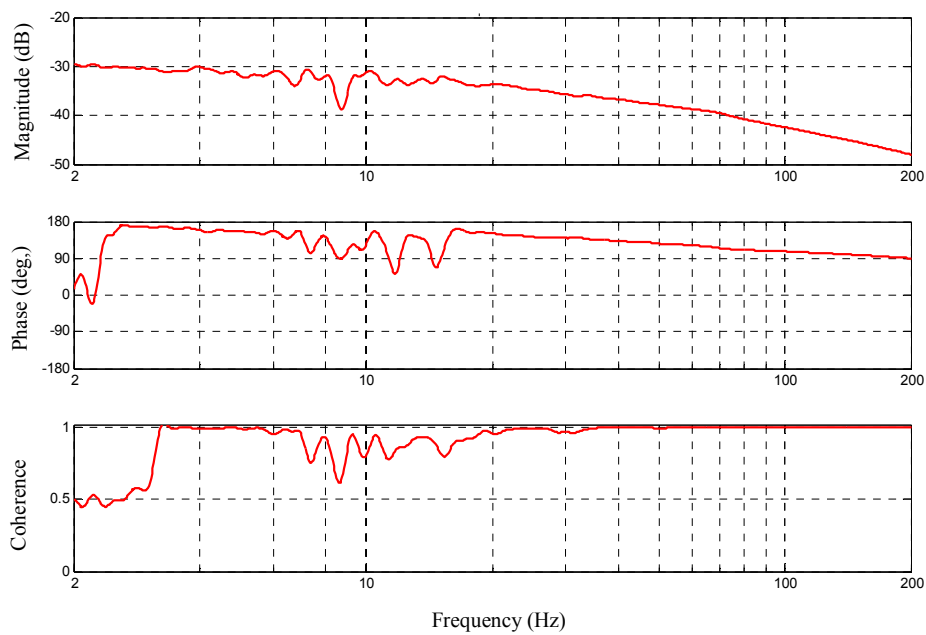


Figure 7.8: Frequency response between shielded and non-shielded geophones exposed to solenoid electromagnetic field excitation (FFT properties: DC coupled, 128 averages, 1600 lines, Hanning window, 24,000Hz sampling frequency).

Chapter 8

Experimental Measurements of Vibration Transmissibility

8.1 Introduction

The performance of the proposed 6-DOF maglev isolator was examined by measuring the external vibration transmissibility of the isolator in six DOFs. In order to carry out the transmissibility measurements, a 6-DOF vibration excitation platform was designed and built. The design of the platform constraints the excitation of the vibration isolator to a single DOF per assembly, and the platform can be assembled in six different forms to realise excitations in each of the six individual DOFs. During the experiments, multiple geophones with hybrid filters (Section 7.3.1) were used to measure the vibration transmissibility of the isolator in six DOFs. In this chapter, the design of the 6-DOF excitation platform will be discussed first, followed by the results of the vibration transmissibility measurements. The experimental data will be compared against the theoretical prediction of the vibration transmissibilities. The transmissibility measurements were also made with different levels of skyhook damping applied, and were compared to the predicted transmissibility from theory.

Chapter 8 Experimental Measurements of Vibration Transmissibility

The cross coupling between each DOF of the isolator is also presented at the end of this chapter.

8.2 6-DOF vibration excitation

Measurements of the 6-DOF vibration transmissibility require excitations to the isolator in all six DOFs. Due to the limitations of the project resources, it was not possible to perform measurements with simultaneous excitation in all six DOFs. Instead, an excitation platform was designed and built to carry out the required experiments with single axis excitation of each axis. Figure 8.1 shows a photograph of the developed excitation platform, assembled to achieve excitation in the Y direction.

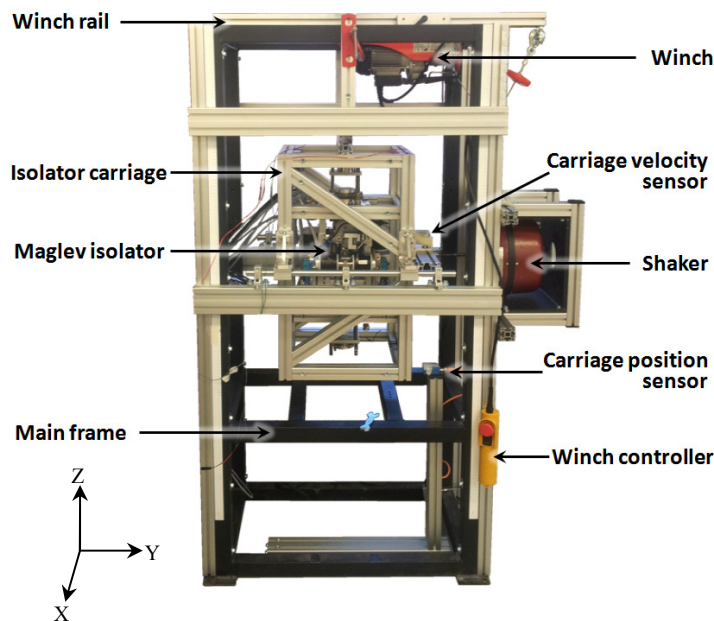


Figure 8.1: 6-DOF excitation platform (current view showing Y direction excitation).

In the excitation platform, an isolator carriage is designed to provide reinforcement to the isolator frame, as well as to attach the maglev isolator to the shaker (specifications are listed in Appendix D.7). Both linear and rotational bearings are used to constrain the isolator excitation to be within only one DOF. The design of the excitation platform allows it to be assembled in multiple ways to realise single axis excitation in each DOF. Figure 8.2 shows the CAD models of the platform assembled for exciting each DOF:

8.2 6-DOF vibration excitation

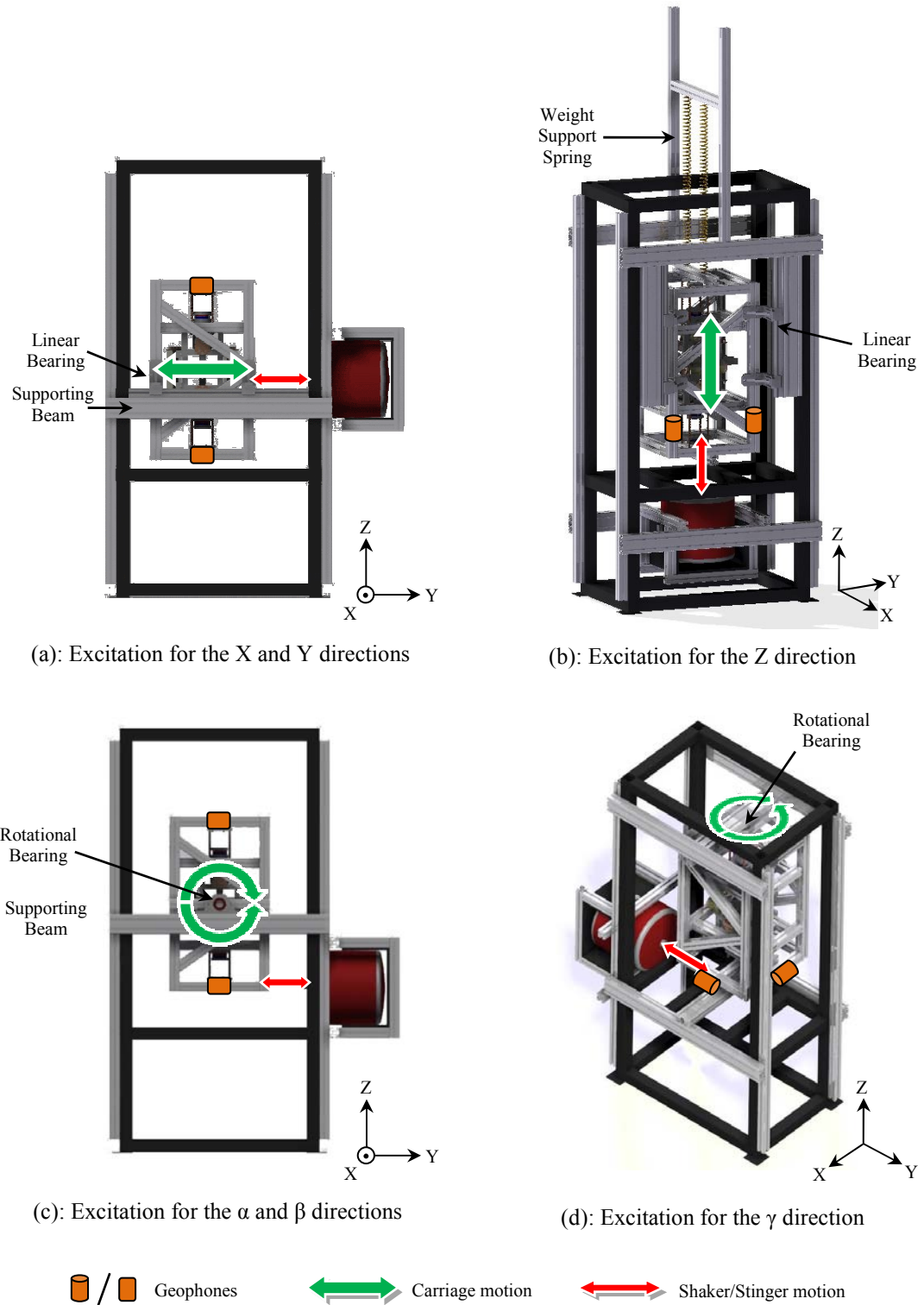


Figure 8.2: CAD assemblies of the 6-DOF excitation platform.

Chapter 8 Experimental Measurements of Vibration Transmissibility

- Excitation for the X and Y directions: Figure 8.2(a).

The carriage that contains the maglev isolator has two linear bearings installed on each side of the carriage, which are mounted on the horizontal supporting beams to constrain the motion of the carriage in the horizontal direction. The current view shows the Y direction excitation. The isolator orientation within the carriage can be rotated by 90degrees around the Z axis to allow excitation in the X direction. Two geophones are fitted on the top and bottom of the carriage to monitor the horizontal motion velocity. The magnitude of the carriage velocity is calculated as the average of the two geophone outputs.

- Excitation for the vertical direction: Figure 8.2(b).

The linear bearings are mounted on the left and right sides of the carriage to the vertical rails to constrain the carriage motion to the Z direction. Since the shaker is unable to bear any significant static load, two coil springs are used to balance the weight of the carriage assembly and the isolator which have a combined mass of about 38 kg. The natural frequency of the spring-carriage system was designed to be 0.3Hz, significantly below the natural frequency of the isolator in the Z direction. Hence, measurements of the isolator transmissibility in the vertical direction are not affected by the resonance of the excitation platform. Two geophones are fitted on the side of the carriage to monitor the vertical carriage velocity. The magnitude of the carriage velocity is calculated as the average of the two geophone outputs.

- Excitation for the α and β directions: Figure 8.2(c).

In the view shown, two rotational bearings are fitted at the centre of the carriage to constrain the carriage motion in the α direction. Hence, the linear excitation force generated by the shaker induces carriage rotational motion because of the constraints of rotational bearings shown in Figure 8.2(c). The isolator may be rotated by 90degrees to allow excitation of the isolator in the β direction. Two geophones are fitted on the top and bottom of the carriage to monitor the carriage angular velocity. The magnitude of the angular velocity is calculated as the difference of the two geophone outputs divided by the height of the carriage.

8.3 6-DOF transmissibility of the isolator

- Excitation for the γ direction: Figure 8.2(d).

The two rotational bearings are fitted on both the top and bottom of the carriage. The shaker stinger is connected to one side of the carriage so that linear motion of the shaker induces carriage rotation in the γ direction due to the constraints from the rotational bearings. Two geophones are fitted as shown in Figure 8.2(d) to measure the carriage angular velocity in the γ direction, and the magnitude of the velocity is calculated as the sum of the two geophone outputs divided by the width of the carriage.

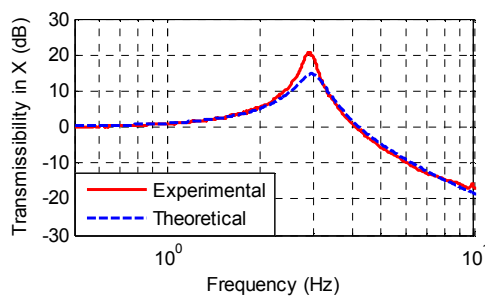
8.3 6-DOF transmissibility of the isolator

The vibration transmissibility of the isolator was measured in all six DOFs by comparing the measured vibration levels between the floater geophones (Figure 7.1) and the geophones on the isolator carriage (Figure 8.2). All the geophone outputs were filtered using the hybrid filtering technique (discussed in Section 7.3.1) to extend the geophone flat response bandwidth down to 1Hz. Since the geophones on both the floater and the carriage are almost identical, and their outputs are all processed with identical filters, the dynamics of the sensing system cancel each other when calculating the vibration transmissibility between the floater and the carriage. Experiments have shown that the developed sensing system was able to accurately measure the vibration transmissibility down to at least 0.5Hz.

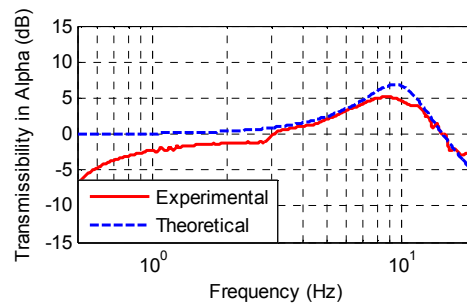
Six experiments were conducted to determine the vibration transmissibility of the isolator in each of the six DOFs. During each experiment, the isolator was excited by the shaker in one DOF with a swept sine (0.5 Octave/min) input signal, and the geophone outputs were recorded by a Brüel & Kjær Photon+ dynamic signal analyser. The PID controllers for maglev stability control were set in the low gain mode, and the gains used during the experiments are listed in Table 6.2. Due to the limitations imposed by the finite structural rigidity of the excitation platform, the upper limits of the excitation frequencies were 10Hz and 20Hz for the translational and rotational DOFs respectively. Excitation above these frequencies results in cross-coupled platform motion having larger amplitude than the primary DOF of interest.

Chapter 8 Experimental Measurements of Vibration Transmissibility

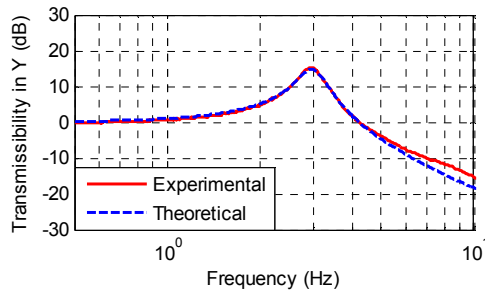
Figure 8.3 shows the measured transmissibilities of the isolator in six DOFs. The red solid curves represent the measured isolator transmissibility for external vibrations, and the blue dotted lines are the theoretical responses of isolation system assuming zero stiffness in all directions. The theoretical zero stiffness system responses are derived using the control system structure described in Figure 8.4, which is a schematic of each PID control loop for stabilising a single DOF. The control system has six such loops to stabilise the floater in 6-DOF. The derivation of the theoretical zero-stiffness responses is based on the following facts:



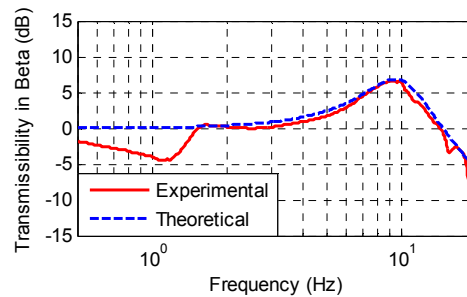
(a): Transmissibility in the X direction



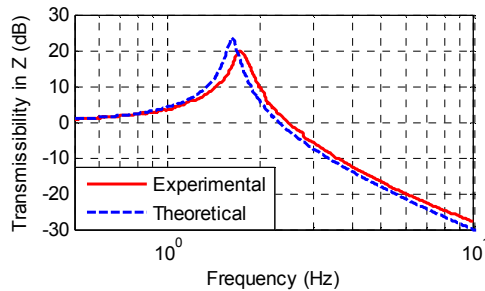
(d): Transmissibility in the α direction



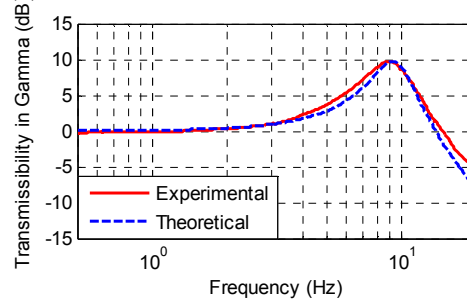
(b): Transmissibility in the Y direction



(e): Transmissibility in the β direction



(c): Transmissibility in the Z direction



(f): Transmissibility in the γ direction

Figure 8.3: Vibration transmissibilities of the isolator in six DOFs. Red curve: measured isolator response; Blue curve: predicted isolator response with assumed zero stiffness (FFT properties: DC coupled, 128 averages, 1600 lines, Hanning window, 24,000Hz sampling frequency).

8.3 6-DOF transmissibility of the isolator

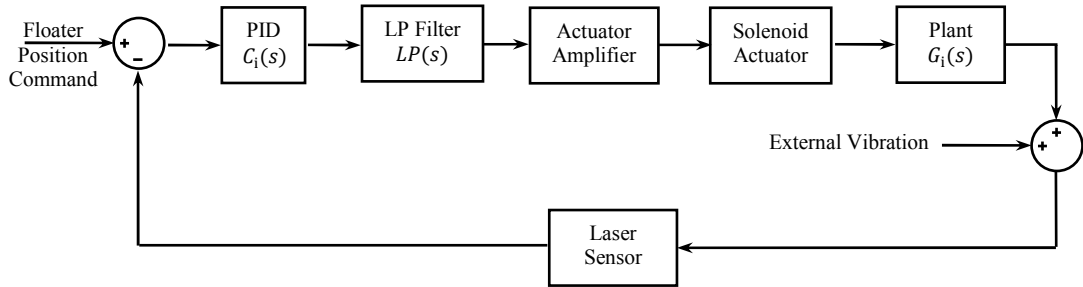


Figure 8.4: Schematic of the individual PID stabilisation control loop.

- There is negligible inherent damping between the floater and the supporting frame due to the nature of the non-contact magnetic levitation.
- The frequency responses of the Solenoid Actuator, Actuator Amplifier and Laser Sensor are shown to be linear in the frequency range of the measurements (0.5-20Hz). The transfer function across these components can thus be considered as constant.
- The laser displacement sensors are attached to the frame assembly of the isolator. Hence, the bodies of the laser sensors are considered to have the same vibration amplitude and phase as the external vibration.

Therefore, if the isolator stiffness is assumed to be zero in all six directions, and in the absence of the feedback controller, the transfer function of the plant may be simplified to

$$G_i(s) = \frac{1}{ms^2}; G_j(s) = \frac{1}{J_{ii}s^2} \quad , \quad (8.1)$$

where m is the mass of the floater, J_{ii} is the floater moment of inertia with respect to its COG, $G_i(s)$ and $G_j(s)$ ($i \in (X, Y, Z)$ and $j \in (\alpha, \beta, \gamma)$) represent the transfer function of the plant in the translational and rotational DOFs respectively. With the simplified plant transfer functions, the frequency response of the controlled levitation to external vibration is analogous to a linear mass-spring-damper system with the stiffness and damping provided by the PID controllers. The closed-loop transfer function of the isolation system can be written as

$$\left. \begin{aligned} TF_i(s) &= \frac{C(s) \cdot LP(s) \cdot G_i(s)}{1 + C(s) \cdot LP(s) \cdot G_i(s)} \\ TF_j(s) &= \frac{C(s) \cdot LP(s) \cdot G_j(s)}{1 + C(s) \cdot LP(s) \cdot G_j(s)} \end{aligned} \right\}, \quad (8.2)$$

where $TF_i(s)$ and $TF_j(s)$ represent the system transfer functions in the translational and rotational DOFs respectively. $C(s)$ is the transfer function of the maglev stability controller (Equation (5.3), and $LP(s)$ describes the dynamics of the low-pass filters (Equation (5.5). Substituting Equations (5.3), (5.5) and (8.1) into Equation (8.2) yields

$$\left. \begin{aligned} TF_i(s) &= \frac{\omega_{LP}^2 D_i s^2 + \omega_{LP}^2 P_i s + \omega_{LP}^2 I_i}{ms^5 + 2m\omega_{LP} s^4 + m\omega_{LP}^2 s^3 + \omega_{LP}^2 D_i s^2 + \omega_{LP}^2 P_i s + \omega_{LP}^2 I_i} \\ TF_j(s) &= \frac{\omega_{LP}^2 D_j s^2 + \omega_{LP}^2 P_j s + \omega_{LP}^2 I_j}{J_{ii} s^5 + 2J_{ii} \omega_{LP} s^4 + J_{ii} \omega_{LP}^2 s^3 + \omega_{LP}^2 D_j s^2 + \omega_{LP}^2 P_j s + \omega_{LP}^2 I_j} \end{aligned} \right\}, \quad (8.3)$$

which are the transfer functions used to derive the theoretical system responses in Figure 8.3 assuming zero inherent stiffness of the maglev system in all six DOFs. In Equation (8.3), ω_{LP} is the cut-off frequency of the low-pass filters; P_i, I_i, D_i and P_j, I_j, D_j are the proportional, integrative and derivative gains of the PID controllers for stabilising levitation in the translational and rotational DOFs respectively. The floater mass and moment of inertia are provided in Table 4.1, and the PID gains used in the transmissibility tests are listed in Table 6.2.

The measured isolator responses in all six DOFs shown in Figure 8.3 reveal similar behaviour to the predicted isolator response derived with the inherent levitation stiffness assumed to be zero in all directions. Therefore, it is practically demonstrated that the proposed maglev isolation system has the ability to realise inherent zero-stiffness levitation in all six DOFs. Figure 8.3 also shows that the isolator system response is dominated by the gains of the PID controllers since the experimental results are comparable to the theoretical response derived with consideration of the

8.3 6-DOF transmissibility of the isolator

influence of the control system dynamics alone. The PID gains used during the transmissibility measurements were found to be a suitable combination for both minimising the vibration transmissibility and maintaining a stable levitation based on the current mechanical and electronic system used in the isolator prototyping. With improved hardware quality, such as improvements to the uniformity of magnetisation of the magnets, the mechanical component alignment, the laser sensor resolution, the electronic system noise, the solenoid actuator performance, and the amplifier performance, the stability of the maglev system may be achieved with lower controller stiffness. This would potentially result in improved vibration isolation performance. The potential of the proposed maglev vibration isolation method is thus currently limited by the quality of the hardware, rather than physical limits relating to the proposed method.

Figure 8.3(c) shows a small difference between the resonance frequencies for the experimental and theoretical results. This is due to the fact that quasi-zero stiffness levitation, in the vertical (Z) direction, only exists for a small displacement from the nominal operation position. Due to the relatively low isolator resonance frequency in the Z direction, large amplitude excitations (approximately $\pm 2.5\text{mm}$ floater displacement relative to the frame assembly) were used in the transmissibility measurements. This amplitude of excitation was necessary to overcome the initial static friction in the linear bearings used in the testing apparatus, as well as to ensure high SNR (signal to noise ratio) in the inertial sensors (geophones). The large floater offset from the nominal operation position resulted in a small amount of stiffness addition caused by the vertical magnetic forces, and this effect slightly increased the overall resonance frequency of maglev isolator in the vertical direction. However, in practical situations of relevance, the magnitude of typical indoor vibration in the vertical direction is expected to be substantially smaller than the excitation amplitude used here. Hence, the maglev system is expected to maintain the quasi-zero stiffness levitation in the vertical direction during normal operation.

According to Figure 8.3, the experimental and theoretical resonance frequencies for the X, Y and Z directions are approximately 2.9Hz, 3Hz, 1.8Hz and 3Hz, 3Hz, 1.6Hz

Chapter 8 Experimental Measurements of Vibration Transmissibility

respectively. Vibration attenuation achieved experimentally at 10Hz is -17dB, -15dB and -28dB in the X, Y and Z directions. These performance measures are comparable to the top of the range active vibration isolation products offered in the market, such as products from Newport and Herzan. However, as mentioned previously, the performance of the developed isolation system is dominated by the maglev stabilisation controller of the maglev system. The vibration isolation performance may be improved with system hardware of higher quality. As the proposed maglev system is actively stabilised, the performance of the isolator is able to be actively tuned to satisfy the requirements for different applications. For example, low controller gains can be used to address ground vibration isolation, while high controller gains may be used to realise low isolator compliance to eliminate on board equipment vibrations. The passive payload weight support using magnetic forces in the vertical direction also allows the system to be stabilised with minimal power consumption. Experiments have shown that the maglev only consumes less than 1W of electricity for levitating a mass of 6.693kg, much of which is parasitic losses in the linear power stage of the actuator amplifiers.

In Figure 8.3(a), the peak response of the isolator in the X direction shows a larger amplitude than the theoretical response. This may be caused by the cross coupling effect existing on the vibration testing platform. For excitation frequencies above 3Hz, the limited rigidity of the excitation platform is no longer able to constrain the excitation energy to be purely within a single DOF. This phenomenon can also be observed in Figure 8.5 as the coherences of most of the cross coupling measurements show a significant increase beyond 3Hz. The cross coupled excitation energy is transmitted into the floater through the complex mechanical linkages of the excitation platform, and results in increased floater vibration at the resonance frequency in the X direction.

Figure 8.3(d) and Figure 8.3(e) show the frequency responses of the isolator in the α and β directions. The unpredictable behaviour of the isolator responses at low frequencies is a result of coupling with the gravitational field. During the measurements of the rotational transmissibility of the isolator, large excitation angles

were used to obtain accurate measurements at low frequencies. This caused a large misalignment between the magnetic payload supporting force and the gravitational field (also shown in Figure 3.15 and explained in Section 3.6.1), which resulted in the unexpected floater movements at low frequencies.

8.4 6-DOF isolator cross coupling

The cross-coupled transmissibility of the proposed maglev vibration isolator was measured between all six orthogonal DOFs through six experiments. In each experiment, the isolator was excited in predominately one DOF, and the vibration velocity of the floater was recorded in all six DOFs. Figure 8.5 shows the measured transmissibility between each pair of DOFs. The transmissibility plots are mapped from the column index to the row index; for example, the amplitude of cross transmissibility from the Y direction to the α direction is shown by the plot in column two and row seven. The coherence (Coh) plot directly below each transmissibility amplitude (Amp) plot shows the coherence of the corresponding measurement in the frequency domain. For example, the plot in column two and row eight shows the coherence of the transmissibility measurement in the column two and row seven plot. Plot colours in Figure 8.5 are arranged as:

- Blue: Transmissibility measurements from the translational DOFs to the translational DOFs;
- Red: Transmissibility measurements from the rotational DOFs to the rotational DOFs;
- Green: Transmissibility measurements from the rotational DOFs to the translational DOFs;
- Yellow: Transmissibility measurements from the translational DOFs to the rotational DOFs.

Chapter 8 Experimental Measurements of Vibration Transmissibility

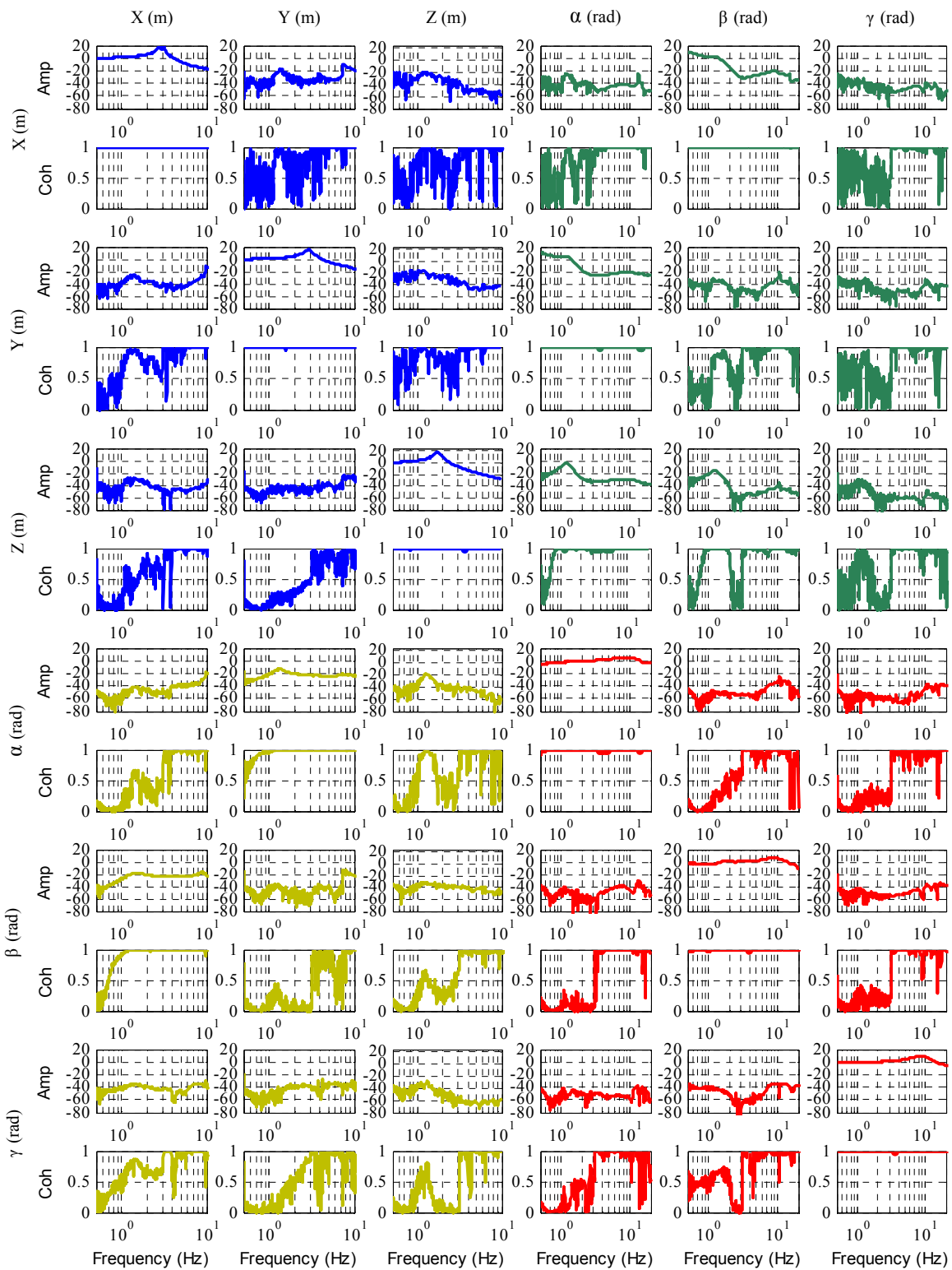


Figure 8.5: Measurements of the cross coupling between DOFs. Horizontally across represents the input axis, vertically represents the response axis (FFT properties: DC coupled, 128 averages, 1600 lines, Hanning window, 24,000Hz sampling frequency).

8.4 6-DOF isolator cross coupling

It can be seen that the diagonal plots of both the blue and red coloured curves (plot X to X, Y to Y, Z to Z, α to α , β to β and γ to γ) have significantly higher amplitudes (by approximately 40 dB on average) than the cross-DOF transmissibilities. This indicates that each translational DOF is highly decoupled from the other translational DOFs, and each rotational DOF is highly decoupled from the other rotational DOFs. It was discussed in Sections 3.6.2 and 3.6.3 that the maglev system has cross coupling between the X and β directions, as well as between the Y and α directions. These cross couplings can be observed in the measurements shown by the green and yellow coloured curves. Plots X to β , β to X, Y to α and α to Y all show relatively high (close to 1) values of coherence, which indicate the cross coupling effects between the X and β , and the Y and α directions. The cross couplings shown from the α and β directions into the Z direction are caused by the misalignments between the directions of the payload supporting force and the gravity. As discussed in Section 8.3, these misalignments are a result of the large amplitudes of excitation used to capture isolator transmissibilities at low frequencies.

In Figure 8.5, the coherence curves of all the cross transmissibility measurements show values close to 1 beyond 3Hz. As mentioned previously, this is due to the finite stiffness of the testing platform which allowed excitation energy in the testing DOF to couple into other DOFs of the testing platform.

8.5 Transmissibility with skyhook damping

Vibration transmissibility of the developed maglev isolator was also measured in six DOFs with the active skyhook damping system. The principles of operation and the composition of the skyhook damping system were discussed in Chapter 7. This section presents both the theoretical and experimental improvements on vibration transmissibility achieved using the skyhook damping system.

The skyhook damping system operates in parallel with all of the other sub-control systems. Based on the operating principles described in Chapter 7, the skyhook damping system only changes the dynamics of the maglev system. With the addition of the inertial damping effect, the system dynamics changes from that described by Equation (8.1) to

$$GS_i(s) = \frac{1}{ms^2 + sh_i \cdot H_f \cdot s}; GS_j(s) = \frac{1}{J_{ii}s^2 + sh_j \cdot H_f \cdot s} \quad , \quad (8.4)$$

where $GS_i(s)$ and $GS_j(s)$ ($i \in (X, Y, Z)$; $j \in (\alpha, \beta, \gamma)$) are the transfer functions of the maglev system in the translational DOFs and rotational DOFs respectively, m is the mass of the floater, and J_{ii} is the moment of inertia of the floater around the i^{th} axis, and H_f is the transfer function (Equation (7.4)) of the floater velocity sensing system. In Equation (8.4), sh_i and sh_j are the effective damping coefficients of the skyhook damping system, which are derived from the local damping coefficients described in Equation (7.1) as

$$\begin{cases} sh_X = sh_{X_{ab}} + sh_{X_{cd}} \\ sh_Y = sh_{Y_{ab}} + sh_{Y_{cd}} \\ sh_Z = sh_{Z_{ab}} + sh_{Z_{cd}} \\ sh_\alpha = (sh_{Z_{ab}} - sh_{Z_{cd}}) \cdot L'_Z \\ sh_\beta = (sh_{X_{ab}} - sh_{X_{cd}}) \cdot L'_X \\ sh_\gamma = (sh_{Y_{cd}} - sh_{Y_{ab}}) \cdot L'_Y \end{cases} \quad . \quad (8.5)$$

The addition of the skyhook damping system only alters the dynamics of the maglev system. Therefore, the overall transfer function of the vibration isolation system remains similar to Equation (8.2) as

8.5 Transmissibility with skyhook damping

$$\left. \begin{aligned} TFS_i(s) &= \frac{C(s) \cdot LP(s) \cdot GS_i(s)}{1 + C(s) \cdot LP(s) \cdot GS_i(s)} \\ TFS_j(s) &= \frac{C(s) \cdot LP(s) \cdot GS_j(s)}{1 + C(s) \cdot LP(s) \cdot GS_j(s)} \end{aligned} \right\} \quad (8.6)$$

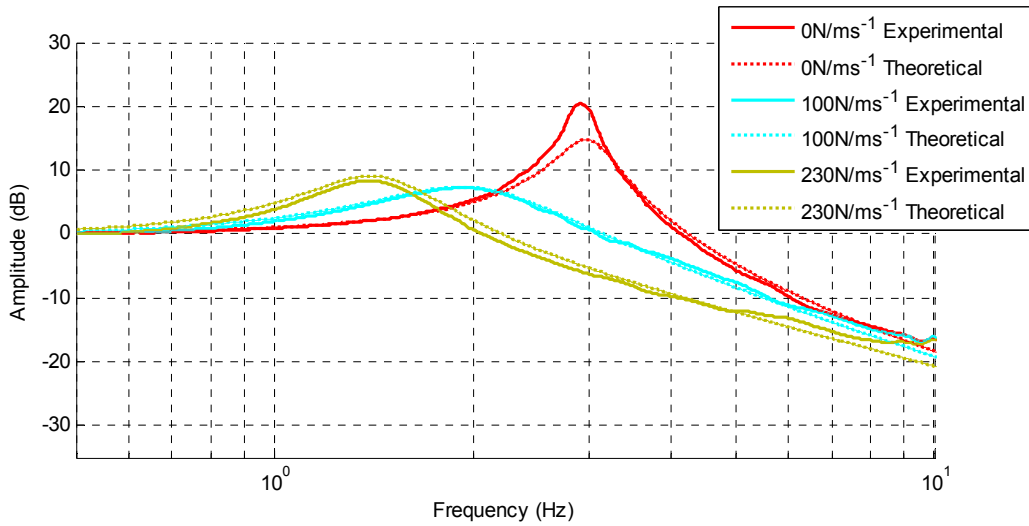
for translational and rotational DOFs respectively. Substituting Equations (5.3), (5.5) and (8.4) into Equation (8.6) yields the overall transfer functions

$$\left. \begin{aligned} TFS_i(s) &= \frac{(\omega_{LP}^2 D_i s^2 + \omega_{LP}^2 P_i s + \omega_{LP}^2 I_i)(s + \omega_d)^2}{(\omega_{LP}^2 D_i s^2 + \omega_{LP}^2 P_i s + \omega_{LP}^2 I_i)(s + \omega_d)^2 + (s + \omega_{LP})^2 (ms^3 (s + \omega_d)^2 + Ks^4 sh_i)} \\ TFS_j(s) &= \frac{(\omega_{LP}^2 D_j s^2 + \omega_{LP}^2 P_j s + \omega_{LP}^2 I_j)(s + \omega_d)^2}{(\omega_{LP}^2 D_j s^2 + \omega_{LP}^2 P_j s + \omega_{LP}^2 I_j)(s + \omega_d)^2 + (s + \omega_{LP})^2 (j_{ii} s^3 (s + \omega_d)^2 + Ks^4 sh_j)} \end{aligned} \right\} , \quad (8.7)$$

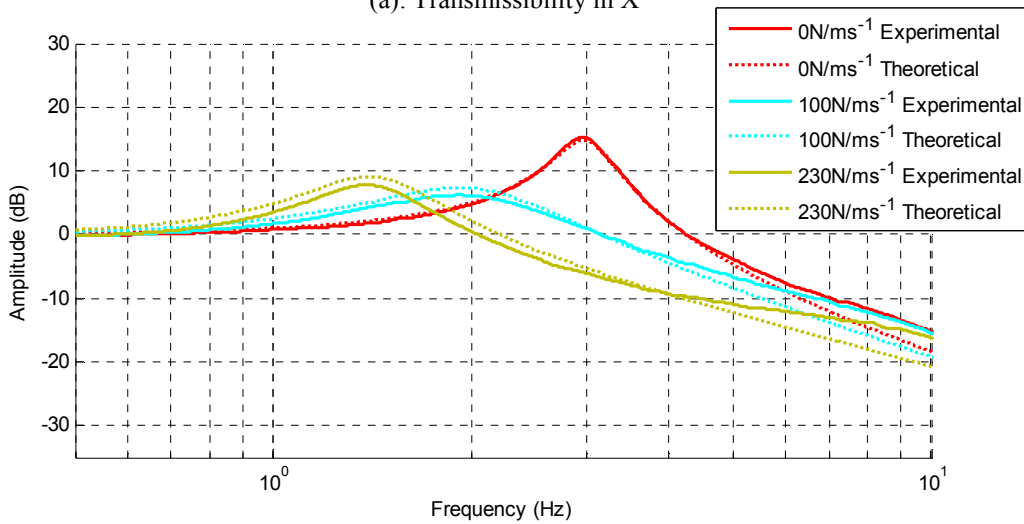
which describe the vibration transmissibilities of the maglev isolator with the skyhook damping system, and were used to derive the theoretical responses shown in Figure 8.6 and Figure 8.7.

The experimental transmissibilities of the isolator with the skyhook damping system were measured through six sets of experiments. In each set, the isolator was excited predominately in a single DOF with a swept sine signal (0.2 octave/min), and the vibration transmissibility was recorded for a series of skyhook damping coefficients in each DOF. Figure 8.6 and Figure 8.7 show the comparisons between the theoretical and experimental responses of the isolator for several of the selected skyhook damping coefficients, and Figure 8.8 shows the complete results of the measured vibration transmissibility with the skyhook damping system in all six DOFs. During the measurements, the PID levitation controllers were set to the low gain mode (normal operation mode), and Table 6.2 lists the PID gains used in the tests.

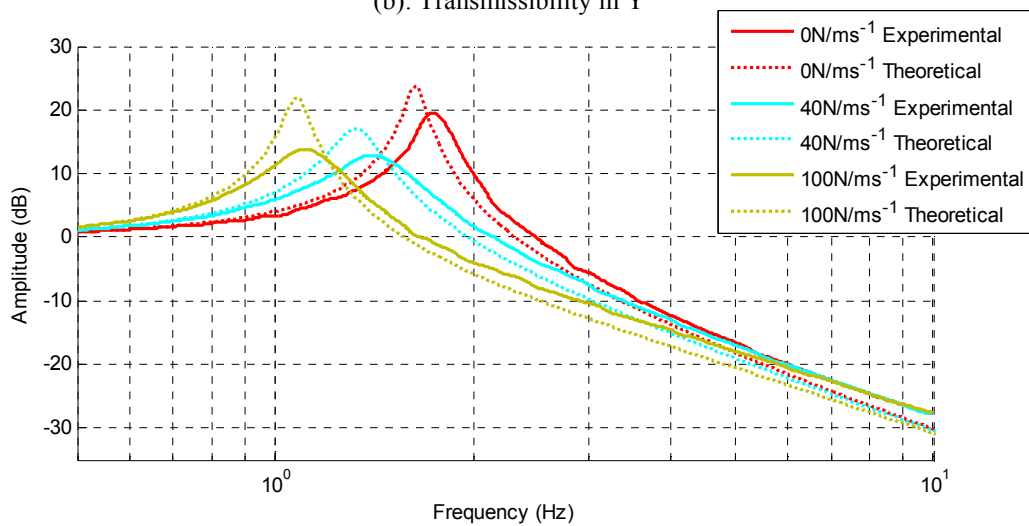
Chapter 8 Experimental Measurements of Vibration Transmissibility



(a): Transmissibility in X



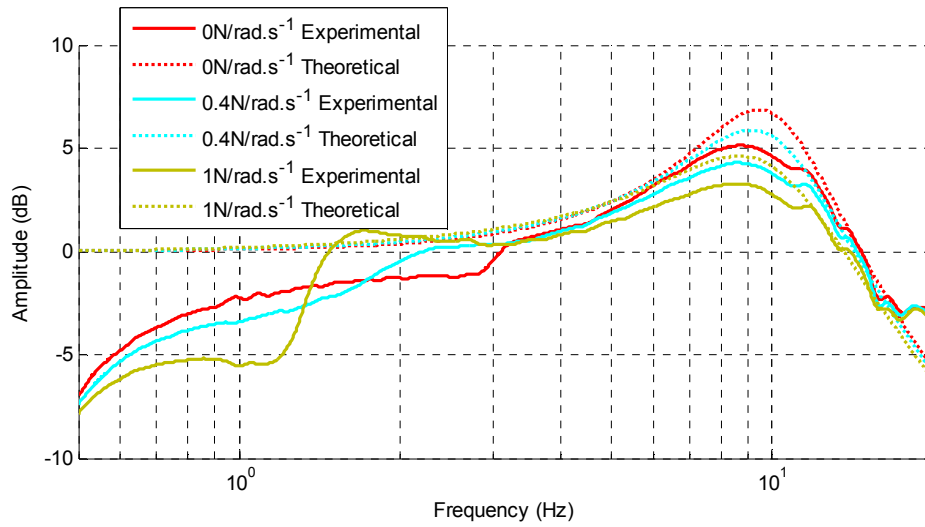
(b): Transmissibility in Y



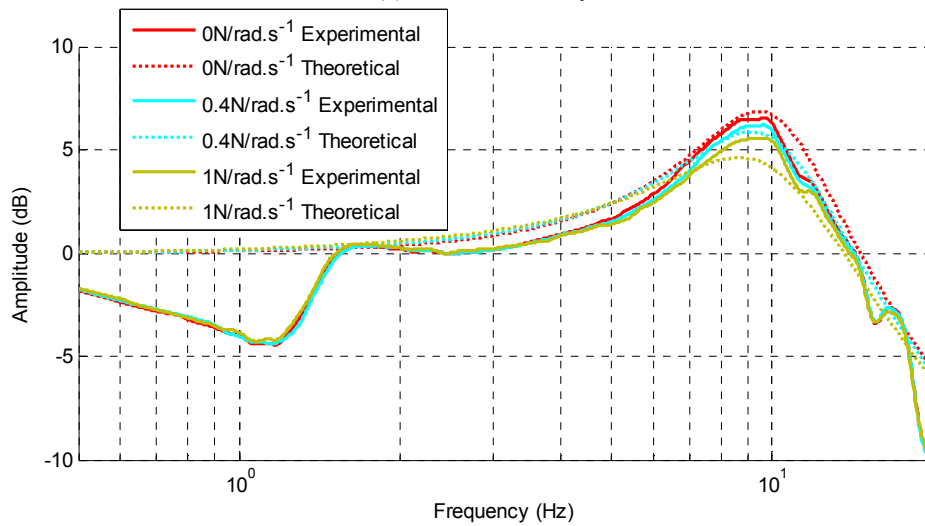
(c): Transmissibility in Z

Figure 8.6: Comparison between the theoretical and experiment transmissibilities with various skyhook damping coefficients in the translational DOFs (FFT properties: DC coupled, 128 averages, 1600 lines, Hanning window, 24,000Hz sampling frequency).

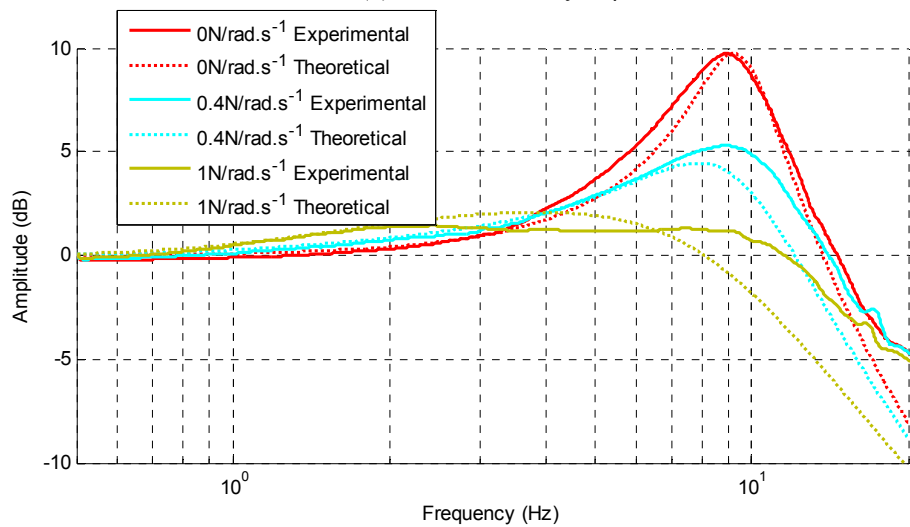
8.5 Transmissibility with skyhook damping



(a): Transmissibility in α



(b): Transmissibility in β



(c): Transmissibility in γ

Figure 8.7: Comparison between the theoretical and experiment transmissibilities with various skyhook damping coefficients in the rotational DOFs (FFT properties: DC coupled, 128 averages, 1600 lines, Hanning window, 24,000Hz sampling frequency).

Chapter 8 Experimental Measurements of Vibration Transmissibility

In Figure 8.6 and Figure 8.7, the red curves are the responses of the original system with a value of zero as the skyhook damping coefficient. Both the theoretical and experimental responses have a similar shape to the measurements shown in Figure 8.3. With non-zero skyhook damping coefficients, the experimental results for the isolator responses in the vertical direction (Figure 8.6(c)) and all the rotation directions (Figure 8.7(a), Figure 8.7(b) and Figure 8.7(c)) show some differences between the peak amplitudes of the theoretical responses. These peak amplitude differences are likely to be partially caused by the un-modelled eddy current damping effect, which provides additional damping to the system that reduces the peak responses at isolator resonances. The eddy current damping was ignored in the system modelling due to the small magnitudes of the floater motion relative to the frame, which is the case during normal operation when the isolator is only excited by typical laboratory ground vibration (Appendix B). However, as previously explained, excitations with large amplitudes were used during the transmissibility measurements to ensure the quality of results. Therefore, the eddy current damping effect may have contributed to the differences between the theoretical and experiment peak responses. Another possible cause of the peak amplitude differences is the interference introduced by the geophone cables. As introduced in Chapter 7, six geophones were installed on the floater to monitor the floater vibration velocity. Due to the intense magnetic interference induced by the solenoid actuators, the output cables of the geophones require high performance shielding, which limits the ability to reduce the cable size for minimising its influence on the floater dynamics. Six pairs of shielded cables were connected between the geophones and the isolator frame. The damping effect provided by the heavy cables may have also contributed to the amplitude differences observed at the isolator resonances.

In Figure 8.6 and Figure 8.7, most of the theoretical transmissibility curves in both the translational and rotational DOF plots deviate from the experimental responses at frequencies above approximately 3Hz. The experimental responses show larger magnitudes than the predicted curves in almost all of the measurements. This is mainly due to the cross coupling effects on the excitation platform discussed in Section 8.2, which can also be observed from the increases in coherence values shown

8.5 Transmissibility with skyhook damping

in Figure 8.5 beyond 3Hz in the measurements of the cross-coupled transmissibilities. In Figure 8.7 the zigzag pattern at high frequencies (beyond 10Hz) may be a result of the resonance modes of the output cables connected to the geophones, or some higher order dynamics of the maglev system.

In order to fully demonstrate the performance of the skyhook damping system, Figure 8.8 presents the complete results with the entire set of skyhook damping coefficients for which measurements were obtained. In the translational directions, it can be seen that the skyhook damping system not only reduced the peak vibration amplitudes compared to the un-damped responses, but also reduced the fundamental resonance frequency of the maglev isolator. For an ideal 1-DOF system governed by a second order differential equation, in theory the skyhook damping has no influence on the system resonance frequency. As discussed in Section 2.3.4, the active damping system should be unconditionally stable provided that the sensors and actuators are collocated and have flat frequency response in the bandwidth of interest for the active damping. However, Equation (7.4) suggests that the transfer function of the sensing system used in the proposed skyhook damping system has two poles at 1Hz. Therefore, increasing the coefficients of the skyhook damping control increases the weighting of the dynamics of the skyhook damping system over the original isolator system dynamics (shown by the red un-damped response curve). Figure 8.8 shows that, in the X, Y and Z directions, increasing the damping gains pulled the overall system resonance frequency towards the 1Hz point from the original resonance frequencies of the un-damped modes. It can also be observed that with the increase of the skyhook damping coefficients, the peak response of the isolator reduced to a point, beyond which the amplitude started to grow again. This is due to the phase lag introduced by the double pole of the sensing system at 1Hz. With an increase in the skyhook damping coefficients, the phase lag leads to reduced system stability, and will eventually drive the entire maglev system unstable when the gain margin is exceeded.

Chapter 8 Experimental Measurements of Vibration Transmissibility

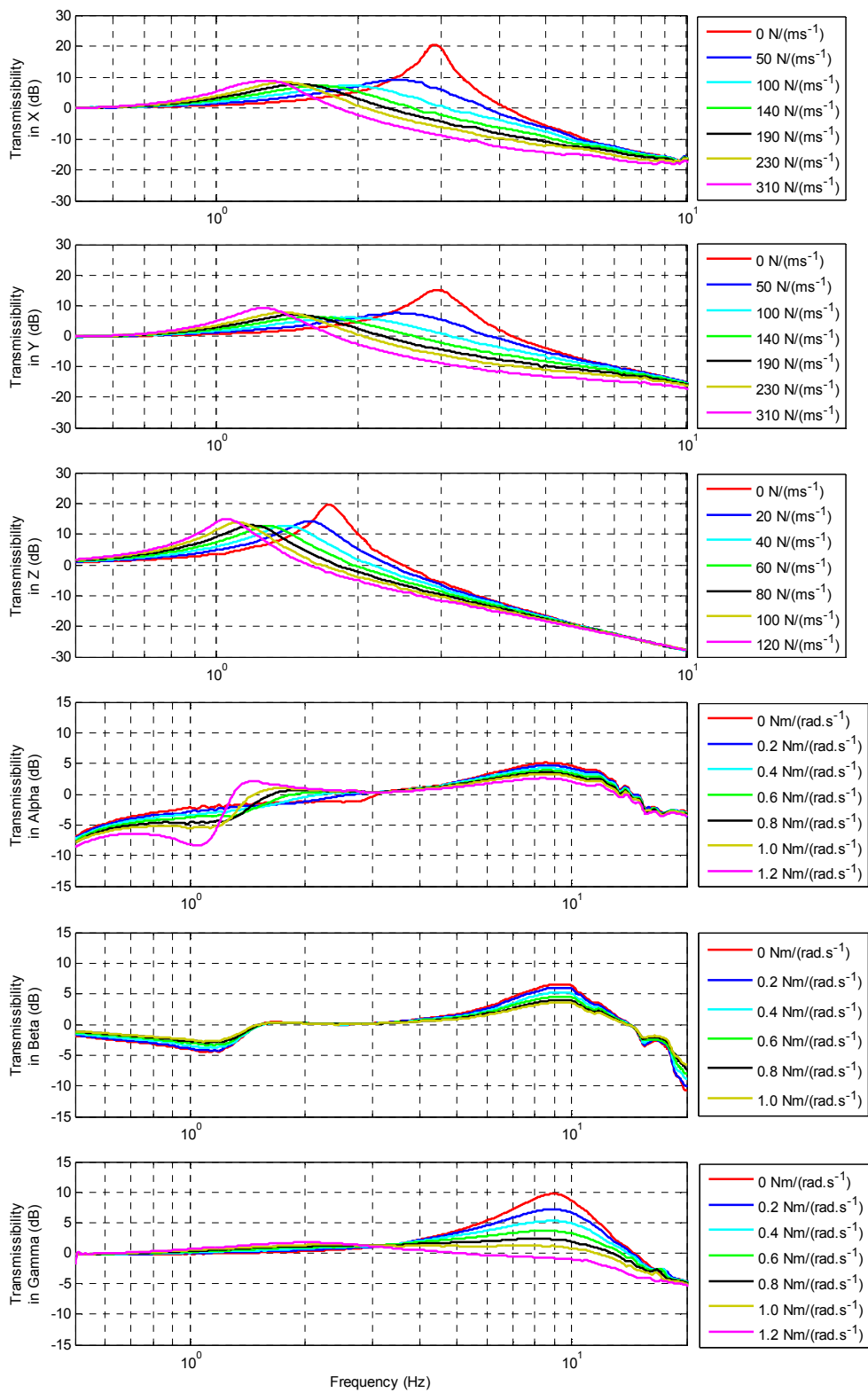


Figure 8.8: 6-DOF isolator transmissibility with active skyhook damping (FFT properties: DC coupled, 128 averages, 1600 lines, Hanning window, 24,000Hz sampling frequency).

8.5 Transmissibility with skyhook damping

The aforementioned effects caused by the poles of the sensing system are not as obvious in the rotational DOFs. Figure 8.8 shows the 1Hz poles of the velocity sensing system caused only a small amount of shifting of the system resonance frequencies in the rotational DOFs. This is due to fact that the characteristic frequencies of the maglev system in the rotational DOFs are approximately one order of magnitude higher than the poles of the sensing system. The effects of the sensing system non-linearity have much less impact on the overall system response at this relatively high frequency (about 10Hz). Therefore, Figure 8.8 displays a minor resonance frequency shift and no tendency of system instability. Figure 8.8 also shows that the skyhook damping system has achieved larger peak response reduction in the γ direction compared to the α and β directions. This is simply because the floater has a significantly lower moment of inertia (see Table 4.1) in the γ direction than in the α and β directions. The PID controller gains for stabilising the maglev in the γ direction are also significantly smaller.

In general, the proposed skyhook damping system has practically demonstrated its effectiveness in attenuating the isolator resonance response in all six DOFs. Vibration transmissibilities were also reduced at higher frequencies in all six DOFs with moderate skyhook damping coefficients. The transmissibility measurements showed the tendency of system instability with excessive damping coefficients, which was primarily due to the undesirable non-linearity of the velocity sensing system.

Chapter 9

Conclusions and Future Research

9.1 Summary of thesis

The research presented in this thesis aimed to investigate the possibility of developing a 6-DOF vibration isolation solution based on a quasi-zero stiffness maglev system. The proposed solution was expected to provide low stiffness payload support in 6-DOF with a static magnetic force balancing the payload weight. Hence the trade-off in the traditional isolator designs between vibration isolation and payload capacity was avoided in the proposed maglev based vibration isolation approach.

In this thesis, the theoretical background of the proposed maglev vibration isolator was firstly discussed, which demonstrated how the maglev based design can achieve quasi-zero stiffness levitation in the vertical direction and zero stiffness in the remaining five DOFs while still generating a static variable payload supporting force in the vertical direction. Modelling of the proposed maglev isolator was also presented, from which the cross coupling effects in the maglev system were explored. Following the theoretical background, a physical design realisation of the proposed physical maglev vibration isolation system was presented. The active control systems

Chapter 9 Conclusions and Future Research

necessary to enable the operation of the vibration isolator were also presented, followed by the proposition of a 6-DOF active skyhook damping system for attenuating the peak response of the isolator and reducing vibration transmissibility in a broad range of frequencies. The fully integrated vibration isolation system was tested on a specially designed vibration excitation platform. The vibration isolation performance of the maglev isolator was presented in Chapter 8 for various combinations of control system parameters.

9.1.1 Theoretical background

A novel magnetic levitation system was proposed as a solution for isolating vibration. Both schematic and mathematical models of the proposed maglev system were presented and discussed. A method for modelling the magnetic forces and torques in 3D was demonstrated, which forms the basis of the subsequent analysis on levitation stiffness of the maglev in six DOFs.

In the vertical direction, the maglev system was theoretically demonstrated to be able to achieve quasi-zero levitation stiffness in the nominal operation condition. It was also shown that the static magnetic forces in the vertical direction generated by the two pairs of permanent magnets are adjustable by changing the magnet separations. It was proven that, when the payload weight is supported using this static magnetic force, the maglev system is able to realise quasi-zero stiffness levitation in the vertical direction while maintaining a constant payload supporting force. Therefore, the proposed maglev design allows vibration isolation and payload support to be addressed concurrently.

It was also theoretically proven that the proposed maglev system has zero stiffness in the other five DOFs. The force and torque analysis showed that while the maglev isolator was under nominal operation condition, floater motion in the X, Y, α , β and γ directions do not result in forces/torques in the corresponding DOFs. Therefore, the maglev has zero levitation stiffness in these five DOFs. It was also observed that cross coupling exists between the translational and rotational DOFs of the maglev system. Floater motion in the X and Y directions creates torques in the β and the α directions

respectively, and rotations in the α and β directions result in forces in the Y and X directions respectively. Although these cross coupling effects are not desirable during the normal operation, they were proven to have non-significant impacts on the vibration isolation performance of the maglev isolator. In addition, the cross coupling characteristics of the maglev were utilised to develop an adaptive-passive payload support system to balance the static force and torque inputs from the payload, which was demonstrated in Chapter 5.

9.1.2 Design of the mechanical and control systems

In this research, a physical maglev isolator was designed and built based on the quasi-zero/zero stiffness levitation theories. The design consisted of four major components: the maglev system to realise quasi-zero/zero stiffness levitation, the magnet position control unit for adjusting the separations between the magnets, the sensing system for monitoring the floater position in 6-DOF, and the 6-DOF actuation system for maglev stabilisation and active skyhook damping.

This thesis also presented the unique control systems designed to enable the operation of the maglev isolator. The sub-systems included in the controller design were: the maglev stabilisation controller, which was designed to maintain a steady levitation position; the adaptive-passive payload support controller for autonomously adjusting the payload supporting forces and torques to balance the static payload inputs; and the autonomous maglev tuning system designed to maintain quasi-zero vertical levitation stiffness. Details of these sub-system designs were discussed in Chapter 5. An active vibration control system was also proposed in Chapter 7 to achieve 6-DOF skyhook damping for reducing the peak responses and vibration transmissibilities of the isolator. A hybrid geophone filtering method was designed to place the poles of the geophone sensing system such that the usable flat response bandwidth of the geophones was extended from 10 Hz down to approximately 1Hz. Performance of the hybrid filtering system was demonstrated using the measured frequency responses of the filter system.

9.1.3 Performance of the maglev vibration isolator

The performance of the proposed maglev vibration isolator was examined practically in two major aspects: the performance of the isolator sub systems and the external vibration transmissibilities of the maglev isolator.

Isolator sub systems

In order to ensure accurate assessment of the performance of the proposed vibration isolator, the performance of the system electronic components were firstly tested to identify the characteristics of the hardware. The electrical noise and frequency response of the laser sensors were examined. The results showed that the electrical noise of the laser sensors had approximately the same magnitude as the sensor resolution claimed by the manufacturer, and the sensors behaved linearly within the 0-200Hz bandwidth of interest for active feedback control. The sensitivity and frequency response of the actuation system was examined with different amplifier settings, and it was discovered that the actuation system could achieve ± 3 dB linearity within the 0-200Hz range when the amplifier was set in the output current regulation mode. The internal structural vibration modes of the floater were obtained using a 3D laser vibrometer. Two resonant modes (at 164Hz and 199Hz) were identified below 200Hz, which could potentially degrade the system performance when excited by the active control signals. Possible solutions to this problem were suggested in Chapter 6 such as stiffening the floater structure or applying notch filters in the active loops. However, the impact of these resonant modes was not found to significantly degrade the performance of the system, so no modifications to the floater structure were undertaken.

With the knowledge of the behaviour of the system components, performance of the sub control systems were examined. The proposed maglev stability control system was assessed in terms of its self-induced vibration for the low gain mode, and position command tracking for the high gain mode. In the low gain mode, the self-induced vibration level of the stability control system was measured to be below the VC-E threshold, which indicated that the proposed maglev system is applicable to the most

9.1 Summary of thesis

demanding vibration sensitive equipment; and in the high gain mode, excellent position command tracking ability was demonstrated to guarantee a steady and accurate levitation position when the adaption processes of the controller (adaptive-passive payload support and maglev auto-tuning) are in progress.

The controller performance for the proposed adaptive-passive payload support system was examined by assessing the effectiveness of the adaption process on supporting an added mass or payload with both resultant force and torque inputs. The controller demonstrated the successful transition from payload support using electromagnetic forces to forces generated by the permanent magnets. The adaptive-passive payload support controller reduced the maglev energy consumption from 45W to less than 1W for levitating a 6.693kg payload, achieving a 97.8% power reduction compared to the pre-adaption energy consumption. The performance of the maglev auto-tuning controller was also assessed. The auto-tuning controller design demonstrated its effectiveness by accurately (approximately 0.1mm error) restoring the quasi-zero vertical levitation stiffness from a manually offset levitation position.

Transmissibility of the maglev isolator

The transmissibilities of the isolator were measured in 6-DOF using a purpose built vibration excitation platform. The un-damped resonances of the proposed design were shown to be at 2.9Hz, 3Hz and 1.8Hz in the X, Y and Z directions, and 9.5Hz, 9.5Hz and 9Hz in the α , β and γ directions. These performance measures are comparable to the top of the range vibration isolation devices that are commercially available on the market. The transmissibility measurements also included cross transmissibilities between the orthogonal DOFs of the isolator. The cross-coupling behaviours observed from the experimental results were consistent with ones derived from the theory.

The effectiveness of the skyhook damping system was assessed by measuring the vibration transmissibilities with various skyhook damping coefficients. The theoretical system responses with the skyhook damping system were derived in six DOFs, and the results were presented along with the experimentally measured vibration transmissibilities. The results showed that the added inertial damping effects

Chapter 9 Conclusions and Future Research

not only reduced the peak response of the isolator, but also reduced the system resonance frequency due to the double 1Hz poles existing in the dynamics of the floater velocity sensors. In general, the proposed design of the skyhook damping system demonstrated its effectiveness at reducing the vibration transmissibilities around the isolator resonance frequencies.

9.2 Conclusion

The research presented in this thesis has demonstrated that it is possible to develop a high performance 6-DOF vibration isolator based on the proposed quasi-zero stiffness maglev system. The theories and experimental validations presented in this thesis revealed the potential of the proposed maglev system as a 6-DOF vibration isolation approach. It was demonstrated that the maglev system is able to practically realise inherent quasi-zero stiffness levitation in the vertical direction while providing a static payload supporting force, and the inherent stiffness of the levitation in the remaining five DOFs are also zero. Although other quasi-zero stiffness isolator designs have been reported in the literature, the vast majority of them are only able to provide quasi-zero stiffness in one DOF.

It was shown that a stabilisation system is necessary to enable the operation of the proposed maglev system as a vibration isolator. Both the theoretical and experimental results of the isolator transmissibilities showed that, with the added stabilisation system, there exists finite levitation stiffness in all six DOFs. Although the maglev system has inherent quasi-zero/zero stiffness, the overall stiffness of the maglev system is also dominated by the added controller stiffness. As discussed previously, the controller stiffness may be reduced by improving the hardware performance and the controller design, and the overall levitation stiffness can approach the inherent stiffness behaviour of the maglev system, which also indicates the potential of the proposed maglev isolator.

In this research, adaptive-passive payload support and maglev auto-tuning were investigated as performance optimisation methods for the maglev system. Control methods were proposed for automating the optimisation processes. Experimental

9.2 Conclusion

results demonstrated the effectiveness of the proposed controller designs for the automated payload balancing and quasi-zero stiffness restoration. The cross coupling effects in the maglev system were successfully utilised to balance the force and torque inputs from the payload in five DOFs (X , Y , Z , α and β).

This research investigated the theories and designs of a single maglev vibration isolator. Ideally, multiple units of the proposed isolator may be used together to realise an isolation platform such as shown in Figure 4.5. The control methods and system designs to optimise the performance of the proposed maglev isolator incorporated in a multi-isolator system are yet to be investigated.

The major significance of the proposed vibration isolation method is its ability to passively support the payload weight with quasi-zero/zero stiffness in all six DOFs. Therefore, the proposed maglev system design may also be used in other vibration isolators as an add-on mechanism for payload weight support, and the addition of the maglev system results in minimal influences to the stiffness behaviour of the original isolator due to the low stiffness characteristics of the maglev system. With the added maglev payload weight support, a reduction can be achieved in the stiffness of the isolator that was originally necessary for supporting the payload weight.

The developed maglev vibration isolator can also be tuned to work as a precision positioning system. The command following test of the maglev stability controller in the high gain mode demonstrated the excellent command tracking ability of the design. In addition, the adaptive-passive payload support ensures the payload can be levitated with only minimal energy consumption, and the floater levitation pose control gives the positioning system 6-DOF mobility.

9.3 Future research

The research presented in this thesis leads to a number of potential future research topics for further investigation, which are discussed in the following sections.

9.3.1 Non-linear controller structure for maglev system stabilisation

In order to control the levitation stiffness and damping of the maglev system directly, linear PID controllers were used in this research to stabilise the maglev. According to Section 5.2.2, the vertical controller stiffness for stabilising the levitation is required to be large that the overall system stiffness is positive. The current stabilisation controller design in this research has a lower stiffness limit that is theoretically determined by the boundary of the required stabilisation zone (Figure 5.2). However, the required controller stiffness reduces when the floater is closer to the nominal operation position. The linear PID controllers induce the same stiffness for all vertical floater displacements from the nominal operation position, which unnecessarily increased the levitation stiffness for smaller floater displacements. This effect stiffens the isolator in the vertical direction, and degrades its vibration isolation performance. Therefore, one way to further improve the performance of the proposed maglev vibration isolation method is to apply nonlinear control methods to stabilise the levitation, which are potentially able to stabilise the maglev system in the vertical direction with minimum stiffness according to the real-time floater position.

It was discussed in Section 3.7 that the separation between the magnet pairs is actively adjusted to adapt changes in payload weight. The adjustments in magnet separation lead to variation in the stiffness gradient of the magnetic forces. Therefore, in order to maintain the controller induced stiffness at a minimal value, the parameters in the stabilisation controller need to be optimised according to the real-time separation between the magnets. The continuation of this research should include development of an adaptive control algorithm which optimises the controller gains according to the real-time payload condition.

The minimum controller stiffness for stabilising the maglev system is also influenced by the signal noise from the sensors. One potential solution to reduce the controller stiffness is employing an observer based control method to stabilise the maglev system. Future work may also include investigations of observer based control techniques for stabilising the proposed quasi-zero stiffness maglev system.

9.3.2 Centralised control for multi-isolator applications

As shown in Figure 4.5, multiple units of the proposed maglev isolator can be used together to create a vibration isolation table. The load connecting beams included in the mechanical isolator design can also be used to realise 6-DOF vibration isolation of any system by connecting multiple isolators to the target system. However, the current maglev stability controller is only designed for a single isolator system. A centralised controller structure will have to be developed to optimise the performance of the isolation system when multiple isolators are used together. The future works on the centralised controller design will also have to identify and address the issues related to adaptive-passive payload support and autonomous magnet position tuning in a multi-isolator system.

9.3.3 Passive maglev stabilisation

The proposed maglev vibration isolator uses an active control system to maintain stability of the levitation. Although the active control enables easy configuration to isolator parameters (such as stiffness and damping coefficient), it unavoidably increases the system complexity and cost. The increased system complexity and cost limit the commercial value of the proposed solution. The active maglev stability control used in the design is based on PID control structures, whose control effort, in theory, is fully realisable through passive mechanisms. Future research may generate passive stabilisation systems that can replace the current active maglev stability controller, which will broaden the applicability of the proposed maglev vibration isolator.

References

Acuity AR200-12 laser sensor specifications. Accessed on 20/06/2013.

URL: http://www.acuitylaser.com/products/item/ar200-laser-measurement-sensor?lid=9?lead_leadid=8293

Ahmadian, M., Song, X., Southward, S. C., 2004. No-jerk skyhook control methods for semiactive suspensions. *Journal of Vibration and Acoustics*, 126(4), 580-584.

Ahmed Ahu, H., Preumont, A., 2011. Multi-axis vibration isolation using different active techniques of frequency reduction. *Journal of Vibration & Control*, 17(5), 759-768.

Akoun, G., Yonnet, J. P., 1984. 3D analytical calculation of the forces exerted between two cuboidal magnets. *IEEE Transactions on Magnetics*, 20(5), 1962-1964.

Alabuzhev, P., Gritchin, A., Kim, L., Migirenko, G., Chon, V., Stepanov, P., 1989. *Vibration Protecting and Measuring Systems with Quasi-Zero Stiffness*, Hemisphere Publishing, New York, 1989.

Allag, H., Yonnet, J.-P., 2009. 3-D Analytical calculation of the torque and force exerted between two cuboidal magnets. *IEEE Transactions on Magnetics*, 45(20), 3969-3972.

Alleyne, A., 1995. Nonlinear adaptive control of active suspensions. *IEEE Transactions on Control Systems Technology*, 3(1), 94-101.

Anderson, E. H., How, J. P., 1997. Active vibration isolation using adaptive feedforward control. In: *Proceedings of American Control Conference*, 3, 1783-1788, Albuquerque, NM.

Araki, Y., Asai, T., Kimura, K., Maezawa, K., Masui, T., 2013. Nonlinear vibration isolator with adjustable restoring force. *Journal of Sound and Vibration*, 332(23), 6063-6077.

Azadi, M., Behzadipour, S., Faulkner, G., 2011. Performance analysis of a semi-active mount made by a new variable stiffness spring. *Journal of Sound and Vibration*, 330(12), 2733-2746.

Balas, M. J., 1978. Active control of flexible systems. *Journal of Optimization Theory and Applications*, 25(3), 415-436.

References

Balas, M. J., Canavin, J. R., 1977. An active modal control system philosophy for a class of large space structures. In: Proceedings of the First VPI & SU/AIAA Symposium on Dynamics and Control of Large Flexible Spacecraft, Blacksburg, Virginia, 271–285.

Benassi, L., Elliott, S. J., 2004. Active vibration isolation using an inertial actuator with local displacement feedback control. *Journal of Sound and Vibration*, 278(4-5), 705-724.

Boehm J., Gerber R., Kiley N. R. C., 1993. Sensors for magnetic bearings. *IEEE Transactions on Magnetics*, 29(6), 2962-2964.

Brennan, M. J., Ananthaganeshan, K. A., Elliott, S. J., 2007. Instabilities due to instrumentation phase-lead and phase-lag in the feedback control of a simple vibrating system. *Journal of Sound and Vibration*, 304(3-5), 466-478.

Berry, M. V., Geim, A. K., 1997. Of flying frogs and levitrons. *European Journal of Physics*, 18(1997), 307-313.

Brüel & Kjær type 4381 accelerometer specifications. Accessed on 20/06/2013.

URL: <http://www.bksv.com/Products/transducers/vibration/accelerometers/accelerometers/4381.aspx?tab=specifications>

Carrella, A., Brennan, M. J., Waters, T. P., 2007. Static analysis of a passive vibration isolator with quasi-zero-stiffness characteristic. *Journal of Sound and Vibration*, 301(3-5), 678-689.

Carrella, A., Brennan, M. J., Waters, T. P., Shin, K., 2008. On the design of a high-static-low-dynamic stiffness isolator using linear mechanical springs and magnets. *Journal of Sound and Vibration*, 315(3), 712-720.

Chetouani, H., Jeandey, C., Haguet, V., Rostaing, H., Dieppedale, C., Reyne, G., 2006. Diamagnetic Levitation With Permanent Magnets for Contactless Guiding and Trapping of Microdroplets. *IEEE Transactions on Magnetics*, 42(10), 3557-3559.

Choi, K. B., Cho, Y. G., Shinshi, T., Shimokohbe, A., 2003. Stabilization of one degree-of-freedom control type levitation table with permanent magnet repulsive forces. *Mechatronics*, 13(6), 587-603.

References

- Clarence, W. S., 2005. *Vibration and Shock Handbook*, Taylor & Francis Group, Boca Raton.
- Cohen, R., Lide, D. R., Trigg, L. G., Cohen, E. R., 2003. *AIP physics desk reference*, third ed., New York, Berlin.
- Conover, W., 1956. Fighting noise with noise. *Noise Control*, 92(2), 78–82.
- Dange, Y. K., Gore, S. R., 1978. Analysis of a nonlinear vibration isolator with the help of an analog computer. *Indian Journal of Technology*, 16, 282-285.
- Den Hartog, J. P., 1931. Forced vibrations with constrained Coulomb damping and viscous friction. *Transactions of the ASME Advance Papers*, 107-115.
- Ding, C., Janssen, J. L. G., Damen, A. A. H., van den Bosch, P. P. J., 2010. Modeling and control of a 6-DOF contactless electromagnetic suspension system with passive gravity compensation. In: *Proceedings of the XIX international Conference on Electrical Machines*, Rome.
- Dspace DS1103 PPC controller specifications. Accessed on 20/06/2013.
URL: <https://www.dspace.com/en/pub/home/products/hw/singbord/ppconbo.cfm>
- Earnshaw, S., 1842. On the nature of the molecular forces which regulate the constitution of the luminiferous ether. *Transactions of the Cambridge Philosophical Society*, 7, 97–112.
- Elliott, S. J., Serrand, M., Gardonio, P., 2001. Feedback stability limits for active isolation systems with reactive and inertial actuators. *Transactions of the ASME, Journal of Vibration and Acoustics*, 123(2), 250–261.
- Fahy, F., Walker, J., 1998. *Fundamentals of Noise and Vibration*. E & FN Spon, London and New York.
- Frizenschaf, Y., Giles, S., Miller, J., Pitman, T., Stapleton, C., Cazzolato, B., Robertson, W., 2011. Development of a magnetic levitation vibration isolator using inclined permanent magnet springs. In: *Proceedings of Acoustics 2011*, Gold Coast, Australia.
- Furlani, E. P., 1993. A formula for the levitation force between magnetic disks. *IEEE Transactions on Magnetics*, 29(6), 4165-4169.

References

Fuller, C. R., Elliott, S. J., Nelson, P. A., 1996. *Active Control of Vibration*. Academic Press Ltd, London.

Futami, S., Kyura, N., Hara, S., 1983. Vibration absorption control of industrial robots by acceleration feedback. *IEEE Transactions on Industrial Electronics*, IE-30(3), 299-305.

Gentili, L., Marconi, L., 2003. Robust nonlinear disturbance suppression of a magnetic levitation system. *Automatica*, 39(4), 735-742.

Goh, C. J., Caughey, T. K., 1985. On the stability problem caused by finite actuator dynamics in the collocated control of large space structures. *International Journal of Control*, 41(3), 787–802.

Gordon, G. C., 1991. Generic criteria for vibration-sensitive equipment. *SPIE Proceedings*, Volume 1619, Optics, and Metrology, 71.

Hasirci, U., Balikci, A., Zabar, Z., Birenbaum, L., 2011. A novel magnetic-levitation system: Design, implementation, and nonlinear control. *IEEE Transactions on Plasma Science*, 39(1), 492-497.

Harris, C.M., 1996. *Shock and Vibration Handbook*. Fourth ed., McGrawHill, New York.

Hirani, H., Samanta, P., 2007. Hybrid (hydrodynamic + permanent magnetic) journal bearings. In: *Proceedings of the Institution of Mechanical Engineers, Part J: Journal of Engineering Tribology*, 126(8), 881-891.

Hodges, T., 1989. The active simulation and modification of structural frequency response, PhD Thesis, University of Southampton, UK.

Hoque, M. E., Takasaki, M., Ishino, Y., Mizuno, T., 2006. Development of a three-axis active vibration isolator using zero-power control. *IEEE/ASME Transactions on Mechatronics*, 11(4), 462-470.

Howard, C. Q., 1999. Active isolation of machinery vibration from flexible structures. Ph.D. thesis, Department of Mechanical Engineering, The University of Adelaide, Australia.

Howard, C. Q., Hansen, C. H., 1997. Active isolation of a vibrating mass. *Acoustics Australia*, 25(2), 65–67.

- Ibrahim, R. A., 2008. Recent advances in nonlinear passive vibration isolators. *Journal of Sound and Vibration*, 314(3), 371-452.
- Ikezoe, Y., Hirota, N., Nakagawa, J., Kitazawa, K., 1998. Making water levitate. *Nature*, 393, 749-750.
- Janssen, J. L. G., Paulides, J. J. H., Compter, J. C., Lomonova, E. A., 2010. Three-dimensional analytical calculation of the torque between permanent magnets in magnetic bearings. *IEEE Transactions on Magnetics*, 46(6), 1748-1751.
- Janssen, J. L. G., Paulides, J. J. H., Lomonova, E. A., 2012. Study of magnetic gravity compensator topologies using an abstraction in the analytical interaction equations. *Progress in Electromagnetics Research, PIER* 128, 75-90.
- Janssen, J. L. G., Paulides, J. J. H., Lomonova, E. A., Delinchant, B., Yonnet, J. P., 2013. Design study on a magnetic gravity compensator with unequal magnet arrays. *Mechatronics*, 23(2), 197-203.
- Jenkins, M. D., 1989. Active control of periodic machinery vibrations. PhD thesis, University of Southampton.
- Jiang, L., Stredulinsky, D., Szabo, J., Chernuka, M. W., 2002. Numerical characterization of nonlinear stiffness properties of pre-stressed vibration isolation mounts. *Canadian Acoustics: Acoustique Canadienne*, 30, 70-71.
- Jia, P., Liu, W., Kan, J., 2010. Study on fuzzy feed-forward-feedback control of two-layer vibration isolation system based on voice coil motor. In: *Proceedings of the 29th Chinese Control Conference*, 2619-2623. In Mandarin.
- Kim, S.M., Elliott, S. J., Brennan, M. J., 2001. Decentralised control for multichannel active vibration isolation. *IEEE Transactions on Control Systems Technology*, 9(1), 93-100.
- Khamesee, M. B., Shamel, E., 2005. Regulation technique for a large gap magnetic field for 3D non-contact manipulation. *Mechatronics*, 15(9), 1073-1087.
- Krishna, Y., Shrinivasa, U., 2009. Semi-active vibration isolation using a near zero-spring-rate device: steady state analysis of a single-degree-of-freedom model. In: *Proceedings of the Institution of Mechanical Engineers, Part D: Journal of Automobile Engineering*, 223, 1395-1403.

References

Kwak, S. K., Washington, G., Yedavalli, R. K., 2002. Acceleration feedback-based active and passive vibration control of landing gear components. *Journal of Aerospace Engineering*, 15(1), 1-9.

Lang, Z. Q., Jing, X. J., Billings, S. A., Tomlinson, G. R., Peng, Z. K., 2009. Theoretical study of the effects of nonlinear viscous damping on vibration isolation of sdof systems. *Journal of Sound and Vibration*, 323(1-2), 352-365.

Levitron, Home page. The amazing anti-gravity top. Accessed on 25/11/2012.
URL: <http://www.levitron.com/>.

Li, H., Goodall, M., 1999. Linear and nonlinear skyhook damping control laws for active railway suspensions. *Control Engineering Practice*, 7(7), 843-850.

LIGO Scientific Collaboration, 2012. Advanced LIGO – The next step in gravitational wave astronomy. Accessed on 06/12/2012.
URL <https://www.advancedligo.mit.edu/>

Liu, X., Huang, X., Hua, H., 2013. On the characteristics of a quasi-zero stiffness isolator using Euler buckled beam as negative stiffness corrector. *Journal of Sound and Vibration*, 322(14), 3359-3376.

Liu, Y., Matsuhisa, H., Utsuno, H., 2008. Semi-active vibration isolation system with variable stiffness and damping control. *Journal of Sound and Vibration*, 313(1–2), 16-28.

Liu, Y., Waters, T. P., Brennan, M. J., 2005. A comparison of semi-active damping control strategies for vibration isolation of harmonic disturbances. *Journal of Sound and Vibration*, 280(1-2), 21-39.

Maxon servo-amplifier LSC 30/2 specifications. Accessed on 20/06/2013.
URL: <http://maxonmotor.exportpages.com/productdetail/1065726121-1.htm>

Meirovitch, L., 1986. *Elements of Vibration Analysis*. McGraw-Hill, Inc., New York

Miller, H., 1995. Transit noise and vibration impact assessment. Final Report, U.S. Department of Transportation, Washington, D. C.

Mizuno, T., Takasaki, M., Kishita, D., Hirakawa, K., 2007. Vibration isolation system combining zero-power magnetic suspension with springs. *Control Engineering Practice*, 15(2), 187-196.

References

- Mizuno, T., Hoque, M. E., Takasaki, M., Ishino, Y., 2006. Development of a six-axis hybrid vibration isolation system using zero-power control. In: Proceedings of the 45th IEEE Conference on Decision & Control, 6531-6536, San Diego, CA.
- Mizuno, T., Toumiya, T., Takasaki, M., 2003. Vibration isolation system using negative stiffness. JSME International Journal Series C, Mechanical Systems, Machine Elements and Manufacturing, 46(3), 807-812.
- National Instruments, 2006. Calculation of interface resolution. Accessed on 15/08/2013.
URL: <http://www.ni.com/white-paper/4806/en/>
- Nagaraj, H. S., 1988. Investigation of magnetic fields and forces arising in open-circuit-type magnetic bearings. Tribology Transactions, 31(2), 192-201.
- Nagaya, K., Ishikawa, M., 1995. A noncontact permanent magnet levitation table with electromagnetic control and its vibration isolation method using direct disturbance cancellation combining optimal regulators. Transactions on Magnetics, 31(2), 885-896.
- Nakra, B. C., 1998. Vibration control in machines and structures using visco-elastic damping. Journal of Sound and Vibration, 211(3), 449-465.
- Nayfeh, T. A., Emaci, E., Vakakis, A. F., 1997. Application of nonlinear localization to the optimization of a vibration isolation system. American Institute of Aeronautics and Astronautics Journal, 35, 1378-1386.
- Neild, S., Wagg, D., 2010. Nonlinear vibration with control for flexible and adaptive structures. 1st Ed. Springer, Netherlands.
- Olson, H. F., 1956. Electronic control of noise, vibration and reverberation. Journal of the Acoustical Society of America, 28(5), 966-972.
- Platus, D. L., 1991. Negative-stiffness-mechanism vibration isolation systems, Vibration Control in Microelectronics. Optics and Metrology, 1619 (1991), 44-54.
- Preumont, A., 2002. Vibration Control of active structures: an introduction. Kluwer Academic Publishers, Dordrecht.
- Preumont, A., Francios, A., Bossens, F., Abu-Hanieh, A., 2001. Force feedback versus acceleration feedback in active vibration isolation. Journal of Sound and Vibration, 257(4), 605-613.

References

- Preumont, A., Horodinca, M., Romanescu, I., de Marneffe, B., Avraam, M., Deraemaeker, A., Bossens, F., Abu Hanieh, A., 2007. A six-axis single-stage active vibration isolator based on Stewart platform. *Journal of Sound and Vibration*. 300(3-5), 644-661.
- Ravaud, R., Lemarquand, G., Lemarquand, V., 2009. Force and stiffness of passive magnetic bearings using permanent magnets. *IEEE Transactions on Magnetics*, 45(7), 2996-3002.
- Rivin, I. E., 2003. *Passive Vibration Isolation*. ASME Press, New York.
- Robertson, W., Wood, R., Cazzolato, B., Zander, A., 2006. Zero-stiffness magnetic spring for active vibration isolation. In: *Proceedings of Active 2006*, Adelaide, Australia.
- Robertson, W., Wood, R., Cazzolato, B., Zander, A., 2010. Maximising the force between two cuboid magnets. *Magnetic letters*, 1(2010), 9000102.
- Robertson, W., Cazzolato, B., Zander, A., 2011. A simplified force equation for coaxial cylindrical magnets and thin coils. *IEEE Transactions on Magnetics*, 47(8), 2045-2049.
- Robertson, W., Wood, R., Cazzolato, B., Zander, A., 2012. Theoretical analysis of a non-contact spring with inclined permanent magnets for load-independent resonance frequency. *Journal of Sound and Vibration*, 331(6), 1331-1341.
- Robertson, W., Kidner, M. R. F., Cazzolato, B., Zander, A., 2009. Theoretical design parameters for a quasi-zero stiffness magnetic spring for vibration isolation. *Journal of Sound and Vibration*, 326(1/2), 88-103.
- Robertson, W., Matlab code on calculation of the magnetic forces and torques between cubic magnets, Accessed on 28/05/2010.
URL: <https://github.com/wspr/magcode/tree/master/matlab>.
- Robertson, W., Matlab code on calculation of the magnetic forces between cylindrical magnets, Accessed 30/09/2011.
URL: <https://github.com/wspr/magcode/tree/master/matlab>.
- Ross, C. F., Scott, J. F., Sutcliffe, S. G. C., 1989. Active control of vibration. US Patent No: 5,433,422.
- SENSOR SM-24 Geophone specifications. Accessed on 20/06/2013.

URL: <http://www.geophone.com/techpapers/SM-24%20Brochure.pdf>

Serrand, M., Elliott, S. J., 2000. Multichannel feedback control for the isolation of base-excited vibration. *Journal of Sound and Vibration*, 234(4), 681–704.

Shaw, A. D., Nelid, S. A., Wagg, D. J., Weaver, P. M., Carrella, A., 2013. A nonlinear spring mechanism incorporating a bistable composite plate for vibration isolation. *Journal of Sound and Vibration*, In Press.

Simon, M. D., Heflinger, O. L., Ridgway, S. L., 1997. Spin stabilized magnetic levitation. *American Journal of Physics*, 65(4), 286-292.

Simon, M. D., Geim, A. K., 2000. Diamagnetic levitation: Flying frogs and floating magnets. *Journal of Applied Physics*, 87(9), 6200-6204.

Soong, T. T., Dargush, G. F., 1997. *Passive energy dissipation in structural engineering*. Wiley, New York.

Stephens, M., Saulson, P., Kovalik, J., 1990. A double pendulum vibration isolation system for a laser interferometric gravitational wave antenna. *Review of Scientific Instruments*, 62(4), 924-932.

Sun, J., Feng, J., 2011. A novel structure of permanent-magnet-biased radial hybrid magnetic bearing. *Journal of Magnetism and Magnetic Materials*, 323(2), 202-208.

Sutcliffe, S. G. C., Eatwell, G. P., Hutchins, S. M., 1989. Active control of vibration. UK Patent No: GB 2,222,657.

Su, Y. X., Zheng, C. H., Sun, D., Duan, B. Y., 2004. An enhanced fuzzy PD controller with two discrete nonlinear tracking differentiators. *IEEE Proceedings on Control Theory and Applications*, 151, 675-682.

Tanaka, N., Kikushima, Y., 1988. Optimal design of active vibration isolation system. *Transactions of the ASME, Journal of Vibration, Acoustics, Stress and Reliability in Design*, 110, 42–48.

Tao, J., Mak, C. M., 2006. Effect of viscous damping on power transmissibility for the vibration isolation of building services equipment. *Applied Acoustics*, 67(8), 733-742.

References

- Trimboli, M. S., Wimmel, R., Breitbach, E. J., 1994. Quasi-active approach to vibration isolation using magnetic springs. *Smart Structures and Materials 1994: Passive Damping* C. D. Johnson, Ed., SPIE, 2193(1), 73-83.
- Vér, L. I., Beranek, L. L., 2006. *Noise and Vibration Control Engineering*. Wiley, USA.
- Verma, S., Kim, W. J., Shakir, H., 2004. Multi-axis Maglev nanopositioner for precision manufacturing and manipulation applications. In: *Conference Record of the 2004 IEEE Industry Applications Conference, 39th IAS Annual Meeting*, 3(3-7), 2084- 2091.
- Wai, R. J., Lee, J. D., 2008. Backstepping-based levitation control design for linear magnetic levitation rail system. *IET Control Theory Application*, 2(1), 72–86.
- Wang, J., Wang, S., Deng, C., Zeng, Y., Song, H., Huang, H., 2005. A superhigh speed HTS maglev vehicle. *International Journal of Modern Physics B*: 19(1-3), 399-401.
- Winterflood, J., Blair, D. G., Slagmolen, B., 2002. High performance vibration isolation using springs in Euler column buckling mode. *Physics Letters A*, 300(2-3), 122-130.
- Xu, D., Yu, Q., Zhou, J., Bishop, S. R., 2013. Theoretical and experimental analyses of a nonlinear magnetic vibration isolator with quasi-zero-stiffness characteristic. *Journal of Sound and Vibration*, 332(14), 3377-3389.
- Yasuda, M., Osaka, T., Ikeda, M., 1996. Feed-forward control of a vibration isolation system for disturbance suppression. In: *Proceedings of the 35th IEEE Conference on Decision and Control*, 1229-1233.
- Yang, Z. J., Fukushima, Y., Kanae, S., Wada, K., 2009. Robust nonlinear output-feedback control of a magnetic levitation system by K-filter approach. *IET Control Theory and Applications*, 3, 852-864.
- Yi, K., Song, B. S., 1999. A new adaptive sky-hook control of vehicle semi-active suspensions. In: *Proceedings of the Institution of Mechanical Engineers, Part D, Journal of Automobile Engineering*, 213(3), 293-303.
- Yoshimura, T., Isari, Y., Li, Q., Hino, J., 1997. Active suspension of motor coaches using skyhook damper and fuzzy logic control. *Control Engineering Practice*, 5(2), 175-184.

References

- Yu, X., Zhu, S. J., Liu, S. Y., 2006. Nonlinear normal modes for multi-degree-of-freedom nonlinear vibration isolation system. In: Proceedings of the ASME Dynamic Systems and Control Division DSC, Chicago, USA, 1-5.
- Zhou, D. F., Li, J., Hansen, C. H., 2011. Application of least mean square algorithm to suppression of maglev track-induced self-excited vibration. *Journal of Sound and Vibration*, 330(24), 5791-5811.
- Zhou, N., Liu, K., 2010. A tunable high-static-low-dynamic stiffness vibration isolator. *Journal of Sound and Vibration*, 329(9), 1254-1273.
- Zhu, H. W., Tryggvason, B., Piedboeuf, J. C., 2005. On active acceleration control of vibration isolation systems. *Control Engineering Practice*, 14(8), 863-873.
- Zhang, Z., Menq, C. H., 2007. Six axis magnetic levitation and motion control. *IEEE Transactions on Robotics*, 23(2), 196-205.
- Zhu, T., Cazzolato, B., Robertson, W., Zander, A., 2011. The development of a 6 degree of freedom quasi-zero stiffness Maglev vibration isolator with adaptive-passive load support. In: Proceedings of the 15th International Conference on Mechatronics Technology, 1-6, Melbourne.
- Zhu, T., Cazzolato, B., Robertson, W., Zander, A., 2013. Vibration isolation using six degree-of-freedom quasi-zero stiffness magnetic levitation. *Journal of Sound and Vibration*, Manuscript under review.
- Zhu, T., Cazzolato, B., Robertson, W., Zander, A., 2013. Vibration isolation using six degree-of-freedom quasi-zero stiffness magnetic levitation with adaptive-passive payload support and autonomous levitation optimisation. *Mechanical Systems and Signal Processing*, Manuscript under review.
- Zimmerman, D. C., Cudney, H. H., 1989. Practical implementation issues for active control of large flexible structures. *Transactions of the ASME, Journal of Vibration, Acoustics, Stress and Reliability in Design*, 111, 283–289.

Appendices

Appendix A: Inherent instability of passive magnetic levitation

The energy U of a magnetic dipole (which can be considered as a bar type permanent magnet) with a magnetic dipole moment M_i (i represents the three translational directions in a Cartesian coordinate system, X Y and Z, with the coordinates denoted using x , y and z respectively) in a magnetic field strength B_i may be expressed as

$$U = -\mathbf{M} \times \mathbf{B} = -(M_X B_X + M_Y B_Y + M_Z B_Z) . \quad (\text{A.1})$$

The position of the magnetic dipole is only stable when the energy is at the minimum state. The energy is only at minimum when the Laplacian of the energy is greater than zero (Cohen *et al.*, 2003), which is

$$\nabla^2 U = \frac{\partial^2 U}{\partial x^2} + \frac{\partial^2 U}{\partial y^2} + \frac{\partial^2 U}{\partial z^2} > 0 . \quad (\text{A.2})$$

However, for a steady magnetic field and a fixed dipole direction (such as a permanent magnet) both divergence and curl of the field are zero. It can be derived (Cohen *et al.*, 2003) that

$$\frac{\partial^2 U}{\partial x^2} = 0 , \quad \frac{\partial^2 U}{\partial y^2} = 0 , \quad \frac{\partial^2 U}{\partial z^2} = 0 . \quad (\text{A.3})$$

Hence,

$$\nabla^2 U = \frac{\partial^2 U}{\partial x^2} + \frac{\partial^2 U}{\partial y^2} + \frac{\partial^2 U}{\partial z^2} = 0 , \quad (\text{A.4})$$

which shows that in a steady passive magnetic field, the energy state of a magnetic dipole has neither a maximum nor a minimum state. It contradicts the minimum energy state required for a stable levitation. Therefore, it can be concluded that stable magnetic levitation using only passive static magnetic fields is impossible.

Appendix B: Floor vibration in the research laboratory

The floor vibration of the research laboratory, the Vibrations Lab in the School of Mechanical Engineering at the University of Adelaide, was quantified in the three translational directions with a B&K (type 4366) accelerometer. The displacement data was obtained through double integration using a B&K (type 2635) charge amplifier with high-pass filter set at 1Hz. Figure B.1 and Figure B.2 present the vibration displacements of the vibration in the X, Y and Z directions in mm and inches respectively.

Appendices

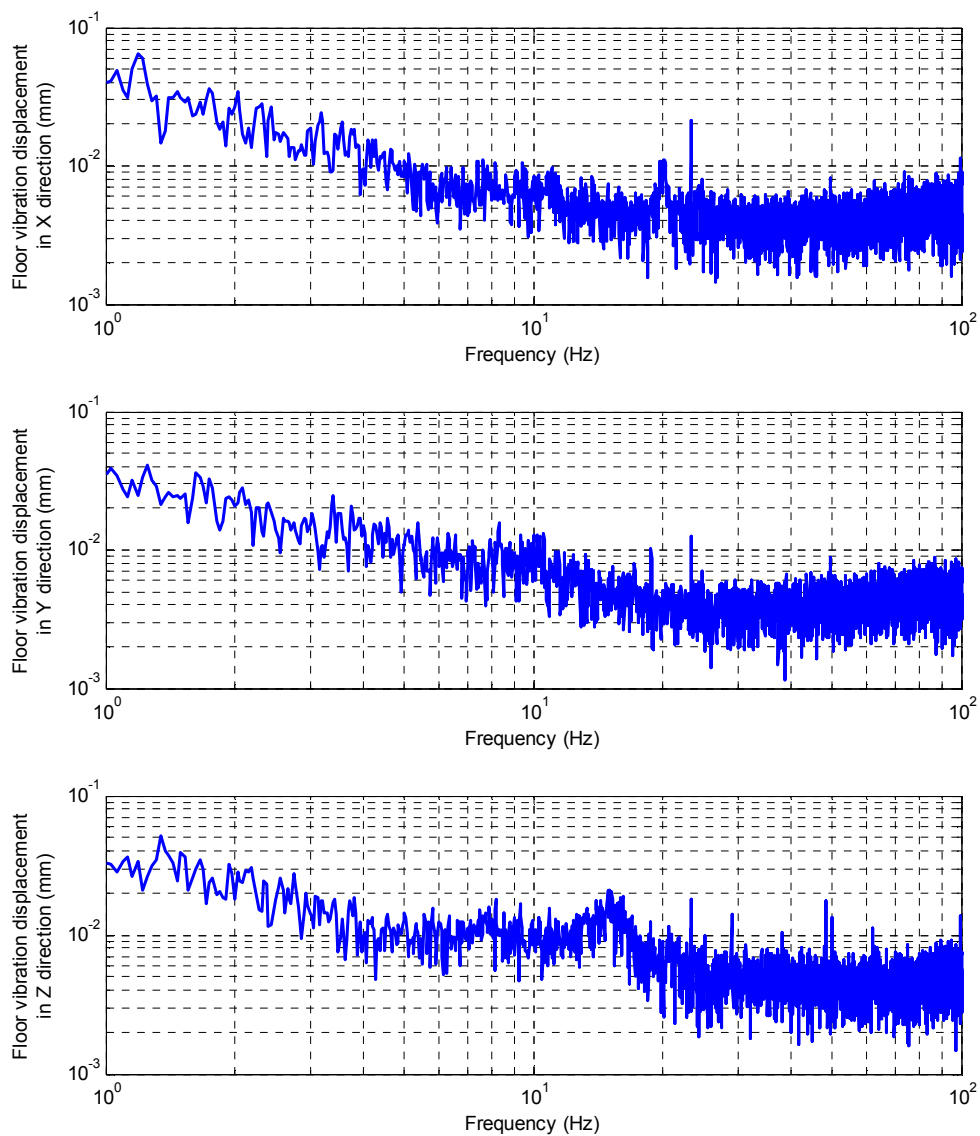


Figure B.1: Displacement of laboratory floor vibration in mm (FFT properties: DC coupled, 128 averages, 3200 lines, Hanning window, 24,000Hz sampling frequency).

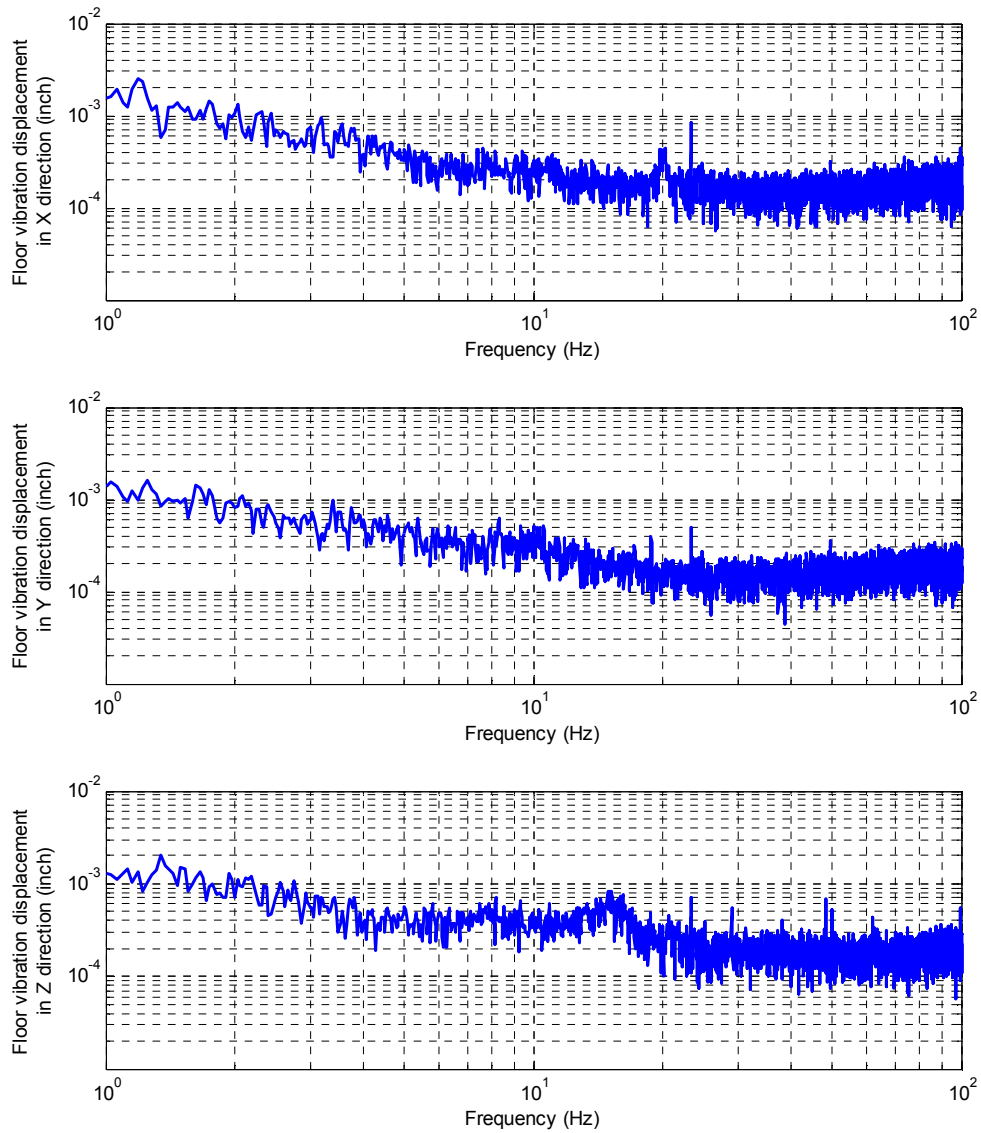


Figure B.2: Displacement of laboratory floor vibration in inch (FFT properties: DC coupled, 128 averages, 3200 lines, Hanning window, 24,000Hz sampling frequency).

Appendix C: Coefficients of the polynomial fitting for maglev force and toque modelling

The coefficients of the pose polynomial used in the polynomial regression shown in Section 3.5.2 are

$K=[$

Column 1 to 8

3.886E-16	1.332E-14	-9.377E-15	4.209E-14	4.967E-15	-8.139E-02	2.271E-15	1.231E-16
7.589E-16	-9.674E-15	1.177E-14	8.777E-15	8.139E-02	4.753E-15	3.593E-15	-7.544E-16
3.913E+01	1.325E-12	-2.014E-13	-9.510E-14	3.992E-13	-1.583E-13	-5.471E-16	-9.212E-03
2.459E-16	2.072E-15	1.693E-02	8.244E-15	-1.458E-15	-3.265E-16	2.869E-16	1.465E-15
-2.394E-15	-1.693E-02	1.381E-15	5.139E-16	-3.869E-16	-2.920E-16	2.390E-16	7.589E-16
0.000E+00							

Column 9 to 16

8.195E-16	-9.234E-16	-8.505E-17	8.498E-17	-3.039E-18	-1.993E-15	-1.835E-16	-9.705E-16
-4.845E-16	1.053E-15	9.041E-17	-8.775E-19	-8.904E-17	9.006E-16	-6.284E-16	-1.077E-15
-9.212E-03	3.321E-02	-5.505E-04	-5.505E-04	-9.358E-17	-7.514E-14	1.570E-14	8.237E-15
7.015E-16	-2.217E-15	3.593E-17	-3.406E-17	-2.080E-18	7.834E-17	-3.975E-06	-6.145E-16
-1.217E-16	-9.579E-17	-1.495E-17	5.642E-18	1.424E-17	3.975E-06	-2.445E-16	-1.271E-16
0.000E+00							

Column 17 to 24

5.298E-19	1.242E-06	-2.427E-17	-6.084E-15	-1.834E-02	-1.222E-16	8.588E-17	-3.847E-18
-1.242E-06	-9.683E-18	7.212E-18	2.803E-15	3.872E-15	-8.302E-17	9.952E-17	-1.033E-16
1.279E-16	6.345E-16	-1.465E-15	-2.876E-13	-3.020E-13	9.931E-17	5.508E-17	8.240E-18
3.175E-18	3.086E-18	-1.500E-18	-2.376E-16	-3.199E-16	-2.920E-17	-1.650E-17	-5.560E-17
9.156E-19	4.713E-19	-1.499E-19	-9.531E-17	1.259E-16	-8.709E-18	3.316E-17	1.825E-18
0.000E+00							

Column 25 to 32

3.242E-16	1.443E-16	-4.435E-16	5.753E-05	8.826E-16	-1.417E-16	-8.671E-17	-6.355E-18
-4.412E-16	-1.668E-16	-1.910E-05	1.340E-16	-3.554E-16	4.742E-16	8.519E-17	1.971E-17
3.504E-15	2.301E-15	-3.204E-14	-1.359E-14	4.954E-14	-2.187E-14	-2.775E-14	-1.177E-15
-3.972E-06	-4.712E-17	-1.645E-17	-6.709E-19	4.781E-17	5.891E-18	3.907E-17	-6.268E-18
3.466E-18	1.092E-17	-6.851E-18	-5.440E-18	9.734E-18	3.972E-06	-2.218E-05	2.548E-07
0.000E+00							

Column 33 to 40

-1.996E-17	1.407E-17	-4.705E-15	4.839E-17	-6.322E-18	-1.652E-18	-1.277E-16	-4.744E-16
3.174E-19	2.166E-18	-1.834E-02	-8.066E-17	-1.229E-16	-5.172E-17	1.411E-16	-5.753E-05
-9.612E-16	-9.306E-16	-2.565E-13	1.253E-16	1.256E-16	9.975E-17	-7.347E-16	-3.214E-14
-7.693E-18	-1.640E-18	-2.192E-16	-2.106E-17	-2.696E-17	-5.506E-18	5.157E-18	-2.352E-17
6.012E-07	-2.996E-18	-2.750E-17	-7.568E-18	-8.007E-18	-4.726E-18	-1.107E-17	7.979E-18
0.000E+00							

Column 41 to 48

1.910E-05	8.562E-16	-2.792E-17	4.775E-18	1.019E-17	1.938E-17	1.938E-18	-2.119E-17
1.228E-16	-3.294E-16	4.394E-17	8.598E-18	4.499E-18	1.293E-18	-8.700E-17	-9.656E-17
-1.354E-14	4.957E-14	2.050E-15	-2.044E-16	2.385E-16	3.248E-16	1.375E-16	8.218E-17
-4.093E-18	4.898E-17	2.218E-05	-6.012E-07	-2.548E-07	-2.493E-18	-1.651E-04	-3.136E-17
3.265E-18	6.688E-18	-2.384E-17	-2.430E-20	5.714E-20	2.191E-20	-1.040E-17	-1.651E-04
0.000E+00							

Column 49 to 56

-3.111E-17	-4.994E-16	-1.067E-04	8.993E-16	5.381E-18	1.389E-17	5.711E-19	-2.311E-17
-5.391E-17	1.067E-04	1.319E-16	-3.194E-16	-3.788E-18	6.930E-18	8.626E-18	-1.223E-17
1.209E-16	-3.210E-14	-1.358E-14	4.958E-14	2.214E-17	6.964E-17	9.770E-17	-3.096E-16
-8.991E-18	-2.142E-17	2.689E-20	5.641E-17	-1.382E-18	-1.482E-18	-1.059E-18	1.118E-17
-5.086E-18	-1.249E-17	-5.445E-18	3.698E-18	4.044E-19	7.005E-19	-6.981E-19	-4.050E-20
0.000E+00							

Column 57 to 64

-1.920E-18	1.266E-06	-1.237E-17	-3.602E-18	3.354E-18	-7.485E-18	-1.286E-17	-3.701E-18
1.181E-17	1.427E-17	2.489E-18	-1.266E-06	6.467E-18	-2.129E-18	7.975E-18	-1.549E-18
-1.507E-16	4.224E-17	-3.477E-16	-4.834E-16	4.778E-16	-1.666E-16	-6.514E-16	6.825E-16
7.297E-18	-2.491E-19	-1.370E-18	-2.111E-18	5.082E-18	9.138E-18	-1.237E-18	3.296E-18
8.651E-19	-7.787E-20	-4.918E-19	6.951E-19	2.313E-19	-1.631E-19	-1.397E-19	4.575E-19
0.000E+00	0.000E+00	0.000E+00	0.000E+00	0.000E+00	0.000E+00	0.000E+00	0.000E+00

]

Appendix D: System Component Specifications

D.1 Relevant specifications of the Acuity AR200-12 laser displacement sensor

Table D.1: Specifications of the Acuity AR200-12 laser displacement sensor.

Parameter	Specification
Brand	Acuity
Model	AR200-12
Span	12.7mm
Stand-off to middle of span	21mm
Linearity +/- 0.2% of span	25.4µm
Resolution 0.03% of span	3.8µm
Laser spot size at Standoff; at ends of span	40µm; 200µm
Laser type	650 nm, 1 mW max. visible RED, Class 2. Complies with 21 CFR 1040 with Laser Notice #50 and IEC/EN 60825-1:2001
Sample Rates	0.2 - 1250 Hz, or sample on command (serial command or hardware trigger)
Output interfaces	RS232; Analog: 4-20mA or 0-10V
Product URL	http://www.acuitylaser.com/products/item/ar200-laser-measurement-sensor?lid=9?lead_leadid=8293

D.2 Specifications of the magnets and solenoids

Table D.2: Specifications of the primary levitation magnet.

Parameter	Specification
Magnet type	Neodymium rare-earth magnet
Dimensions	2 inch diameter; 1 inch thickness
Material and grade	NdFeB, Grade N52
Plating/Coating	Ni-Cu-Ni (Nickel)
Magnetization direction	Axial (Poles on flat ends)
Surface field	5233 Gauss
Max Operating Temp.	80°C
Brmax	14800 Gauss
BHmax	52 MGOe
Product URL	http://www.kjmagnetics.com/products.asp?cat=10

Table D.3: Specifications of the secondary actuator magnet.

Parameter	Specification
Magnet type	Neodymium rare-earth magnet
Dimensions	3/4 inch diameter; 3 inch length
Material and grade	NdFeB, Grade N52
Plating/Coating	Ni-Cu-Ni (Nickel)
Magnetization direction	Axial (Poles on flat ends)
Surface field	6619 Gauss
Max Operating Temp.	80°C
Brmax	14800 Gauss
BHmax	52 MGOe
Product URL	http://www.kjmagnetics.com/products.asp?cat=13

Table D.4: Specifications of the solenoid.

Parameter	Specification
Winding wire type	Enamelled copper wire
Winding wire diameter	0.85mm (including enamel)
Maximum continuous input current	3A
Number of turns	1000
Coil resistance	3.7 ohm
Coil inductance	14 mH
Sensitivity factor	3.82 N/A (when paired with the actuator magnet and positioned according to Figure 6.5)

D.3 Relevant specifications of the dSPACE DS1103 real-time control system

Table D.5: Specifications of the dSPACE DS1103 real-time control system.

Parameter		Specification
Manufacturer	Brand Model	dSPACE DS1103 PPC
Processor	PowerPC Type CPU clock Cache Bus frequency	- PPC 750GX - 1 GHz - 32 KB level 1 (L1) instruction cache - 32 KB level 1 (L1) data cache - 1 MB level 2 (L2) - 133 MHz
Memory	Local memory Global memory	- 32 MB application SDRAM as program memory, cached - 96 MB communication SDRAM for data storage and data exchange with host
Timer	2 general-purpose timers 1 sampling rate timer (decrement) 1 time base counter	- One 32-bit down counter - Reload by software - 15-ns resolution - One 32-bit up counter with compare register - Reload by software - 30-ns resolution - 32-bit down counter - Reload by software - 30-ns resolution - 64-bit up counter - 30-ns resolution
A/D converter	Channels Resolution Input voltage range Overvoltage protection Conversion time Offset error Gain error Offset drift	-16 multiplexed channels equipped with 4 sample & hold A/D converters (4 channels belong to one A/D converter. 4 consecutive samplings are necessary to sample all channels belonging to one A/D converter.) - 4 parallel channels each equipped with one sample & hold A/D converter - Note: 8 A/D converter channels (4 multiplexed and 4 parallel) can be sampled simultaneously. - 16-bit - ± 10 V - ± 15 V - Multiplexed channels: 1 μ s - Parallel channels: 800 ns - ± 5 mV - $\pm 0.25\%$ - 40 μ V/K

	Gain drift	- 50 ppm/K
	Signal-to-noise ratio	- >83 dB
D/A converter	Channels	- 8 Channels
	Resolution	- 16-bit
	Output voltage range	- ± 10 V
	Settling time	- 5 μ s (14-bit)
	Offset error	- ± 1 mV
	Gain error	- $\pm 0.5\%$
	Offset drift	- 30 μ V/K
	Gain drift	- 25 ppm/K
	Signal-to-noise ratio	- >83 dB
	I_{\max}	- ± 5 mA
	CI_{\max}	- 10 nF
Product URL	https://www.dspace.com/en/pub/home/products/hw/singbord/ppconbo.cfm	

D.4 Relevant specifications of the Maxon servo-amplifier

Table D.6: Specifications of the Maxon servo-amplifier.

Parameter	Specification
Brand	MaxonMotor
Model	4-Q-DC Servo-amplifier LSC 30/2
Supply voltage V_{CC}	12-30 VDC
Max. output voltage	25V
Max. output current I_{max}	2A
Max. power output	50W
Input set value	-10V to10V
Product URL	http://maxonmotor.exportpages.com/productdetail/1065726121-1.htm

D.5 Relevant specifications of the B&K 4381 accelerometer

Table D.7: Specifications of the B&K 4381 accelerometer.

Parameter	Specification
Brand	Brüel & Kjær
Model	4381
Frequency	0.1Hz-4800Hz
Sensitivity	100 pC/g
Residual Noise Level in Spec Freq Range (rms)	± 0.02 mg
Maximum acceleration	2000g
Output	Charge-PE
Resonance Frequency	16 kHz
Weight	43 gram
Product URL	http://www.bksv.com/Products/transducers/vibration/accelerometers/accelerometers/4381.aspx?tab=specifications

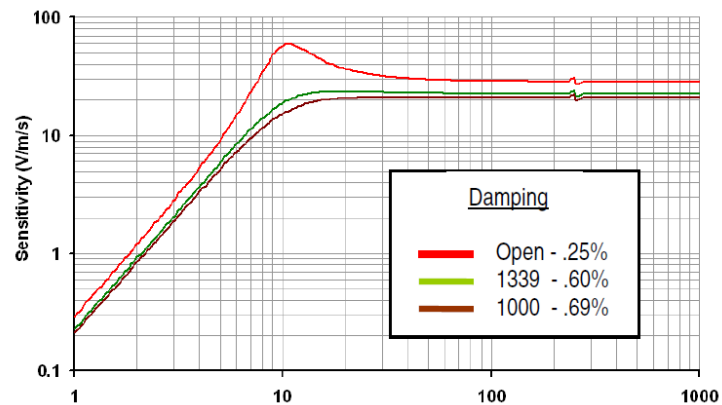
D.6 Relevant specifications of the SM-24 Geophone

Table D.8: Specifications of the SM-24 Geophone.

Parameter	Specification
Brand	SENSOR Nederland b.v.
Model	SM-24
Natural frequency	10 Hz
Tolerance	± 2.5%
Damping	Open circuit (typical) 0.25 Damping calibration- shunt resistance: 1339Ω Damping ratio with calibration shunt: 0.6 Tolerance with calibration shunt: + 5 %, - 0 %
Sensitivity	28.8 V/(m/s) (0.73 V/in/s)
Max coil excursion p.p.	2 mm (0.08 in)
Moving mass	11 g (0.38 oz)
Product URL	http://www.geophone.com/techpapers/SM-24%20Brochure.pdf



(a): Geophone section view



(b): Sensitivity plot of the SM-24 geophone

Figure D.1: SM-24 series geophone form SENSOR (SENSOR, 2013).

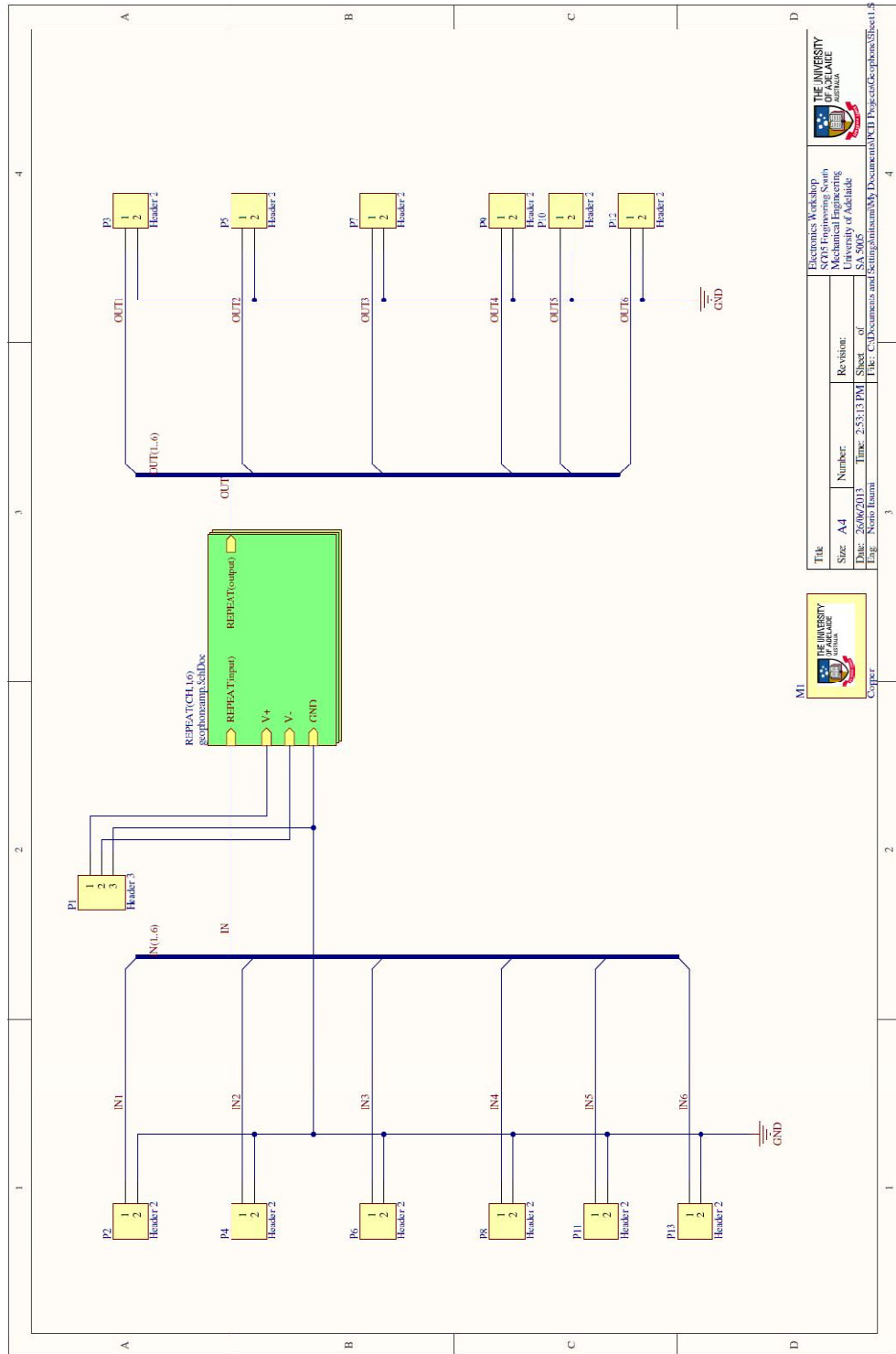
D.7 Relevant specifications of the MB-Modal 110 shaker

Table D.9: Specifications of the MB-Modal 110 shaker.

Parameter	Specification
Brand	MB dynamics
Model	MODAL 110
Force	500N (forced-air cooled); 250 (convection cooling)
Stroke	38mm
Bandwidth	DC-5000Hz
Moving element	0.6kg
Shaker weight	22kg
Longitudinal stiffness	5.2N/mm
Product URL	http://mbdynamics.com/assets/datasheets/MODAL%20110%20MB500VI%20Data%20Sheet,%202008,11,15.pdf

Appendix E: Geophone Analogue Filter Circuit

Figure E.1 and Figure E.2 are the circuit diagrams of the analogue filter used to achieve the transfer function described in Equation (7.7).



			
Title: Electronics Workshop Course: Mechanical Engineering University of Adelaide SA 5005		Revision: _____ Sheet of _____ Date: 26/06/2013 Time: 2:53:13 PM File: C:\Documents and Settings\m3am\My Documents\PCD Project\Geophone\Sheet1.D	
Size: A4 Date: 26/06/2013 Eng: Neo Isami	Number: _____ Time: 2:53:13 PM	Revision: _____ Sheet of _____	Title: Electronics Workshop Course: Mechanical Engineering University of Adelaide SA 5005

Figure E.1: Circuit diagram of the analogue geophone filter (outer layer).

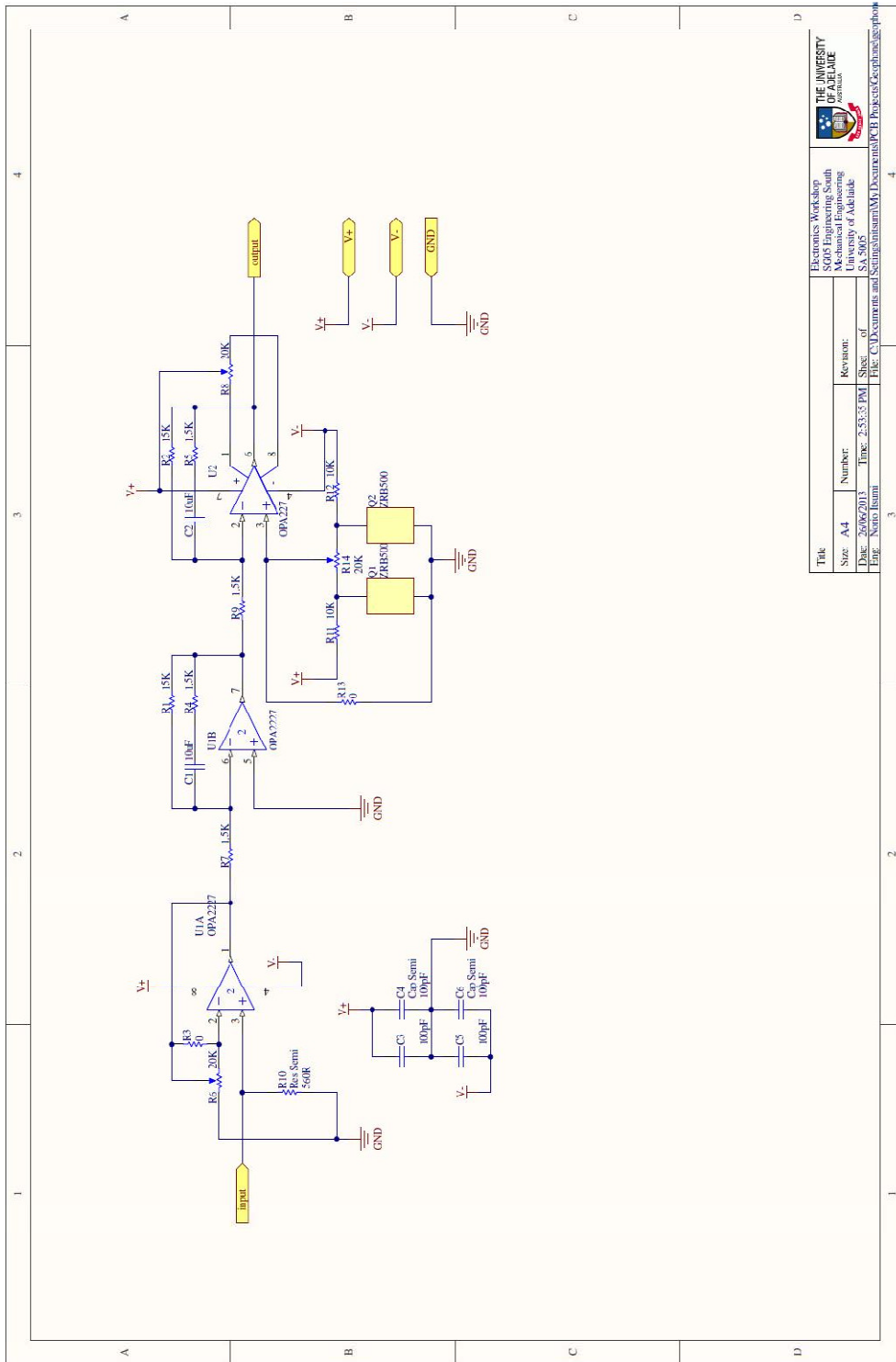


Figure E.2: Circuit diagram of the analogue geophone filter (inner layer).

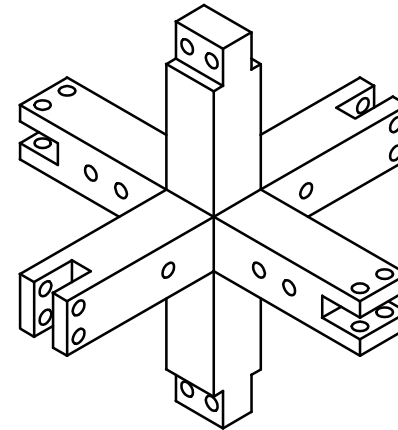
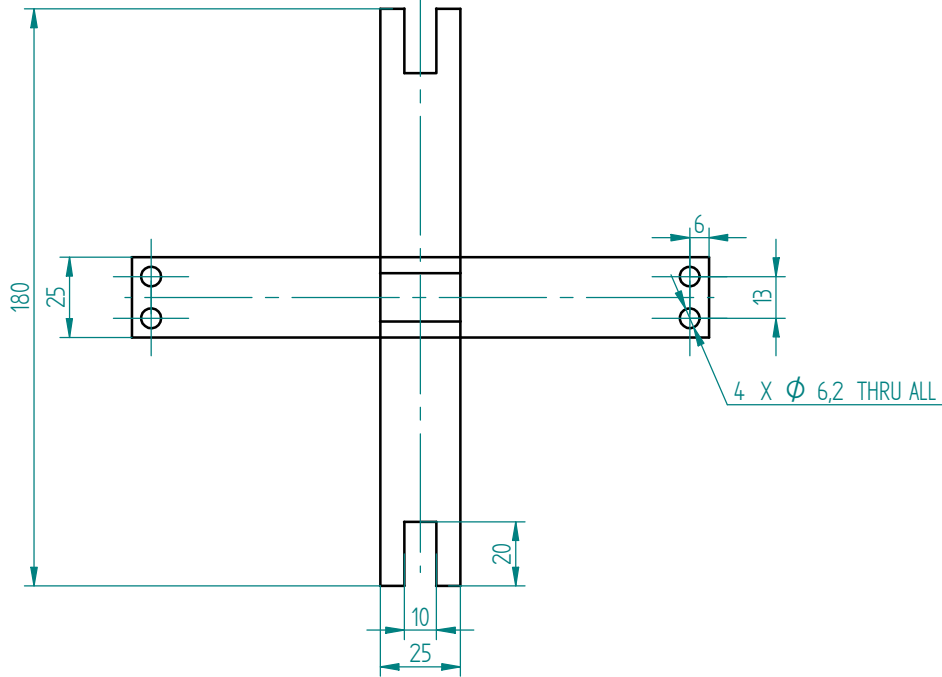
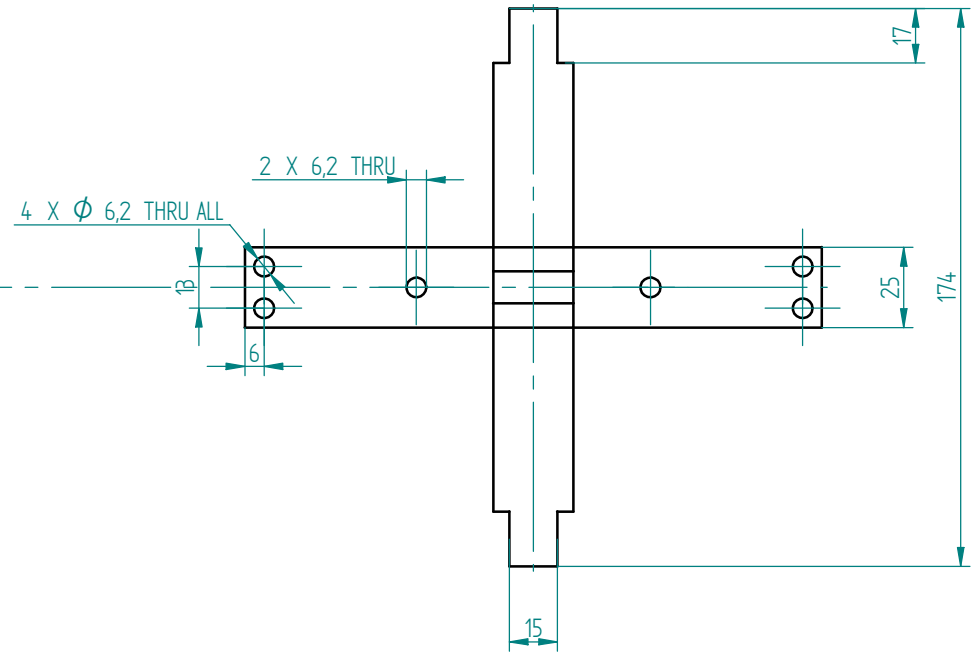
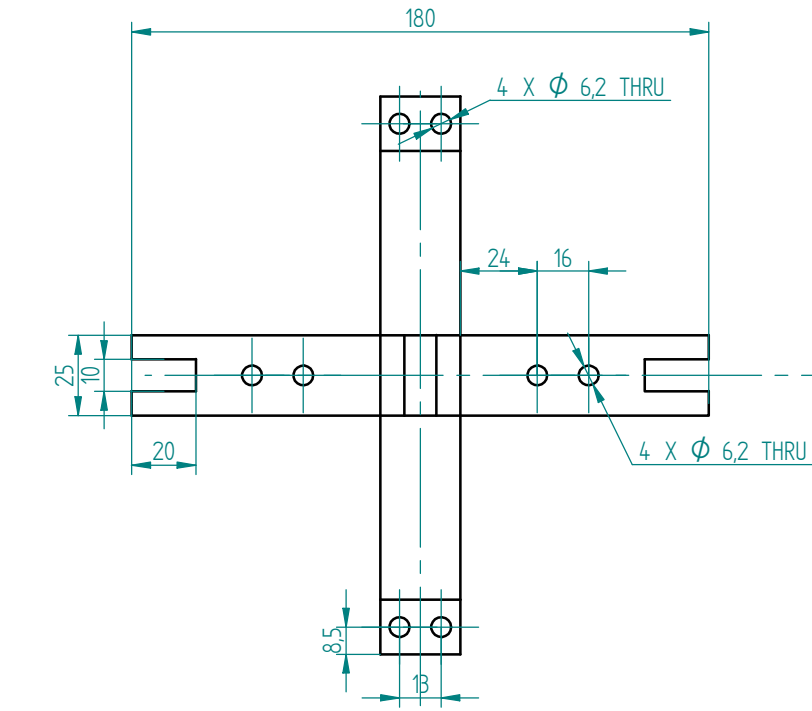
Title		Revision	
Size: A4	Number:	Revision:	
Date: 2006/2013	Time: 2:53:35 PM	Sheet: of	
File: Note.html		Fig: C:\Documents and Settings\mami\Desktop\WCH Project\Geophone\geophone	



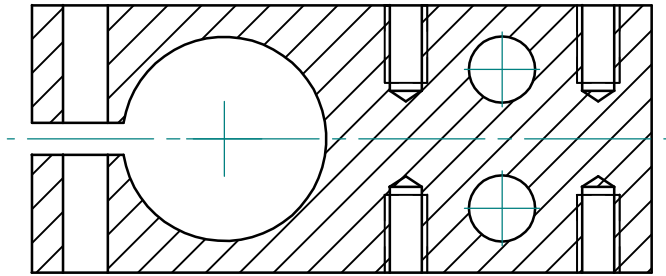
Electronics Workshop
 SGO5 Engineering South
 Mechanical Engineering
 University of Adelaide
 SA 5005

Appendix F: Drawings of the Isolator Mechanical Design

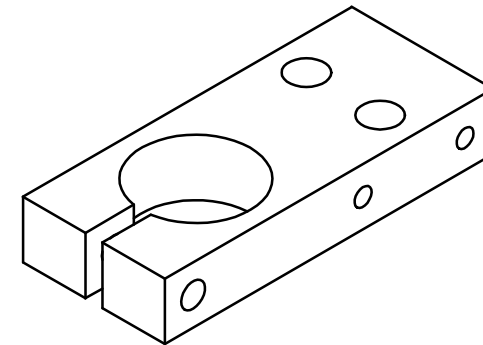
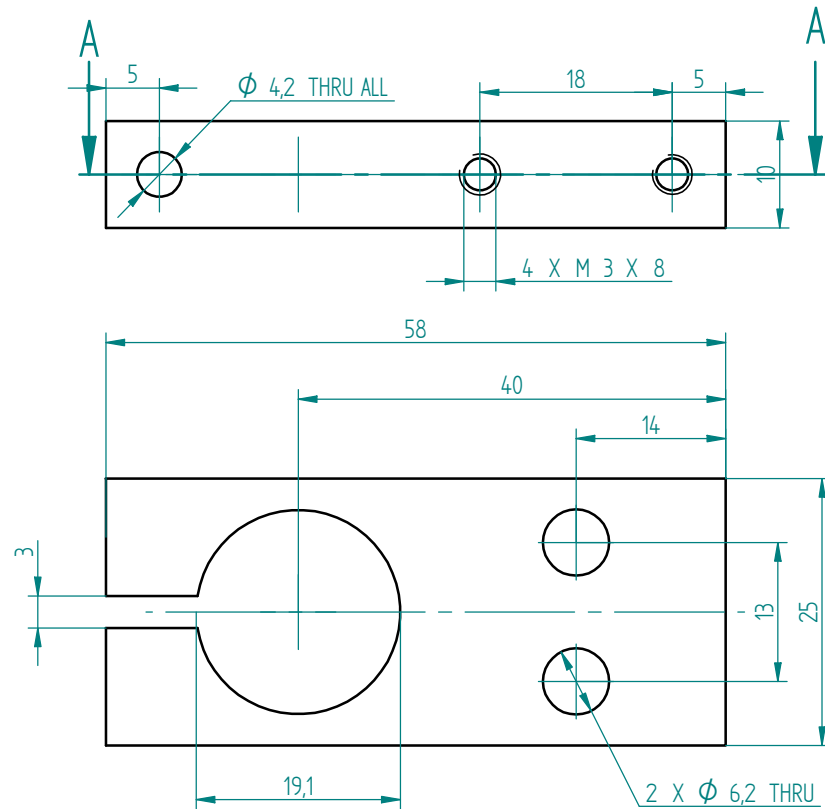
This appendix includes all the engineering drawings generated for manufacturing the mechanical design of the maglev isolator. All part drawings and assembly drawings are attached.



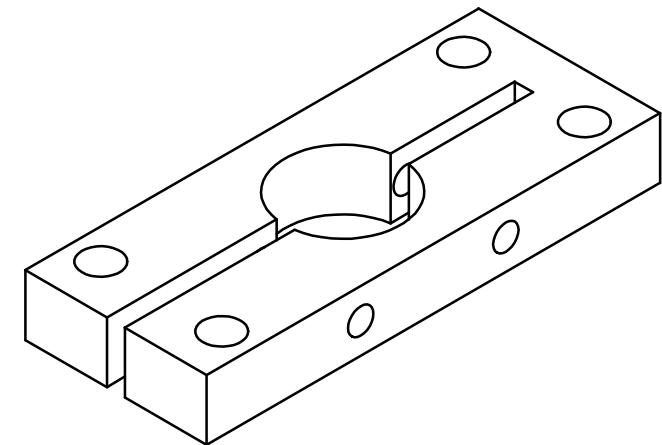
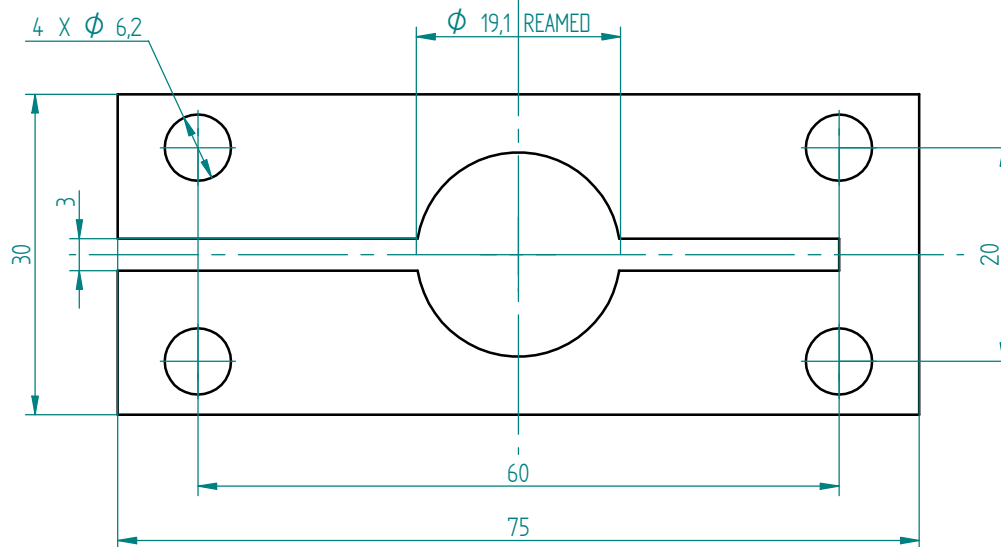
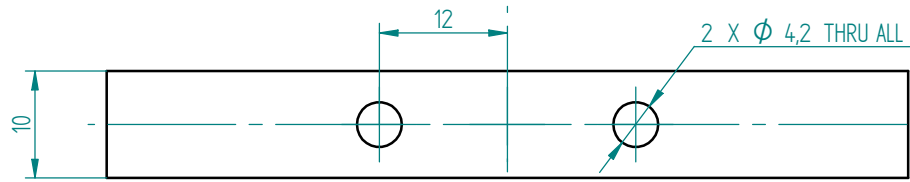
Tolerance	Name:	Tao Zhu	Mobile:	0413647219
General Tolerance ISO 2768-f	Email:	tao.zhu@adelaide.edu.au	Supervisor & signature	Ben Cazzolato
0,5-3 +/-0,05	Project:	Six Degree of Freedom Maglev Isolator		
3-6 +/-0,05	Drawing Name:	Core frame		
6-30 +/-0,1	Material:	Aluminium 6061-T6	DRG No.	1
30-120 +/-0,15	Quantity:	1	Date:	02/10/2010
400-1000 +/-0,3				
Above 1000 N/A				
Angle: +/-0,2 Degree				



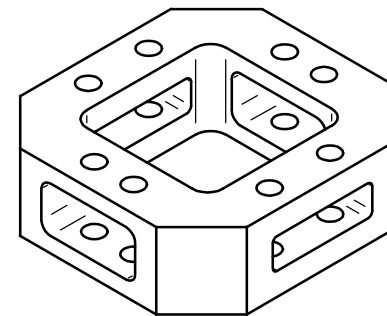
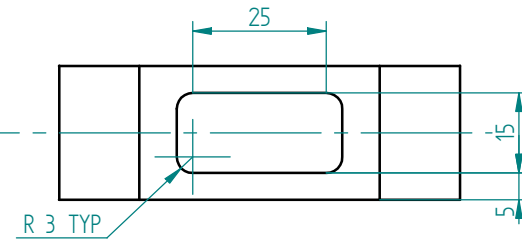
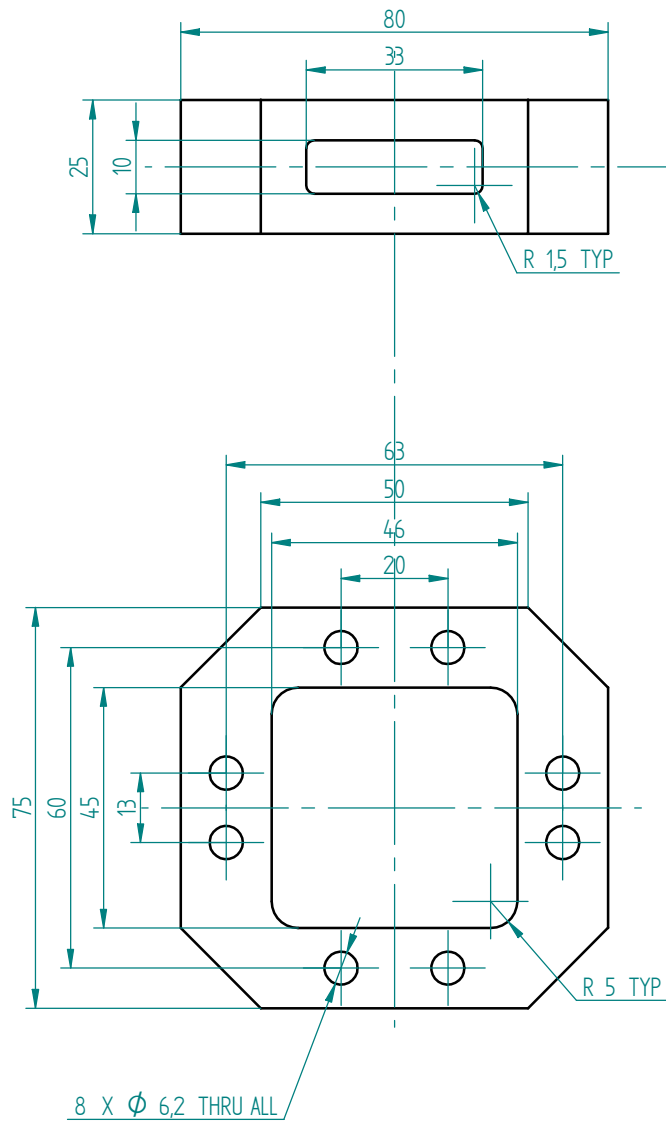
SECTION A-A



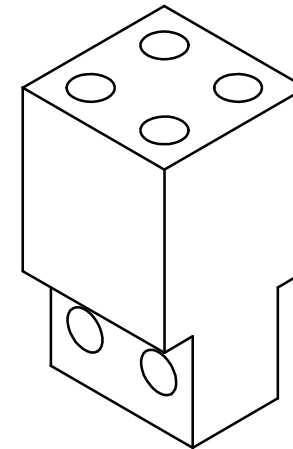
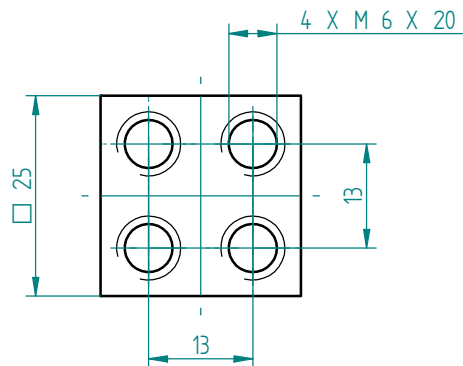
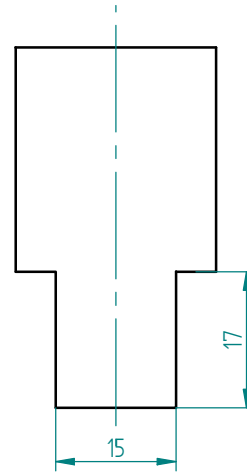
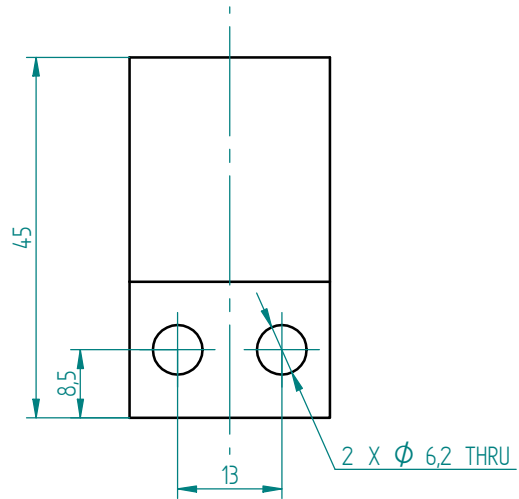
Tolerance	Name:	Tao Zhu	Mobile:	0413647219
General Tolerance ISO 2768-f	Email:	tao.zhu@adelaide.edu.au	Supervisor &signature	Ben Cazzolato
0,5-3 +/-0,05	Project:	Six Degree of Freedom Maglev Isolator		
3-6 +/-0,05	Drawing Name:	Side magnet holder		
6-30 +/-0,1	Material:	Aluminium 6061-T6	DRG NO.	2
30-120 +/-0,15	Quantity:	4	Date:	20/10/2010
400-1000 +/-0,3				
Above1000 N/A				
Angle: +/-0,2 Degree				



Tolerance	Name:	Tao Zhu	Mobile:	0413647219
General Tolerance ISO 2768-f	Email:	tao.zhu@adelaide.edu.au	Supervisor & Signature	Ben Cazzolato
0.5-3 +/-0.05	Project:	Six Degree of Freedom Maglev Isolator		
3-6 +/-0.05	Drawing Name:	Square side magnet holder		
6-30 +/-0.1	Material:	Aluminium 6061-T6	DRG NO.	3
30-120 +/-0.15	Quantity:	2	Date:	21/10/2010
400-1000 +/-0.3				
Above 1000 N/A				
Angle: +/-0.2 Degree				

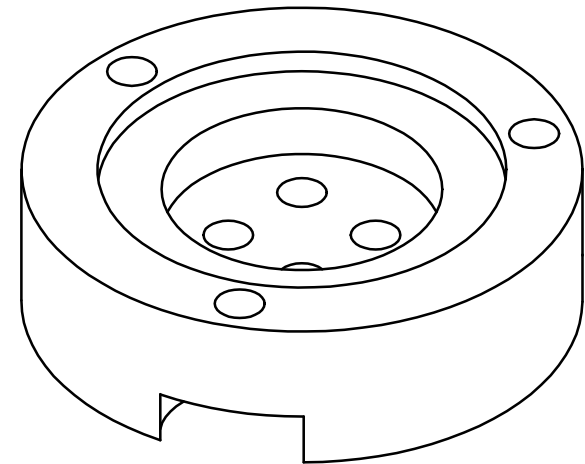
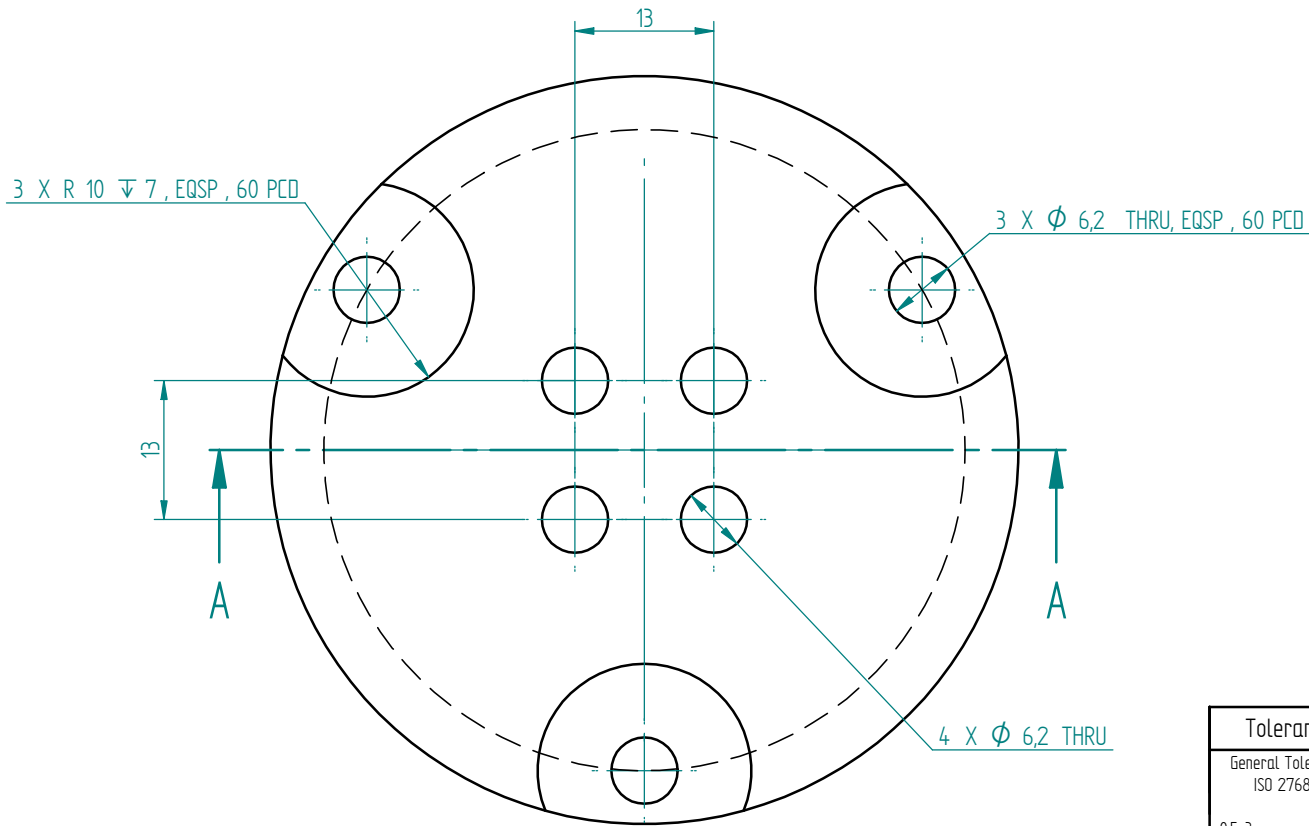
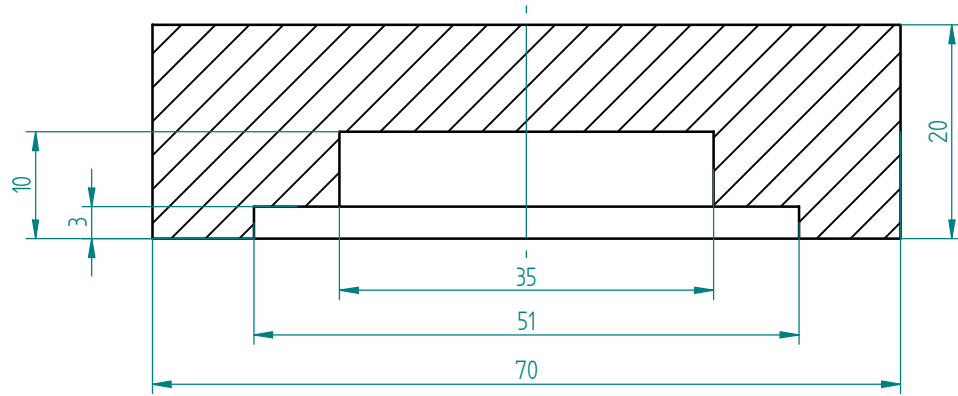


Tolerance	Name:	Tao Zhu	Mobile:	0413647219
General Tolerance ISO 2768-f	Email:	tao.zhu@adelaide.edu.au	Supervisor & signature	Ben Cazzolato
0,5-3 +/-0,05 3-6 +/-0,05 6-30 +/-0,1 30-120 +/-0,15 400-1000 +/-0,3 Above1000 N/A Angle: +/-0,2 Degree	Project:	Six Degree of Freedom Maglev Isolator		
	Drawing Name:	Top magnet connector		
	Material:	Aluminium 6061-T6	DRG NO.	4
	Quantity:	2	Date:	17/10/2010

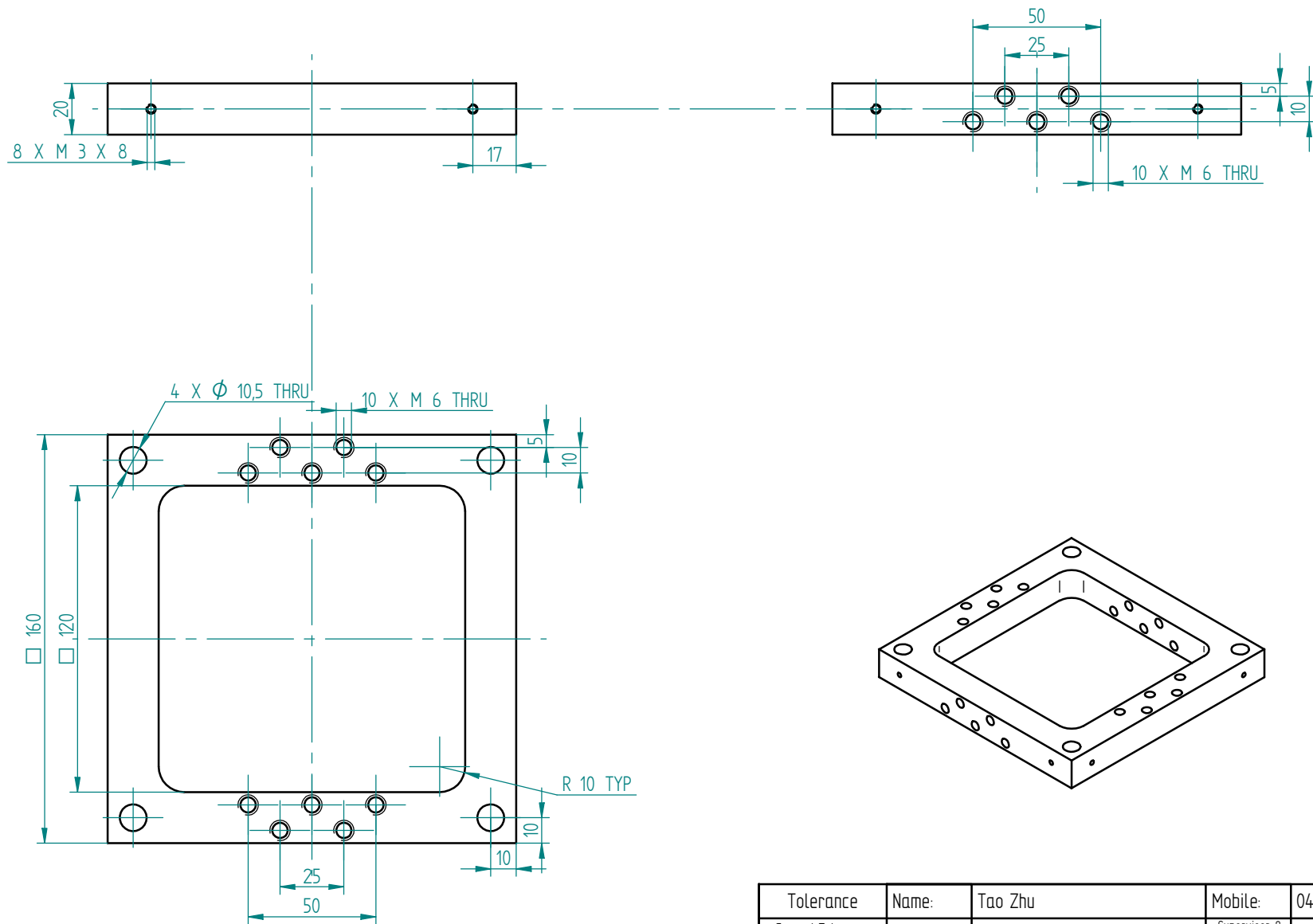


Tolerance	Name:	Tao Zhu	Mobile:	0413647219
General Tolerance ISO 2768-f	Email:	tao.zhu@adelaide.edu.au	Supervisor & signature	Ben Cazzolato
0.5-3 +/-0.05 3-6 +/-0.05 6-30 +/-0.1 30-120 +/-0.15 30-120 +/-0.15 400-1000 +/-0.3 Above 1000 N/A Angle: +/-0.2 Degree	Project:	Six Degree of Freedom Maglev Isolator		
	Drawing Name:	Top magnet support connector		
	Material:	Aluminium 6061-T6	DRG NO.	5
	Quantity:	2	Date:	24/10/2010

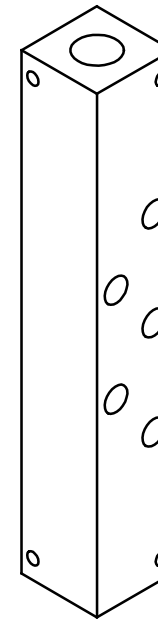
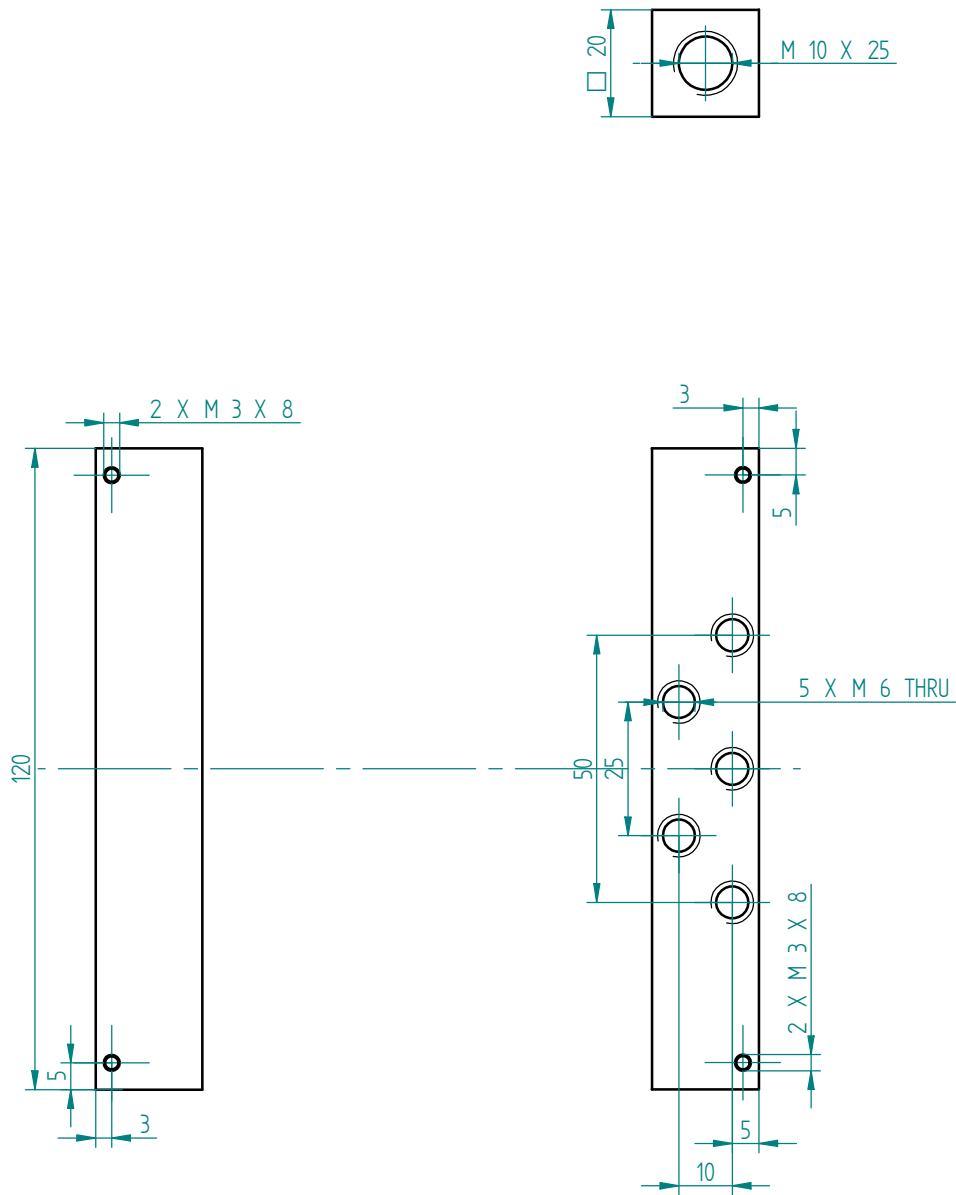
SECTION A-A



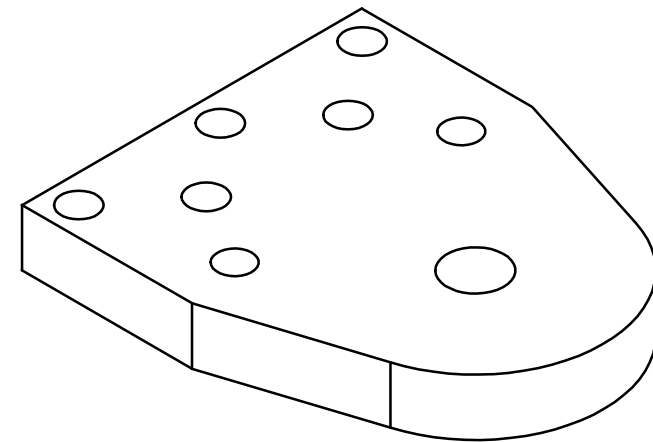
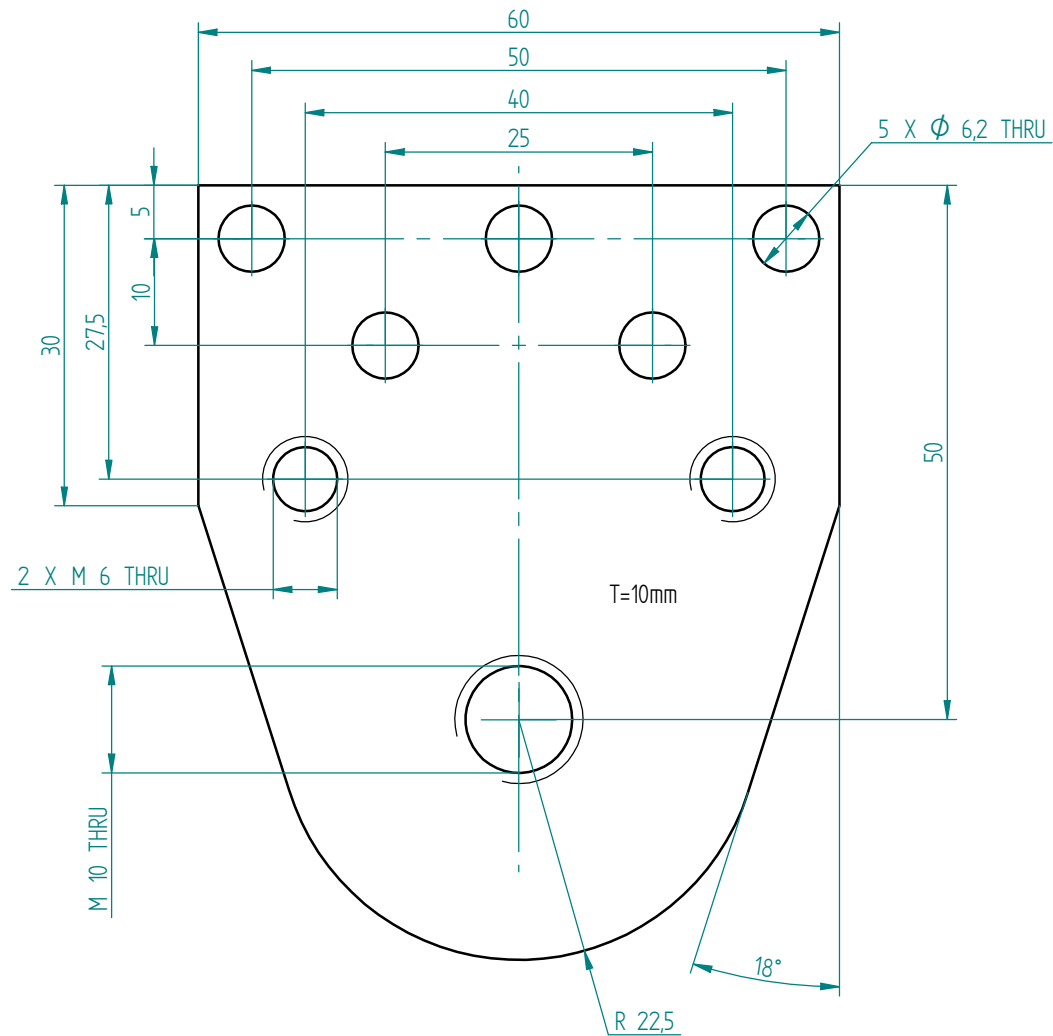
Tolerance	Name:	Tao Zhu	Mobile:	0413647219
General Tolerance ISO 2768-f	Email:	tao.zhu@adelaide.edu.au	Supervisor & Signature	Ben Cazzolato
0.5-3 +/-0.05	Project:	Six Degree of Freedom Maglev Isolator		
3-6 +/-0.05	Drawing Name:	Top magnet seat plate		
6-30 +/-0.1	Material:	Aluminium 6061-T6	DRG NO.	6
30-120 +/-0.15	Quantity:	2	Date:	24/10/2010
400-1000 +/-0.3				
Above 1000 N/A				
Angle: +/-0.2 Degree				



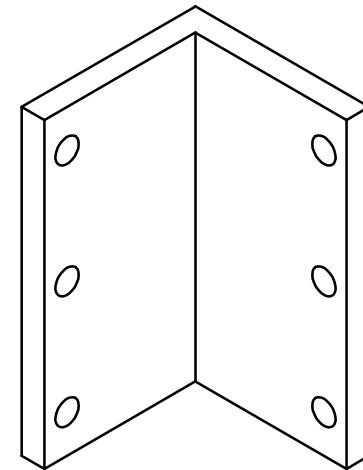
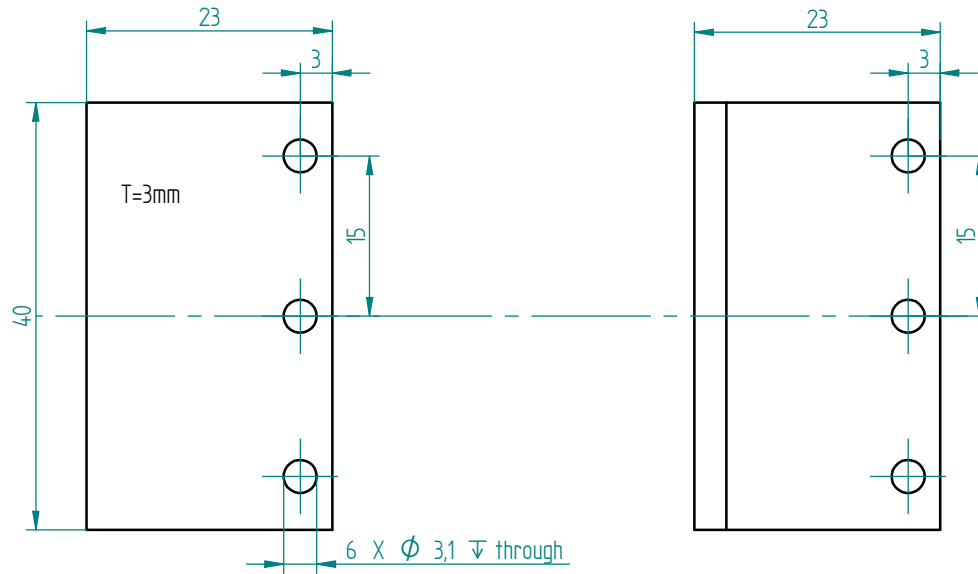
Tolerance	Name:	Tao Zhu	Mobile:	0413647219
General Tolerance ISO 2768-f	Email:	tao.zhu@adelaide.edu.au	Supervisor & signature	Ben Cazzolato
0.5-3 +/-0.05	Project:	Six Degree of Freedom Maglev Isolator		
3-6 +/-0.05	Drawing Name:	Mid supporting plate		
6-30 +/-0.1	Material:	Aluminium 6061-T6	DRG NO.	7
30-120 +/-0.15	Quantity:	2	Date:	02/10/2010
400-1000 +/-0.3				
Above1000 N/A				
Angle: +/-0.2 Degree				



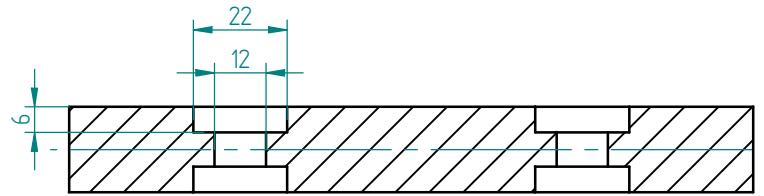
Tolerance	Name:	Tao Zhu	Mobile:	0413647219
General Tolerance ISO 2768-f	Email:	tao.zhu@adelaide.edu.au	Supervisor & signature	Ben Cazzolato
0.5-3 +/-0.05	Project:	Six Degree of Freedom Maglev Isolator		
3-6 +/-0.05	Drawing Name:	Mid supporting plate connection bar		
6-30 +/-0.1	Material:	Aluminium 6061-T6	DRG NO.	8
30-120 +/-0.15	Quantity:	4	Date:	02/10/2010
400-1000 +/-0.3				
Above1000 N/A				
Angle: +/-0.2 Degree				



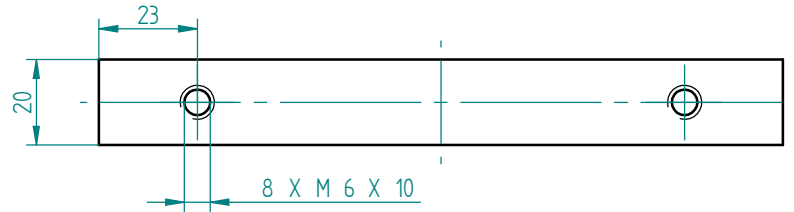
Tolerance	Name:	Tao Zhu	Mobile:	0413647219
General Tolerance ISO 2768-f	Email:	tao.zhu@adelaide.edu.au	Supervisor & signature	Ben Cazzolato
0.5-3 +/-0.05	Project:	Six Degree of Freedom Maglev Isolator		
3-6 +/-0.05	Drawing Name:	Coil Holder		
6-30 +/-0.1	Material:	Aluminium 6061-T6	DRG NO.	9
30-120 +/-0.15	Quantity:	12	Date:	17/10/2010
400-1000 +/-0.3				
Above 1000 N/A				
Angle: +/-0.2 Degree				



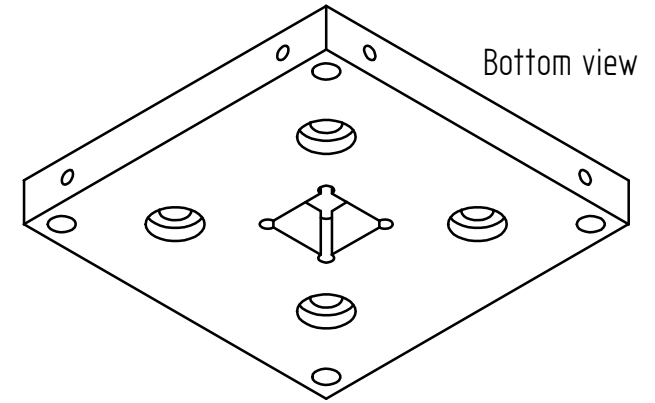
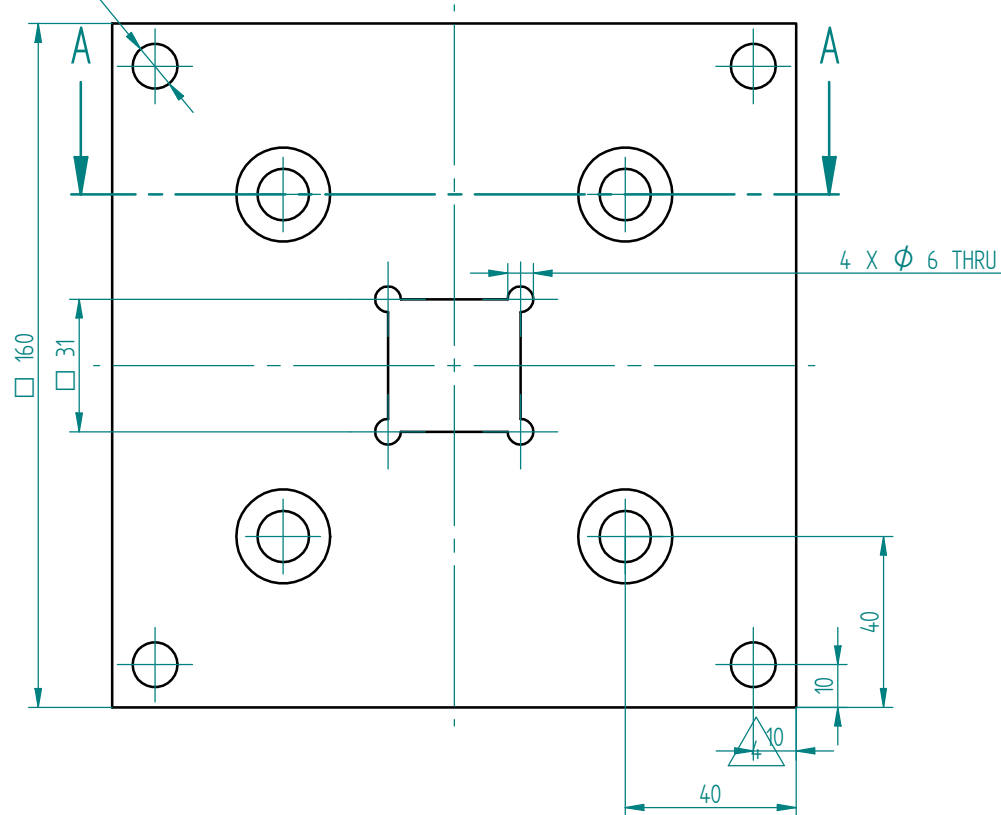
Tolerance	Name:	Tao Zhu	Mobile:	0413647219
General Tolerance ISO 2768-f	Email:	tao.zhu@adelaide.edu.au	Supervisor & signature	Ben Cazzolato
0.5-3 +/-0.05 3-6 +/-0.05 6-30 +/-0.1 30-120 +/-0.15 400-1000 +/-0.3 Above1000 N/A Angle: +/-0.2 Degree	Project:	Six Degree of Freedom Maglev Isolator		
	Drawing Name:	L side fitting		
	Material:	Aluminium 6061-T6	DRG NO.	10
	Quantity:	8	Date:	21/10/2010



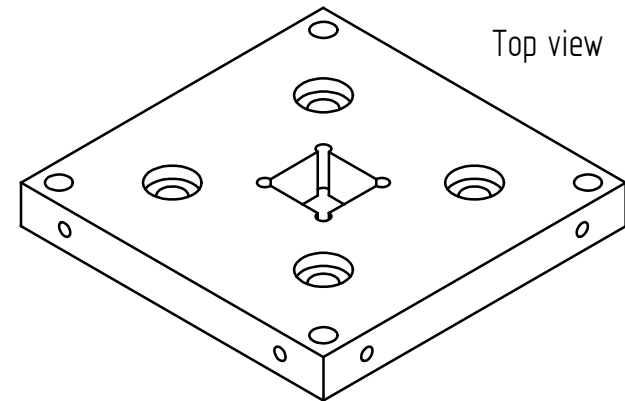
SECTION A-A



4 X ϕ 10,5 THRU

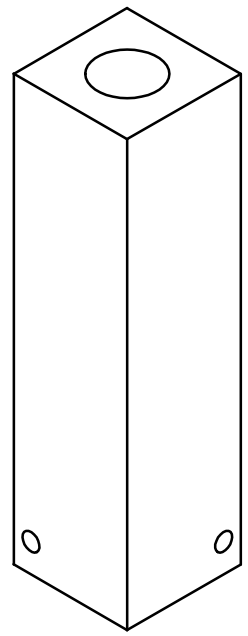
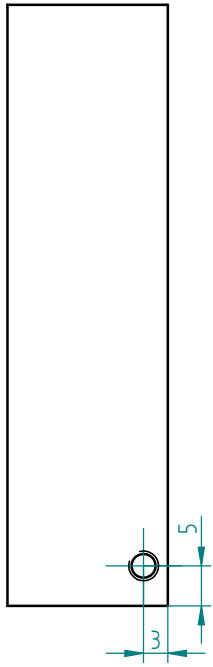
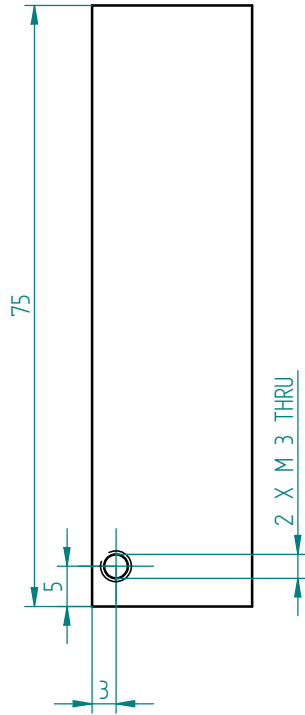
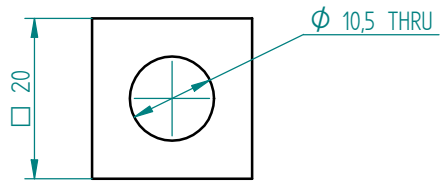


Bottom view

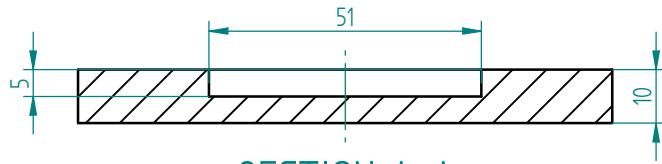


Top view

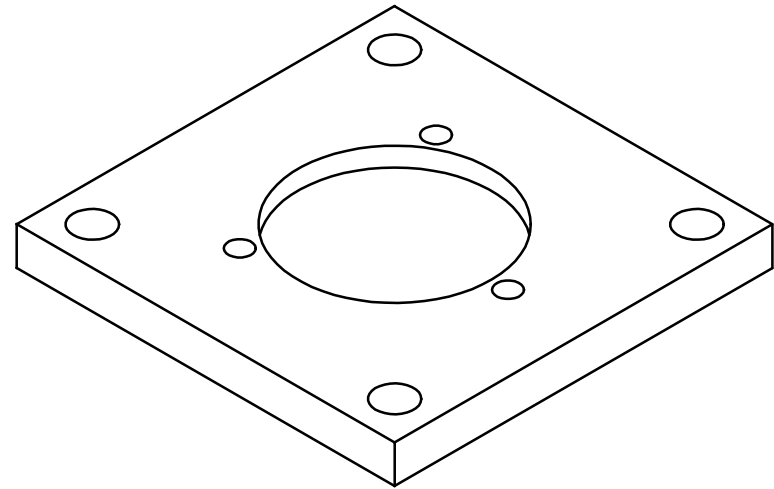
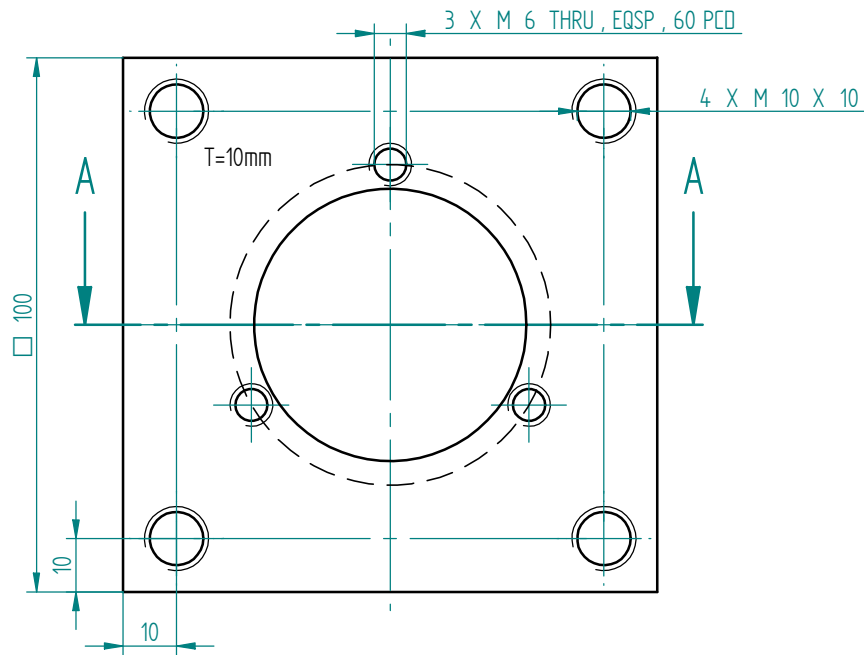
Tolerance	Name:	Tao Zhu	Mobile:	0413647219
General Tolerance ISO 2768-f	Email:	tao.zhu@adelaide.edu.au	Supervisor & signature	Ben Cazzolato
0,5-3 +/-0,05	Project:	Six Degree of Freedom Maglev Isolator		
3-6 +/-0,05	Drawing Name:	Top supporting plate		
6-30 +/-0,1	Material:	Aluminium 6061-T6	DRG NO.	11
30-120 +/-0,15	Quantity:	2	Date:	02/10/2010
400-1000 +/-0,3				
Above 1000 N/A				
Angle: +/-0,2 Degree				



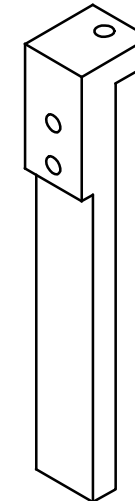
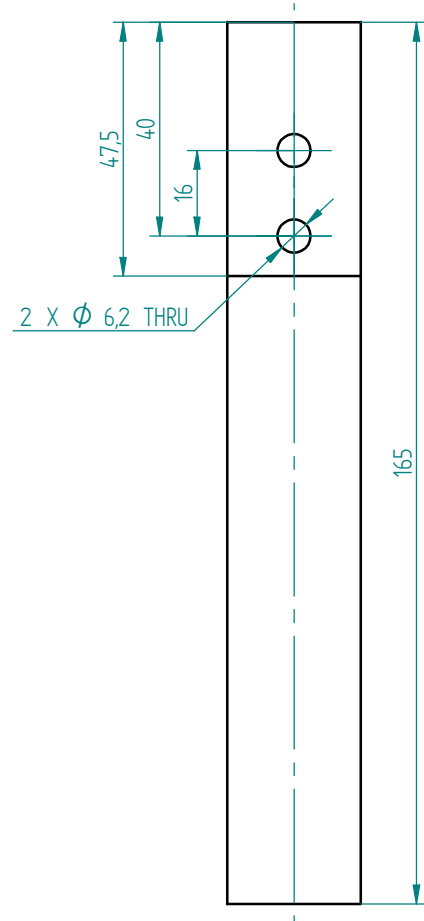
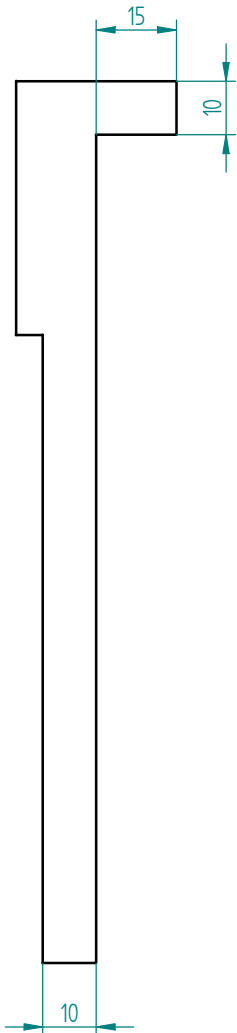
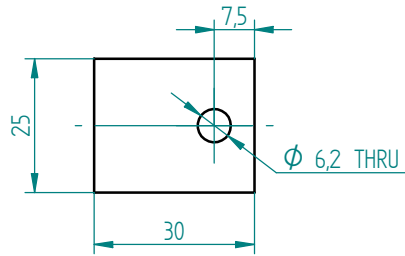
Tolerance	Name:	Tao Zhu	Mobile:	0413647219
General Tolerance ISO 2768-f	Email:	tao.zhu@adelaide.edu.au	Supervisor & signature	Ben Cazzolato
0.5-3 +/-0.05 3-6 +/-0.05 6-30 +/-0.1 30-120 +/-0.15 400-1000 +/-0.3 Above1000 N/A Angle: +/-0.2 Degree	Project:	Six Degree of Freedom Maglev Isolator		
	Drawing Name:	Top connection bar		
	Material:	Aluminium 6061-T6	DRG NO.	12
	Quantity:	8	Date:	02/10/2010



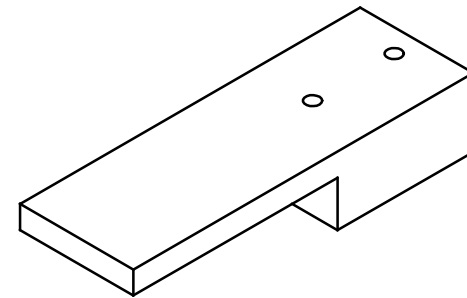
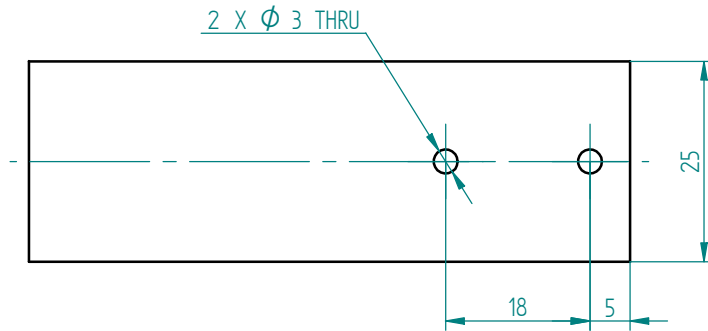
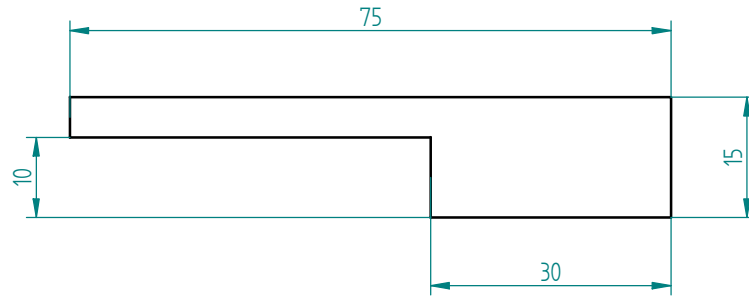
SECTION A-A



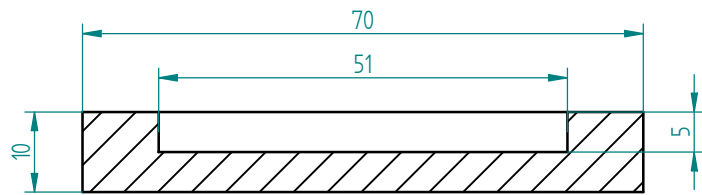
Tolerance	Name:	Tao Zhu	Mobile:	0413647219
General Tolerance ISO 2768-f	Email:	tao.zhu@adelaide.edu.au	Supervisor & signature	Ben Cazzolato
0.5-3 +/-0.05 3-6 +/-0.05 6-30 +/-0.1 30-120 +/-0.15 400-1000 +/-0.3 Above1000 N/A Angle: +/-0.2 Degree	Project:	Six Degree of Freedom Maglev Isolator		
	Drawing Name:	Top magnet support		
	Material:	Aluminium 6061-T6	DRG NO.	13
	Quantity:	2	Date:	24/10/2010



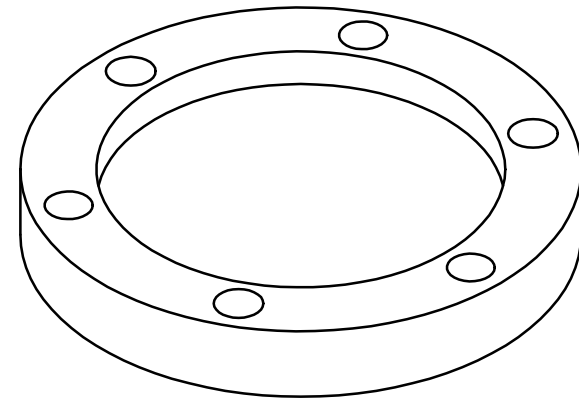
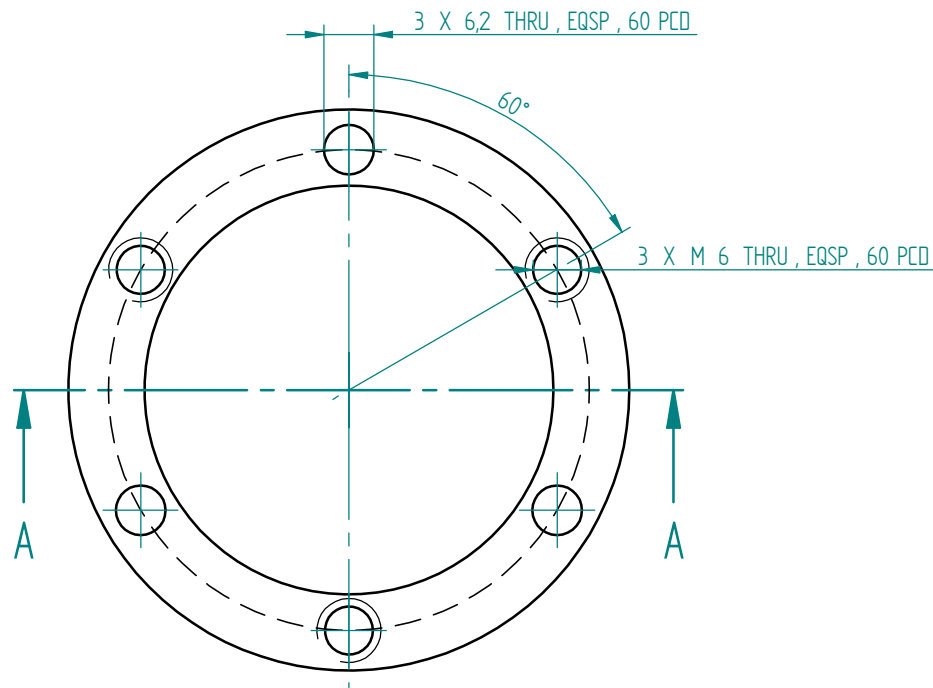
Tolerance	Name:	Tao Zhu	Mobile:	0413647219
General Tolerance ISO 2768-f	Email:	tao.zhu@adelaide.edu.au	Supervisor & signature	Ben Cazzolato
0.5-3 +/-0.05 3-6 +/-0.05 6-30 +/-0.1 30-120 +/-0.15 400-1000 +/-0.3 Above1000 N/A Angle: +/-0.2 Degree	Project:	Six Degree of Freedom Maglev Isolator		
	Drawing Name:	Load Connector		
	Material:	Aluminium 6061-T6	DRG NO.	14
	Quantity:	4	Date:	07/11/2010



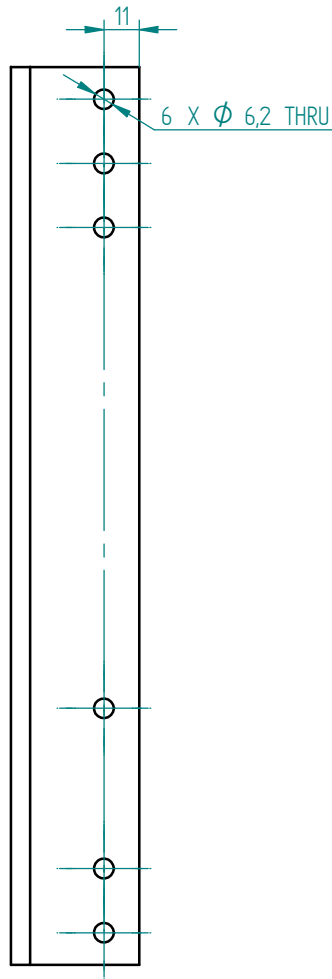
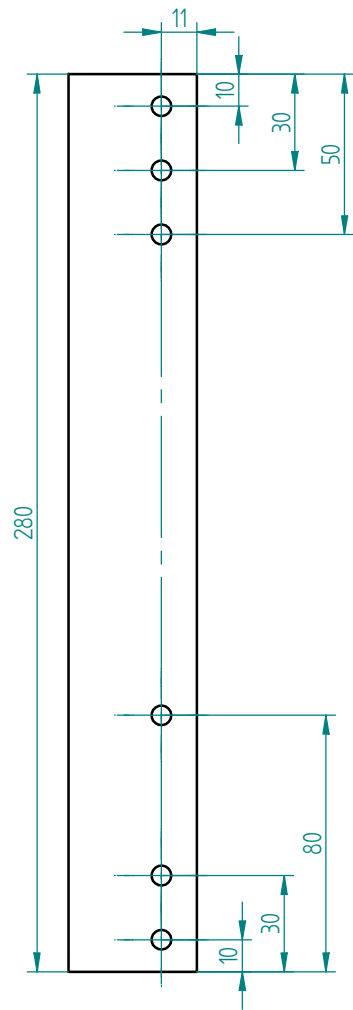
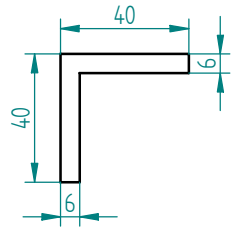
Tolerance	Name:	Tao Zhu	Mobile:	0413647219
General Tolerance ISO 2768-f	Email:	tao.zhu@adelaide.edu.au	Supervisor & Signature	Ben Cazzolato
0.5-3 +/-0.05	Project:	Six Degree of Freedom Maglev Isolator		
3-6 +/-0.05	Drawing Name:	Sensor reference plate		
6-30 +/-0.1	Material:	Aluminium 6061-T6	DRG NO.	15
30-120 +/-0.15	Quantity:	3	Date:	07/11/2010
400-1000 +/-0.3				
Above1000 N/A				
Angle: +/-0.2 Degree				



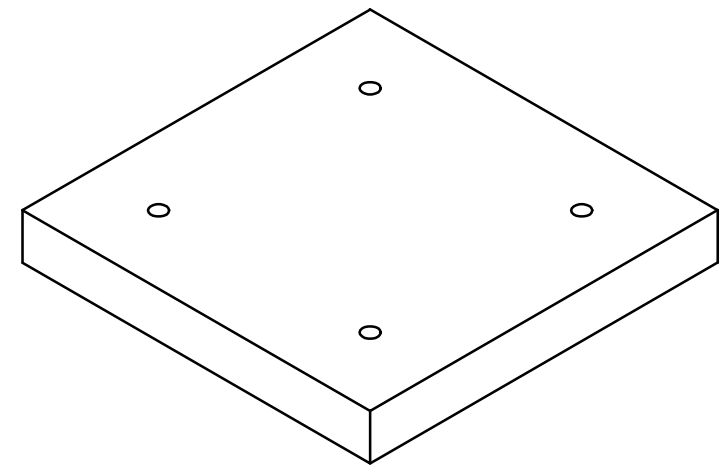
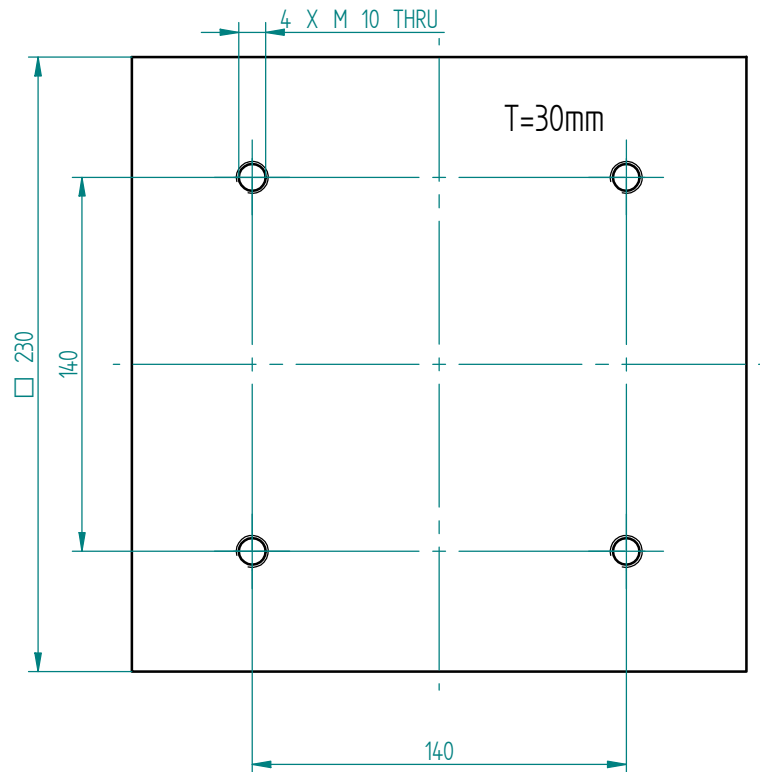
SECTION A-A



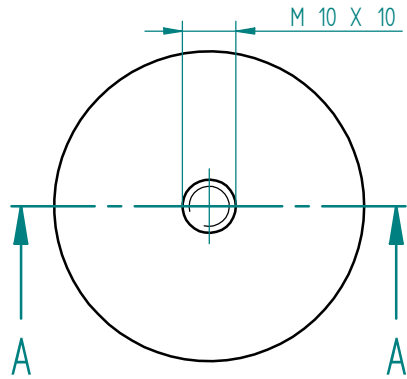
Tolerance	Name:	Tao Zhu	Mobile:	0413647219
General Tolerance ISO 2768-f	Email:	tao.zhu@adelaide.edu.au	Supervisor & Signature	Ben Cazzolato
0.5-3 +/-0.05 3-6 +/-0.05 6-30 +/-0.1 30-120 +/-0.15 400-1000 +/-0.3 Above1000 N/A Angle: +/-0.2 Degree	Project:	Six Degree of Freedom Maglev Isolator		
	Drawing Name:	Magnet cap		
	Material:	Aluminium 6061-T6	DRG NO.	16
	Quantity:	4	Date:	12/11/2010



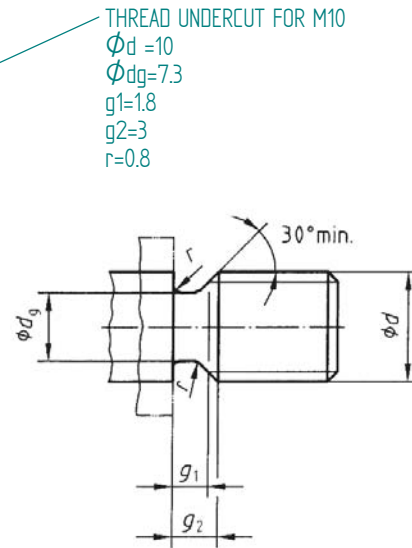
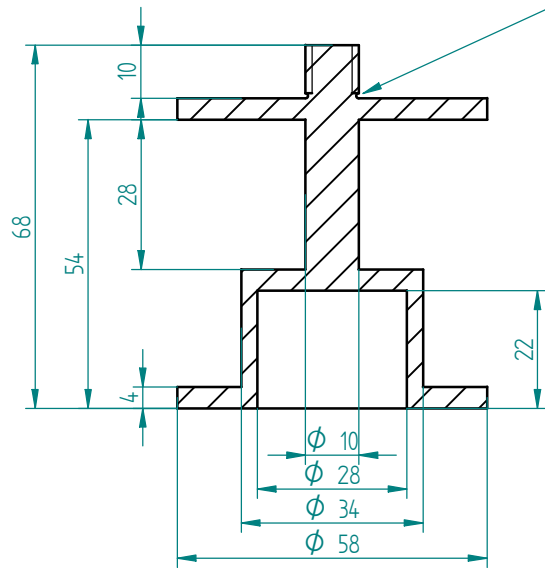
Tolerance	Name:	Tao Zhu	Mobile:	0413647219
General Tolerance ISO 2768-f	Email:	tao.zhu@adelaide.edu.au	Supervisor & signature	Ben Cazzolato
0.5-3 +/-0.05	Project:	Six Degree of Freedom Maglev Isolator		
3-6 +/-0.05	Drawing Name:	Supporting leg		
6-30 +/-0.1	Material:	Aluminium 6061-T6 Equal Angle	DRG NO.	17
30-120 +/-0.15	Quantity:	4	Date:	07/11/2010
400-1000 +/-0.3				
Above1000 N/A				
Angle: +/-0.2 Degree				



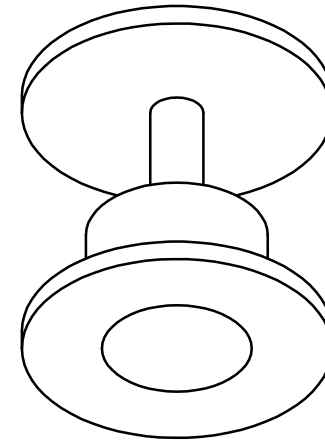
Tolerance	Name:	Tao Zhu	Mobile:	0413647219
General Tolerance ISO 2768-f	Email:	tao.zhu@adelaide.edu.au	Supervisor & Signature	Ben Cazzolato
0.5-3 +/-0.05	Project:	Six Degree of Freedom Maglev Isolator		
3-6 +/-0.05	Drawing Name:			
6-30 +/-0.1	Material:	316 Stainless steel	DRG NO.	18
30-120 +/-0.15	Quantity:	1	Date:	07/11/2010
400-1000 +/-0.3				
Above 1000 N/A				
Angle: +/-0.2 Degree				



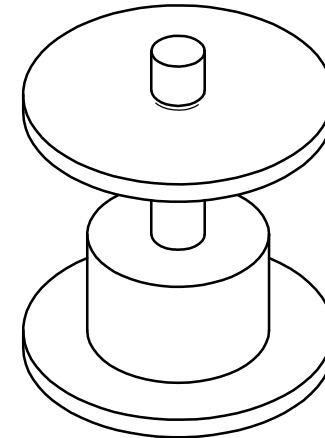
SECTION A-A



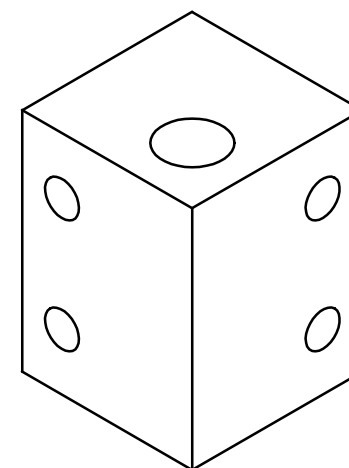
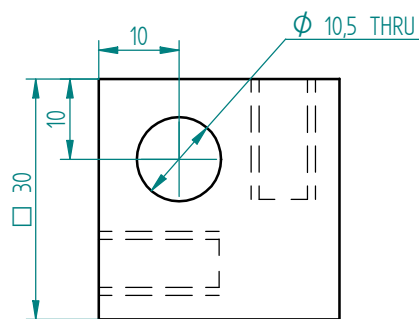
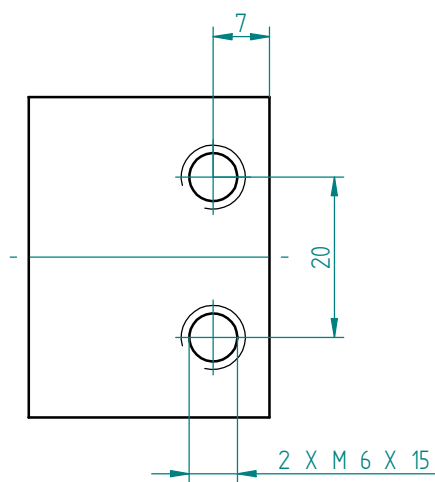
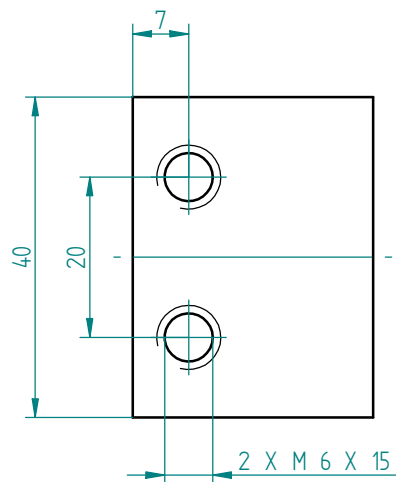
Bottom View



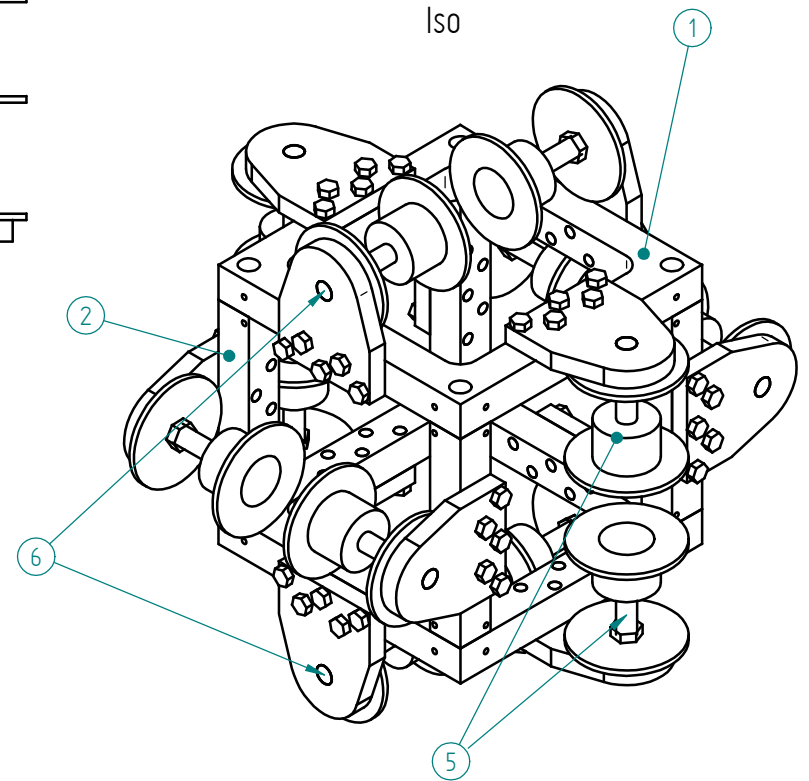
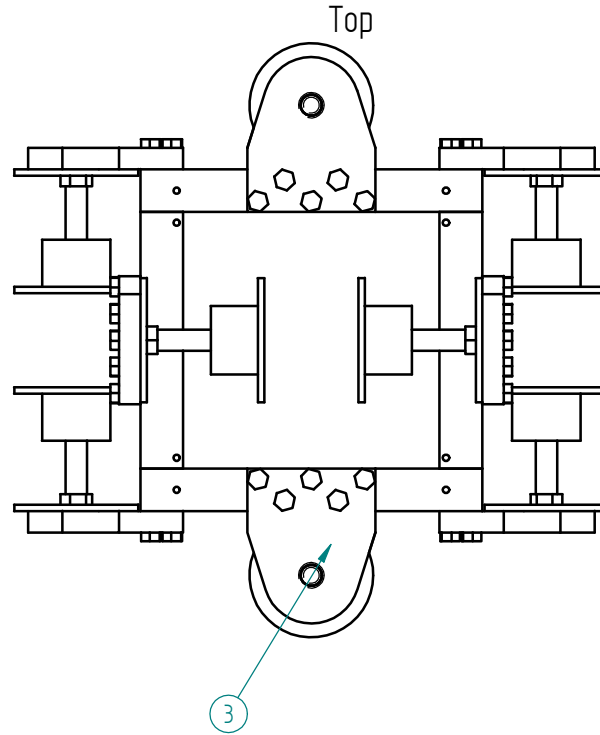
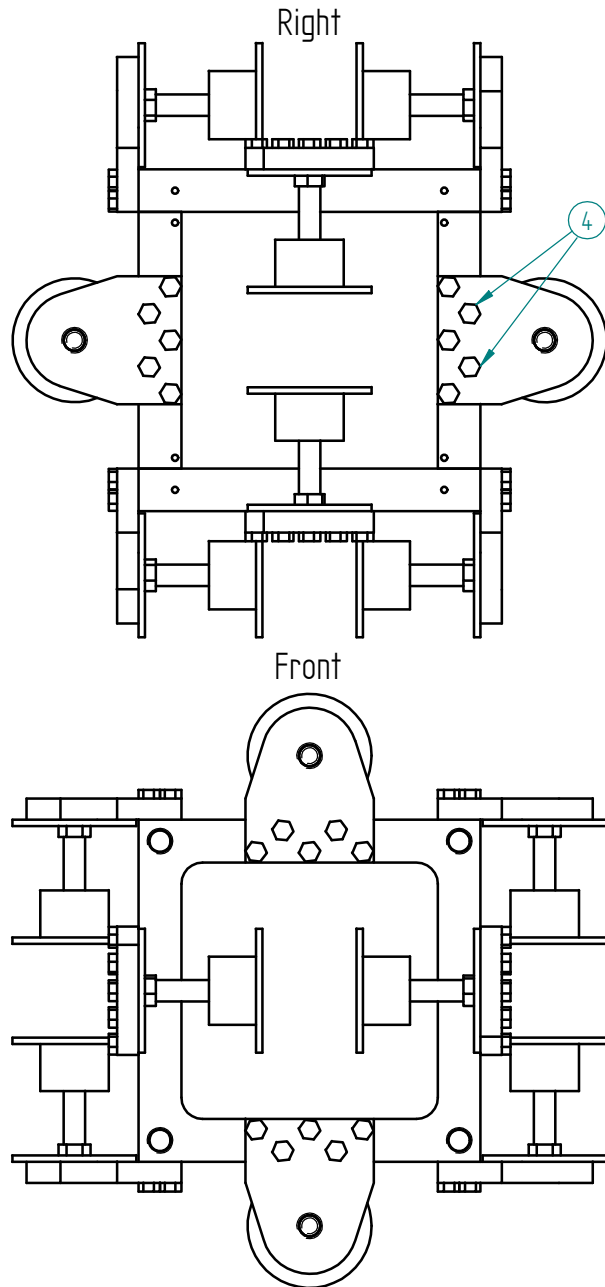
Top View



Tolerance	Name:	Tao Zhu	Mobile:	0413647219
General Tolerance ISO 2768-f	Email:	tao.zhu@adelaide.edu.au	Supervisor & signature	Ben Cazzolato
0.5-3 +/-0.1	Project:	Six Degree of Freedom Maglev Isolator		
3-6 +/-0.1	Drawing Name:	Solenoid Core		
6-30 +/-0.1	Material:	Nylon 66	DRG Scale	1 : 1
30-120 +/-0.15	Quantity:	13	Date:	19/05/2011
400-1000 +/-0.3				
Above 1000 N/A				
Angle: +/-0.2 Degree				

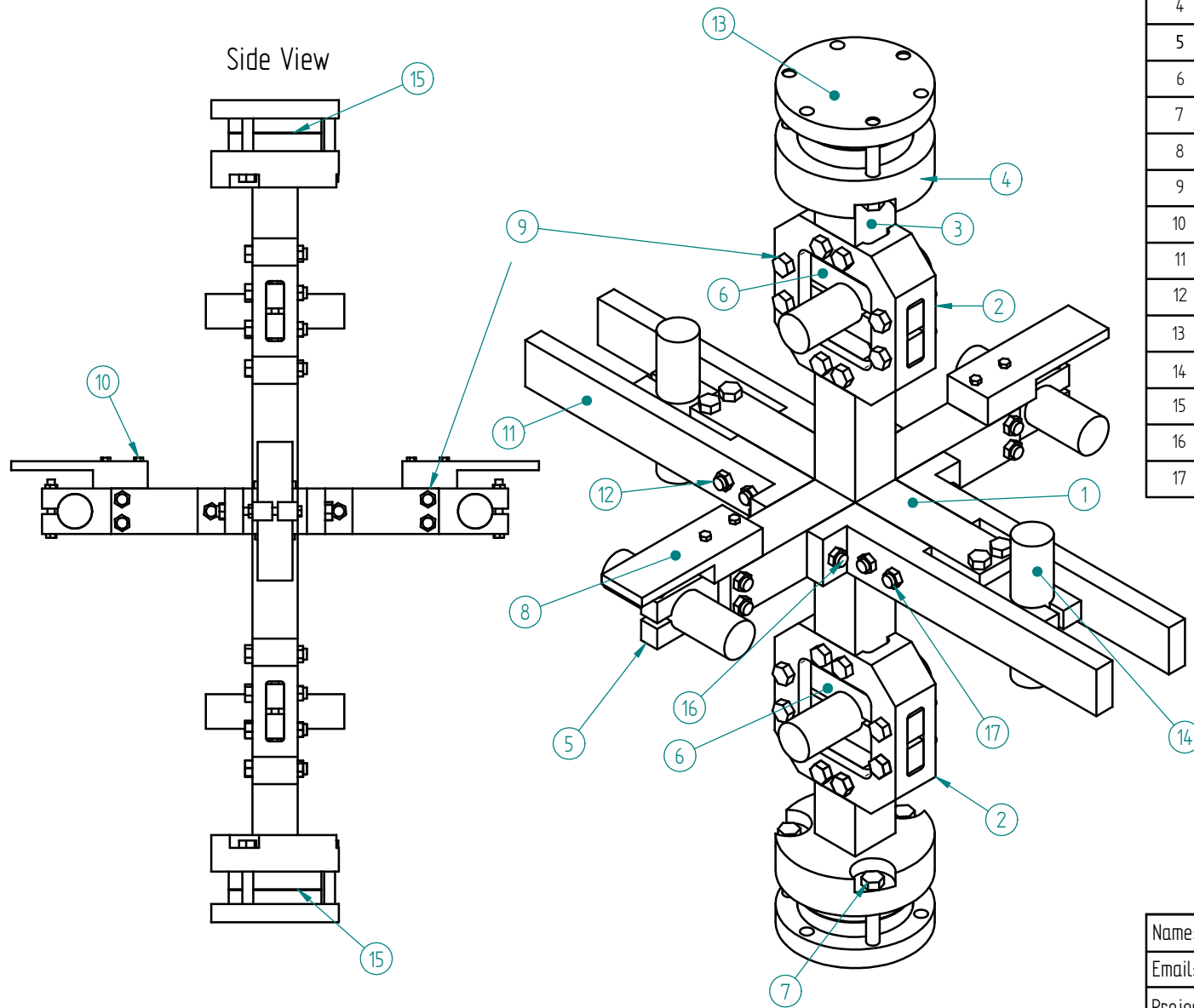


Tolerance	Name:	Tao Zhu	Mobile:	0413647219
General Tolerance ISO 2768-f	Email:	tao.zhu@adelaide.edu.au	Supervisor:	Ben Cazzolato
0.5-3 +/-0.05 3-6 +/-0.05 6-30 +/-0.1 30-120 +/-0.15 400-1000 +/-0.3 Above 1000 N/A Angle: +/-0.2 Degree	Project:	Six Degree of Freedom Maglev Isolator		
	Drawing Name:	Connecting Foot Block		
	Material:	Aluminium 6061-T6	DRG NO.	20
	Quantity:	8	Date:	16/11/2010

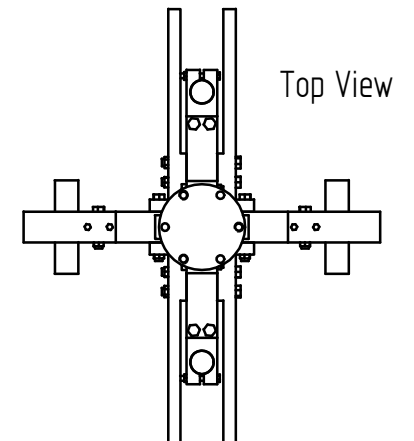


Part No.	Part Name and Description	DRG NO.	Quantity
1	Mid supporting plate	7	2
2	Mid connection bar	8	4
3	Coil holder	9	12
4	M6 X 30mm Hex Head Bolt & Washer 316 Stainless Steel	N/A	60
5	Solenoid Core	19	12
6	M10 X 13mm Hex Head Bolt & Washer 316 Stainless Steel	N/A	12

Name:	Tao Zhu	Mobile:	0413647219
Email:	tao.zhu@adelaide.edu.au	Supervisor & Signature	Ben Cazzolato
Project:	Six Degree of Freedom Maglev Isolator		
Drawing Name:	Center frame-asm		
DRG NO.	21	Date:	04/11/2010
Quantity:	1		

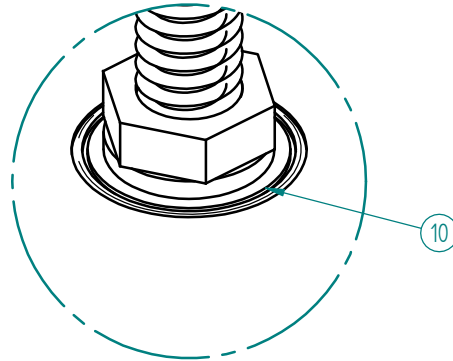
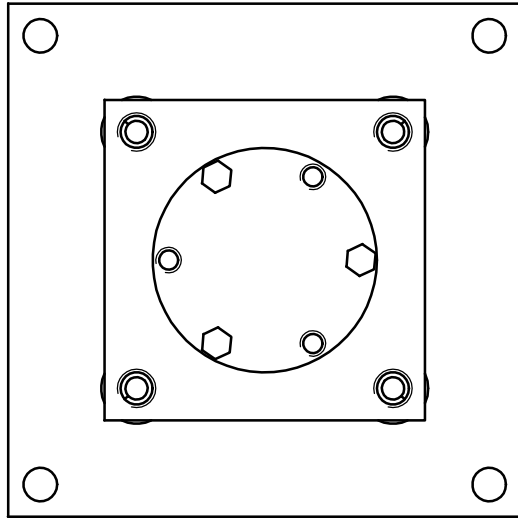


Part No.	Part Name and Discription	DRG NO.	Quantity
1	Core frame	1	1
2	Top magnet connector	4	2
3	Top magnet support connector	5	2
4	Top magnet seat plate	6	2
5	Side magnet holder	2	4
6	Square side magnet holder	3	2
7	M6 X 40mm Hex Head & Washer 316 Stainless Steel	N/A	8
8	Sensor reference plate	15	3
9	M6 X 30mm Hex Head Bolt & nut & Washer 316 Stainless Steel	N/A	24
10	M3 X20mm Hex Head Bolt & Washer 316 Stainless Steel	N/A	12
11	Load connector	14	4
12	M6 X 60mm Hex Head Bolt & nut & Washer 316 Stainless Steel	N/A	4
13	Magnet cap	16	2
14	Side magnet (supplied)	N/A	6
15	Top magnet (Supplied)	N/A	2
16	M6 X 40mm Hex Head Bolt & nut & Washer 316 Stainless Steel	N/A	2
17	M6 X 60mm Hex Head Bolt & nut & Washer 316 Stainless Steel	N/A	4



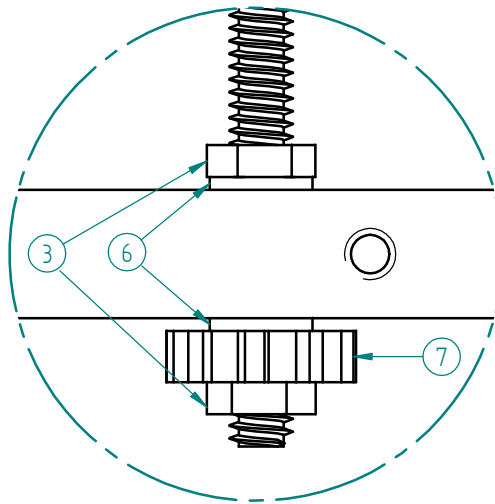
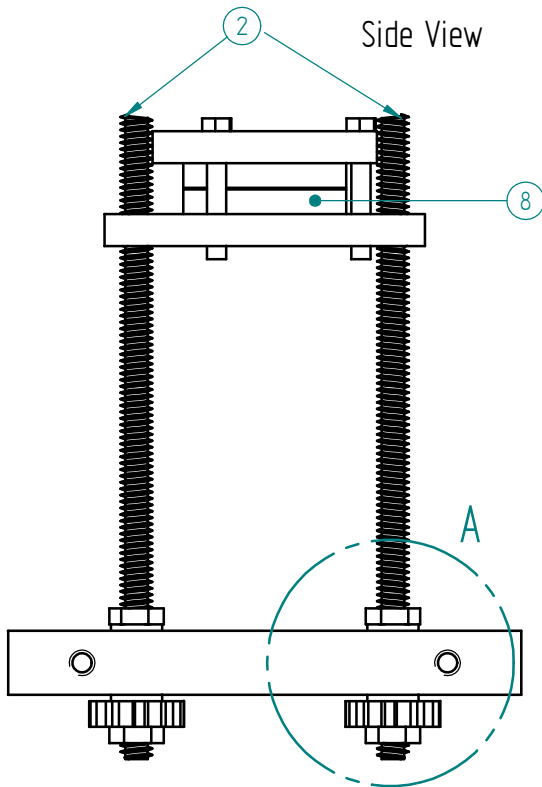
Name:	Tao Zhu	Mobile:	0413647219
Email:	tao.zhu@adelaide.edu.au	Supervisor & Signature	Ben Cazzolato
Project:	Six Degree of Freedom Maglev Isolator		
Drawing Name:	Core-asm		
DRG NO.	22	Date:	04/11/2010
Quantity:	1		

Top View



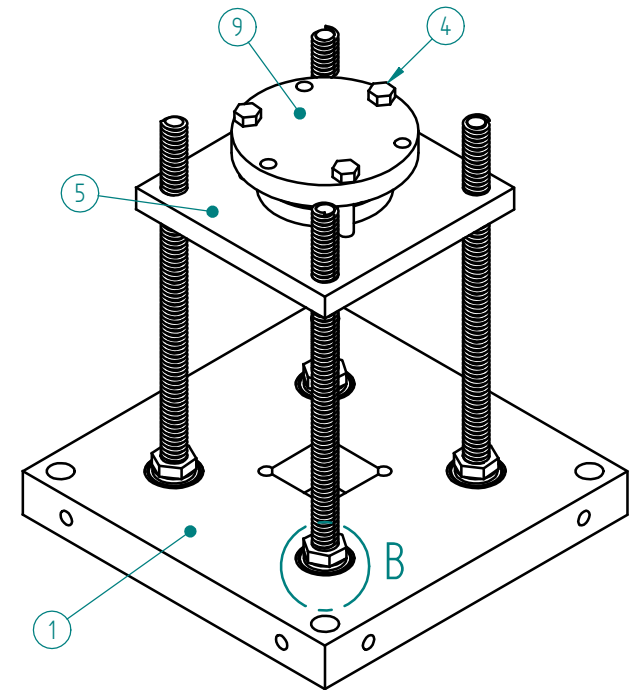
DETAIL B

Side View

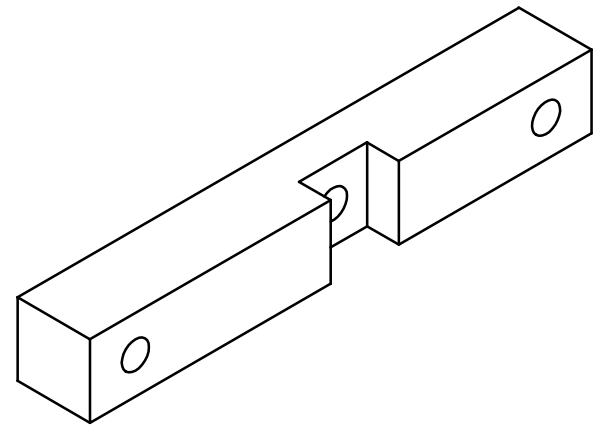
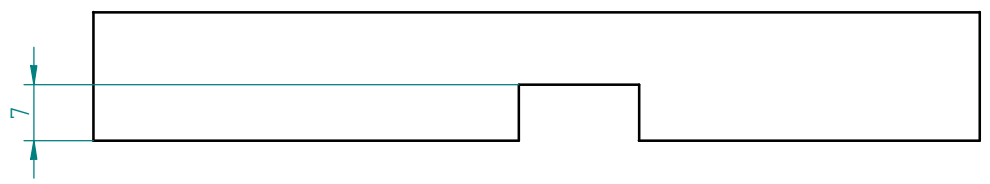
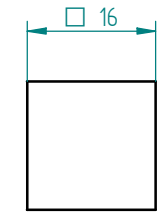
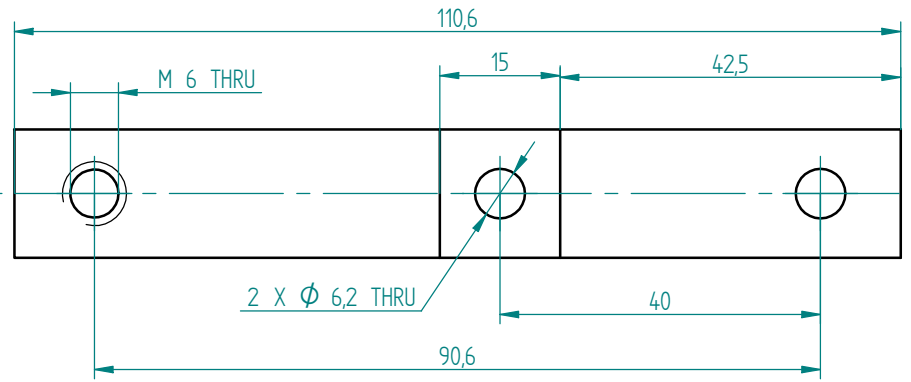


DETAIL A

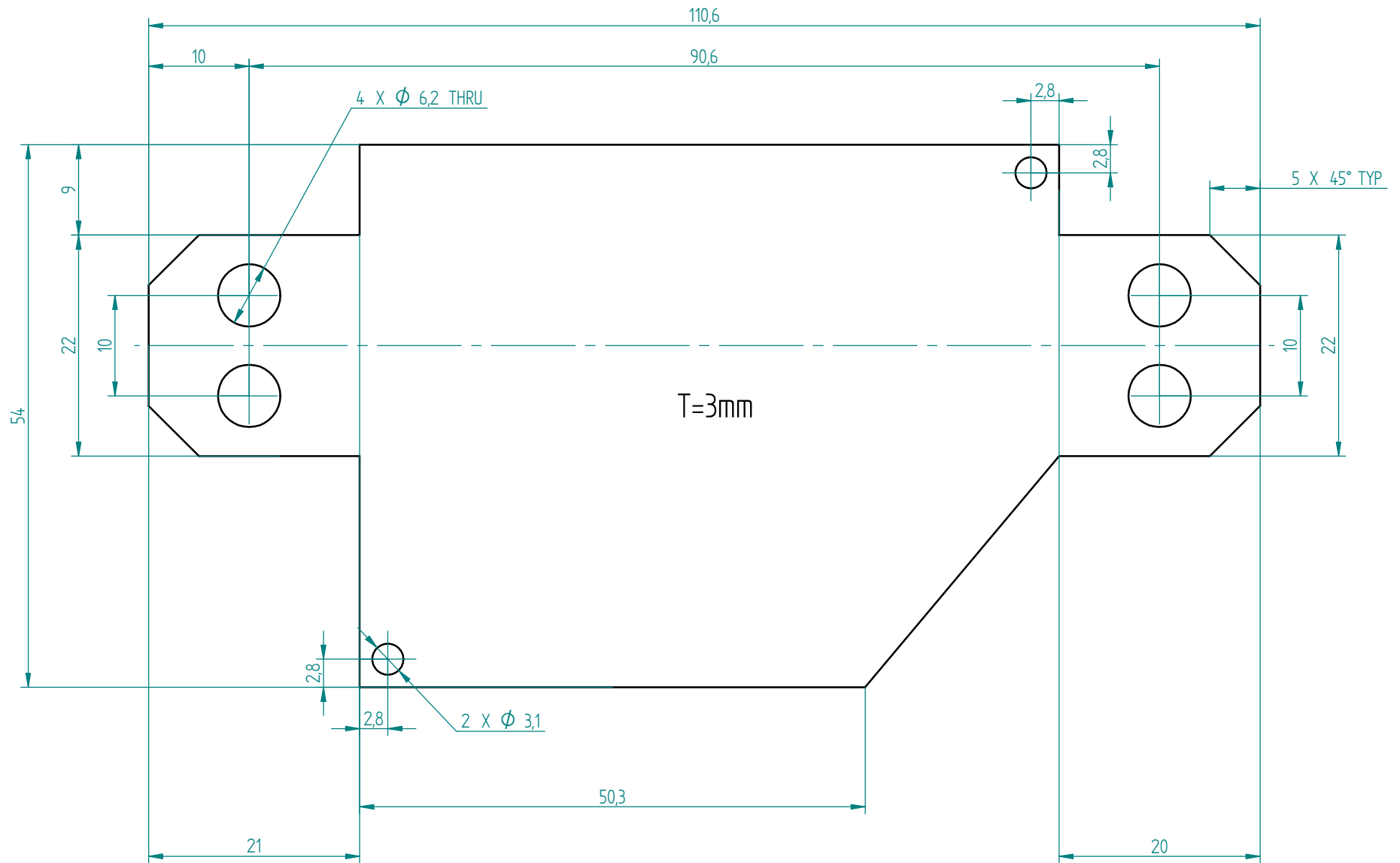
Part No.	Part Name and Description	DRG NO.	Quantity
1	Top Supporting Plate	11	1
2	L=200mm M10 316Stainless steel Threaded Rod	N/A	4
3	M6 Nut 316 Stainless steel	N/A	8
4	M6 X 40mm Hex Head Bolt & Washer 316 Stainless steel	N/A	3
5	Top magnet holder	13	1
6	10mm ID 316 Stainless steel washer	N/A	8
7	Aluminium tooth pulley (supplied)	N/A	4
8	Top magnet (supplied)	N/A	1
9	Magnet cap	16	1
10	10 ID 22 OD Ball bearing (supplied)	N/A	8



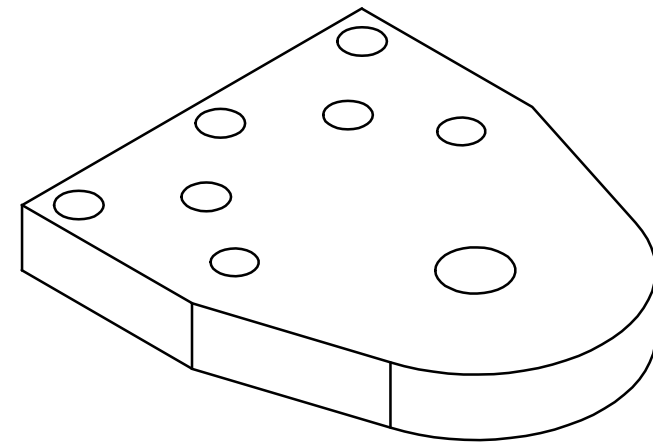
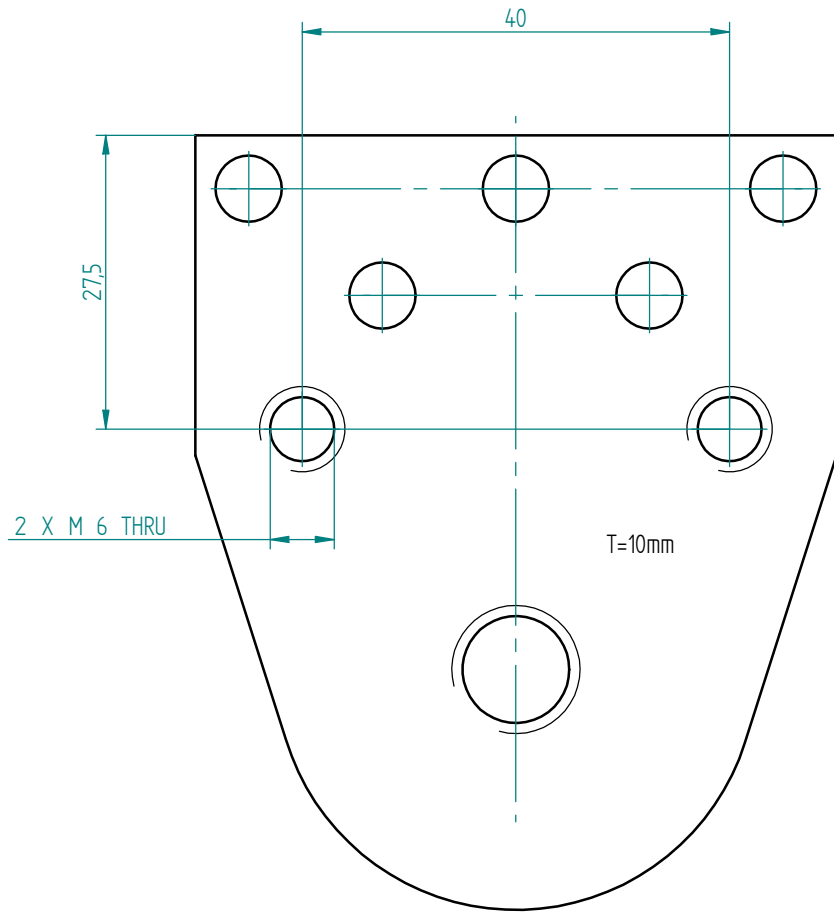
Name:	Tao Zhu	Mobile:	0413647219
Email:	tao.zhu@adelaide.edu.au	Supervisor & Signature	Ben Cazzolato
Project:	Six Degree of Freedom Maglev Isolator		
Drawing Name:	Top magnet support-asm		
DRG NO.	23	Date:	03/11/2010
Quantity:	2		



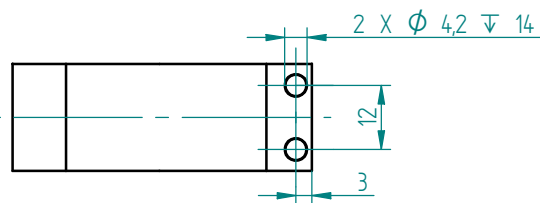
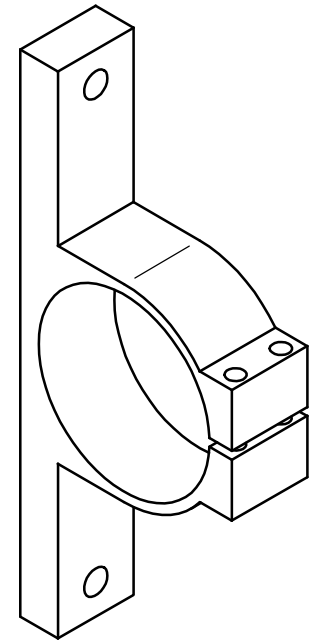
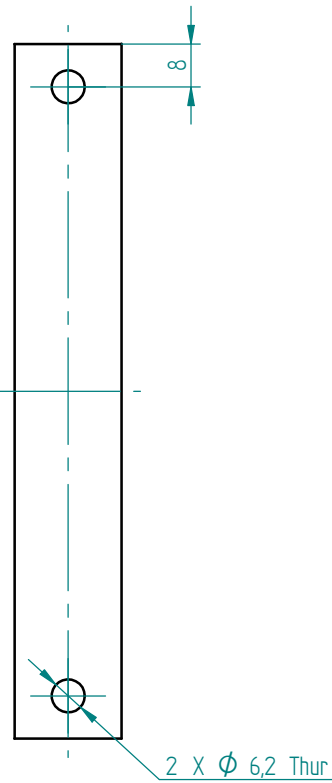
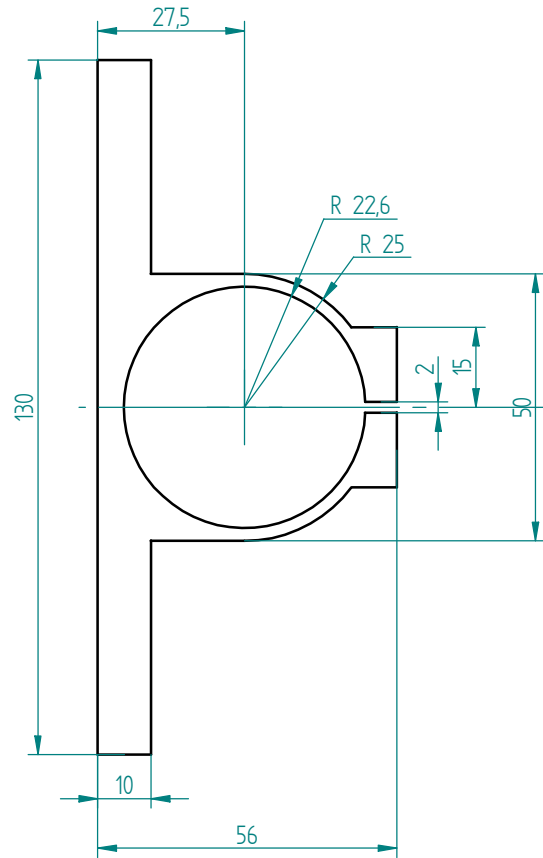
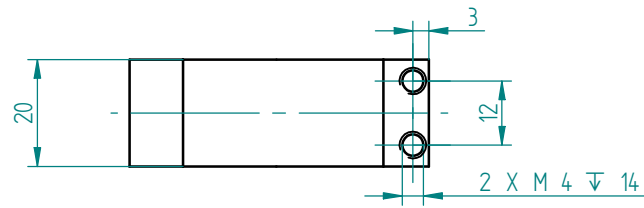
Tolerance	Name:	Tao Zhu	Mobile:	0413647219
General Tolerance	Email:	tao.zhu@adelaide.edu.au	Supervisor Sig.	
0,5-3 3-6 6-30 30-120 400-1000 Above 1000 Angle: +/- 0,2 Degree	+/- 0,1 +/- 0,1 +/- 0,2 +/- 0,3 +/- 0,6 N/A	Project:	Six Degree of Freedom Maglev Isolator	
		Drawing Name:	Laser sensor connection bar	
	Material:	Aluminium 6061-T6	Checked by	Michael Riese
	Quantity:	6	Date:	13/01/2011 DRG NO 24



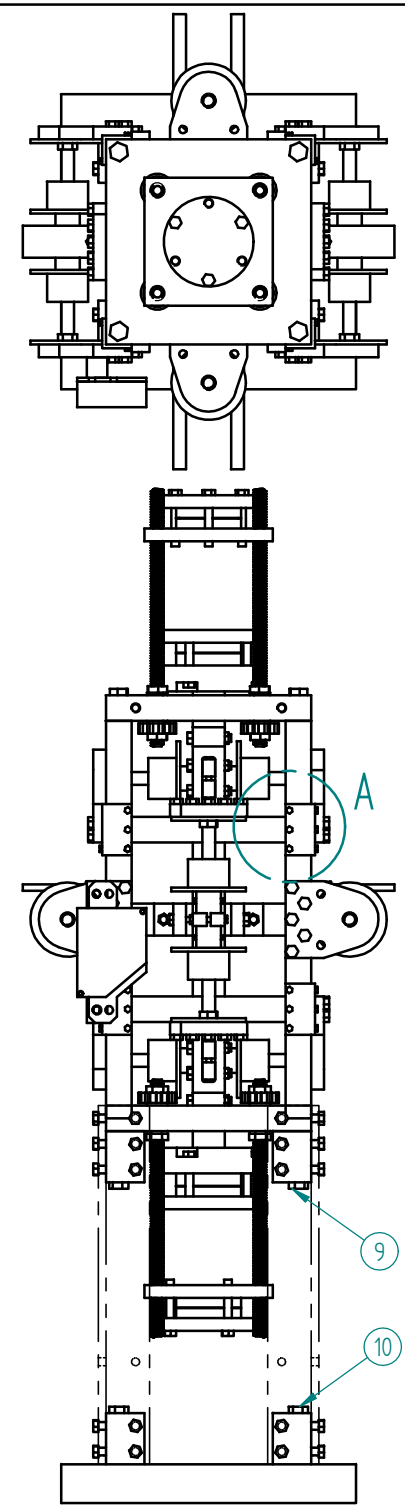
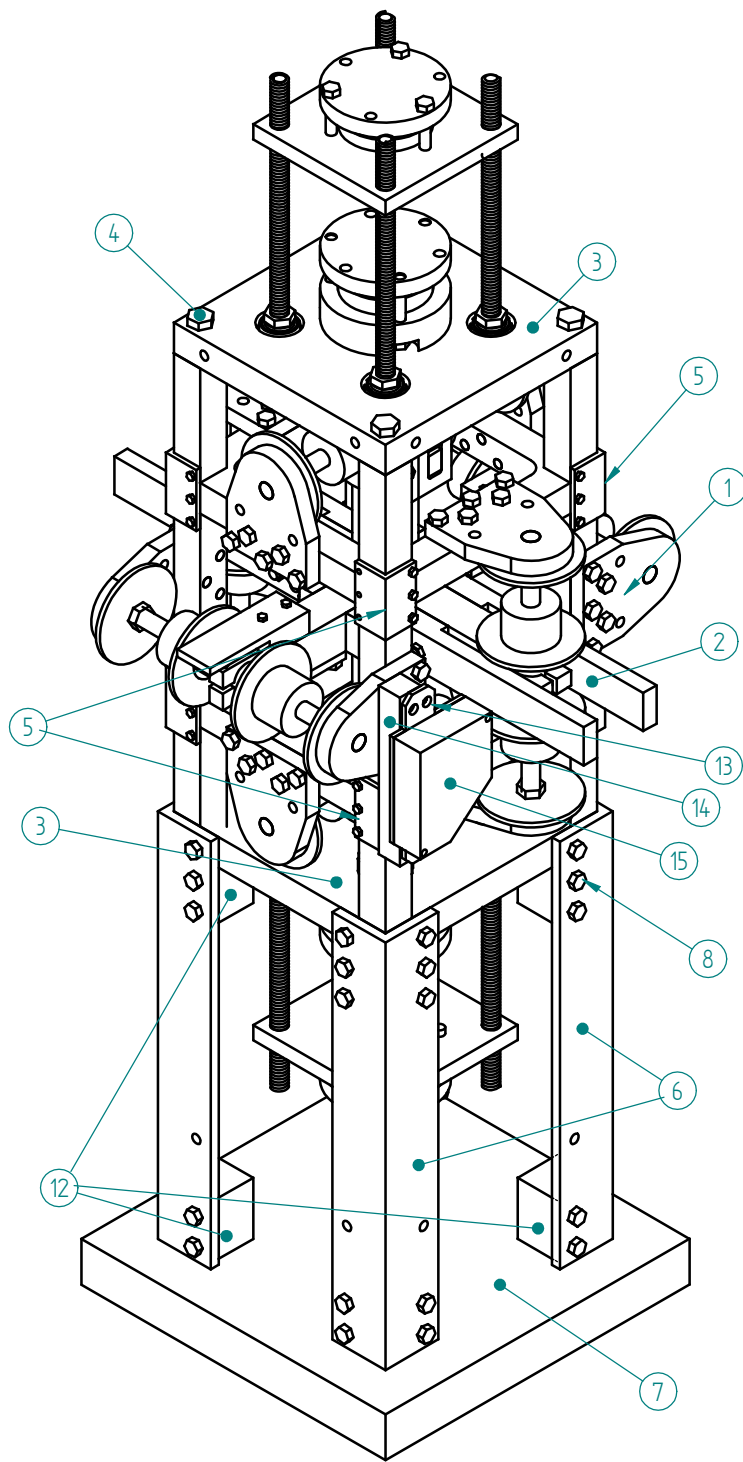
Tolerance	Name:	Tao Zhu	Mobile:	0413647219
General Tolerance	Email:	tao.zhu@adelaide.edu.au	Supervisor Sig.	
0.5-3	+/-0.1	Project:	Six Degree of Freedom Maglev Isolator	
3-6	+/-0.1	Drawing Name:	Laser sensor connection plate	
6-30	+/-0.2	Material:	Aluminium 5083-H116	Checked by Michael Riese
30-120	+/-0.6	Quantity:	6	Date: 10/01/2011
400-1000	+/-0.6			DRG NO 25
Above 1000	N/A			
Angle:	+/-0.2 Degree			



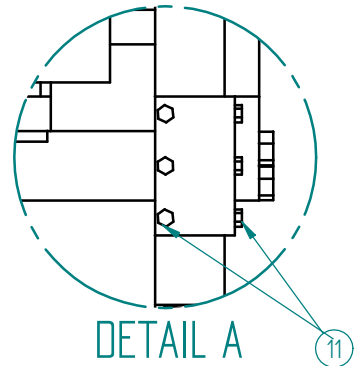
Tolerance	Name:	Tao Zhu	Mobile:	0413647219
General Tolerance ISO 2768-f	Email:	tao.zhu@adelaide.edu.au	Supervisor & signature	Ben Cazzolato
0.5-3 +/-0.05	Project:	Six Degree of Freedom Maglev Isolator		
3-6 +/-0.05	Drawing Name:	Modification to DRG 9 Coil Holder		
6-30 +/-0.1	Material:	Aluminium 6061-T6	DRG NO.	9
30-120 +/-0.15	Quantity:	12	Date:	17/10/2010
400-1000 +/-0.3				
Above 1000 N/A				
Angle: +/-0.2 Degree				



Tolerance	Name:	Tao Zhu	Mobile:	0413647219
General Tolerance	Email:	tao.zhu@adelaide.edu.au	Supervisor:	Ben Cazzolato
0.5-3 3-6 6-30 30-120 400-1000 Above 1000 Angle: +/- 0.2 Degree	+/- 0.1 +/- 0.1 +/- 0.1 +/- 0.15 +/- 0.3 N/A	Project:	Six Degree of Freedom Maglev Isolator	
Drawing Name:		Motor mounting bracket		
Material:	Aluminium	Version:	1	
Quantity:	1	Date:	16/05/2011	



Part No.	Part Name and Discription	DRG NO.	Quantity
1	Center frame-asm	21	1
2	Core-asm	22	1
3	Top magnet support-asm	23	2
4	M10 X 130mm Hex Head Bolt & Washer 316 Stainless steel	N/A	4
5	L side fitting	10	8
6	Supporting leg	17	4
7	Base plate	18	2
8	M6 X 15mm Hex Head Bolt and Washer 316 Stainless steel	N/A	40
9	M10 X 170mm Hex Head Bolt & Washer 316 Stainless steel	N/A	4
10	M10 X 70mm Hex Head Bolt & Washer 316 Stainless steel	N/A	4
11	M3 X 10mm Hex Head Bolt & Washer 316 Stainless steel	N/A	48
12	Connecting foot block	20	8
13	Laser sensor connection plate	25	6
14	Laser sensor connection bar	24	6
15	Laser displacement sensor (supplied)	N/A	6
Note:	1. Only one (out of six) laser sensor is shown in the drawing as the installation of part 13, 14 & 15 is not required. 2. ALL bolts, nuts & washers have to be grade 316 SS. 3. Special anti-corrosion jel has to be applied on ALL Stainless Steel & Aluminium contact surfaces.		



Name:	Tao Zhu	Mobile:	0413647219
Email:	tao.zhu@adelaide.edu.au	Supervisor Sig:	
Project:	Six Degree of Freedom Maglev Isolator		
Drawing Name:	Complete assembly-asm		
Version:	1	Date:	03/01/2011
Quantity:	1	Checked by	Michael Riese